The University Of Sheffield.

School of

Biosciences

The influence of non-sensory cells on the development of mammalian inner hair cells.

Piece Yen

July 2022

Supervisors: Professor Walter Marcotti

The University of Sheffield
Faculty of Science
School of BioSciences

Dissertation submitted to the University of Sheffield
in fulfilment of the requirements for the degree of

Doctor of Philosophy

Acknowledgements

I would like to thank my supervisor Prof Walter Marcotti for providing me this opportunity to study the physiology of developing cochlear hair cells. Together we faced a lot of bumps in the project, the most difficult one being the COVID lockdown, but we endured them all and managed to produce an interesting study. I appreciate the full trust from him on my autonomy and his strict challenging on the science. One thing I will be forever grateful from him is the full studentship which allows me to continue my career in academic when I was almost changed my path due to unable to pay the extra international tuition. I hope I have developed into a good scientist worthy of this award and have brought a positive influence into the lab.

This project received help from so many people. Without them, I could not have learnt and done all of these things in the highest standard of quality. I would like to thank Dr Federico Ceriani and Dr Francesca De Faveri for their help with the calcium imaging. Without their proficiency I would only have had half of the n numbers doing the experiments on my own. I would like to thank Mrs Michelle Bird for helping me monitor the animals so I can get a more accurate age from them, which is crucial for Cre-induction. I would like to thank the lab technicians Ms Maria Pakendorf, Mrs Laila Moushtaq-Kheradmandi and Ms Catherine Gennery for their help with the genotyping. I would like to thank my jolly good fellow PhD students and all other members in the shared lab for the company and the brainstorm when there's a wall in front of anyone. It was a great office/lab space that I really enjoyed working in there.

Last but not the least, I have to thank my friends and family. Thanks to my brother and parents for tolerating my long absence from the family. A tiny joke from them worth being archived forever: after four long years of PhD study, my parents still think my job is feeding the mice… They've got to be joking, right? Big thanks to Dr Adam Carlton for being such a good friend on so many aspects. You're like an English little brother to me. I hope one day we can go grab a pint and play games with my actual little brother. The special mentioning goes to my dearest wife Dr Jing-Yi Jeng. For 47% of my entire life (let's call it half) we've been through highs and lows together. She has always supported and respected me; always been my best friend in life, and the best rival on the pursuit of science, pushing me to be my better self. Thank you Ginny, and I will always love you until death do us apart.

Summary

Immature auditory inner hair cells (IHCs) in the mammalian inner ear are capable of firing spontaneous calcium-dependent action potentials, which are required for their maturation into sensory receptors (Johnson *et al.*, 2013; Johnson *et al.*, 2017).

Recent studies revealed that non-sensory cells can regulate the frequency and synchronicity of the action potentials of nearby IHCs by depolarizing them with ATP released through connexin hemichannels (Tritsch *et al.*, 2007; Tritsch & Bergles, 2010). The released ATP also induces a secondary fluid secretion from non-sensory cells, which was reported to depolarize the IHCs, thus synchronising their electrical activity (Tritsch *et al.*, 2007; Tritsch & Bergles, 2010; Wang & Bergles, 2015). However, the role of this secondary event in the maturation of IHC remains unknown.

TMEM16A knockout mice were shown to prevent the fluid secretion from non-sensory cells and thus reduce the action potential activity in the IHCs (Wang & Bergles, 2015). In this study, I set out to explore the influence of the TMEM16A-mediated fluid secretion on the action potential activity in the IHCs and their maturation. To achieve this goal, I used the Cre-induction system to conditionally knockout TMEM16A in the non-sensory cells of the mouse cochlea, isolating the ATP signalling from the subsequent TMEM16A-mediated fluid secretion.

Based on the results documented here, cochlea-wide deficiency of TMEM16A in the non-sensory cells decreased the instances of spontaneous action potentials in immature IHCs. However, their electrophysiological properties did not change at all, including the pattern of the spontaneous action potentials, current-voltage response, and the threshold of excited action potential. Calcium imaging showed a disruption on the synchronicity within at least 8 nearby IHCs in TMEM16A-deficient animals. Knocking out TMEM16A produced a delay on the development, where some but not all of the IHCs retained their immature phenotype after hearing onset. Nevertheless, all of the sampled IHCs gained their functional electrophysiological properties at the fourth postnatal weeks.

These findings show that TMEM16A-mediated fluid secretion regulates the firing rate of the spontaneous action potential in immature IHCs. However, this secondary event might not directly participate in the functional maturation of IHCs. ATP signalling alone is likely to be enough for driving IHCs towards their mature phenotype.

Contents

List of Figures

List of Tables

List of Appendix

Abbreviations (alphabetical)

ACh	acetylcholine
AZ	activation zone
BM	basilar membrane
CICR	calcium-induced calcium release
CaBP	calmodulin-like calcium binding protein
CF	characteristic frequency
DIC	differential interference contrast (filter/microscopy)
EP	endocochlear potential
$[K^+]_e$	extracellular K^+ concentration
IPSP	inhibitory post-synaptic potential
IBC	inner border cells
IHC	inner hair cell
IPhC	inner phalangeal cell
ISI	inter-spike interval
$[Ca^{2+}]_i$	intracellular calcium level
KO	knocking/knocked out (a specific gene)
BK	large conductance calcium-activated potassium (channels)
LOC	lateral olivary complex
MET	mechano-electro-transducer
MOC	medial olivary complex
nAChR	nicotinic acetylcholine receptor
OHC	outer hair cell
P2XR, P2YR	P2X or P2Y purinoreceptors
P*n*	postnatal day *n*
RRP	readily-releasable pool
RyR	ryanodine receptor
HC	sensory hair cell
SGN	spiral ganglion neuron
SAP	spontaneous action potential
SC	supporting cell
Syt	synaptotagmin
TM	tectorial membrane
TEA	tetraethylammonium chloride
TMC	transmembrane channel-like (protein family)
Vm	transmembrane potential; membrane potential
VGCC	voltage-gated calcium channels

Chapter 1 General introduction

1.1 Auditory System in Mammalian

While the saying goes "not all pyramids are built the same", all mammalian ears are in fact built almost the same. They all originated from an ancient ear dated back to Triassic period (Manley, 2012). The morphology of the ear varies among species in size and structure, but mammalian ear usually consists of three parts, the outer, middle, and inner ear. The outer ear includes the pinna and the auditory canal (Figure 1.1) and funnels sound-induced vibrations in the like a horn. The tympanic membrane, known as the "ear drum", located at the end of the ear canal and borders the outer and mid ear. The tympanic membrane and the three ossicles reside in the middle ear. When sound waves compress the air in the ear canal, it vibrates the tympanic membrane and the connected ossicles of the middle ear: malleus, incus, and stapes. The stapes act as a mechanical piston to compresses the fluid inside the cochlea, which together with the vestibular system forms the inner ear. The middle ear converts sound vibrations from air-medium in the outer ear into liquid-medium in the cochlea, where sound is transduced into an electric signal that can be perceived by the brain (Figure 1.1). The cells that perform this mechano-electrical transduction are called hair cells (HCs), which are the target of this study. Another important organ in the inner ear is the vestibular organ, but it will not be covered here.

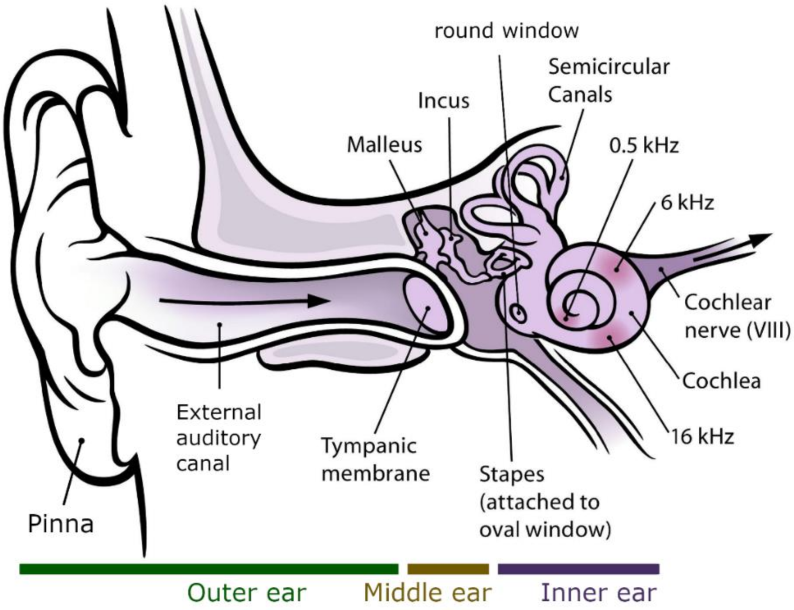

Figure 1.1 Coronal section view of human ear.

Cartoon depicting the anatomical structure of a human ear in a coronal section view, starting with pinna at the left which, together with the auditory canal, form the outer ear (marked green). The tympanic membrane (ear drum) separates outer and mid ear (yellow), in which reside the ear ossicles; malleus, incus, and stapes. The inner ear (purple) consists of two important parts; the cochlea organ necessary for hearing and the vestibular system (semi-circular canals) necessary for the sense of balance. The snail-shaped cochlea is a tonotopic frequency analyser, with the tip of the coil sensing lower frequencies and the bottom of the coil sensing higher frequencies. The auditory nerves run through the middle of the cochlea and route towards auditory brain stem from the bottom coil. Image adapted from Brockmann (2009); CC-BY-2.5.

The cochlea is a high-fidelity energy transducer as it can perceive and process sound spanning several orders of frequencies and amplitudes with high precision. Taking the human ear as an example, it can transduce sound signal from 20Hz to 20kHz with a high dynamic range, that is "from the soft click of a pin dropping to the roar of a jet engine" (Marcotti, 2012). The morphology of the cochlea looks like a liquid filled tube (Figure 1.2) rolled into snail-shaped spiral (Figure 1.1). The tip of the spiral is defined as the apex while the bottom of it is termed the base. At the centre of the spiral is the modiolus, a spongy tissue housing the cell bodies of the auditory neurons. The outer layer of the cochlea is a bony shell which has two eclipses opening at base, the round window and the oval window (Figure 1.1). The inside of the cochlea is divided into three liquid-filled ducts; the scala vestibuli, scala media, and scala tympani (Figure 1.2 B). The scala vestibuli and scala tympani sandwich the scala media in the middle to form a "tube-in-tube" configuration, and they are joined with at the helicotrema (coil hole in Greek) at the very apex (Figure 1.2 A). While Reissner's membrane separates the scala vestibuli and the scala media, the basilar membrane borders between scala media and scala tympani (Figure 1.2 B).

The three scalae are filled with two different types of liquid (Figure 1.2 B). The scala vestibuli and scala tympani are filled with perilymph, which contains a higher concentration of sodium (~138 mM) and calcium (~ 1.4 mM) ions (Sauer *et al.*, 1999), similar to normal extracellular fluid. The scala media is filled with endolymph, which has a high concentration of potassium ions (~150 mM) but a low concentration of calcium ions (~20 µM; Wangemann, 2006). This ionic gradient creates an endocochlear potential (EP) of about +80 mV between the endolymph and perilymph (Békésy, 1952). The Reissner's membrane (Figure 1.2 B) prevents the diffusion of ions and chemical compounds between perilymph and endolymph. Unlike the impermeable

Reissner's membrane, the basilar membrane (BM, Figure 1.2 B) has a relatively "leaky" structure and is permeable to the perilymph (reviewed in Glueckert *et al.*, 2018).

The BM plays a crucial role in determining the frequency selectivity of the cochlear partition. As demonstrated in the Nobel-winning experiments (Békésy, 1960), sound-induced travelling waves inside the cochlea cause the vibration of the BM at different locations depending on the acoustic frequency. This is because the characteristics of the BM gradually changes along the length of the cochlea, from being narrower and thicker towards the base to wider and thinner toward the apex (Figure 1.2 A; reviewed in Fettiplace & Hackney, 2006). Because of these morphological differences, the BM is stiffer at the base compared to its apex (Békésy, 1960; Emadi *et al.*, 2004; Teudt & Richter, 2014). Each location along the cochlea spiral has a corresponding characteristic frequency (CF) at which the BM has the maximum response, from high frequency at the base to low frequencies at the apex. These characteristics makes the cochlea a tonotopic apparatus, that is, anatomically organized with specific sound frequencies.

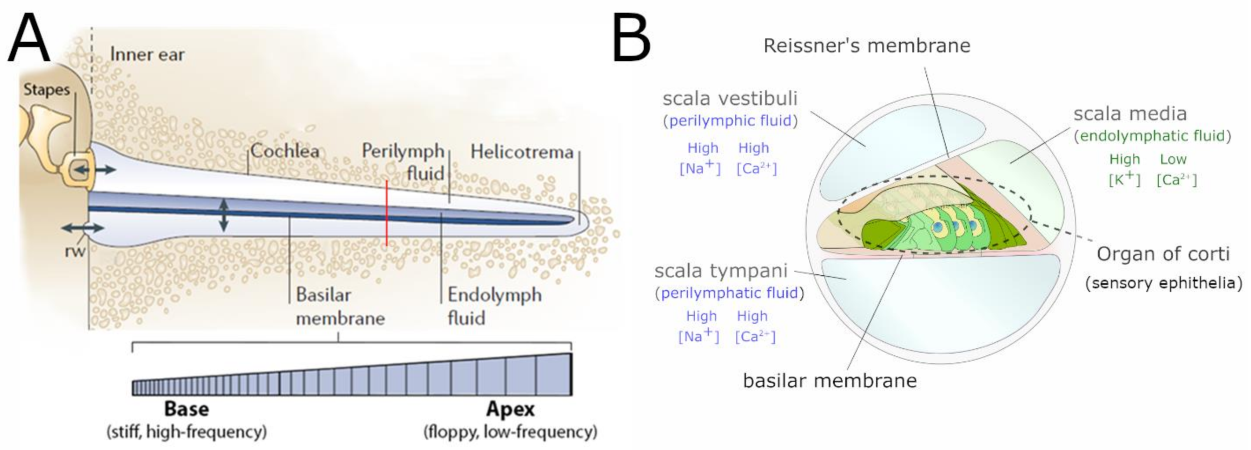

Figure 1.2 Human cochlea "unrolled".

A) An abstract sketch of the cochlear labyrinth with the helix unrolled into a straight tube. The abbreviations in the middle ears stand for: t, tympanic membrane; rw, round window. The double arrow symbols mark the direction of sound induced vibrations in corresponding anatomical structures. The red line indicates the plane of the cross-sectional view showed in B). Image in A) is adapted from Fettiplace & Hackney, 2006; B) is drawn by the author.

1.1.1 Organ of Corti

Within the cochlea, the sensory epithelia lies on top of the BM (Figure 1.2 B). Discovered and named after the Italian scientist Alfonso Giacomo Gaspare Corti, the sensory epithelia is often referred as the organ of Corti (Corti, 1851). It houses a single row of inner hair cells (IHC), and three rows of outer hair cells (OHCs; Figure 1.3). As their name suggests, each hair cell has hair bundle growing at their apical surface (endolymph side). The hair bundle looks like a staircase-shaped array that consists of actin-rich structures named stereocilia (Hudspeth, 1982). Figure 1.4 gives a clear structural view of the bundled stereocilia on OHC under scanning electron microscopy.

In addition to the HCs, there are several types of non-sensory supporting cells (SCs) in the organ of Corti. Starting from the modiolar side, inner border cells (IBCs) form a curved furrow called the inner sulcus, which marks the edge of organ of Corti (Figure 1.3, B). By the IBCs is the row of IHCs interlaced with inner phalangeal cells (IPhCs) in between.

During development, the inner sulcus region is occupied by a thick layer of epithelial cells forming the Kolliker's organ (Figure 1.3). These cells have an important role in the maturation of the auditory pathways and will be covered again in later sections (1.3.2, page 37). The Kolliker’s organ changes into a thin layer of IBCs just a few days before hearing onset. This detailed progression has not yet been mapped out but it was proposed to involve thyroid hormone dependent apoptotic pathway (Liu *et al.*, 2017; Peeters *et al.*, 2015). These cells are often referred as the “greater epithelial ridge” (GER), compared with the much slimmer “lesser epithelial ridge” (LER) at the OHC side (Figure 1.3, A).

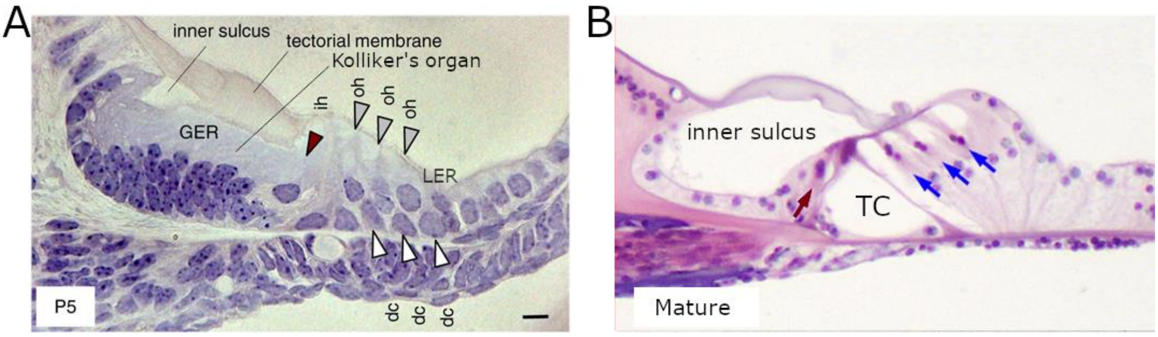

Figure 1.3 Histology of immature and mature-like organ of Corti
A) histology image of a coronal sectioned organ of Corti at the 5th postnatal day (P5; immature stage). The inner sulcus and tunnel of Corti have not formed at this age. Abbreviations are: ih, IHCs; oh, outer hair cells; dc, deiter's cells; GER, greater epithelial ridge; LER, lesser epithelial ridge. B) Mature organ of Corti has a fully hollowed inner sulcus and tunnel of Corti (TC). The conformation of hair cells is also different, with the fully elongated tectorial membrane attached to the top of the OHC (blue arrow) but not the IHC (red arrow). Images adapted from Iyer *et al.*, (2016) and Peeters *et al.*, (2015) respectively.

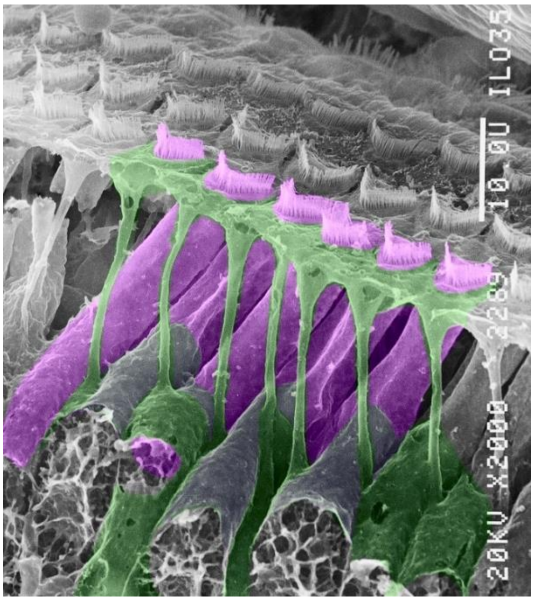

Figure 1.4 Dieter's cells and OHC under SEM.
An SEM image showing the morphology of the OHCs (magenta) with the Dieter's cells (green) surrounding them. Dieter's cells are in contact with OHCs only around their basolateral membrane and at their apical surface. Image source: Prof Andrew Forge, UCL (CC-BY-4.0).

Next to the IHCs are inner and outer pillar cells (PC). They are generally considered to be the border between GER and LER. Mature PCs form the tunnel of Corti, a hollowed structure running through the sensory epithelia and separate the row of IHCs from the OHCs (Figure 1.3, B). While IHCs are surrounded by three different types of SCs, every OHC is only associated with a Deiter's cell (DC) at their basolateral end. Each Deiter's cell raise a thin, tall stem with a flat end surface bracketing OHCs (Figure 1.4, green shaded cells).

A thick collagen-rich structure, the tectorial membrane (TM), protrudes from the edge of inner sulcus and gradually covers the hair bundles of the OHCs during the development (Figure 1.3 A & B). It plays a structural role during the sound transduction, which will be discussed briefly in the next section.

1.1.2 Transduction of sound

When sound waves compress the fluid in the cochlear duct, the vibration of the basilar membrane pushes and pulls the organ of Corti against and away from the tectorial membrane (Figure 1.5). This sound-induced displacement moves the hair bundles of the HCs and triggers the opening of the mechano-electrical transduction (MET) channels at the tip of the shorter rows of stereocilia (reviewed in Fettiplace & Kim, 2014). Cation current flows through the MET channels and depolarizes the hair cells (Figure 1.5). This is a key step in sound transduction to faithfully encode the phase of the vibration into graded membrane potential (V_m) in HCs.

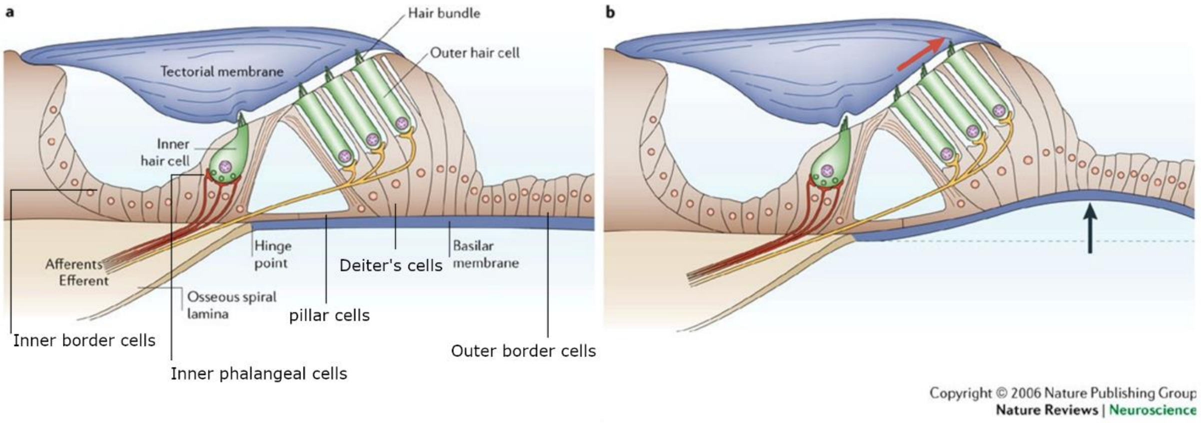

Figure 1.5 Organ of Corti in action
Transection sketches of **a**) organ of Corti in silence and **b**) sound induced BM vibration. The red arrow in b depict the direction of movement of the basilar membrane (bottom). The red arrow in b) indicates the flow of endolymph and the movement of stereocilia when the BM moves upward. Image adapted from Fettiplace & Hackney (2006).

OHCs have a special property called electromotility, which allows them to elongate and contract at different V_m during the cycling of sound waves (Mammano & Ashmore, 1993). With the tip of their stereocilia anchored into the tectorial membrane, OHCs act as a linear motor to actively enhance the vibration of the BM (Figure 1.5). This process can amplify the sound signal up to a thousand fold and hence the OHCs are named the "cochlear amplifier" (Cheatham *et al.*, 2004; Gold *et al.*, 1948).

The MET-current-triggered depolarization in the IHCs leads to the release of the neurotransmitter glutamate from their afferent synapses. The number of vesicles released by IHC is proportional to the receptor potential induced by the MET current. In this manner, IHCs encodes the amplitude of a sound signal at their characteristic frequency. Unlike OHCs, the hair bundles on the IHCs do not touch the tectorial membrane, but is instead suspended in the endolymph. As a result, their displacement solely relies on the endolymph flow created by the movement of the organ of Corti, which therefore highlights the importance of cochlear amplification. If the cochlear amplification is impaired, the hearing threshold could elevate 45-60 dB SPL in all frequencies, causing profound hearing loss (Cheatham *et al.*, 2004).

Although non-sensory cells do not directly participate in sound transduction, they are critical for maintaining a physiological environment around the hair cells to allow them function properly. For instance, IBC and IPhC are responsible for the clearance of glutamate released from IHC (Furness & Lawton, 2003; Furness & Lehre, 1997; Hakuba *et al.*, 2000). They are also involved in the maintenance the endocochlear potential via gap junctions, which connects the non-sensory cells into a huge cellular network and enable the recycle and active transportation of potassium ions (K^+) from the perilymph into the endolymph (Cohen-Salmon *et al.*, 2002; Rickheit *et al.*, 2008; Teubner *et al.*, 2003).

1.1.3 Innervation of the Inner Ear

In the matured cochlea, afferent nerve fibres innervate both IHCs and OHCs, while efferent fibres only innervate OHCs. (Figure 1.6). Most afferent fibres (around 95%) are myelinated type I spiral ganglion neuron (SGN) (Burda & Branis, 1988; Keithley & Feldman, 1982; Pujol *et al.*, 1998). Each type I SGN only forms a single synapse onto an IHC, which itself can form up to 20 afferent synapses, depending on its tonotopic location (Liberman *et al.*, 1990; Slepecky, 1996). The remaining 5% of SGNs are smaller, unmyelinated type II fibres that can innervate multiple OHCs (Berglund & Ryugo, 1987). The functional role of type II SGNs has not been fully explored. They have extremely low efficacy of excitation, which is not favoured during sound transduction (Weisz *et al.*, 2009; Weisz *et al.*, 2012). Some studies portraits them as nociceptors which only activate upon excessive sound stimuli and modulate the activity of OHCs through an inhibitory efferent reflex. However, this hypothesis is still under debate and more evidence is required (Froud *et al.*, 2015; Liu *et al.*, 2015; Nayagam *et al.*, 2011).

The cholinergic efferent fibres innervate the OHCs from the medial olivary complex (MOC) during the maturation of the cochlea, and remain in contact with the OHCs throughout the lifespan of the animal (Vicencio-Jimenez *et al.*, 2021). In contrast, IHCs are innervated by a different population of efferent neurons from the lateral olivary complex (LOC), which only maintain axosomatic synapses before hearing onset. After that, these efferent neurons innervate and modulate type I SGNs with axodendritic synapses. The input from efferent synapse has been proven critical to the development of IHC (Johnson *et al.*, 2013), and this synaptic shift is often used to define the developmental state of the organ of Corti (Figure 1.7).

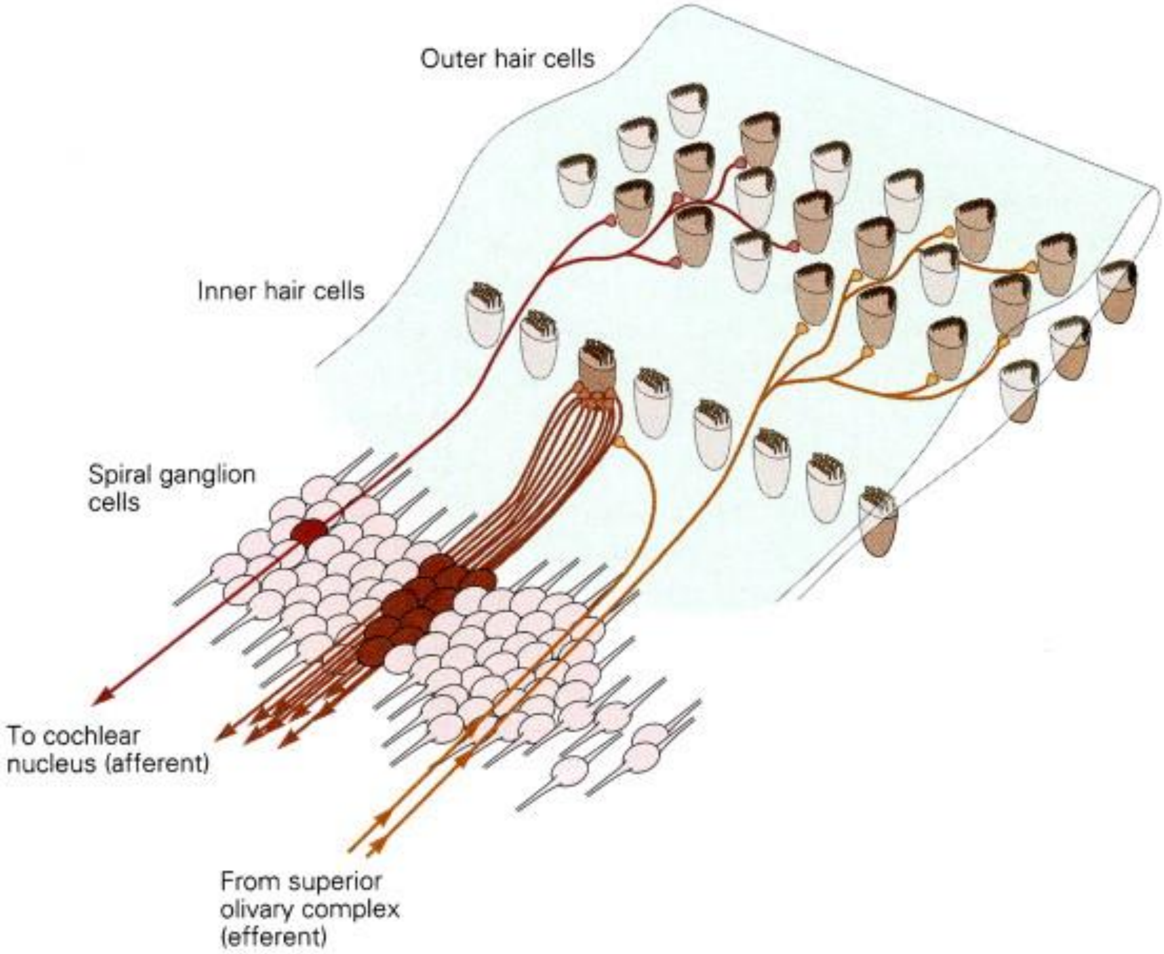

Figure 1.6 Innervation pattern in the mature organ of Corti.
A cartoon figure representing the wiring of nerve fibres in the cochlear sensory epithelia. With their somata gather in the modiolus (red cells at the bottom of the figure), type I spiral ganglion neurons (SGNs) innervate IHCs in a one-to-one manner and one type II SGNs innervates multiple OHCs. Efferent fibres are painted in yellow, and innervate OHCs directly but form axodendritic synapses with type I SGNs instead of IHCs. Image adapted from Graven & Browne, 2008.

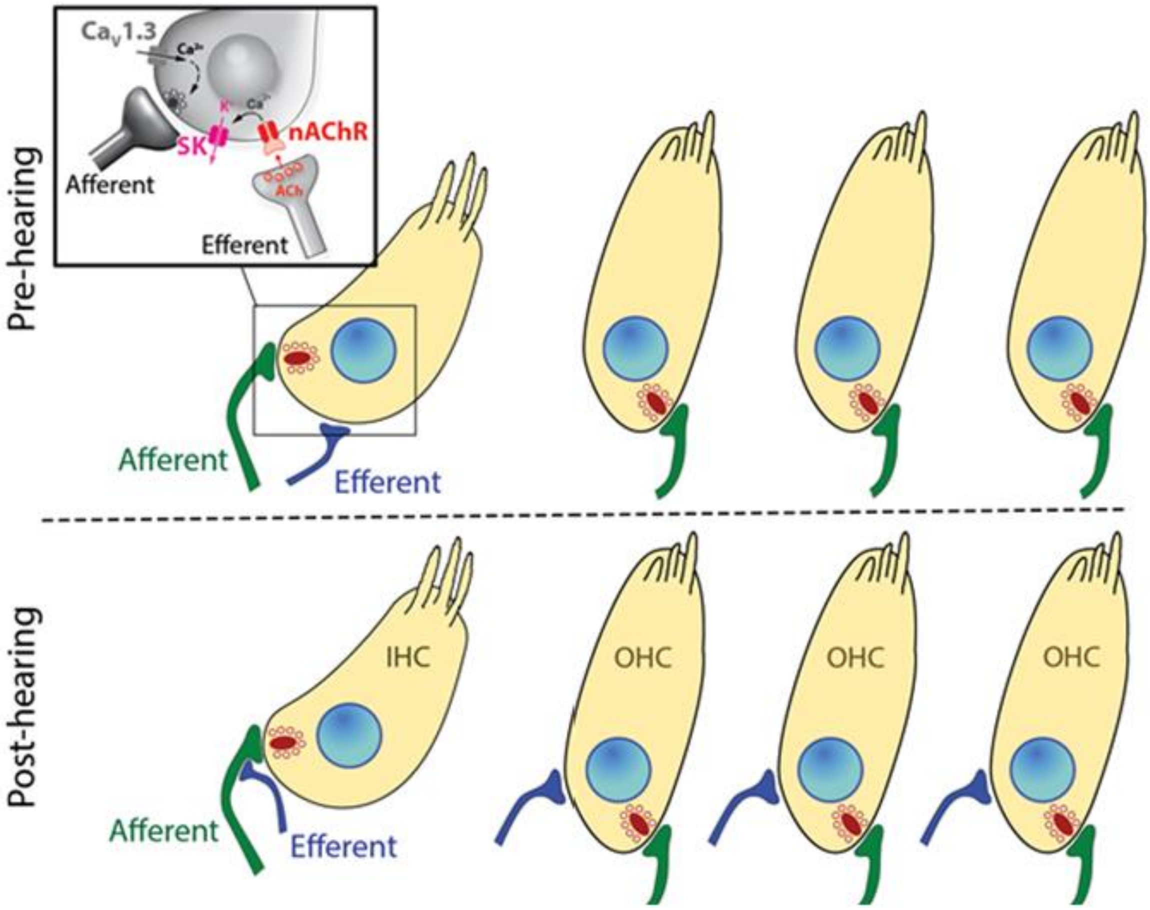

Figure 1.7 Shift of efferent innervation before and after hearing onset.
The inhibitory efferent fibre from the olivary complex (OC) forms an axosomatic synapse with IHCs before hearing onset, whereas OHCs receive their efferent innervation after the cochlea is mature. During maturation, the efferent terminals shift from IHCs to form axodendritic synapses with spiral ganglion neurons (SGNs). Unpublished drawing by the author and Dr Stuart Johnson.

1.2 The Make of a Hair Cell

Cochlear hair cells serve two very distinct roles in the transduction and amplification of sound. Hair cells are not born ready for this tough task. They must go through a maturing period where drastic changes occur from the day they first differentiated until the onset of hearing. This maturing period is critical to hearing function and is shared between mammalian species. In humans, terminal mitosis of HC precursors occurs around the 12th week of pregnancy, and undergo 5 weeks of development until the baby starts to hear in the 5th month. While HC development occurs prenatally in human, mice have a quite different timeline. The onset of hearing in most altricial rodents is about 12-13 days after birth (Figure 1.8; Roccio & Edge, 2019).

Although the timespans are not the same between humans and rodents, the key developmental stages are strikingly similar. In the following sections, I will address some of the key events occurring during development in mice, as they are a prevalent model organism in hearing research, and the model used in this study.

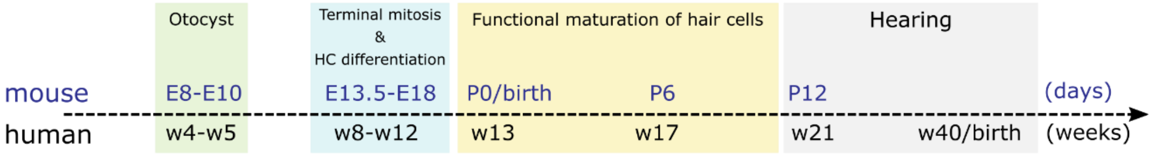

Figure 1.8 Timeline of inner ear development in mouse and human.
Though different in scale, mouse and human cochlea shares several critical check points in the maturation of the inner ear. This makes the mouse a very useful model to study the development of the auditory circuit. E*n*: *n*th embryonic days, P*n*: *n*th postnatal day. Image drawn by the author.

1.2.1 Development of hair bundles

The mechanosensitive hair bundles are unique structures projecting from the apical surface of the hair cells. Hair bundles comprise 20-300 stereocilia depending on the animal species and position of the hair cells along the cochlea (Roberts *et al.*, 1988). These stereocilia are anchored to the cuticular plate with tightly packed actin rootlets (Flock & Duvall, 1965). In mice, a lawn of actin-based microvilli starts to grow on the top of hair cells at the end of E15, followed by a single axoneme structure, the kinocilium. As the planar polarity of HCs gradually forms, the kinocilium moves to the edge of the HC, and the microvilli near it start to elongate (Figure 1.9; Schwander *et al.*, 2010).

The staircase-like structure of stereocilia first comes into shape around the time of mechanosensitivity onset. After that, the excessive microvilli are trimmed off gradually and leaves a clear membrane surface (Figure 1.10). These changes in hair bundle morphology happen earlier in basal hair cells compared with the ones in the apical region, roughly 2 days apart (Waguespack *et al.*, 2007). Hair bundles become fully mature when the elongation stops, usually around P14 in OHC and P16-18 in IHC. The height of the stereocilia is tuned to match the characteristic frequency of each hair cell. Each row has strikingly similar height between HCs in the same region, and these rows increase in height towards the lower frequency region (reviewed in Marcotti, 2012). This incredible consistency is achieved by a series of delicate protein interactions that regulate the actin assembly during the maturation. However, the detailed mechanism is not within the scope of this study and will not be discussed.

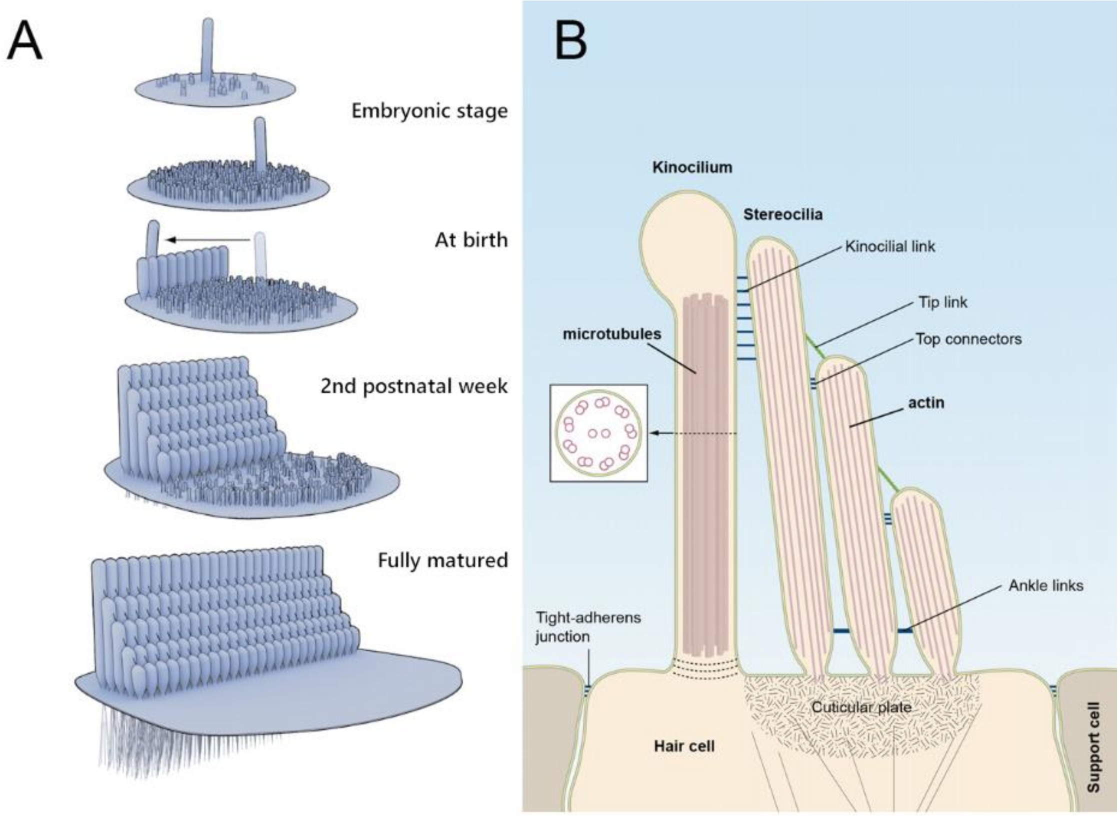

Figure 1.9 Development and structure of the hair bundles.

Cartoon drawings showns that A) stages of hair bundle maturation, and B) the nomenclature of hair bundle components, highlighting the structural difference between the kinocilia and stereocilia. Images adapted from Schwander *et al.*, 2010.

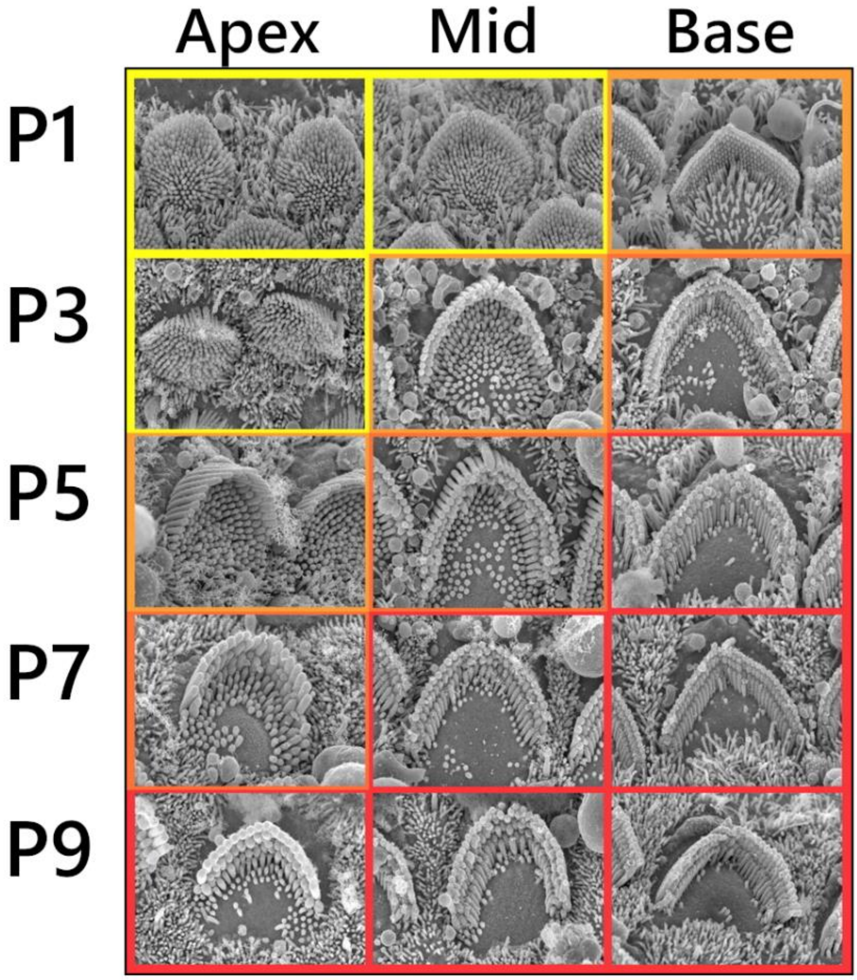

Figure 1.10 Morphological maturation of hair bundles in rodent model.
Scanning electronic microscopy of the OHC hair bundle during the postnatal development in rat. The colours from yellow to red marks the amplitude of the mechanotransduction current from none to a mature response. Each panel is 4 µm in width. Images adapted from Waguespack *et al.*, 2007.

Stereocilia are filamentous structures consisting of actin threads weaved by crosslinker proteins in between. Actin treadmilling drives the elongation of stereocilia during the development stage, but the renewal of actin molecules seems to stop in the shaft region in matured hair bundles. Isotope labelling showed that actin remodelling only happens in a small region (~0.5 µm) at the tip of the stereocilia, indicating a very low turnover rate (Zhang *et al.*, 2012).

Adjacent stereocilia are connected to each other by a variety of linkages, the most famous of which are the tip links (Pickles *et al.*, 1984). Tip links are formed by cadherin 23 (Cdh23) from the taller rows interlinked with protocadherin 15 (Pcdh15) at the tip of the lower stereocilia in a calcium dependent manner (Goodyear & Richardson, 2003; Goodyear & Richardson, 1999). The end of the tip link connecting to the taller stereocilia is embedded with a connection to the myosin VIIa motor protein complex (Senften *et al.*, 2006), which provides tension to gate the MET channel upon bundle displacement, and thus is essential for normal hearing function (Kachar *et al.*, 2000; Kazmierczak *et al.*, 2007; Ricci *et al.*, 2006). Tip links have a slight tension at the resting position of the hair bundle. As a result, a fraction of the MET channels remain open at rest and create a constant current that slightly depolarizes the hair cells (Corey & Hudspeth, 1979).

MET channels are located at the tip of each stereocilium, except those in the tallest row (Beurg et al 2009). They are a nonselective cation channel with a reversal potential near 0 mV in perilymph-like fluid (Johnson *et al.*, 2011; Zidanic & Brownell, 1990). As a result, opening of MET channels upon bundle deflection admits mostly cation current into the cell, and generates a depolarizing receptor potential (Corey & Hudspeth, 1979). The HC depolarization induces the activation of $Ca_V1.3$ calcium channels located at the pre-synaptic site, which regulate the release of glutamate at the afferent terminals (Figure 1.11).

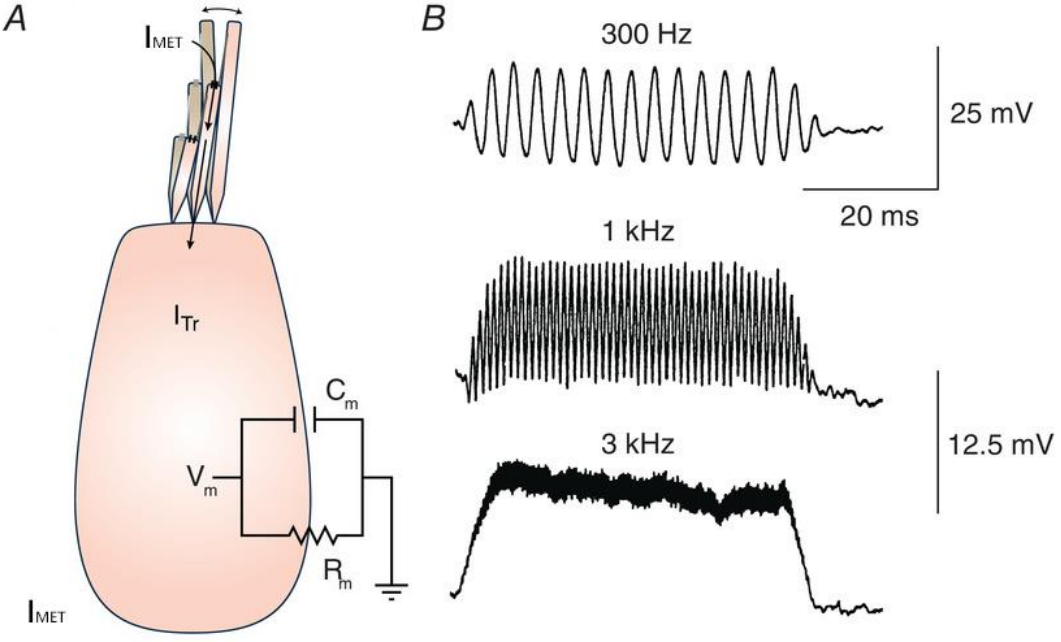

Figure 1.11 Mechano-electro-transducer current in hair cells.

A) Cartoon diagram of the working model of mechano-electric-transduction current. C) Difference in alternating and direct current components of the receptor potential of IHCs with lower (top) and higher (bottom) characteristic frequencies. Images adapted from Rutherford *et al.,* (2021).

In mice, the MET channels can first be detected around E16-E17 (Géléoc & Holt, 2003) and their mechano-sensitivity remains very small at birth in basal OHCs (Waguespack *et al.*, 2007). The size of the maximum current enlarges as the hair bundles mature during the development of the HCs (Kennedy *et al.*, 2003; Kim & Fettiplace, 2012; Waguespack *et al.*, 2007).

While the MET current is driven by mainly K^+ and a smaller portion of Ca^{2+}, the open probability of the MET channel is greatly affected by the calcium level (Corns *et al.*, 2014; Goldring *et al.*, 2019; Ricci & Fettiplace, 1998). Higher calcium shifts the current-displacement curve towards the greater deflection and thus closing the MET channels (Corns *et al.*, 2014; Johnson, Beurg, *et al.*, 2011; Johnson, 2015). In extracellular solutions with higher calcium concentrations, MET channels have a lower resting open probability than in a solution with a lower calcium concentration like the endolymph (Figure 1.12 A; Corns *et al.*, 2014). This modulation allows IHC to have more symmetrical responses to both the push and pull phases of sound stimulation. The calcium-dependent adaptation also dampens the current influx over time during stimulation (reviewed in Fettiplace & Kim, 2014), which compress large or constant signal inputs to enhance the dynamic range of hearing. However, I will not discuss further on the details since this study focuses on the prehearing stage, where the resting current is theoretically the only activity from the MET channel.

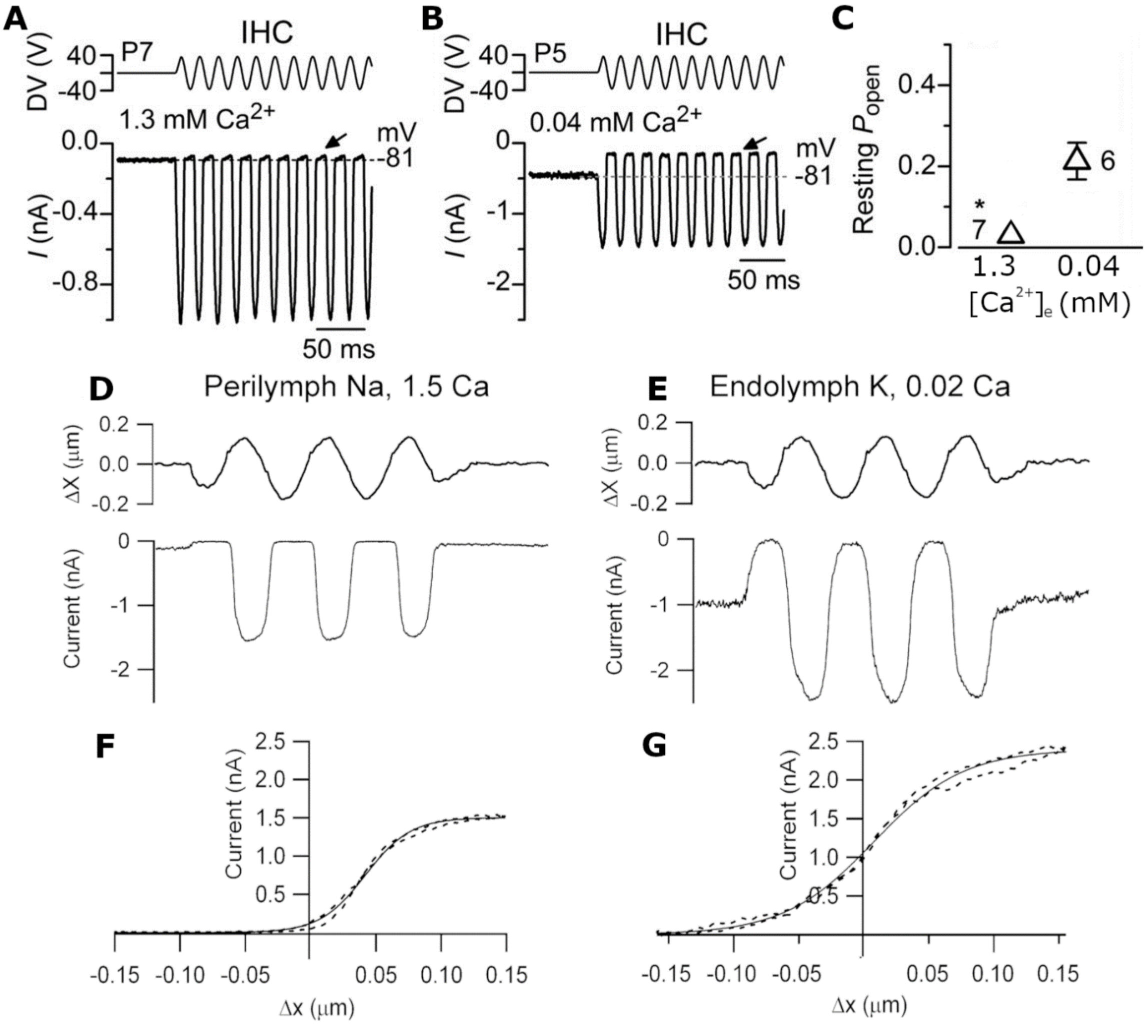

Figure 1.12 Calcium dependent modulation of the mechano-electro-transducer current. A, B) When applying a sine wave displacement to the hair bundles with a fluid jet, the resting current of a hair cell can be measured by subtracting the holding current (dashed grey line) with the minimal current (arrowhead). C) Resting open probability can be calculated by dividing the resting current with the peak-to-peak current different between maximum and minimum current in stimulation. D, E) Experiments in OHC with perilymph-like and endolymph-like extracellular solution shows similar modulation as in IHC. F, G) The opening function is more symmetric to the displacement in endolymph-like fluid (G) compared with a shifted curve in perilymph (F). Images adapted from Corns *et al.*, 2014 and Johnson *et al.*, 2011.

1.2.2 Development of Ribbon Synapses

Ribbon synapses are a highly specialized synaptic structure featured only in some sensory systems, the most famous examples including retinal photoreceptor and cochlear hair cells. They have an electron-dense core, the synaptic ribbon, which anchors their base to the presynaptic activation zone. A massive number of vesicles tether around the synaptic ribbon which allows the hair cells to sustain the non-fatiguing, rapid release of neurotransmitters, which is required to encode sound signals constantly and accurately into neuronal signals.

In hair cells, the numbers, shape and cellular location of synaptic ribbons differ between immature and matured state, with the former having spherical ribbons and the latter elongated "droplet" shaped ribbons (Figure 1.14; Michanski *et al.*, 2019). These different shapes are functionally related to the specific task performed by immature and adult hair cells, and the ability to drive different subsets of afferent neurons after hearing onset. Figure 1.13 illustrates the timeline of ribbon synapse development. Small-sized ribbon precursors can be detected at the time of birth (E18-P0). They randomly anchor to the activation zone (AZ), with a fraction of them floating in the cytosol (Michanski *et al.*, 2019). During the development, mini ribbons on AZ turn into larger, more matured synaptic ribbons. Right before hearing onset at P12, the floating pre-ribbons merge into large ones on the membrane. This process is considered an important event to maturation of the AZ. As a ribbon grows, the number of synaptic vesicles (SV) associated with the synaptic ribbon also increases.

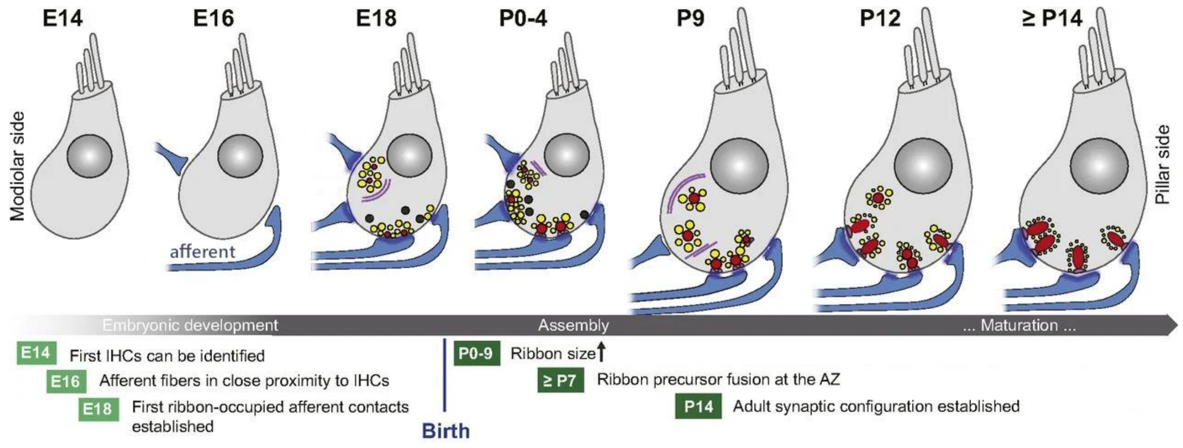

Figure 1.13 A diagram of the timeline of ribbon synapse formation in mouse.
Mini synaptic ribbons start the assembly around the day of birth and gradually mature into a functional ribbon synapse during the first two postnatal weeks. Image adapted from (Michanski *et al.*, 2019).

Three pools of vesicles support the continuous exocytosis from hair cells (Figure 1.14; Michanski *et al.*, 2019). Most of the vesicles bind to the synaptic ribbon are the ribbon-associated pool (RAP, marked in blue). The vesicles waiting in the cytosol are the outlying pool (OP). The vesicles simultaneously "docked" to the ribbon and at the activation zone are the presumptive readily releasable pool (RRP) (marked in red). RRP vesicles fuse to the membrane to release neurotransmitters in response to the calcium influx from the specialised L-type voltage-gated calcium channel, Ca$_V$1.3 (Glowatzki & Fuchs, 2002). The calcium dependence of exocytosis has a non-linear relationship in immature IHCs and transforms into a near-linear relation after hearing onset (Johnson *et al.*, 2005).

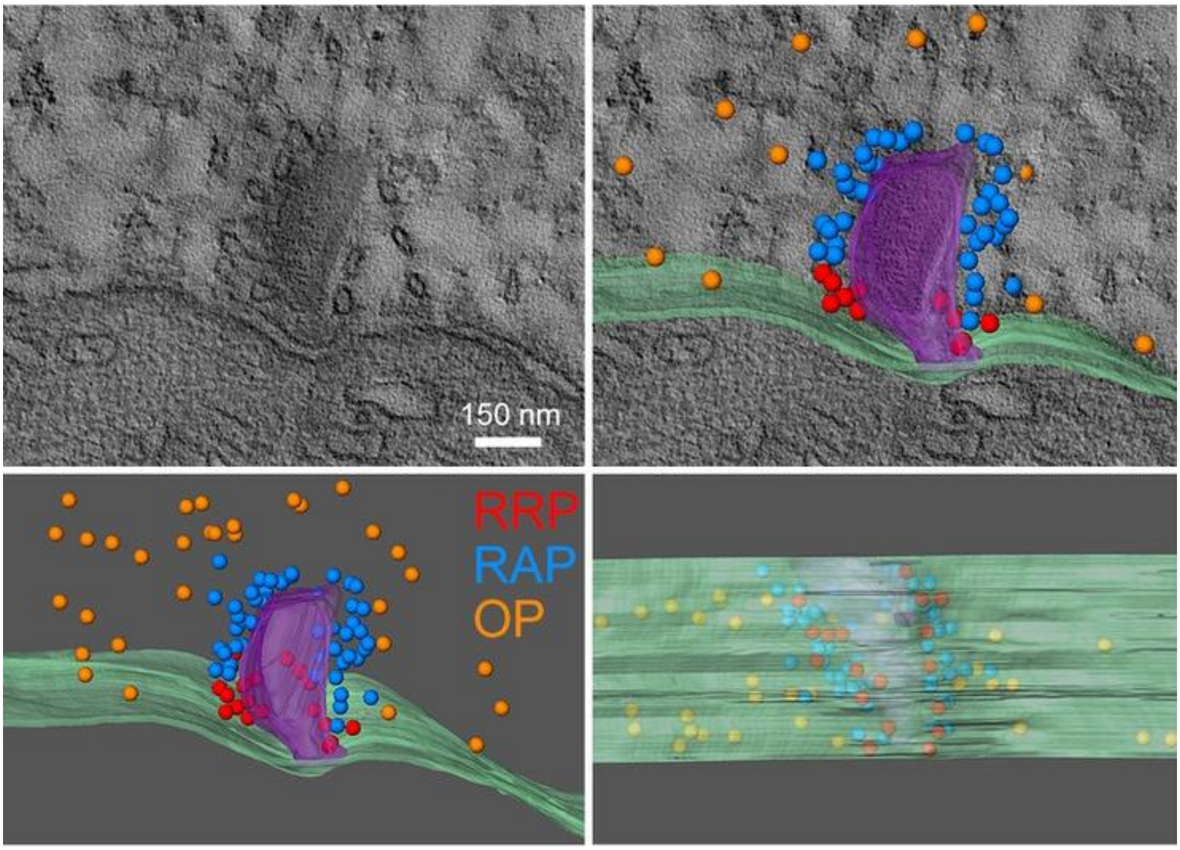

Figure 1.14 Structure of a synaptic ribbon.
A) Representative single slice of a synaptic ribbon in transmission electron micrographs (TEM) and B) same image from A overlaid with 3D model. C) Reconstructed 3D model shows three pools of synaptic vesicles. D) bottom view of the reconstructed 3D stacks to show the spatial distribution of the synaptic vesicles. RRP, readily releasable pool, in red; RAP, ribbon-associated pool, in blue; OP, outlaying pool, in orange. Image adapted from Michalski *et al.*, 2017.

1.2.3 Maturation of Electrophysiological Properties

Mature IHCs respond to current injection with a graded potential (Figure 1.15 F), whereas immature IHCs generate spontaneous action potential-like spikes (Figure 1.15 D). The composition and expression of ion channels in rodent IHCs undergo a drastic change during postnatal development to achieve this total transformation from an excitable membrane to a fast-transmitting graded voltage response (Figure 1.15 G).

Right after terminal mitosis, the IHC is not yet capable of generating action-potential-like spikes during current injection (Figure 1.15 A; Kros *et al.*, 1998). In the following few days, they start to express the immature type K^+ currents, $I_{\mathrm{K,DR}}$ and I_{K1}, which at this stage provide limited rectifying power which is not enough to generate the hyperpolarization phase during an action potential (Figure 1.15 C; Marcotti *et al.*, 2003). Right before birth, the size of immature K^+ currents increases and, with an increased expression of voltage-gated calcium and sodium currents, thus enables the IHC to generate sensory-independent spontaneous action potentials (SAPs) without any exogenous stimulus (Figure 1.15 D; Marcotti *et al.*, 2003).

From the date of birth (postnatal day 0, P0) to hearing onset at around P12, IHCs are capable of firing action potentials upon current injection (Figure 1.15 G; Marcotti *et al.*, 2003; Marcotti *et al.*, 2003). Although SAPs cannot be detected ex-vivo with patch-clamp recording during the second postnatal week, indirect evidence suggest it remain robust in-vivo (Johnson *et al.*, 2012). In the same period, IHCs are innervated by the efferent synapses (Spoendlin, 1972) with functioning inhibitory post-synaptic currents from the nicotinic acetylcholine receptors and their coupled SK2 channels (Fuchs & Murrow, 1992). The efferent synapses disconnect from IHC after hearing onset, when IHCs gain their mature-type currents $I_{\mathrm{K,n}}$ and $I_{\mathrm{K,f}}$ (Kros *et al.*, 1998). By then, IHCs have become more hyperpolarized and present graded voltage response instead of spiking upon current injection (Figure 1.15 F). The $I_{\mathrm{K,n}}$ and $I_{\mathrm{K,f}}$ currents take another week to reach their full size, but IHCs are considered as functionally matured after they have acquired these currents (Figure 1.15 G; Marcotti *et al.*, 2003).

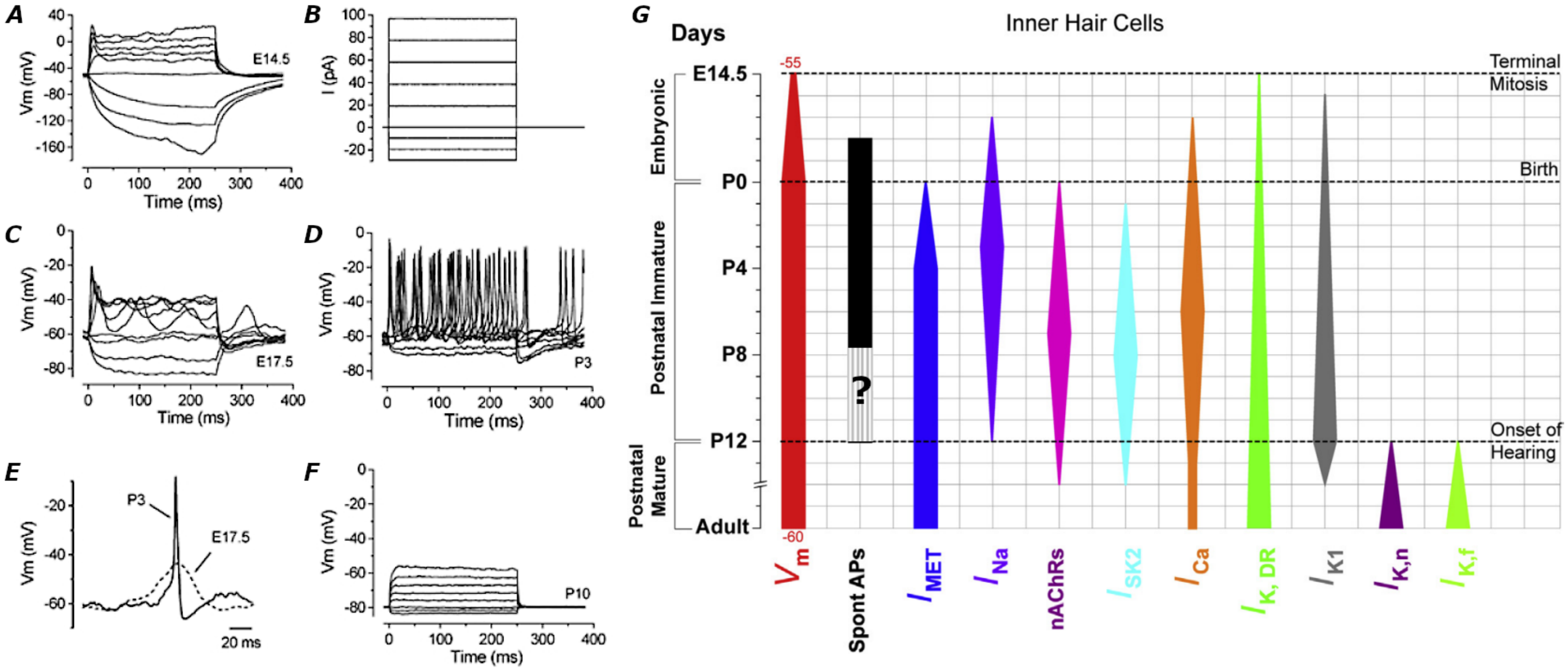

Figure 1.15 Developmental changes of the inner hair cells.
A-F) Whole cell voltage responses of IHCs at different ages plotted again time. B) The protocol of current injection from -30 to +100 pA in 10 pA steps. E) Overlay of the action-potential like events from embryonic and early postnatal stages. G) A summary graph of changes in electrophysiological properties and current expression during the postnatal development. The width of each column indicates the size of the event with age along the y-axis. P*n*: *n*th postnatal day. Images adapted from Corns, Bardhan, *et al.*, 2014; Marcotti *et al.*, 2003.

In the following sections I will describe the relevant electrophysiological components at different developmental stages. Since IHCs are the main target of this study, I will mainly focus on this cell type.

Calcium current in both immature and mature IHC

Ca^{2+} participates in critical functions involved in hearing such as mechano-transduction, vesicle release and frequency selection (reviewed in Ceriani & Mammano, 2012; Fettiplace, 2017). In IHCs, the major calcium source comes from the voltage-gated calcium channel (VGCC). L-type VGCCs containing the $Ca_V1.3$ subunit (in short as $Ca_V1.3$ channel) are almost exclusively expressed in cochlear hair cells and have been proven indispensable for normal auditory function (Brandt *et al.*, 2003; Kollmar *et al.*, 1997; Platzer *et al.*, 2000). Other species of VGCCs in hair cells have been reported in various vertebrate models including the mouse (Martini *et al.*, 2000, p. 200; Rodriguez-Contreras & Yamoah, 2001), but their roles are still under investigation.

The $Ca_V1.3$-mediated calcium current (I_{Ca}) is expressed from late embryonic stage. At this early stage of development, calcium channels are present throughout the basolateral membrane of IHCs and are capable of driving the exocytosis of synaptic vesicles during voltage stimulus (Beutner & Moser, 2001; Johnson *et al.*, 2005). The activation of I_{Ca} starts at −70 mV (1% of peak conductance) during immature stage (Johnson & Marcotti, 2008). The peak size of the current gradually increases from −100 pA at around birth to around −400 pA at P6, before it is downregulated in the second postnatal week and remains stable after hearing onset (Figure 1.16; Johnson *et al.*, 2005). Except for the size change, the dynamics of the channel also becomes more desensitised after hearing onset, with a more depolarized initial activation (−65 mV) and a 10 mV increase on half activation voltage (Johnson & Marcotti, 2008).

The amount of exocytosis with the same voltage stimulus grows as the current gets larger, but stays at similar level after the I_{Ca} is downregulated after P6 (Figure 1.16 A, B; Johnson *et al.*, 2005). After hearing onset, the Ca^{2+} efficiency at driving exocytosis increases several folds and the power relationship turns almost linear at driving the release of the readily releasable pool (Figure 1.16 D; Johnson *et al.*, 2005). This trend correlates with the merging of ribbon precursors into a more matured ribbon-shaped structure from P7 onward and the coupling of $Ca_V1.3$ with the activation zone (Wong *et al.*, 2014). This seemed to be a reasonable mechanism, however study in gerbil found tonotopic difference in the shift of power relationship between the apical and basal coil of the cochlea (Johnson *et al.*, 2009), while the Ca$_V$1.3 channels in both coil regions seemed be tightly packed with synaptic ribbon in nanometre range (Johnson & Marcotti, 2008). The influence is more likely from the mature-related morphological or molecular changes in the ribbon synapse, such as vesicle tethering or calcium-buffer proteins, instead of the configuration of the synapse (Johnson *et al.*, 2005, 2009; Johnson, Olt, *et al.*, 2017; Johnson & Marcotti, 2008; Pangršič *et al.*, 2015).

A possible cause for the difference efficiency might be the tonotopic difference in the Ca$_V$1.3 short isoform (Bock *et al.*, 2011; Huang *et al.*, 2013) as they were proposed to only mediates the release of RRP (Vincent *et al.*, 2017). Agreeing with this hypothesis, basal-coil IHCs from post-hearing gerbils have significantly larger calcium-dependent inactivation (CDI) than those in the apical region (Johnson & Marcotti, 2008). This tonotopic difference was not observed in immature IHCs (Johnson & Marcotti, 2008). As the dynamics of inactivation and recovery was unaltered between immature and mature stages (Inagaki & Lee, 2013; Johnson & Marcotti, 2008), the shift is likely to be a change of auxiliary properties instead of the VGCC species.

During the prehearing development, Ca$_V$1.3 plays a pivotal role in generating the sensory-independent action-potentials (SAPs) in immature hair cells (Johnson *et al.*, 2007; Marcotti *et al.*, 2003; Marcotti *et al.*, 2003). Constitutive knockout of Ca$_V$1.3 (Ca$_V$1.3 KO, or Ca$_V$1.3$^{-/-}$) eliminated the spiking capability of immature IHC upon current injection, and the synaptic transmission from ribbon synapses was completely lost (Brandt *et al.*, 2003). After hearing onset, the Ca$_V$1.3$^{-/-}$ IHCs failed to mature and retained similar properties to their immature state. These IHC had no functioning $I_{\mathrm{K,f}}$ two weeks after the timing of normal hearing onset. The efferent system maintained functioning synapse with the IHCs instead of forming axodendritic synapses with afferent fibres (Brandt *et al.*, 2003).

There are multiple mechanisms tightly regulating the firing of these calcium action potentials. Disruption of SAPs often causes IHCs to retain immature physiological characteristics. Being the centre piece in this thesis, the regulatory factors on SAP will be discussed further in 1.3.

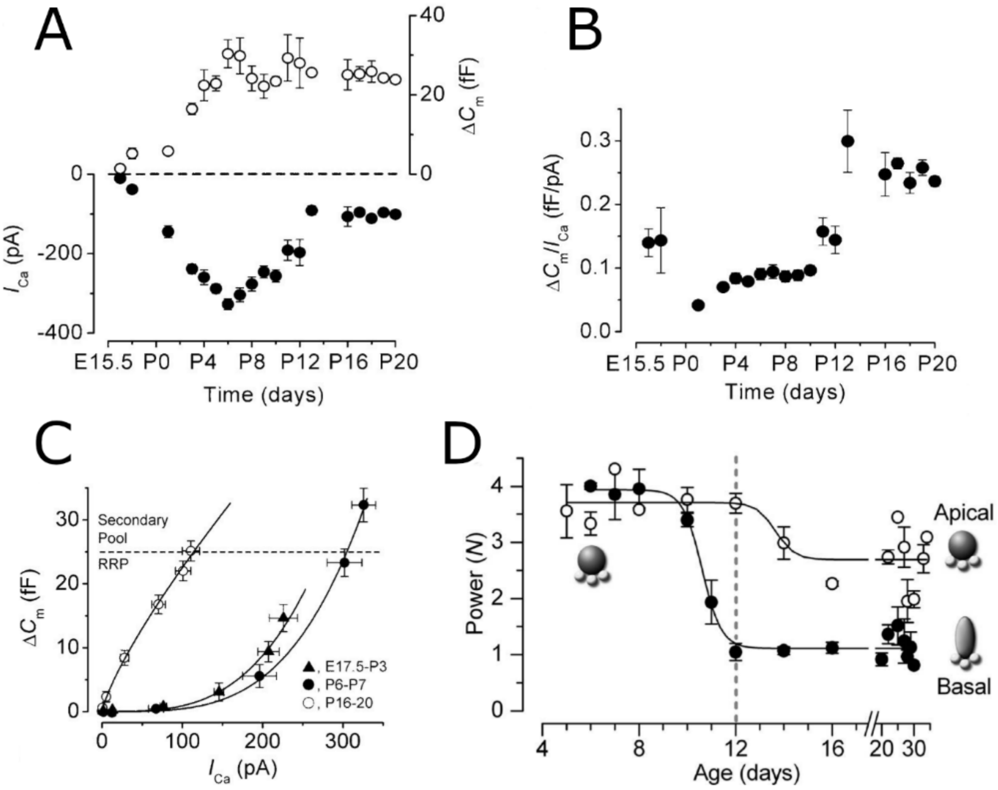

Figure 1.16 Maturation of Ca$_v$1.3 mediated calcium current and synaptic release.
A) Change of I_{Ca} peak size and corresponding amount of vesicle release during the development of the IHC **B**) the Ca^{2+} efficiency on driving the vesicle release at the same time scope. **C**) the relationship between calcium current size and vesicle release in around date of birth (closed triangle), end of first postnatal week (closed circle) and fully mature (open circle). Fitting data with power function (solid line) indicated a reduce of power from around 4 in immature to 0.7 in matured state. **D**) Change of power relation between the calcium current and vesicle release during the maturation of IHC from basal and apical coil. Images adapted from Johnson *et al.*, (2005) and Johnson *et al.*, (2009).

Ion channels in developing IHCs

Upon depolarization, immature IHCs present a slow outward current, the delayed rectifier $I_{K,DR}$. This current trait is in fact present at all developmental stages, but with varied composition and dynamics. To avoid mixing terms, it was named differently in each stage; $I_{K,emb}$ for embryonic (E14.5-E19.5), $I_{K,neo}$ for neonatal (P0-P12), and $I_{K,s}$ for mature type slow current (>P12) (Dallos & Fay, 2012; Marcotti *et al.*, 2003). $I_{K,DR}$ is one of the first current present in embryonic stage right after the differentiation of hair cells at E14 (Marcotti *et al.*, 2003). The size of the maximum current has a 50-fold growth from around 200 pA at E15 to 8 nA at P10 onward, while the activation of the current gradually shift towards a lower voltage from −58 mV to −74 mV (Figure 1.17 B; Marcotti, *et al.*, 2003).

During development, a second conductance with different inactivation dynamics becomes detectable from birth, and gradually takes over the embryonic current. This second conductance is likely to be (at least mainly) the increasing 4-AP sensitive conductance, which will become the major conductance (~80%) in mature $I_{K,s}$ (Marcotti *et al.*, 2003).

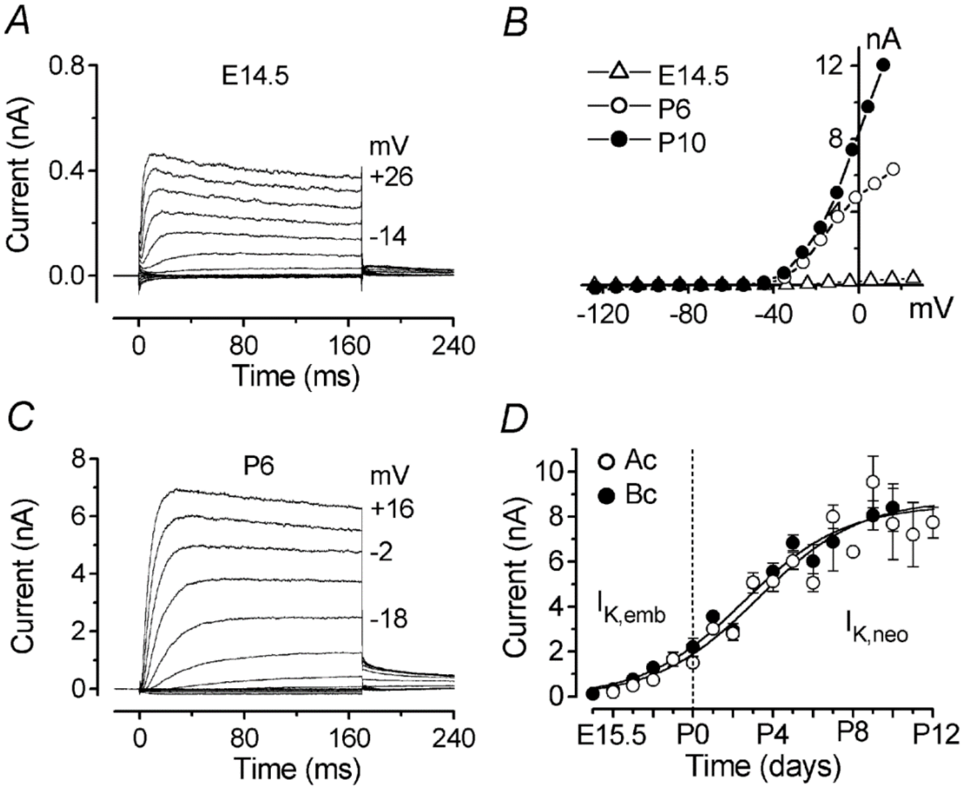

Figure 1.17 Delayed rectifier current in immature IHC.
A) $I_{K,emb}$ and C) $I_{K,neo}$ measured from −120 mV to +20 mV with 10 mV increment each step, holding at -84mV. B) Current-voltage response of the delayed rectifier current from embryonic stage (open triangle, E14.5) to early (open circle, P6) and late (filled circle, P10) neonatal stage. D) Steady current size of $I_{K,DR}$ during the postnatal development, measured at 0 mV step. Images adapted from Marcotti *et al.*, 2003.

Easily distinguished from the slow outward current, the inward rectifier I_{K1} has faster dynamics and opens at more hyperpolarised voltages than −80 mV (Marcotti & Kros, 1999). IHCs express this current throughout the developmental stage. The size of the current rapidly increases after terminal mitosis and reaches its maximum at P12 before it disappears from P14 onward (Marcotti *et al.*, 2003; Marcotti & Kros, 1999).

The role of I_{K1}, as with any other K^+ current discussed so far, is setting the resting potential and the time constant of the cell membrane. Hair cells in the apical coil were found to have a smaller I_{K1}, and a slightly more depolarized V_{m} than the basal cells with a larger I_{K1} (Marcotti & Kros, 1999). This regulatory effect of I_{K1} is critical for regulating the spontaneous firing rate in immature hair cells. Applying extracellular caesium (Cs^+) selectively blocks inward K^+ current and depolarized the IHC by nearly 15 mV. This depolarization increased the probability of firing induced action potentials with a broader repolarizing dynamics (Marcotti & Kros, 1999).

Tetrodotoxin-sensitive sodium current (I_{Na}) was reported to be expressed in both inner and outer hair cells for a brief period in prehearing rodents (Eckrich *et al.*, 2012; Kros, 1996; Marcotti *et al.*, 2003; Oliver *et al.*, 1997). The sodium conductance was observed in 60-70% of mouse IHCs shortly after birth (Marcotti *et al.*, 2003). The size of current was gradually upregulated before taking a sharp decay from P6, and completely disappeared before hearing onset at P12 (Figure 1.18; Eckrich *et al.*, 2012; Marcotti *et al.*, 2003). The expression of this sodium current may differ between species, as it was observed in 100% of rat IHCs and their maximum current size was observed at birth (Eckrich *et al.*, 2012). Unlike their homologue in neurons, the sodium current in the immature hair cells is not required for generating the spontaneous action potentials. Instead, I_{Na} regulates the firing frequency by speeding up the time for membrane potential to reach the threshold (Figure 1.18, Marcotti *et al.*, 2003).

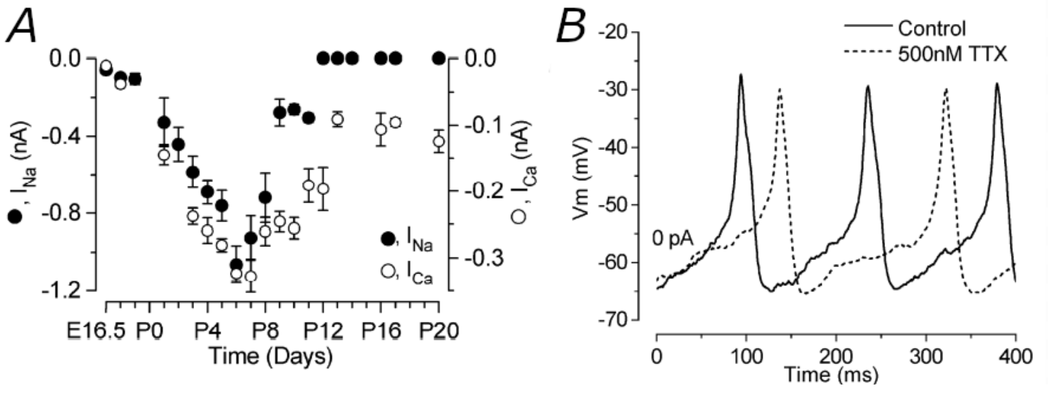

Figure 1.18 Physiology of sodium current from immature mouse IHC.

A) The I_{Na} (closed circle) increased during the first postnatal week and rapidly disappeared during the second. B) Blocking I_{Na} with TTX delayed but did not abolish the spontaneous calcium action potentials. Images adapted from Marcotti *et al.,* 2003.

Another important K^+ conductance presents in immature hair cells is the small-conductance calcium-activated potassium (SK2) current. In the cochlea, this current was first identified in mature OHCs, with which cholinergic efferent fibres forms inhibitory synapses (Fex, 1967). Efferent fibres do not innervate mature IHCs, but briefly form functional synapses with immature IHCs before hearing onset (Spoendlin, 1972). Ionotropic nicotinic acetylcholine receptors (nAChRs) with α9α10 subunits are the postsynaptic target of these inhibitory synapses. Efferent fibres releases acetylcholine (ACh) and triggers postsynaptic calcium influx through the nAChRs (Elgoyhen *et al.*, 1994, 2001). Functioning α9α10 nAchR can be detected in IHC at the date of birth, and their calcium current gradually becomes larger from P1 to P3 and reaches maximum at P8 (Roux *et al.*, 2011). However, the depolarizing calcium current does not contribute to the inhibitory postsynaptic potential (IPSP), which is mainly potassium current carried out by the SK2 channels, which colocalising with the nAChRs (Dulon *et al.*, 1998; Fuchs & Murrow, 1992; Nenov *et al.*, 1996; Oliver *et al.*, 2000; Roux *et al.*, 2011). The coupling between the nAchR and SK2 can be observed in IHCs from P1 and reaches 100% coverage at P3, where the number of SK2 clusters also increased (Roux *et al.*, 2011). IHCs stop to express SK2 channels when efferent synapse are cleared from matured IHCs after hearing onset (Marcotti *et al.*, 2004a). As a result, when an efferent synapse with a functional SK2 current is present in IHC, it is usually recognized as a marker of an immature phenotype.

The SK2 current is crucial for regulating the SAP firing pattern in immature IHCs. Genetically deleting SK2 channels (SK2-KO) removed a large part of the repolarising power and prevented the continuous firing of SAP in developing IHCs. The firing pattern became slower and saturated into static depolarization upon constant current stimulus (Figure 1.19, Johnson *et al.*, 2007). In contrast, overexpressing SK2 produced sharper, faster SAPs with the mean firing rate almost doubled (Johnson *et al.*, 2013). Surprisingly, both of these mutations did not prevent the IHC from acquiring their mature-type currents $I_{K,f}$ and $I_{K,n}$ (see page 26; Johnson *et al.*, 2007; Johnson *et al.*, 2013). IHC and OHC seemed to retain the response and sensitivity to pure tone (Clause *et al.*, 2017; Maison *et al.*, 2007), but the frequency separation and sound localization upon complex signals was impaired in nAChR knockout mice (Clause *et al.*, 2017).

This is likely to be a result of impaired sustain vesicle release, because the efficacy of ribbon synapses failed to acquire the linear mature response in both mouse models with knock-out and over-expression (OE) of SK2 channel (Johnson *et al.*, 2013). Another symptom of SK2 deficiency is the loss of nAchR expression in mature OHC (Johnson *et al.*, 2007; Kong *et al.*, 2008; Marcotti *et al.*, 2004b), which leads to the degeneration of efferent innervation and subsequently olivocochlear neurons (Murthy *et al.*, 2009).

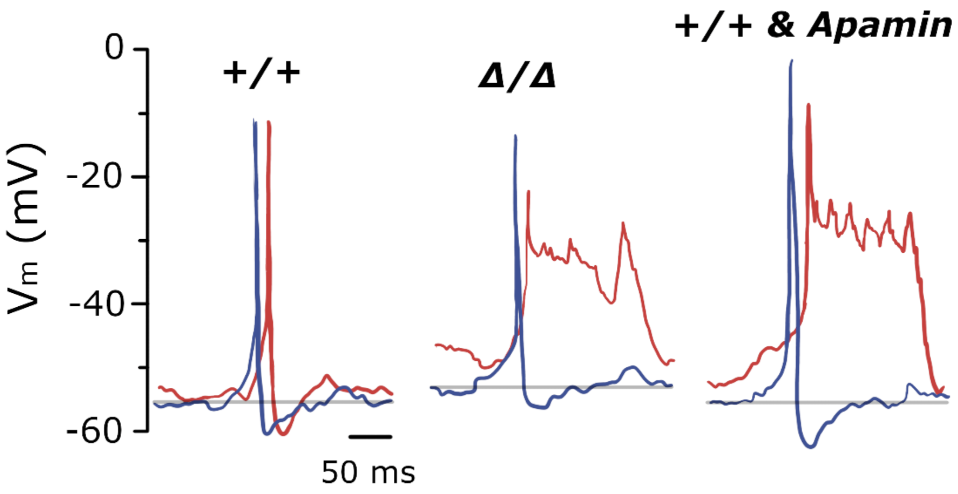

Figure 1.19 Action potential waveforms with deleted or blocked SK2 current.
The waveform difference in IHC with control (*+/+*), deleted (Δ/Δ) or blocked (*+/+* & Apa) SK2 current. The blue traces show the waveform of a normal, non-saturated spike. The red traces show saturated spiking waveform in SK2 current deficiency phenotype or unchanged waveform in the control. Lack of the repolarising power from I_{SK2} turned the cell membrane from an excitable to a graded-like voltage response upon the influx of calcium ions. Image adapted from Johnson *et al.*, 2007.

Ion channels in mature IHCs

Compare with the slower outward current in their immature state, mature IHCs displays a fast outward current upon depolarization (Figure 1.20 F). The reversal potential of this current is about −76 mV, which is close to the equilibrium potential of potassium (−86 mV). As a result, it is likely to be mainly carried by potassium ion and thus was called $I_{K,f}$ for fast-activating potassium current (Kros & Crawford, 1990). This current has a very fast time constant of around 0.15-0.35 ms (Hicks & Marrion, 1998; Kros & Crawford, 1990). It is sensitive to K^+ channel blocker tetraethylammonium chloride (TEA) but resistant to 4-aminopyridine (4-AP;

Kros & Crawford, 1990). Although the expression of $I_{K,f}$ starts around P12-13, the size of the current increases steadily during the third postnatal week before it stabilizes at P18-20 (Kros *et al.*, 1998)

Blocking the fast current in mature IHCs revealed a much slower potassium current ($I_{K,s}$) with an activation time constant around 2-10 ms (Kros & Crawford, 1990). $I_{K,s}$ is TEA resistant but 4-AP sensitive, opposite to $I_{K,f}$. Together they comprise over 95% of the outward current stepping from −84 mV to −5 mV, which covers most of the working range of the receptor potential (Kros & Crawford, 1990).

It is very difficult to dissect the source of $I_{K,s}$ because the current is composed of multiple types of voltage-gated potassium channels (Kros & Crawford, 1990), the role of which have remained elusive for decades. Recently, a single-cell RNA-Seq study together with a pharmacological study highlight four potential candidates, $K_V1.8$, $K_V7.4$, $K_V11.1$, and $K_V12.1$ (Dierich *et al.*, 2020; Liu *et al.*, 2014). Genetically deleting Kv1.8 channel in mice slightly raised the hearing threshold in high and low frequencies (32kHz and 8kHz) although the most sensitive range (16, 24kHz) had no statistical difference (Lee *et al.*, 2013). The result from a study of Kv7.4 deletion suggested the physiological role of $I_{K,s}$ is setting the resting membrane potential toward hyperpolarization, as the resting potential shifted to a more depolarized state (around +17 mV difference) in both IHCs and OHCs (Kharkovets *et al.*, 2006; Marcotti *et al.*, 2003). So far, there is very little evidence to link the Kv11.1 and Kv12.1 channels with specific functional roles in the cochlea.

Another signature current in mature hair cells is the negatively-activating delayed rectifier current ($I_{K,n}$), carried by Kv7.4 channels encoded by the *kcnq4* gene (Marcotti, *et al.*, 2003; Marcotti & Kros, 1999; Oliver *et al.*, 2003). After the hearing onset, the size of $I_{K,n}$ gradually increases in IHC from P14 onward and becomes stable after P20 (Marcotti, *et al.*, 2003). Blocking the $I_{K,n}$ with linopirdine significantly depolarized P19 apical IHCs from resting potential around −74 mV to near −60 mV. $I_{K,n}$-mediated hyperpolarization is also believed to prevent any spiking/oscillating membrane activities in mature hair cells (Marcotti, *et al.*, 2003). The $I_{K,n}$ current starts activating from around −120 mV and reaches an open probability of almost a hundred percent at −60 mV (Housley & Ashmore, 1992; Marcotti, *et al.*, 2003; Marcotti & Kros, 1999; Oliver *et al.*, 2003). As a result, it is mostly open at the theoretical resting membrane potential of the hair cells (−60 to −80 mV) and provides a strong hyperpolarizing current to allow the HCs quickly recover from the receptor potential (Housley & Ashmore, 1992; Kubisch *et al.*, 1999; Marcotti, *et al.*, 2003; Marcotti & Kros, 1999).

The acquisition of the mature currents, $I_{K,n}$ and $I_{K,f}$, coincides with the onset of hearing at around P12-13, at which the size of the fast current increases several folds within a week (Figure 1.20 B, E-G). Both currents were absent in a hearing loss mouse model in which hair cells retained immature characteristics (Marcotti *et al.*, 2006), or in age-related hearing loss model where aged hair cells reverted back to an immature-like phenotype (Jeng *et al.*, 2020). $I_{K,f}$ and $I_{K,n}$ deficiency is also one of the phenotype of failed maturation when the sensory-independent calcium activity was deprived during prehearing development (Brandt *et al.*, 2003; Corns *et al.*, 2018; Johnson *et al.*, 2017). As a result, the presence of $I_{K,n}$ and $I_{K,f}$ are often used as one of the markers to evaluate whether the hair cells are functionally matured during the development.

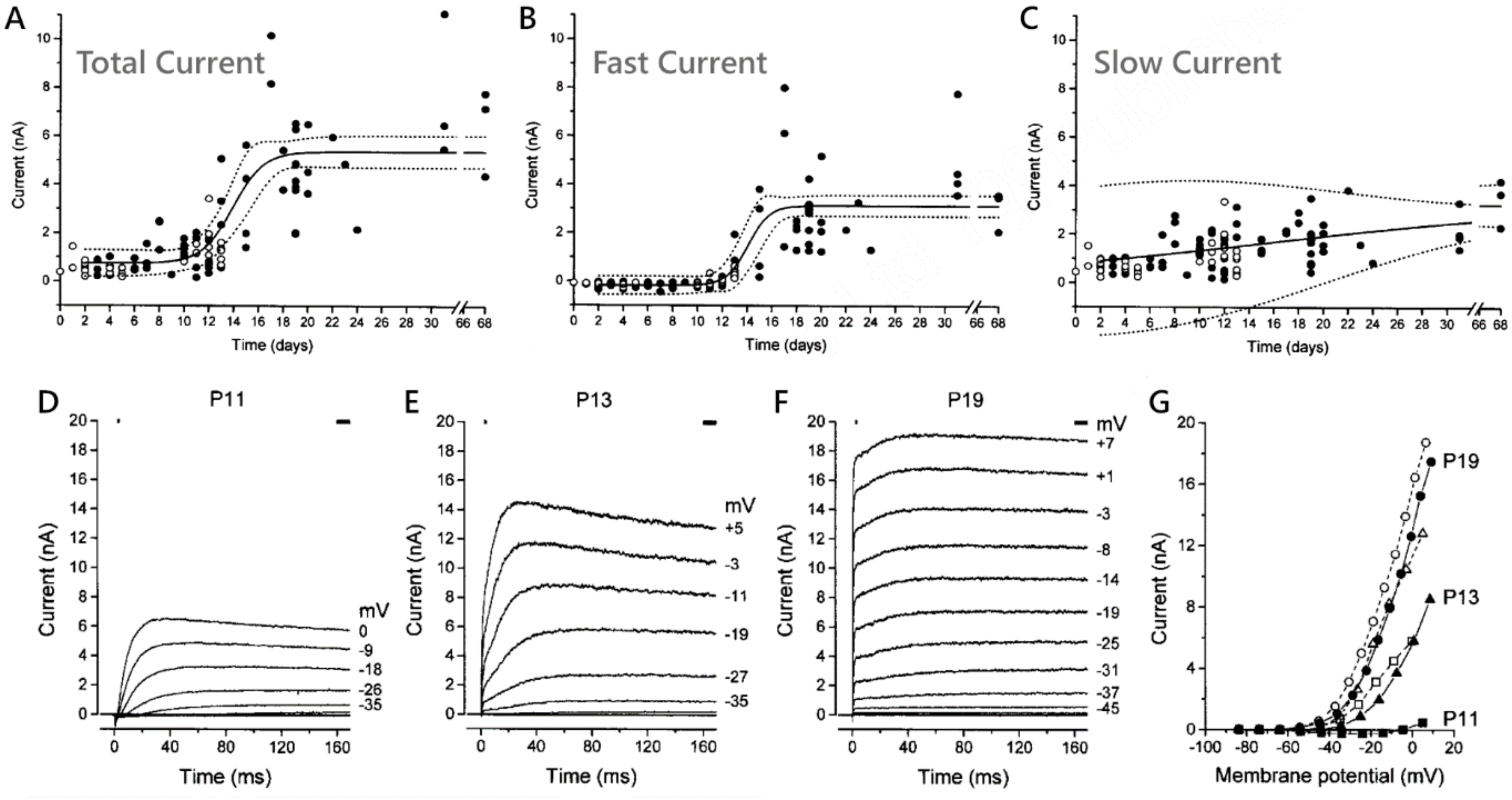

Figure 1.20 Developmental change of outward current in inner hair cells.
A-C) Trends of current size in different ages in apical coil (filled) and basal coil (open) IHCs depolarized from -84 mV to -25 mV. D-F) Different current response upon voltage stepping throughout the maturation period of IHC. Holding potential was -84 mV. G) Current-Voltage response of the fast current (filled) and the steady state current (open). Square, triangle, and circle are designated to P11, P13, and P19. Images adapted from Kros *et al.*, 1998.

1.3 Spontaneous Calcium Activity in the Developing Inner Ear

The importance of spontaneous activity in developing sensory system has been well studied in the past decades (reviewed in Pan & Monje, 2020). Findings in the retina (Galli & Maffei, 1988; Meister *et al.*, 1991) and the cerebellum (Watt *et al.*, 2009) have emphasised the crucial role of spontaneous activity in the maturation of the sensory receptors and the neuronal pathways.

Such sensory-independent spontaneous calcium activity can also be observed in the developing cochlea before the onset of hearing. From around the date of birth, spontaneous calcium signals can be recorded in hair cells of ex-vivo organ of Corti in mice (Brandt *et al.*, 2003; Eckrich *et al.*, 2018; Johnson, Ceriani, *et al.*, 2017; Johnson *et al.*, 2011; Kros *et al.*, 1998; Marcotti *et al.*, 2003; Sendin *et al.*, 2014) and non-sensory cells in the GER (Anselmi *et al.*, 2008; Babola *et al.*, 2018; Rodriguez *et al.*, 2012; Tritsch *et al.*, 2007; Tritsch & Bergles, 2010; Wang & Bergles, 2015).

Spontaneous calcium activities in immature IHCs are in the form of action potentials (Figure 1.15 D; Brandt *et al.*, 2003; Marcotti, *et al.*, 2003), which are critical for IHCs to acquire their mature characteristics. Spontaneous activities in the GER are evident as propagating spontaneous calcium waves mediated by purinergic/IP$_3$-mediated signalling pathways (Figure 1.21; Piazza *et al.*, 2007). In the rest of the thesis, I will refer to the calcium activity in IHC as spontaneous action potentials (SAP), and the activity in the non-sensory cells as spontaneous calcium waves.

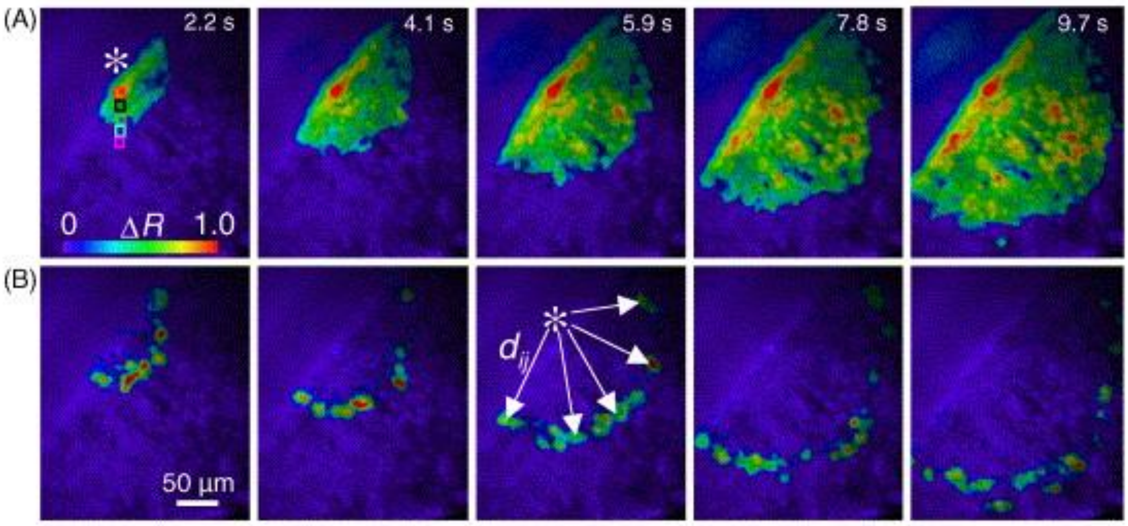

Figure 1.21 Propagating calcium wave in supporting cell networks.
Time lapse images of calcium wave in the GER region. A) shows normalized intensity of calcium activity in pseudo-colour (jet map). B) shows differentiated intensity between frames to highlight the travelling edge of the propagating wave. Unexplained markings are legacy annotation form the original publication. Images adapted from Piazza *et al.*, 2007.

1.3.1 Calcium SAP in immature IHC

A typical calcium action potentials in immature IHC displays a biphasic voltage-current (V-I) response similar to the shape of a neuronal spike (Figure 1.22). The rapidly activating I_{Ca} mediates the depolarization phase and K^+ currents repolarize the membrane potential (Kros, 1996; Kros *et al.*, 1998). Several inward and outward currents work together in the subthreshold range to regulate the resting membrane potential (reviewed in Marcotti, 2012), which has substantial effect on the firing rate of the SAPs. During postnatal development, the potassium currents (I_{K1}, $I_{\mathrm{K,DR}}$) and the resting MET current maintain the resting V_{m} at around −60 to −55 mV (Marcotti *et al.*, 2003), which is close to the activation voltage of the $\mathrm{Ca_V}1.3$ channel (Johnson & Marcotti, 2008). The sodium current contributes to reach the threshold of a spike, with $I_{\mathrm{K,DR}}$ and I_{SK2} repolarizing the V_{m} (Figure 1.22). The role of intrinsic currents in generating SAPs are summarised in Table 1 on page 35.

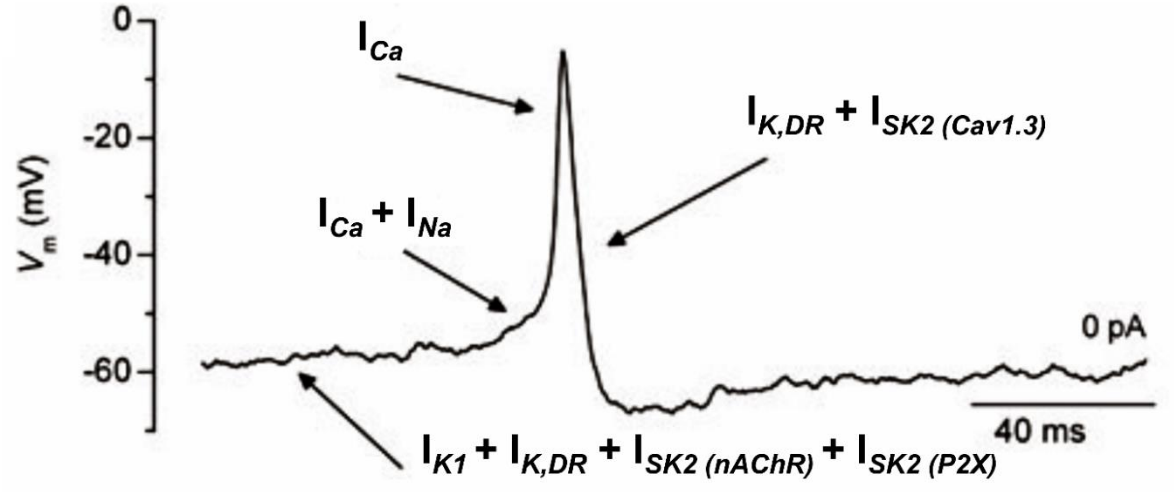

Figure 1.22 Current interplay in a single action potential.
The arrows with text indicate different currents involve in different phases when generating an action potential. The rectifier potassium currents I_{K1} and $I_{K,DR}$ maintain a stable V_m in subthreshold range. When the I_{Na} slowly ramps up the V_m to firing threshold, fast acting I_{Ca} causes the influx of Ca^{2+} ions and further depolarizes the cell, forming the rising phase of a spike. Responding to the depolarization, $I_{K,DR}$ permits the efflux of K^+ to repolarize the cell. The I_{SK2} is activated by multiple calcium sources (nAChR, P2X, and Ca_V1.3) and participate in almost all phase of the spiking cycle. Image adapted from Marcotti, 2012.

Calcium influx from each successfully action potential can trigger vesicle fusion at the ribbon synapses (Marcotti *et al.*, 2003). Transmitter release from IHCs during development has been proven crucial to the survival of the primary auditory neurons (Zhang-Hooks *et al.*, 2016) and the refinement of the synapses throughout the whole auditory pathway (Babola *et al.*, 2018; Clause *et al.*, 2014; Gabriele *et al.*, 2000; Leao *et al.*, 2006).

The earliest SAP events can be observed in *ex-vivo* samples from the 17th embryonic day, when the calcium and potassium current start to be expressed (Marcotti *et al.*, 2003). For IHC, the excitability of induced spikes gradually intensifies during the first postnatal week, where their membrane potential lies around −55 to −60 mV, within the range of spiking threshold (Johnson *et al.*, 2011; Marcotti *et al.*, 2003). At around P12, IHCs gain their mature phenotype current and correspondingly lose the excitability upon current injection (Kros *et al.*, 1998). However, in *ex-vivo* condition SAPs cannot be detected from P7 onward (Marcotti *et al.*, 2003). This observation was proposed to result from a more polarized membrane potential towards maturation due to increasing size of outward K^+ current (Marcotti *et al.*, 2003; Marcotti *et al.*, 2003). Nevertheless, indirect evidence shows IHC are still capable of generating spontaneous spikes even when only induced spikes can be triggered ex-vivo. Johnson *et al.* (2012) estimated the fluid in the scala media would become more endolymphatic-like during the second postnatal week, with a lower calcium level (~0.3 mM). The increased resting I_{MET} due to low extracellular calcium was enough to induce spiking activity in P8-P10 IHCs. In agreement with this hypothesis, spontaneous calcium spikes had been observed in IHCs from rats at P7-P8 (Tritsch *et al.*, 2007; Wang & Bergles, 2015), although they did not confirm whether the events remained a typical biphasic waveform as in the first postnatal week.

A burst firing pattern was consistently observed from IHCs in the apical coil of the organ of Corti (Eckrich *et al.*, 2018; Harrus *et al.*, 2018; Johnson *et al.*, 2011; Sendin *et al.*, 2014; Tritsch *et al.*, 2007). Short trains of rapid firing APs are interlaced with varied length of silent periods from tens to hundreds of seconds (Figure 1.23). However, the mean or median firing rate ranged wildly from 0.1 Hz to almost 5 Hz between various sources. This inconsistency possibly resulted from different experimental configurations, or the ages and species of animals (summarised in Table 2 on page 36).

While some studies reported invariant pattern among the tonotopic axis (Harrus *et al.*, 2018; Sendin *et al.*, 2014), tonic firing was observed in basal IHCs in rat and mouse (Johnson *et al.*, 2011), where the resting membrane potential was more depolarized (about −56 mV) than which observed in apical IHCs (about −59 mV) (Johnson *et al.*, 2011; Marcotti *et al.*, 2003). This difference between apical and basal firing pattern can be compensated by injecting a small current to create a +3 mV depolarization in apical IHC. Under this condition, apical IHCs became capable of firing more sustained APs like their basal counterparts (Johnson *et al.*, 2011).

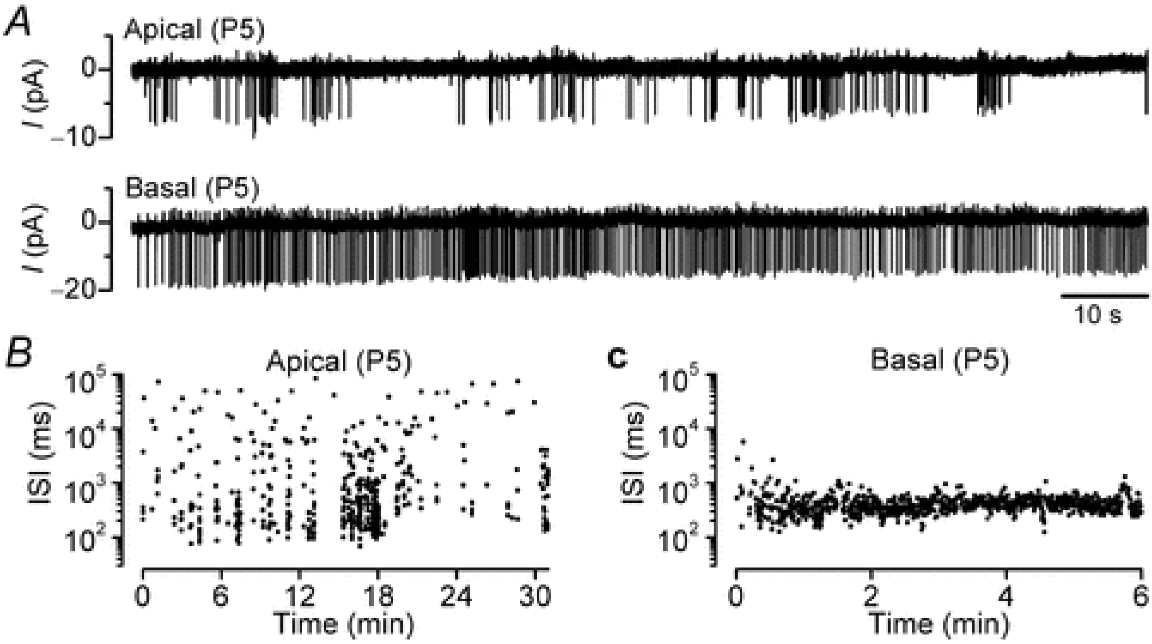

Figure 1.23 Tonotopic difference of spontaneous action potential in immature IHC.
A) exemplary spontaneous action potential recording via a cell-attached technique showed different firing pattern in IHC from apical (top) and basal (bottom) coil. The dynamics of inter-spike interval (ISI) against recording time shows more variety in apical **B**) IHCs than in basal **C**) ones. Images adapted from Johnson *et al*. (2011).

Table 1 Role of currents on generating action potentials in immature IHC.

Abbreviations: V_m, resting membrane potential; AP, action potential. *The hearing loss in Bartter's syndrome (mutation partially reducing I_{K1}) was linked with the disruption of endocochlear potential (Rickheit *et al.*, 2008) and no evidence of immature hair cell was reported.

Current Type	*Direction*	*Role in the AP*	*Deficiency AP phenotype*	*Developmental influence*	*Publication*
I_{K1}	Outward	Resting V_m	Abolished from constant depolarization.	Maybe*	Marcotti *et al.*, 1999
$I_{K,DR}$	Outward	Spike shape and repolarization	Wider and faster induced waveform.	Lack of direct evidence	Marcotti, Johnson *et al.*, 2003
I_{Ca}	Inward	Depolarisation	No spontaneous or induced AP	Critical, IHC don't mature without it.	Brandt *et al.*, 2003
I_{Na}	Inward	Boosting frequency	Slower induced AP upon current injection	Likely minimal, as 1/3 of IHC did not have I_{Na}.	Marcotti, Johnson *et al.*, 2003
I_{SK2}	Mainly Outward	Repolarization, Set frequency	Spike train quickly saturated to DC component.	Impaired calcium efficiency at ribbon synapse	S. L. Johnson *et al.*, 2007; S. L. Johnson, Kuhn, *et al.*, 2013
I_{MET}	Inward	Resting V_m	No spontaneous AP in second postnatal week.	Critical, IHC don't mature without it.	Corns *et al.*, 2018

Table 2 Dynamics of the SAP reported in different studies.

Abbreviations: V_m, resting membrane potential; CV, coefficient of variance, values larger than 1 indicates bursting firing; RT, room temperature. Information not present in the publications were left blank with a "--" mark.

Publication	Technique	Animal	Age (days)	V_m (mV)	Apical Region			Basal Region		
					Mean (Hz)	Median (Hz)	CV	Mean (Hz)	Median (Hz)	CV
Marcotti *et al.*, 2003	Whole cell	Mouse (CD-1)	P2-4	−54	4.9 ± 0.7	--	--	--	--	--
Tritsch *et al.*, 2007	Whole cell	Rat (Sprague–Dawley)	P9	−72	0.053 ± 0.003	--	--	--	--	--
Johnson *et al.*, 2011	Cell-attached	Rat	P2-5	Native	0.60 ± 0.09	2.00 ± 0.14	2.70 ± 0.24	1.23 ± 0.13	1.80 ± 0.13	1.16 ± 0.08
		Mouse	P2-4	Native	1.8 ± 0.2	3.6 ± 0.6	1.5 ± 0.3	3.1 ± 0.5	3.9 ± 0.5	0.6 ± 0.1
		Gerbil	P2	Native	0.76	1.89	2.1	--	--	--
			P6	Native	0.09	0.44	2.7	--	--	--
Sendin *et al.*, 2014	Perforated*	Mouse (Mixed)	P1-3	−74	0.6	--	4	0.55	--	2
			P5	−74	0.7	--	4	0.6	--	7
			P6-7	−74	0.9	--	7	0.6	--	5
Wang & Bergles, 2015	Whole cell	Rat (Sprague Dawley)	P5-10	–82	0.1	--	--	--	--	--
Eckrich *et al.*, 2018	Ca^{2+} Imaging	Mouse (NMRI)	P4-5	Native	0.32	4-10	--	--	--	--
Harrus *et al.*, 2018	Ca^{2+} Imaging (at RT)	Mouse (Swiss)	P1-3	Native	0.008 ± 9.10^{-4}	--	0.69 ± 0.02	0.011 ± 11.10^{-4}	--	0.53 ± 0.03
			P6-7	Native	0.007 ± 7.10^{-4}	--	0.57 ± 0.05	0.009 ± 7.10−4	--	0.54 ± 0.03

1.3.2 Spontaneous calcium waves in the GER

Figure 1.24 shows a detailed, step-by-step illustration on how the spontaneous calcium waves in the GER is generated. Kolliker's organ passively releases ATP through connexin (Cx) hemichannels (Anselmi *et al.*, 2008; Johnson, Ceriani, *et al.*, 2017). ATP diffusing into the extracellular space triggers autocrine or paracrine response in adjacent cells via P2 purinergic receptors, creating a current influx which can depolarize the GER cells to as much as 37 mV (Anselmi *et al.*, 2008; Tritsch *et al.*, 2007).

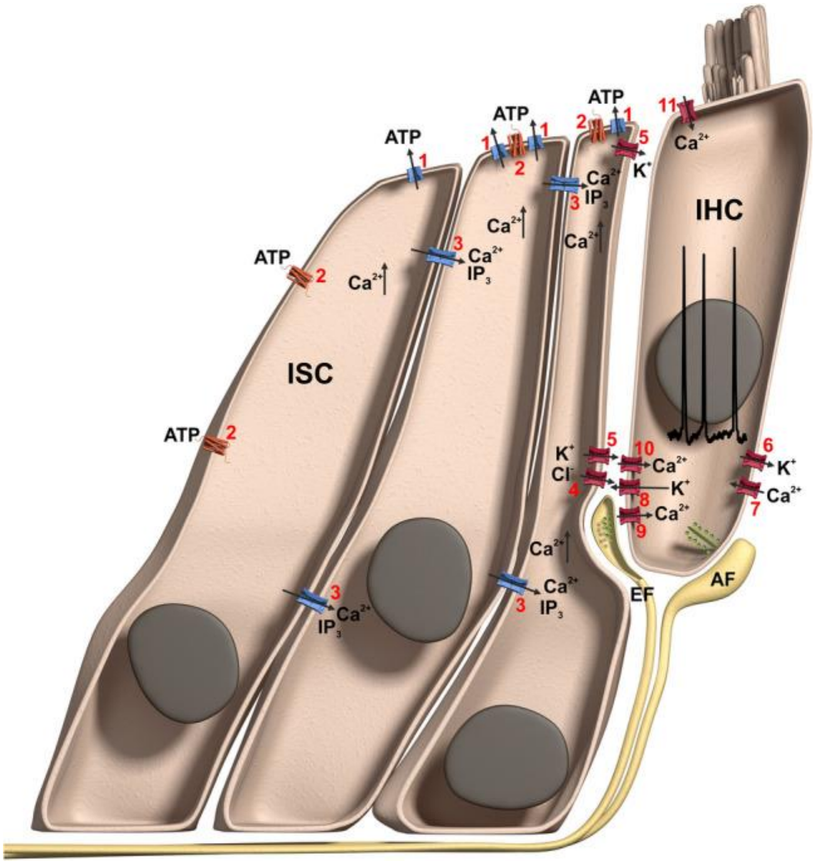

Figure 1.24 Generating the calcium wave in the GER.
Self-potentiating cycle of calcium waves in the GER with step-by-step order of the signalling pathway: **1**) ATP release through connexin hemichannels activates **2**) P2R-mediated IP_3-dependent calcium release. **3**) IP_3 diffuses through gap junctions and induces calcium release in adjacent cells, forming the propagating calcium wave. Increase of intracellular calcium triggers **4**) chloride efflux through TMEM16A channel and **5**) subsequent efflux of K^+ to depolarize IHC and **6, 7**) boost the SAP frequency. **8**) SK2 channel provides repolarizing power to SAP. Multiple calcium sources can active the I_{SK2}, including **7**) I_{Ca} during the action potential, **9**) efferent nAchR at efferent synapse, and **10**) P2XR expressed on basolateral membrane but not **11**) the P2XR expressed near the stereocilia. Image adapted from Jovanovic & Milenkovic, 2020.

ATP-dependent depolarization in the GER was proposed to be mediated by both P2X and P2Y receptors (P2XR, P2YR) (Tritsch *et al.*, 2007; Wang & Bergles, 2015). P2XRs are non-selective ionotropic receptors mediating direct calcium influx; and metabotropic P2YRs activate inositol triphosphate (IP_3)-dependent internal calcium release through G-protein kinase cascade (reviewed in Burnstock, 2007). Although both abundantly expressed in the Kölliker's organ during development (Housley *et al.*, 1998; Huang *et al.*, 2010; Järlebark *et al.*, 2000), the P2Y-selective agonist UTP induced almost the same size of response as ATP (Tritsch *et al.*, 2007; Tritsch & Bergles, 2010). Knocking out the most expressed P2Y1 receptor also severely reduced the amplitude and frequency of the spontaneous events in the non-sensory cell (Babola *et al.*, 2020). These results implies that P2Y1 is likely to be the major mediator to the spontaneous calcium wave in non-sensory cell (Babola *et al.*, 2020; Jovanovic & Milenkovic, 2020).

Just purinergic signalling is not enough to discharge the wide spreading spontaneous calcium waves in the GER (Figure 1.21). The propagation of the calcium response heavily relies on the diffusion of IP_3 molecules through gap junctions that interlink the GER cells (Anselmi *et al.*, 2008; Beltramello *et al.*, 2005; Piazza *et al.*, 2007). Although calcium can travel freely through gap junctions, IP_3 has a far better diffusion coefficient and permeability (reviewed in Decrock *et al.*, 2012), and can directly induce calcium transients (Ceriani *et al.*, 2016). Besides, the concentration of diffused calcium would not be enough to propagate the wave across multiple cells, as calcium-induced calcium release (CICR) is not the major pathway in the spontaneous calcium wave (Babola *et al.*, 2020).

The raise of intracellular calcium ($[Ca^{2+}]_i$) increases the open probability of connexin hemi-channels and results in more ATP release to a certain level before they start to close again (De Vuyst *et al.*, 2006; Leybaert *et al.*, 2003). This forms a self-reinforced cycle that automatically promotes and throttles the ATP release. Rising $[Ca^{2+}]_i$ also activates a Ca^{2+}-activated chloride (Cl^-) channel, the transmembrane protein 16a (TMEM16A), and induces the subsequent efflux of K^+ and water to compensate for the homeostasis changes from the efflux of Cl^- ions (Wang & Bergles, 2015). At the same time, the extrusion of water causes expansion of extracellular space, in a form of visible volume change (crenation) on the non-sensory cell under differential interference contrast (DIC) microscopy (Figure 1.25).

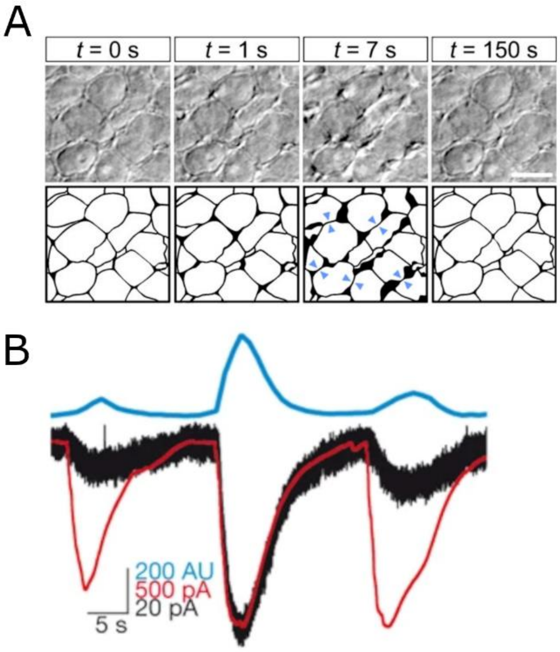

Figure 1.25 Crenation of GER supporting cells during calcium wave. **A**) time lapse imaging of the optical change in GER cells under DIC filter. Lower row highlights the changed (black) and unchanged (blue arrow) extracellular space. **B**) inward current in IHC (black) coincides with both the optical change in GER (blue) and local field potential measured in adjacent non-sensory cell(red). Images adapted from Tritsch & Bergles (2010) and Tritsch *et al.,* (2007) respectively.

Compared with SAP in IHCs (half-width < 4 ms; Johnson *et al.*, 2011), the spontaneous calcium wave in GER has a much slower kinetic. Each surge of activity can last for tens of seconds with time constant larger than one second (Tritsch *et al.*, 2007). In rat organ of Corti, the frequency of ATP-induced inward current in GER was the highest (~0.6 Hz) at the date of birth and gradually lowered toward hearing onset. Conflicting with this trend, the activity of spontaneous calcium wave was very limited at birth and had maximum frequency and spreading area in the second postnatal week (Tritsch & Bergles, 2010; Wang & Bergles, 2015). This was proposed as a result of weaker ATP release at that age, because GER responded to exogenous ATP with larger calcium transients comparable to older samples (Tritsch & Bergles, 2010). Proposed to be the outcome from the disappearance of Kolliker's organ from P9 onward, the frequency, coverage and amplitude of spontaneous calcium wave rapidly declined after hearing onset (Tritsch & Bergles, 2010).

1.3.3 Interaction between spontaneous calcium activities

The timeline of spontaneous calcium wave in the GER overlaps with the proposed "critical period" of the SAP-dependent maturation in IHC (Figure 1.26, Johnson *et al.*, 2013; Tritsch *et* *al.*, 2007). Spontaneous calcium waves, ATP signalling and K^+ secretion are proposed to modulate the excitability of IHC (Johnson *et al.*, 2011; Tritsch *et al.*, 2007; Tritsch & Bergles, 2010; Wang & Bergles, 2015).

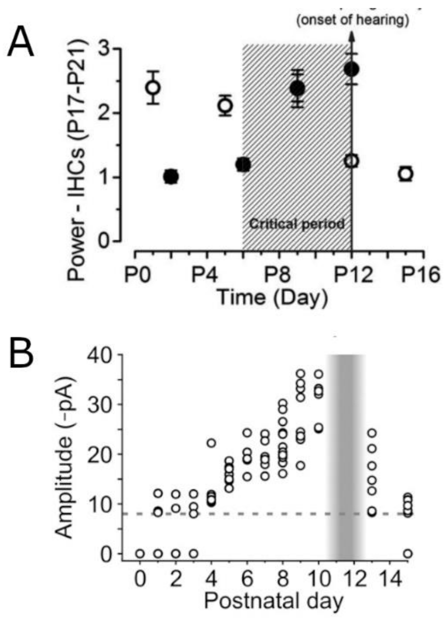

Figure 1.26 Correlation of ATP response in the critical period of maturation in IHC. **A**) the proposed "critical period" (greyed area) for the SAP-driven development perfectly correlates with **B**) ATP-elicit current response in IHC reached the maximum in the second postnatal week. The symbols in **A** indicate the outcome of synaptic efficacy when conditional modulation of SAP is switched on (closed) or off (opened) at certain age. Note that the symbol in **B** has no relation to those in **A**. Images adapted from Johnson *et al.*, (2011) and Tritsch & Bergles (2010).

Paracrine ATP release from connexin hemi-channels was proposed to directly depolarize IHC and promote their spontaneous firing (Tritsch *et al.*, 2007; Tritsch & Bergles, 2010). A later study confirmed the mechanism of action of this depolarization to be SK2 mediated current through P2X calcium influx (Johnson *et al.*, 2011). The involvement of P2Y on depolarizing IHC seemed to be limited, as a P2X-specific agonist TNP-ATP alone produced similar size of depolarization (Johnson *et al.*, 2011).

Nevertheless, ATP seemed to have a concentration-dependent bipolar effect on IHC V_m (Johnson *et al.*, 2011). IHCs always depolarized in high concentration (micromolar range) of ATP and have a drastically increased firing rate (Figure 1.27 A, E). At lower ATP concentration (nanomolar range), the effect turned into a stochastic mix with slightly depolarising, hyperpolarising, or unchanged response (Figure 1.27 B, C, E). The major effect from a physiological ($< 10\ \mu M$) concentration of ATP (Muñoz, 2001; Gale *et al.*, 2004; Muñoz *et al.*, 1995) on IHC V_m was hyperpolarization (Figure 1.27 D, E). The mechanism of this bipolar trend has not been verified but was proposed to be the influence from different activating threshold of P2X species (Johnson *et al.*, 2011; Jovanovic & Milenkovic, 2020).

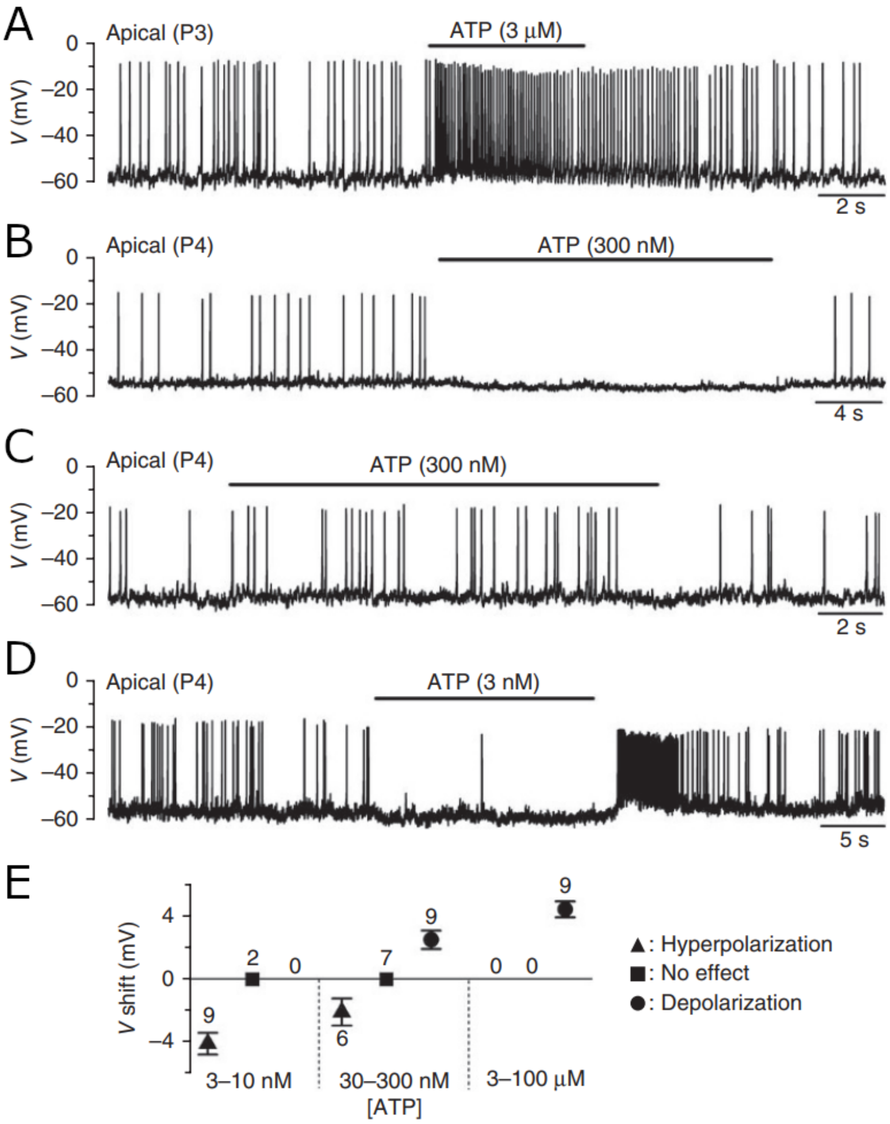

Figure 1.27 Concentration-dependent effect of ATP on IHC membrane potential.
Example traces of SAP rate responding to differing ATP concentrations, from **A**) more firing in micromolar range, **B, C**) suppressed or unchanged firing in nanomolar, to **D**) mostly suppressed firing in physiological range. Summary graph in **E**) shows that the IHC V_m was mostly hyperpolarized with physiological (very low) concentration of ATP and was always depolarized in high concentration. Mid-range concentration had a stochastic bipolar effect. Images adapted from Johnson *et al.* (2011).

The secondary effect from spontaneous calcium wave, K^+ secretion, was also proposed to promote SAP firing of IHC (Babola *et al.*, 2018, 2020; Wang & Bergles, 2015), especially during the second postnatal week when the V_m gradually hyperpolarises below the activation threshold of I_{Ca} (Johnson *et al.*, 2011; Marcotti *et al.*, 2003; Marcotti *et al.*, 2003). In spontaneous calcium waves, the outflow of K^+ from non-sensory cell was believed to change the equilibrium potential of K^+ (E_K) and invert the direction of K^+ current (Wang & Bergles, 2015). As a result, IHCs within the spontaneous calcium wave coverage were depolarized, producing promoted and synchronized SAP activities (Wang & Bergles, 2015). The capability of K^+ release on depolarizing nearby cell was corroborated in a study using glutamate vesicular transporter type 3 (vGlut3) KO mouse model. The auditory neurons cannot receive any input from IHC during SAP, as IHC with this mutation cannot load the neurotransmitter glutamate into the synaptic vesicles. Nevertheless, the auditory neurons seemed to have normal activity from the direct depolarization by the K^+ release during spontaneous calcium waves (Babola *et al.*, 2018).

A later study suggested a new aftereffect from the ATP-induced Cl^- efflux, claiming that enlarged extracellular space from crenation could effectively dilute the K^+ and shift the E_K towards a more hyperpolarized voltage (Babola *et al.*, 2020), which would help K^+ clearance and thus reduce the excitability in the IHC. The study also proposed a time-based model where K^+ accumulates at the beginning of a spontaneous calcium wave and enhances the firing of SAP. As the crenation volume enlarges with time, the extracellular K^+ is diluted and silences the IHCs, hence forms a burst/silence pattern in apical IHCs (Babola *et al.*, 2020).

1.3.4 Role of spontaneous calcium activity in maturing cochlea

It is well-established that the activity-dependent development of the neural system is instructed by a specific temporal pattern of the SAPs, which directly coupled with the dynamics of cytosolic calcium concentration (Berridge *et al.*, 2000; Redmond & Ghosh, 2005; Toth *et al.*, 2016). Ca^{2+}–calmodulin–dependent protein kinase II (CaMKII) was proposed to "decode" the frequency signalling of the calcium oscillation (Hanson *et al.*, 1994) to switch on and off of downstream kinase-phosphatase pathways in neural cells.

Most of the studies described the SAP with a near 1 Hz mean firing rate and 2-4 Hz or higher median (burst) firing rate. This frequency range matches the active range of CaMKII system (1-10Hz) reported in both in-silico modelling (Li *et al.*, 2012) and cultured neurons (Eshete & Fields, 2001), supporting current hypothesis on SAP's physiological role.

SAP in developing IHC has been proven indispensable to the maturation of the auditory pathway. Altering the SAP led to different level of abnormality on mature IHC functions. As reviewed in 1.2.3, elimination of SAP in $Ca_V1.3$ KO mice strain resulted in a full arrest of development in IHCs (Brandt *et al.,* 2003). Similar lack of development was found in mouse model with impaired MET current (Corns *et al.*, 2018). When IHCs are unable to generate SAP in the second postnatal week, they fail to acquire mature-type currents after the hearing onset. Moreover, these IHCs remained in contact with efferent terminals and were excitable upon current injection, which both are phenotypes observed in immature IHC (Corns *et al.*, 2018). Modifying the firing pattern in SAP produced a partially matured phenotype, as demonstrated in SK2-KO/OE model (see 1.2.3). IHCs acquired the matured-type current $I_{K,n}$ and $I_{K,f}$ even with a disrupted SAP firing pattern. However, their synaptic release failed to develop into the more efficient dynamic of the mature form (Johnson *et al.*, 2007; Johnson *et al.*, 2013).

The mechanisms by which spontaneous calcium waves in non-sensory cell modulate SAPs in IHCs is still under scrutiny. Current studies have established that ATP-release through connexin hemi-channels plays a critical role on the maturation of both IHCs and the auditory nerves. In fact, mutations in the connexin family are linked to almost half of the cases of inherited deafness (reviewed in Ahmad *et al.*, 2007).

Knocking out connexins kept the IHCs in their immature form even at the third postnatal week (Figure 1.28 B, Johnson *et al.*, 2017). Like those observed in mice model with abolished SAP (Brandt *et al.,* 2003; Corns *et al.*, 2018), these IHCs failed to acquire their matured I-V responses. The ribbon synapse also failed to develop and have a non-linear relation on the release efficacy (Johnson *et al.,* 2017). Knocking out only one of the two main connexins expressed in the GER, instead of both, partially allowed IHC to acquire their matured biophysical properties (Johnson *et al.*, 2017). Expressing exogenous connexin in deficient mouse model was also found to rescue the hearing loss phenotype (Ahmad *et al.*, 2007). These findings highlight how critical the ATP-releasing from GER is on the development of IHC.

Nevertheless, current evidence cannot confirm that spontaneous calcium waves in non-sensory cell have a direct influence on the SAP-driven maturation in IHC. Knocking out connexin stopped the spontaneous calcium wave and ATP-release, but also nullified the secondary K^+ secretion which was proposed capable of modulating IHC's excitability (Johnson *et al.*, 2017; Wang & Bergles, 2015). Recent studies have exploited cochlear-specific conditional knockout (cKO) of TMEM16A (Babola *et al.*, 2018; Wang & Bergles, 2015) to block the K^+ secretion and keep the ATP release intact at the same time. However, these studies have not provided any evidence of the aftereffect on the SAP and the development course of IHC in this model. Is ATP alone enough to drive the maturation of IHC? What is the real effect from the TMEM16A-mediated fluid secretion on SAP? These are the question I want to find out in this study.

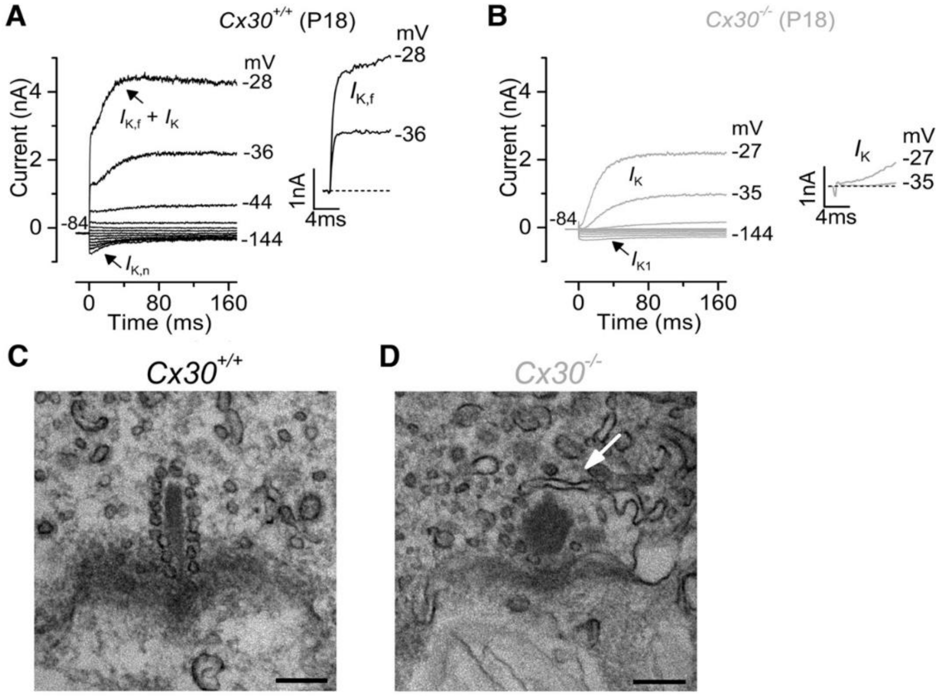

Figure 1.28 Connexin deficiency impaired the maturation of IHC.

A) IHC in control animal had normal current-voltage response with the signature fast outward $I_{K,f}$ and the inward $I_{K,n}$ with strong inactivation at more hyperpolarized voltages. B) Connexin deficient IHC failed to acquire either of the matured-type currents. C) Synaptic ribbons in control animals had a flatter rod shape with more vesicles tethered to it. D) The synaptic ribbons from knockout animals had a smaller round shape with less vesicles, as how they would be during immature stage. Images adapted from Johnson *et al.*, (2017).

1.4 Research Statement

In the model of TMEM16A cKO, the link between the spontaneous calcium waves in GER and the SAP in IHCs is removed, thus the two physiological processes become independent. This thus allows the investigation of the hypothesis:

> The effects of the GER calcium wave, namely the TMEM16A-mediated K^+ secretion, is required to drive a normal level of SAP during the development, and to regulate the maturation of IHC at hearing onset.

Below are listed the 3 aims used to address this hypothesis:

- Characterise and compare the biophysical properties of immature IHC between control and TMEM16A cKO model to identify any fundamental change.
- Characterise and compare the SAPs between control and TMEM16A cKO model to understand the modulation from ATP and K^+ secretion.
- Characterise and compare the biophysical properties of mature IHCs between control and TMEM16A cKO model to test whether ATP is enough to drive the SAP-dependent maturation.

Chapter 2 Material and Methods

2.1 Ethic statement

All animal work was performed at the University of Sheffield and the University of Sussex (UK) and licensed by the Home Office under the Animals (Scientific Procedures) Act 1986 and was approved by the University of Sheffield Ethical Review Committee. For in vitro work, mice were sacrificed by cervical dislocation, which is a Schedule 1 method.

2.2 Animals

The transgenic animals used in this study were TMEM16A^{floxed}, Pax2-Cre, Plp1-Cre$^{\mathrm{ERT}}$, and ROSA-tdTomato mice. Further details about the animals are compiled in Table 3 on page 47. All of the animals were maintained at The University of Sheffield in a 12-hour light-dark cycle according to the Home Office guidelines. Animals were culled by Home Office Schedule 1 methods.

All of the Cre-expressing animals were kept in heterozygote form to prevent complete loss of the promoter gene. The animals were cross-bred into a double knock-in strain (TMEM16A^{floxed}:Pax2-Cre) or a triple knock-in strain with reporter gene (TMEM16A^{floxed}:ROSA-tdTomato:Plp1-Cre$^{\mathrm{ERT}}$) for inducible conditional knockout. Due to the interruption from the COVID lockdown, it was a compromised decision to bred TMEM16A^{floxed}:Pax2-Cre model without the reporter gene in order to fit the timeline of the study within funded period.

Table 3. Transgenic animals used in this study.

Strain	Allele	Reference	Source
TMEM16A^{floxed}	Floxed TMEM16A	Faria *et al.*, 2014	Courtesy of Prof Jason Rock
Pax2-Cre	Tg(Pax2-Cre)1Akg	Ohyama & Groves, 2004	Courtesy of Prof. Andy Groves,
Plp1-Cre^{ERT}	B6.Cg-Tg(Plp1-cre/ERT)3Pop/J	Doerflinger *et al.*, 2003	The Jackson Laboratory (#005975)
ROSA-tdTomato	B6.Cg-Gt(ROSA)26Sor$^{tm9(CAG-tdTomato)Hze}$/J	Madisen *et al.*, 2010	Courtesy of Dr Mirna Mustapha

Contact

Prof Jason Rock	Howard Hughes Medical Institute and Department of Physiology, University of California, San Francisco, CA 94158, USA.
Prof. Andy Groves	Departments of Neuroscience and Molecular and Human Genetics Program in Developmental Biology Baylor College of Medicine, BCM 295 / Room 633E1 Baylor Plaza, Houston, TX 77030.
Dr Mirna Mustapha	School of Biosciences, The University of Sheffield, Western Bank, Sheffield, S10 2TN, United Kingdom.

2.3 Cre-recombinase induction

Tamoxifen (T5648-1G, Sigma-Aldrich) was mixed in 15ml Falcon tube with corn oil (C8267, Sigma-Aldrich) to a final concentration of 20 µg/µl. The mixture was then sonicated for 30 minutes at 55°C in a dark water bath before aliquoting into 1ml Eppendorf tubes for freezing at −20°C.

On the day of experiment, a tube of tamoxifen (typically 400 µl) was covered with foil to avoid the light-sensitive degradation, and defrosted with heating mattress set to approximately body temperature (37-40 °C). The solution was then transfer into a 30G syringe and covered with foil.

Tail-clipping was performed when genotyping was required, otherwise the animals were only tattooed for monitoring purpose. Tamoxifen solution was then administered subcutaneously to P2-P3 pups for a target concentration of 100µg/g body weight. The animals were weighed at least every other day up to a week to keep track of side effects. The humane endpoint was reached when the weight of the animal was 20% lower than the average weight from wild-type animals at the same age.

A proof-of-principle Cre-induction assay with the reporter gene (ROSA-tdTomato) was performed to verify the protocol for tamoxifen administration. The existing protocol for fully developed animals requires a target concentration 200µg/g of body weight with repetitive injection. I reduced this by half to avoid potential harm from overdosing the light-weighed new-borns. Using TMEM16A$^{\textit{floxed}}$:ROSA-tdTomato:Plp1-Cre$^{\mathrm{ERT}}$ strain, one dose of tamoxifen was administrated to neonatal mice at P1 for baseline condition. Another two doses were given at P2 and P3 for testing whether the extra dose produce a better induction rate. This is to evaluate if a lower dosage can be used for the welfare of the animals under procedure, and also, whether excessive handling can be reduced to avoid the stress of the nursing parents.

Figure 2.1 shows the results from different tamoxifen administration protocols. Note that the mouse strain used test the induction of Cre-recombinase had only the ROSA-tdTomato reporter gene but not the TMEM16A-floxed gene. One dose of tamoxifen with 3 days of incubation was enough to activate the Cre-recombinase activity and induce tdTomato expression in at least

50% of the cells in the sampled regions (Figure 2.1 A). For reference, the constantly active Pax2-Cre (Figure 2.1 C) drove near 100% of tdTomato expression. Compared with that, The Plp1-Cre^{ERT} generally had a lower induction rate (Figure 2.1 B). More doses of tamoxifen induction did not seem to improve the induction rate (Figure 2.1 A). The result showed a wide variety of the induction efficiency even in adjacent region. Areas 50-100 µm apart could have near 40% of difference on their induction rates (Figure 2.1 D, E). An increasing trend of induction rate seemed to exist among the tonotopic axis (Figure 2.1 A, Plp1-Cre^{ERT}), but it was not investigated further as only apical IHCs are investigated in this study.

We decided to directly evaluate the KO efficiency in individual animal with TMEM16A immunolabeling in the contralateral cochlea collected during the experiments. Confocal images were collected from the 4 kHz to 10 kHz region of the apical coil.

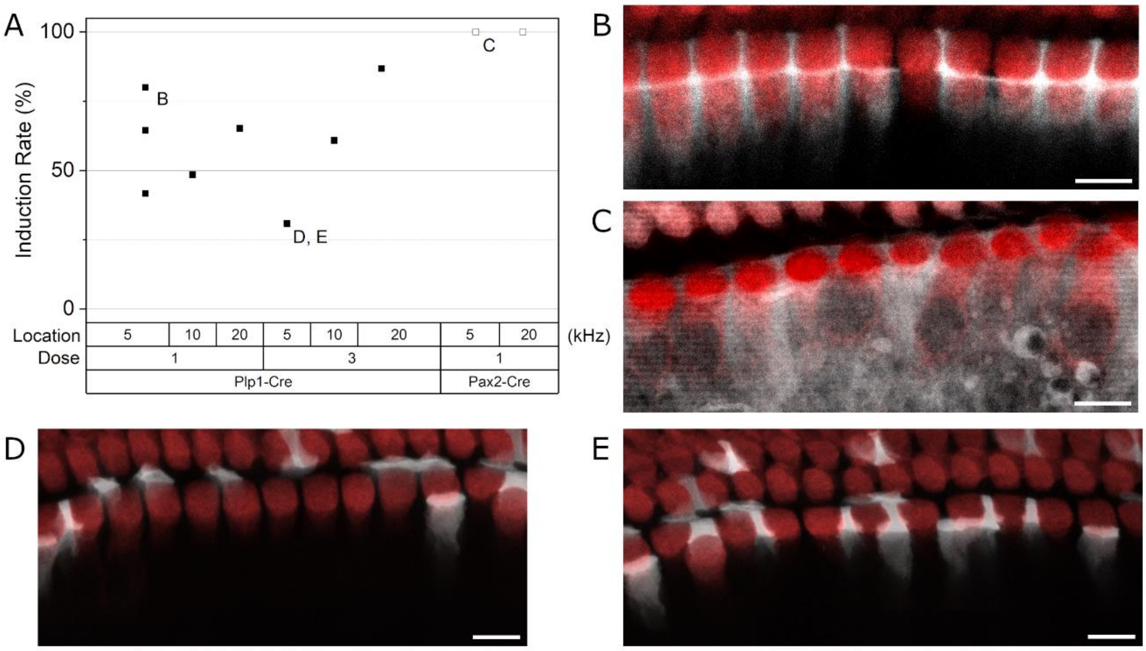

Figure 2.1 Cre-induction by tamoxifen administration.
A) Cre-induction rate at different frequency region with 1 or 3 doses of tamoxifen injection. Each point was calculated from the percentage of tdTomato expression cells within 130 x 130 µm^2, or 260 x 130 µm^2 region at a tonotopic location, specified with their characteristic frequency. Closed symbols are data from ROSA-tdTomato:Plp1-Cre^{ERT} and open symbols are from ROSA-tdTomato:Pax2-Cre animals. B-E) Sample image of tdTomato expression (grey) form corresponding data point marked in A. D, E) are images took from the same region (overlapping edge). They were cropped for a better fit in the image frame. Together they indicate an internal difference of the Cre-induction within the same subject. Biological repeats in A) were: Plp1-Cre^{ERT}, 1 dose at 5kHz, n=3; 1 dose at 10 and 20 kHz, n=1; 3 doses, n=1, Pax2-Cre, 1 dose, n=1.

2.4 Patch-clamp electrophysiology

2.4.1 Hardware configuration

Ex-vivo organ of Corti tissue was mounted in recording chamber and clamp to a custom-made stage on Leica DM LFS electrophysiology microscope. The microscope was fit with x63 water immersion objective (Leica HC APO L 63x/0,90 W U-V-I) and 16x/14B eyepieces. Custom-made micromanipulators were mounted next to the microscope to position the reference electrode and utility pipettes. The recording electrode was connected to the amplifier head stage (Axopatch 200B with original headstage; Axon Instruments, USA) which was mounted on PatchStar (Scientifica, UK) micromanipulators. All above peripherals were installed on a suspended table (TMC, USA) in a Faraday cage to minimize interference from vibration and electrical noise.

During experiments, the recording chamber was constantly supplied with heated or room temperature extracellular solution at flow speed of 9 ml per minute controlled by a pump (Masterflex L/S, Cole-Parmer Instrument Company, US). To set the temperature around the objective at near body-temperature (34-36 °C), solution was heated next to the chamber inlet with a custom-made heat block without feedback control to avoid thermal oscillation. The amplified signals were filtered at 2.5 kHz or 10 kHz (−3dB; varied from protocols) with a custom-made Bessel low-pass filter (LPF) before being sent to a digitizer (Digidata 1550B, Axon Instruments, USA). Digitized data was sampled at 20 kHz by the Clampex 10.7 software (Axon Instruments, USA) and saved on a computer for *post-hoc* analysis.

For inspection of tdTomato fluorescence, a green laser (350-700 nm; COP2-A emitter with LEDD1B driver, Thorlabs Inc., USA) was used to excite the endogenous tdTomato expression driven by successful Cre^{ER}-induction. A Cy3 filter set (Cy3-4040C-LDMK-ZERO, Semrock, USA) was used to isolate the emitted tdTomato fluorescence.

2.4.2 Experimental solutions

Extracellular solution (ECS) was designed to approach physiological condition with composition similar to the perilymph fluid that hair cells are bathed in. Detailed composition of the solution is listed in Table 4. Amino acids (11130-036, Gibco, USA) and vitamins (11120-037, Gibco, USA) were added as a supplement. The final pH of the solution was adjusted to 7.48 with 1M or 4M NaOH. Typical osmolality of the solution was 308–310 mOsm/kg.

Recording pipette was filled with different type of solution according to the protocol. For whole-cell configuration, it was a KCl-based intracellular solution (ICS) with final pH 7.28 (adjusted with 1M KOH) and a typical osmolality 294 mOsm/kg (detailed composition in Table 4). For cell-attached configuration, the pipette solution was similar to ECS but without the supplements. Detailed composition is listed in Table 4. The final pH of cell-attached solution was adjusted to 7.48 with 1M NaOH and the typical osmolality was 294 mOsm/kg.

Table 4. Composition of experimental solutions

Chemical	Extracellular	Intracellular	Cell-attached
		final concentration (mM)	
NaCl	135	--	140
$CaCl_2$	1.3	--	1.3
KCl	5.8	131	5.8
$MgCl_2$	0.9	3	0.9
KOH-EGTA	--	1	--
HEPES	10	5	10
Glucose	5.6	--	5.6
$NaH_2PO_4 \cdot H_2O$	0.7	--	0.7
NaPyruvate	2	--	--
Amino acids	1x	--	--
Vitamins	1x	--	--
Na_2Phosphocreatine	--	10	--
Na_2ATP	--	5	--

2.4.3 Recording electrodes

Chlorinated silver wire with a PTFE coating was insert into microelectrode holder (G23 instruments, UK) and fit onto the head stage of the amplifier. Patching pipettes were pulled from soda glass capillaries (1413027, Hilgenberg, Germany) with a gravity puller (Narishige Instruments, Japan). The curvature tip of the pipette was waxed (Mr Zoggs SexWax, USA) to reduce parasitic capacitance. Each experiment was recorded with a new pipette with freshly loaded solution (depends on protocol). Typical resistance in ECS was 2.4-2.8 MOhm.

2.4.4 Cleaning pipette

Cleaning pipettes were used to suck away debris or manipulate the non-sensory cell to gain access to the basolateral membrane of the IHC. They were pulled from borosillicate glass capillaries (30-0062, Harvard Apparatus, UK). The diameter at the tip was 2-3 µm. The pipette was connected to a syringe filled with ECS for pressure control.

2.4.5 Tissue preparation

Cochleae acutely removed from the temporal bone were transferred to a dish under a dissecting microscope (Leica, Germany). The dish was filled with ice-cold ECS for post-hearing IHC. To prevent thermal shock when transferred into the chamber with body temperature (34-36 °C) fluid, room-temperature ECS was used for immature IHC instead.

The cochlea was dissected with a pair of extra fine forceps (#55 Dumont, Fine Science Tools, Germany). For post-hearing dissection, the apical bone of the cochlea was carefully removed to expose the organ of corti. After severing the modiolar bone, the apical coil of organ of Corti was cut and transferred to the recording chamber. It is paramount not to touch the organ of Corti at any point until it is cut loose from the cochlea. The dissected tissue was secured at the bottom of the chamber with nylon mesh glued to a metal ring. The tectorial membrane was then removed to expose the hair cells underneath.

For immature dissection up to P6, the cartilage was sliced open on the surface from oval window to the apical tip, and then carefully cut along the coil groove to allow removal without pressuring the organ of Corti. Starting from the basal end, the spiral ligament between the coils was gently cut to separate the organ of Corti from the modiolar tissue. The stria vascularis was then removed before the organ of Corti was cut and transfer into the recording chamber.

2.4.6 Cell-attached configuration

This method was applied only on immature IHC recording. Since the main purpose is to investigate the role of non-sensory cell on the SAPs, I believe it is critical to keep all the surrounding cells as intact as possible. In Wang & Bergles, 2015, they stated that cleaning off either BC or PC makes no difference. However, they did not provide any evidence.

To help explain this method, the cleaning procedure to expose an IHC for patch-clamp recording is visualized as critical-frame extractions from a video (Figure 2.2). The BC next to target IHC was approached with a cleaning pipette from modiolar side, aiming close to the edge of IHC's cuticular plate (Figure 2.2 A). To peel the BC away without lysing it, the cleaning pipette was quickly pulled aside while by applying a transient of gentle negative pressure (Figure 2.2 B) which is released after the top of BC was moved away (Figure 2.2 C). Any attempt with lysed BC was discarded. After exposing an accessible basolateral membrane, IHCs were approached with a recording electrode filled with cell-attach solution (Figure 2.2 D). A gentle positive pressure was constantly applied to the electrode to avoid blockage at the tip.

After a visible dimple was spotted on the membrane (Figure 2.2 E), the positive pressure was quickly replaced with a gentle suction to help form a seal (Figure 2.2 F). Typical resistance of a reliable seal is above giga-Ohm, actual values were ranging from 2-8 GOhm. Any recording with a resistance less than 1 GOhm was discarded. The amplifier was set to voltage clamp mode at 0 mV during the recording. The cell-attached protocol was filtered at 10kHz with Bessel LPF and sampled at 20kHz to provide good temporal resolution on a single AP. Average recording time was around seven minutes but can vary from condition or spiking activity. The recording was be terminated if there was no activity after 3 minutes, which is the minimal recording time included. The rationale to stop recording was that, based on GER activity frequency in the literature (0.4 Hz; Tritsch & Bergles, 2010; Wang & Bergles, 2015), during any given 180 seconds time window IHC should receive nearly 75 occasions of the TMEM16A-mediated effect from the GER. If there was no spiking activity presented during this period, the excitability of IHC is probably very low. Longer periods were attempted before the approach was taken and they produced 2 spikes in 420 seconds (0.004 Hz), which is much lower than the typical mean firing rate (~2 Hz; Johnson *et al.*, 2011).

To verify the usability of a recording, I attempted break the seal into whole-cell configuration and observe the I-V response with different voltage steps. When whole-cell is not achievable, stretching membrane by the pulling-away electrode was used as visual confirmation instead. If both checkpoints failed, the recording was discarded.

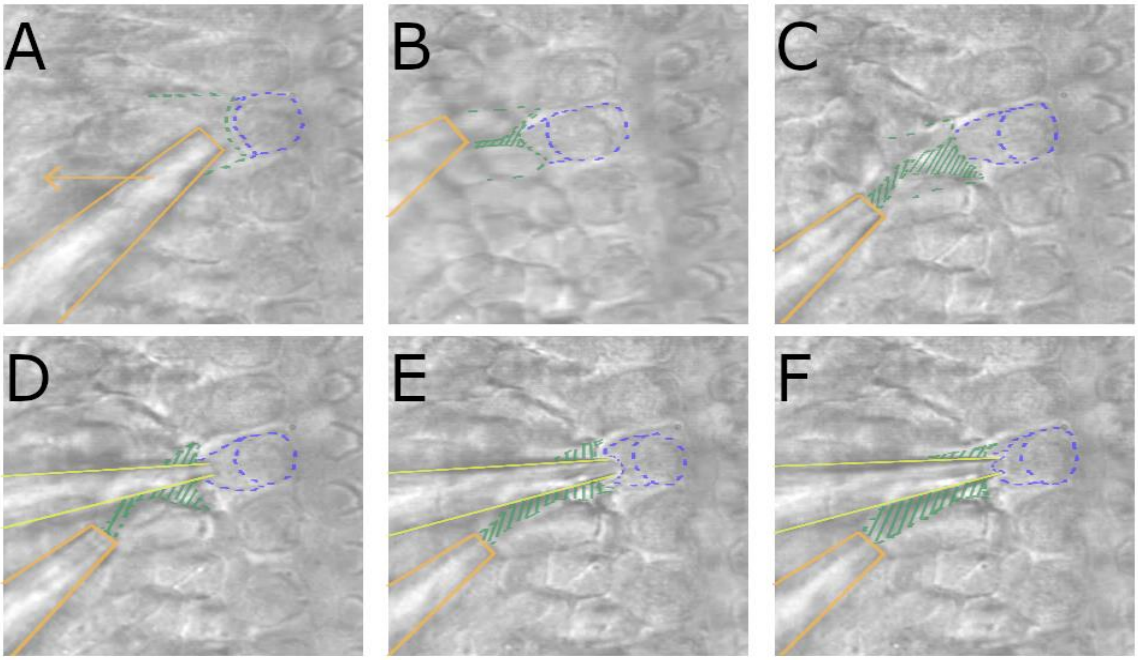

Figure 2.2 Approach of patch-clamp recording on immature IHC.
Critical frames extracted from a video of a successful patch-clamp recording. **A-C**) A cleaning style to make the best effort on preserving the SCs. **D-F**) Steps to forming a giga-seal with recording electrode. Orange line marks the position of cleaning pipette that was used to manipulate BC. Green and blue dashed lines mark the edge of BC and IHC respectively. Pattern-filled green marks the surface of the BC in contact with IHC before being opened. Yellow lines mark the position of the recording electrode. As this is purely for illustration purpose, scale bar was not included.

2.4.7 Whole-cell configuration

For the whole-cell configuration with immature IHC, similar procedure was use as described in 2.4.6 to make good consistency. The solution in the recording electrode was KCl-based ICS instead of cell-attached solution. The recordings were filtered with 2.5kHz LPF and sampled at 20kHz.

For post-hearing IHC, the minimal-damage cleaning was not feasible, because the BC had become very thin and formed tighter bonds with IHC around the cuticular plate, making them harder to manipulate without damaging IHC. Besides, there should be no expression of TMEM16A after P16-17 (Tritsch & Bergles, 2010; Yi *et al.*, 2013). Depending on the relative position of the pipettes, BC or inner phalangeal cells were lysed from the bottom half, near their nucleus. After cleaning all the debris and exposed an area of IHC membrane, the procedure returned to what was described in 2.4.6 on forming a giga-Ohm seal. After the seal was acquired, the holding voltage was set to −80 mV with an external calibrator (custom-made). The seal was then broken by applying gentle suction with a mouthpiece connected to the recording electrode. Typical series resistance was around 2-4 mega-Ohm.

With current-clamp protocols, voltage response of the IHC were induced by injecting 250 ms currents of different amplitudes with 10 pA intervals, followed by 140 ms at the resting membrane potential (Figure 2.3 B). As the injection current became larger, the voltage responses changed from sustained depolarization to induced action potentials in immature IHCs (Figure 2.3 C). The spiking threshold was defined as the amount of current injection to produce the first spike (Figure 2.3 C, centre panel). Since post-hearing IHCs do not generate induced spikes, the interval of injected current steps was increased to 100 pA to generate more pronounced responses.

To investigate the current dynamics upon voltage stimulus (I-V response), IHCs in voltage-clamp protocol was given 170 ms of voltage steps from −124 mV to +26 mV with 10 mV interval (inset of Figure 2.4 A), followed by 170 ms of holding voltage at -40 mV before return to the resting V_m. The voltage stray in voltage-clamping protocol was compensated with online current injection and adjusted accordingly in *post-hoc* analysis with Equation 1, where V_{step} and Rs are the stepping voltage and series resistance measured from the sample. The percentage of the compensation was 80% in all of the recorded samples.

Equation 1 Compensation of voltage drift over access resistance

$$V_{comp} = V_{step} - 80\% \times R_s \times I_{steady}$$

The initial and steady-state currents (I_{init} and I_{steady}) were calculated from averaging 1.5 ms or 30 ms region at the beginning and before the ending of each voltage step (yellow and blue area in Figure 2.4 A), and then plotted against their stepping voltage as in Figure 2.4 C. The values of I_{init} at −25 mV and I_{steady} at 0 mV were arbitrarily selected as indexes to analyse the current size. The reversal potential (E_{rev}) of I_{steady} was extracted by interpolate the zero current point on the voltage axis.

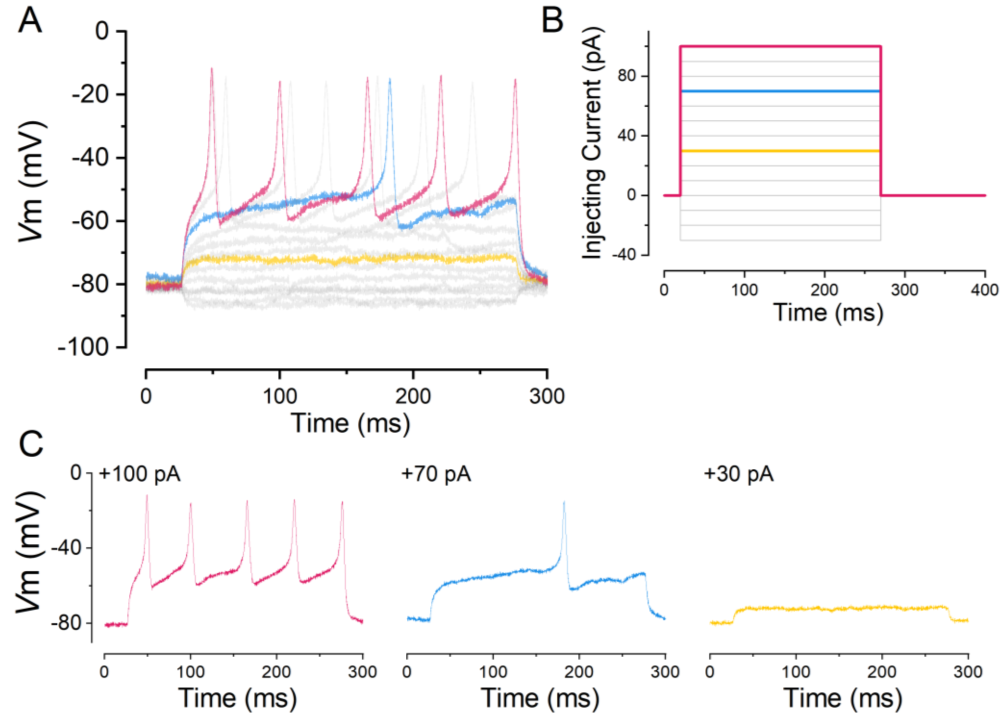

Figure 2.3 Typical voltage response upon current injection in immature IHC
A) Current clamp recording of an IHC's membrane potential with a stimulation protocol shown in B). Current injections were delivered every 390 ms. Each injection lasted 250 ms, with amplitudes stepping up from -30 pA to 100 pA in intervals of 10 pA. The highlighted traces are maximum stimulation (red), threshold (blue), and subthreshold (yellow). C) Individual waveforms of the highlighted traces with the amplitude of injected current marked on top-left.

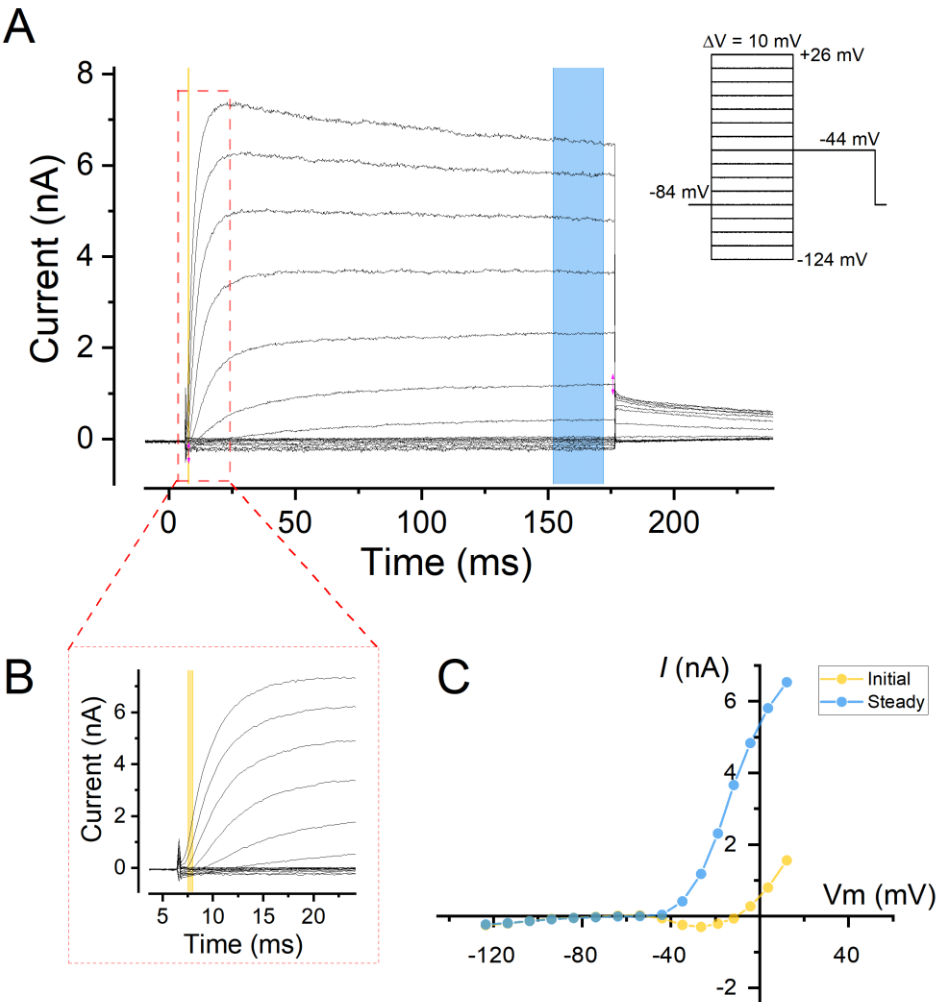

Figure 2.4 Typical current response upon voltage steps in immature IHC

A) Voltage clamp recording of the whole-cell current with stimulation protocol shown as the inset. The IHC was held at −84 mV for 65 ms before given 170 ms of stimulation steps, ranging from −124 mV to +26 mV with 10 mV interval. The zero point on time axis indicates the start of the voltage steps. The cell was then held at −40 mV for 170 ms to generate tail currents for studying channel dynamics (not used in this study). Red dashed square region is enlarged in B) to highlight the slow activation of the outward current. The coloured areas show the sampling region for initial (yellow) and steady (blue) currents in the analysis. C) I-V response of the initial (yellow) and steady (blue) current sampled from each voltage step, with voltage compensation stated in the 2.4.7.

The above protocols were also used on investigating the basic electrophysiological response in IHCs after hearing onset. To investigate $I_{K,n}$, a specialized voltage-clamp protocol was used instead (Figure 2.5 inset). This protocol held the cell at −64 mV and delivered a voltage steps of −144 mV for 170 ms and then −120 mV before returning to the holding potential. As $I_{K,n}$ is almost fully closed at voltages more negative than −120 mV (Marcotti & Kros, 1999), it can then be dissected out by subtracting the current size between the peak and the deactivation in the *post-hoc* analysis (Figure 2.5).

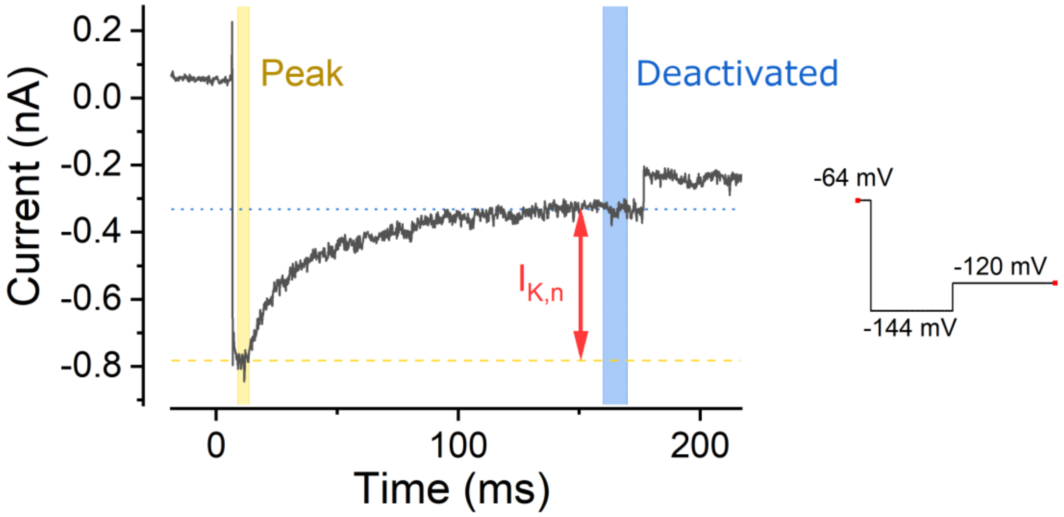

Figure 2.5 Measuring $I_{K,n}$ with a specialized voltage-clamp protocol.
The size of $I_{K,n}$ (red double arrow) was calculated by subtracting the peak current (dashed line, averaged from yellow area) with the fully deactivated steady current (dotted line, averaged from blue area). The inset panel shows the protocol of the voltage steps.

2.5 Two-photon confocal Ca^{2+} imaging

Ex-vivo organ of Corti from P3 to P9 were dissected with the procedure describe in 2.4.5. Before transfer into the recording chamber, the tissue was incubated with a calcium dye mixture for 40 minutes at 37°C. The dye mixture is based on DMEM/F12 medium, supplemented with fluo-4 AM calcium dye (final concentration 10–20 µM; Thermo Fisher Scientific). Pluronic F-127 (0.1%, w/v, Sigma Aldrich, UK) and sulfinpyrazone (250 µM) was added to prevent dye sequestration and secretion.

The sample was then mounted on the recording chamber as described in 2.4.5 and perfused with near body temperature ECS (33-36°C) for 20 min before imaging to allow for de-esterification. Ca^{2+} activities were recorded using a two-photon laser-scanning microscope (Bergamo II System B232, Thorlabs Inc., USA) based on a mode-locked laser system operating at 925 nm, 80-MHz pulse repetition rate, < 100-fs pulse width (Mai Tai HP DeepSee, Spectra-Physics, USA). The two-photon microscope was operated by Dr Federico Ceriani or Dr

Francesca De Faveri. Images were captured at 15 frame-per-second (fps) with a ×60 objective, 1.1 NA (LUMFLN60XW, Olympus, Japan) using a GaAsp photomultiplier tube (Hamamatsu) coupled with a 525/40 bandpass filter (FF02-525/40-25, Semrock). Images were saved on a computer and analysed post-hoc using custom-built software written in Python (Python 2.7, Python3.7; Python Software Foundation, available at http://www.python.org) and Fiji ImageJ software (Schneider *et al.* 2012). Detailed analysis workflow is in 2.7.3.

2.6 Immunofluorescence microscopy

Cochleae were directly perfused in 4% paraformaldehyde in phosphate-buffered saline (PBS, pH 7.4) for 20 minutes at room temperature. The cochleae were washed three times with 10 minutes PBS before dissecting out the organ of Corti. The dissected tissues were incubated in 0.5% Triton X-100 in PBS (PBST) containing 5% normal goat serum (# 31873, Invitrogen) for an hour in RT.

A list of primary and secondary antibodies used can be found in Table 5. Both primary and secondary antibodies were diluted with 1% normal goat serum in PBST (NGST). Samples were perfused in primary antibodies for overnight in 4 °C. Three ten minutes PBS washes were applied to the samples before they were incubated with secondary antibodies for an hour at 37 °C. Another three PBS washes were applied to the samples before they were mounted in VECTASHIELD (H-1000, VECTOR Labs).

Images were collected with LSM880 AiryScan confocal microscope system (Zeiss, Gemany) under 60x oil objective. Images was processed with Fiji ImageJ software (Schneider *et al.* 2012) and compiled with GNU Image Manipulation Program (The GIMP Development Team, 2019. GIMP, Available at: https://www.gimp.org).

Table 5. List of antibodies used in the study.

n/a: not applicable

Species-isotype	Antigen	Fluorophore	Vendor	Catalogue number	Concentration
Rabbit-IgG	hTMEM16A	n/a	Abcam, USA	ab53212	1:500
Mouse-IgG1	Myo7a	n/a	DSHB	No. 138-1c	1:500
Mouse-IgG2a	GLAST	n/a	Miltenyi Biotec	130-095-822	1:500
Goat-IgG	Rabbit-IgG	Alexa 405	Thermo Fisher Scientific	A31556	1:500
Goat-IgG	Mouse-IgG1	Alexa 647	Thermo Fisher Scientific	A21240	1:500
Goat-IgG	Mouse-IgG2a	Alexa 568	Thermo Fisher Scientific	A21134	1:1000
Goat-IgG	Mouse-IgG2a	Alexa 488	Thermo Fisher Scientific	A21131	1:1000

2.7 Data Analysis

2.7.1 Statistics and general analysis

All of the statistics were done with OriginPro 2021 9.8.0.200 (64-bit, Academic, OriginLab Corporation), except the Pearson's correlation coefficient in calcium imaging analysis which was done with Python. The I-box in data graphs indicates *mean±SD* unless specified otherwise.

2.7.2 Analysis workflow for SAP recordings.

Custom-made Python scripts were used for supervised spike sorting, as all of the available options (Clampfit 10.7, Axon Instruments, USA; Minianalysis, discontinued) have less than 70% of acquisition rate and easily bias the statistics, especially in burst firing activity. The graphic interface and processing functions was coded in Python 3.7.9 (Python Software Foundation, available at http://www.python.org) with Jupyter notebook 6.1.4 (Kluyver *et al.*, 2016) in virtual environment managed by Anaconda (Anaconda Software Distribution, Anaconda Inc. Available at https://anaconda.org/). The source code will be available upon request.

Figure 2.6 shows the interface of the custom-made spike sorting software. After a recording is loaded into the workspace, the program will perform baseline analysis with Savitzky–Golay filter (window: 0.15 s; third-degree polynomial) and flatten the recording by subtract the baseline for a better peak detection. The debased trace will then be filtered again with Savitzky–Golay filter (window: 5-8 ms; third-degree polynomial) to remove noise for better preview. The denoised trace was used for viewing and peak seeking. Only the raw trace was used in the analytical process. The detection threshold was automatically set with twice of the SD of the denoised trace, and 10 times of the SD for rejection threshold. Both thresholds were manually adjusted to get the best result.

Since this is designed for cell-attached recordings, the sign (direction) of the current is inverted. Clicking on "Find Spikes" button identifies all of the negative going peaks between the thresholds, and extract a 35 ms period from the raw trace (20 ms before and 15 ms after the peak) to be analysed with supervised spike sorting algorithm. The extraction period of a spike was defined with the minimal inter-spike intervals (ISI) observed during current injection in current-clamp recordings. There were never two spontaneous spikes observed in the same frame.

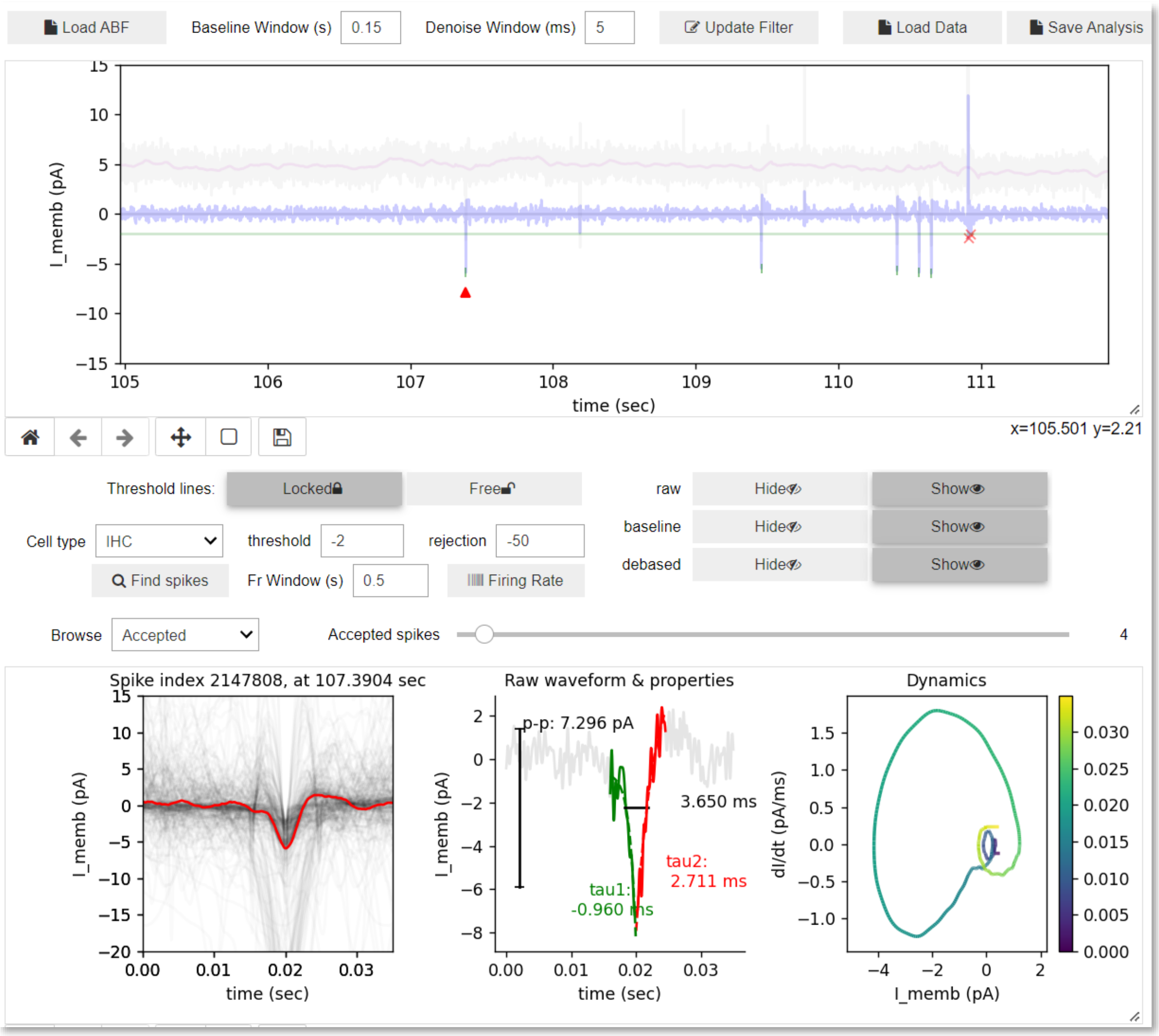

Baseline Window (s) 0.15

Denoise Window (ms) 5

Threshold lines: Locked

Cell type IHC

threshold -2

rejection -50

Fr Window (s) 0.5

Browse Accepted

Accepted spikes 4

x=105.501 y=2.21

Figure 2.6 Interface of the custom-made spike sorting software.
From top to bottom, the first row hosts the functions for data manipulation and initial setting for the filter parameters. View panel in the second row shows the raw trace (grey), filtered baseline (pink), and processed signal (blue), as well as the detecting threshold (green) and rejecting threshold (red, not in the view). It also provides zoom and pan function (bound to mouse) in both axes for a faster and easier previewing. The third row are options for spike sorting and line visibilities. The bottom 3 panels display the characteristics of the selected spike candidate (red triangle in the view panel) for quality control: left, denoised trace of current candidate in red and all others in grey; centre, the raw trace, time constant fitting and rejection status of the candidate; right, the dynamics of current derivative against current value from the candidate, with the colour indicates the time points in seconds. Current view shows the characteristics of a typically acceptable spike.

The spike sorting algorithm extracts the time constant of the rising and falling edges of a spike candidate by fitting the raw trace with a single exponential equation. The initial parameter for the fitting function was set according with the fitted value from 150 spikes hand-picked from three SAP recordings from C57BL/6J mice. If either of the time constant fitting was failed, the candidate will be set as rejected. This method is quite reliable and produce consistent result, except for some extremely vague cases which were usually discard during quality control, for instance, varying size due to sample stray, or indistinguishable peaks that were very close to noise floor.

After the spike sorting algorithm assigned the presumed rejection states, all of the candidates were manually processed again by examining the shape and the dynamics of the candidate as showed in the bottom three panels of Figure 2.6. The left panel gives a preview of the similarity of the candidate to the rest of the dataset. The centre panel shows the raw trace and the time constant for examining the shape and dynamics. If a candidate did not present a biphasic waveform, they will be rejected. The right panel shows the time-derivative of the current against its size. A typical spike would have a shape of asymmetric cardioid, as showed in the bottom right panel in Figure 2.6, with clear depolarization, hyperpolarization, and repolarization phases. Oscillating noise would look like a circle, or a spiral if there are size difference. Electric (switching) noise would be more symmetric instead of a left-dominant cardioid.

If a possible candidate was spotted on the viewing panel, they can be manually added into the pool for examination. After the whole recording has been checked, the time point and extracted features of the spikes were saved into CSV files for further analysis in the OriginPro software. All of the parameters used in the session will be saved into a text file, so that any sorted recording could be loaded again to make adjustment.

The ISIs between the previous (ISI_{i-1}) and the next spike (ISI_{i+1}) were calculated for each spike to study the firing pattern. ISI_{i-1} from individual spikes were plotted against recording time in a scatter plot and coloured with the ISI_{i+1} to give a preview of the SAP activity (Figure 2.7 A). The recording time of each sample varied from 3 to 15 minutes, and had no reference point with each other. As a result, they were used only for preview purpose.

To better understand the bursting pattern, the ISI_{i+1} was plotted against ISI_{i-1} in scatter plot for describing the relationship between three continuous spikes (Figure 2.7 B). The dashed lines mark a reference ISI at 250 ms, equivalent to the instantaneous firing rate of 4 Hz, which was the median/burst firing rate reported in the literatures (Eckrich *et al.*, 2018; Johnson *et al.*, 2011). Along the diagonal line, points locate at more top-right corner of the plot indicate a sparse firing with longer ISI in between, and those at bottom-left corner indicate rapid/burst firing. The occurrence of each ISI range was plotted in histogram to show the distribution of the spiking dynamics (Figure 2.7 C).

The length of each continuous burst was calculated by summing the sequential spikes with ISI_{i+1} value smaller than 216.45 ms, which was the median ISI in the control animals. Encountering any ISI_{i+1} longer than the threshold would stop the summation of ISI and register the total time interval of the burst to the data. Bursts with less than 5 ISI (arbitrarily set) were not included in the analysis to emphasise the capability of generating longer bursts.

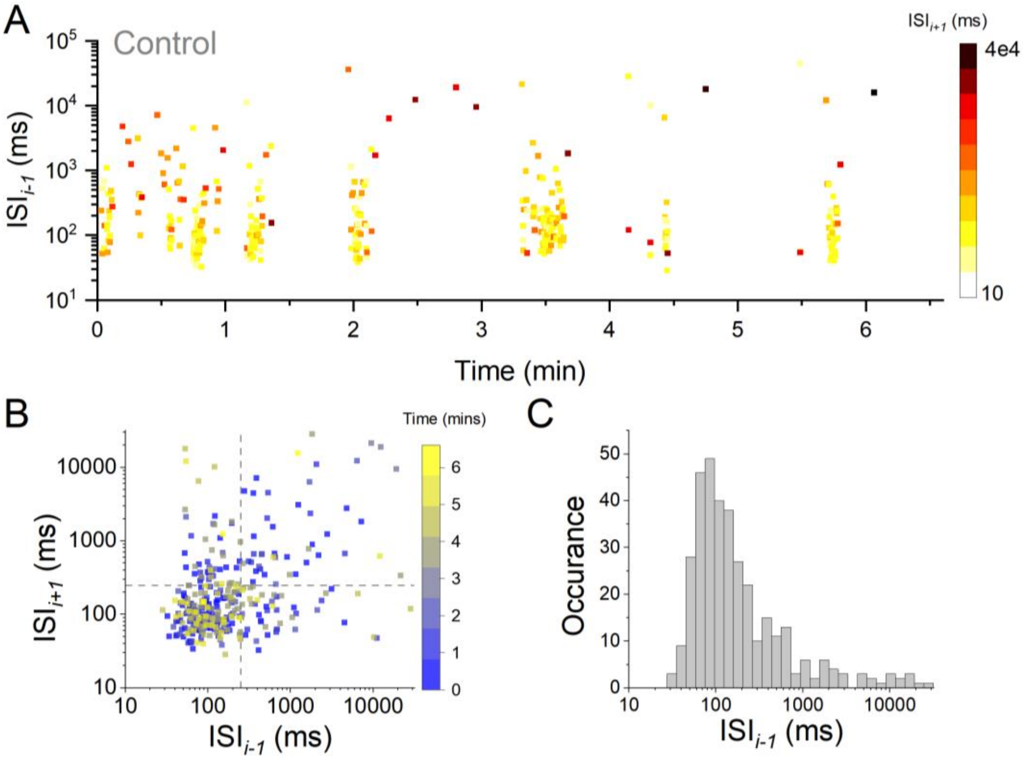

Figure 2.7 Example of analysis workflow on SAP firing pattern

A) ISI between the i^{th} and the i-1^{th} spikes (ISI_{i-1}) plotted as a function of time, coloured from bright yellow to dark red indicates the ISI_{i+1}. B) ISI_{i+1} plotted against ISI_{i-1} in scatter graph, coloured with the recording time from the start (blue) to the end (yellow). The dashed line marks the ISI with instantaneous firing rate of 4 Hz. C) The occurrence of ISI_{i-1} in the recording was plotted in plotted in a logarithmic histogram for distribution analysis.

2.7.3 Analysis workflow for calcium imaging data

The acquired calcium imaging data is processed with RoboPy (Calcium imaging analysis software by Dr Federico Ceriani. Available at: https://github.com/fedeceri85/robopy2 in GPL-3.0 licence) for data extraction. The intensity of Ca^{2+} activity was measured as relative changes of fluorescence emission intensity ($\Delta F/F_0$). $\Delta F = F - F_0$, where F is averaged fluorescence intensity within a region-of-interest (ROI) at a specific frame (Figure 2.8), and F_0 is an algorithm-selected window (7-10 frames) with minimal standard-deviation (SD), which normally represents a period of the lowest activity.

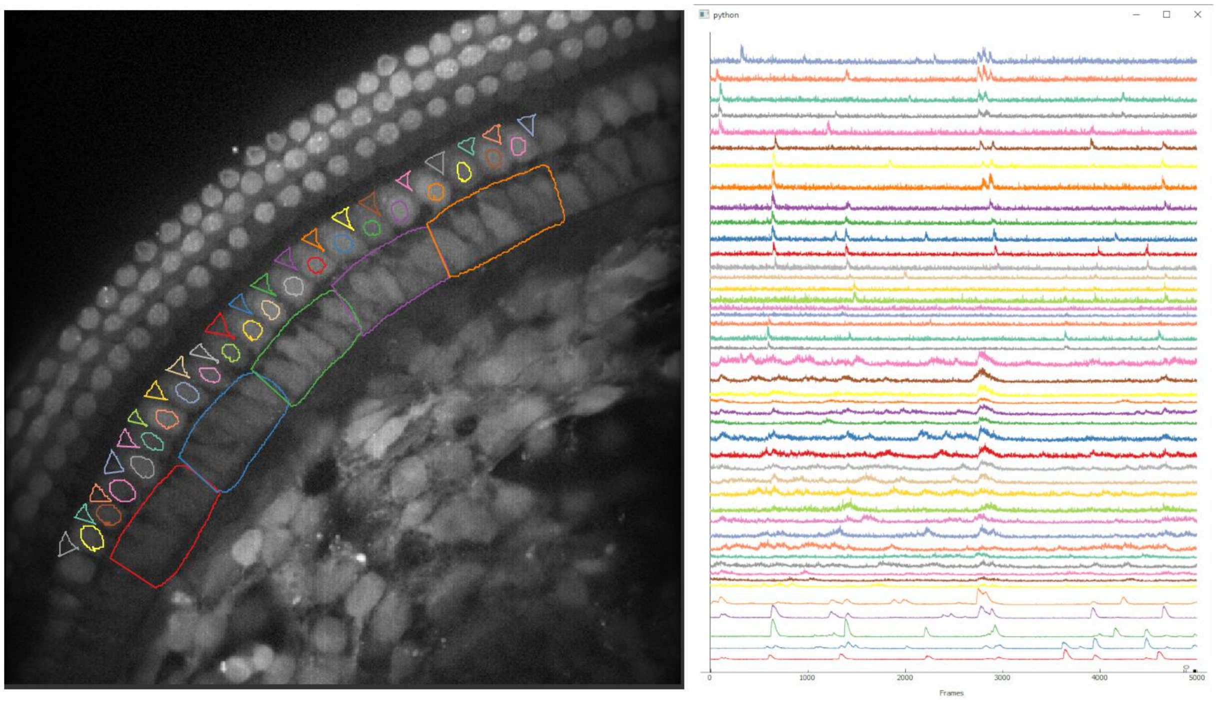

Figure 2.8 Example view of RoboPy analysis workflow.
In the left panel, the GER region (30-40 µm in width), IHCs, and inner phalangeal cells in the visual field were marked with individual ROIs in the sample view window of RoboPy. The right panel shows the preview window of the $\Delta F/F_0$ traces of each ROIs with corresponding colour.

The time frames of each spontaneous calcium wave were extracted from the $\Delta F/F_0$ trace of GER regions with a threshold set at 2.4 times of the SD, slightly higher than the multiplier used in the SAP spike sorting to decrease false trends in the correlation analysis. The synchronicity between IHCs were analysed by calculating the Person's correlation from their $\Delta F/F_0$ activities extracted from the time span of each spontaneous calcium wave (Figure 2.9 A & C). The overall correlation in the imaged sample was plotted in heat map for preview and quality check (Figure 2.9 B), but only the correlation from IHCs within 10-15 µm range (roughly two cells apart) was used in the distribution analysis (Figure 2.9 D).

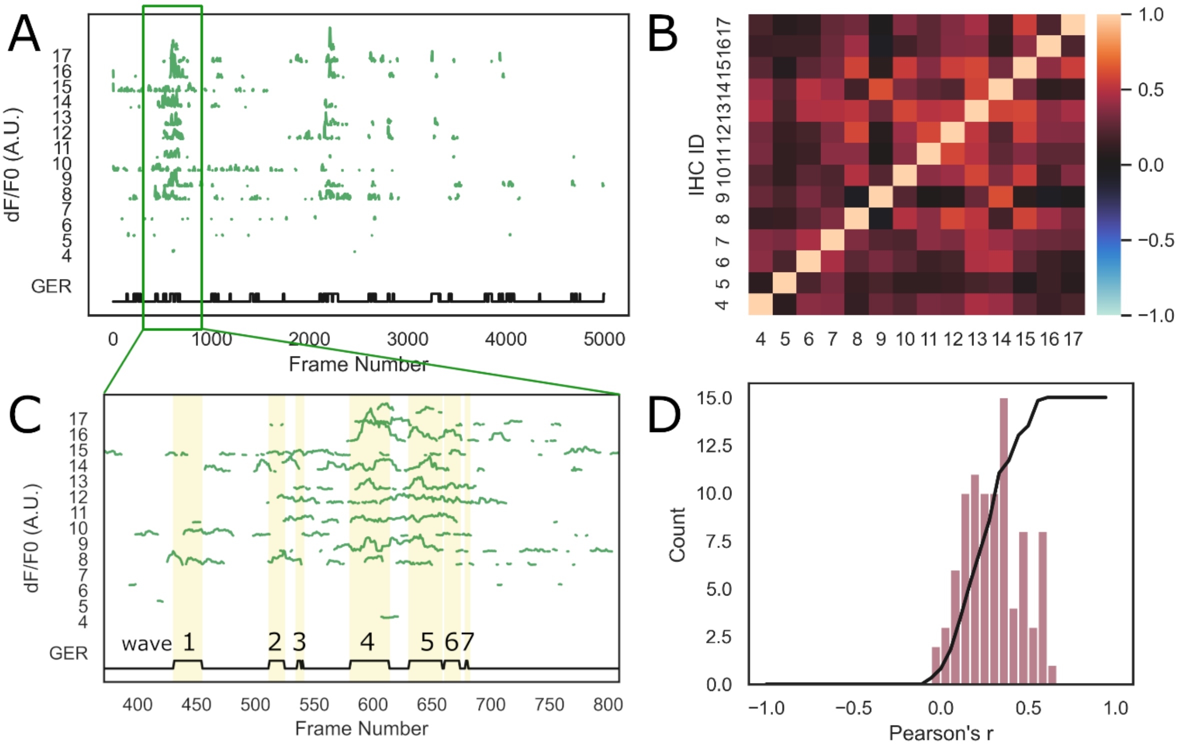

Figure 2.9 Analysis activity correlation in IHCs during spontaneous calcium waves.
A) Supra-threshold ΔF/F$_0$ activity in all of the IHCs (green traces) plotted against time frames. The black trace indicates whether there is spontaneous calcium waves (high) in the GER region or not (low) at a specific time frame. B) A heat map of the Pearson’s correlation index between each IHCs during the spontaneous calcium waves. Black colour indicates no correlation while the brighter red or blue indicates positive or negative correlations. C) A zoomed-in region in A) to explain the sampling range of the ΔF/F$_0$ in IHC for cross-correlation analysis. Yellow shaded areas indicate the time frames of individual spontaneous calcium wave in GER, labelled with a number.

Chapter 3 TMEM16A^{floxed}:Pax2-Cre model

3.1 Introduction

TMEM16A channel is a protein commonly expressed in epithelial cells, and is critical for fluid secretion in the intestinal and mucosal epithelium (Catalán *et al.*, 2015; Huang *et al.*, 2012; Lee *et al.*, 2019; Sheridan *et al.*, 2011). In the cochlea of rodents, TMEM16A is abundantly expressed in the non-sensory cells of the GER from about P2-P3 onward, and is rapidly down-regulated after hearing onset at P12 (Wang & Bergles, 2015; Yi *et al.*, 2013).

Knocking out TMEM16A channels was reported as a successful strategy to decouple IHCs from the fluid secretion of the GER during a calcium wave without affecting the activity of the non-sensory cells. (Wang & Bergles, 2015). Pax2-Cre and Sox2-Cre were used to create a tissue specific functional knockout of TMEM16A gene by driving the recombination of floxed site at the 12th exon (Schreiber *et al.*, 2015). Both Pax2 and Sox2 are early onset genes that regulates cell differentiation during embryonic stages (Burton *et al.*, 2004; Kempfle *et al.*, 2016). As a result, the promoter of both genes would express Cre-recombinase in almost every cell in the sensory epithelia from embryonic stage, and thus preventing any functional TMEM16A being expressed during the postnatal development.

For the work presented in this chapter, I used the TMEM16A^{floxed}:Pax2-Cre model to stop K^+ secretion from all of non-sensory cells in the GER while maintaining the ATP release during calcium waves. This design allowed me to study whether the maturation of IHCs is directly influenced by ATP alone, or it also required the release of K^+ from non-sensory cells.

3.2 Results

3.2.1 Cre-induction had unexpected variance

Previous study (Wang & Bergles, 2015) suggested that the TMEM16A*floxed*:Pax2-Cre model did not have 100 percent of successful rate on knocking out the crenation events in the GER, despite the promoter gene being globally expressed in the cochlear. Furthermore, certain amount of spontaneous current driven by the Cl^{-} efflux was still presented in non-sensory cells during the calcium wave. However, the efficacy of successful knockout was not characterized. This is a lesser issue for imaging studies but might severely bias the data collected from patch-clamp electrophysiology, which has a much lower throughput. To evaluate the potential bias, immunolabelling was used to characterise the efficiency of knockout of TMEM16A.

The percentage of inner phalangeal cells without TMEM16A signal (green) were used to calculate the KO rate in 100-130 µm region along the apical coil. The averaged KO rate was 84.5±23.6 % (n = 36, Figure 3.1 A). Around half of the cochleae samples from P5-P8 animals had 100% of KO rate at the apical region. However, the rest half had varied KO rate ranging from 30% to 90%, with strong TMEM16A labelling remained in some of the inner phalangeal cells (Figure 3.1 B). Samples with KO rate lower than 70% were not included in the analysis in later sections.

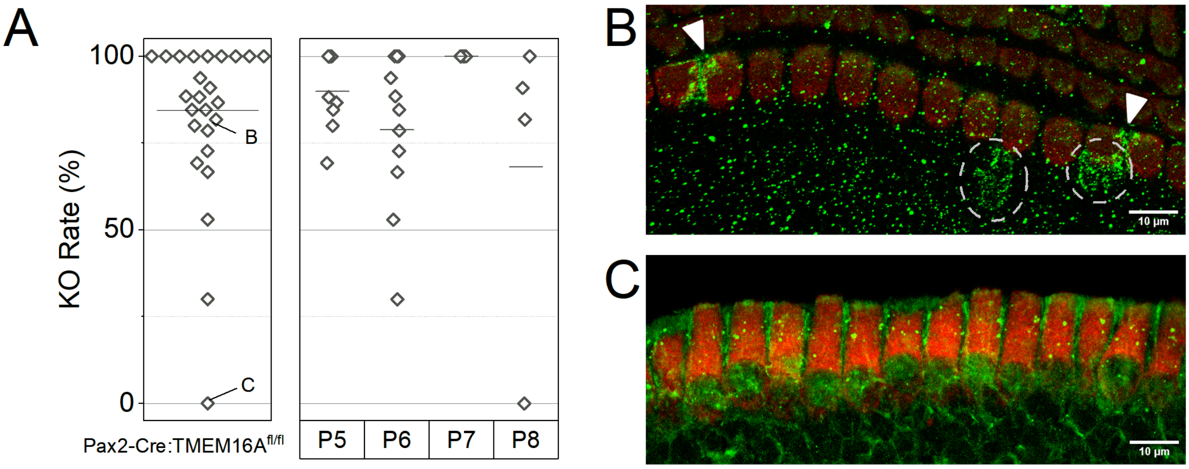

Figure 3.1 Cre-induced TMEM16A cKO in TMEM16A*floxed*:Pax2-Cre model

A) TMEM16A*floxed*:Pax2-Cre model had over 80% of induction rate in average (84.5±23.6 %, n = 36) but there was a great variance in half of the samples that did not have 100% KO rate. The source of the variance could not be identified and did not seem to be age-related. Examples of a good B) and a failed

C) induction were marked in A) and showed in the panels at the right. Solid line marks the population mean. The scale bar is 10 µm.

3.2.2 Spontaneous action potentials were partially affected by TMEM16A KO in non-sensory cells

Spontaneous action potentials (SAPs) in the IHCs of TMEM16A^{floxed}:Pax2-Cre mice were collected with cell-attached patch-clamp recording described in 2.4.6, and analysed with the workflow in 2.7.2 to extract relevant characteristics from the recordings.

The absence of TMEM16A greatly reduced the IHC's capability of generating SAPs. Around 1/3 of the IHCs from the P5-P6 cKO animals did not produce any action potentials. This trend was significantly different compared with control IHCs, all of which generated SAPs (p = 0.0056, Fisher's exact test; Figure 3.2 A). The ratio of non-spiking cells was consistent between P5 and P6 IHCs, and not significantly different between that reported in control and cKO mice (Appendix 1). An issue is, TMEM16Afloxed:Pax2-Cre might not produce KO phenotype in all of the non-sensory cells, which might allow the adjacent IHC to continue firing SAPs if remained TMEM16A-active. To verify whether this is the cause of those 60% spiking IHCs, the probability of recording from an IHC with TMEM16A KO in all adjacent non-sensory cells was estimated from the contralateral cochlea (assumed identical induction efficiency) by the percentage of inner phalangeal cells without TMEM16A immunolabeling signal in a 100-130 µm region along the apical coil (Figure 3.1 and 3.2.1). Plotted against their spiking status, the thoroughness of TMEM16A KO in the sample did not seem to correlate with the excitability of the IHCs. (p = 0.39, Mann-Whitney Test, Figure 3.2 B).

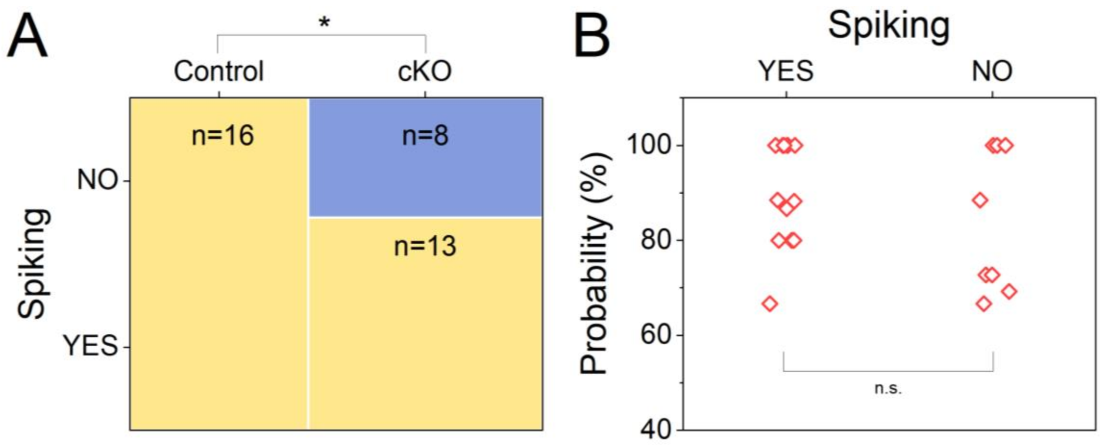

Figure 3.2 Non-spiking IHCs were observed only in cKO animals.
A) Mosaic plot showing the ratio of spiking (yellow) and non-spiking (blue) cells in the control (n=15, from 13 animals, left column) and cKO (n=21, from 15 animals, right column) animals. The cKO animals had significantly more non-spiking cells ($p < 0.05$, Fisher's Exact Test). B) For each recording, the probability of having TMEM16A KO in all adjacent non-sensory cells was plotted in grouped scatter according to their spiking status.

An example recording from a P6 IHC of a control animal is showed in Figure 3.3. All of the ISI_{i-1} from analysed SAPs are plotted against the recording time in Figure 3.3 A to show the spiking dynamics. The symbols are coloured with ISI_{i+1} to indicate the intensity of instantaneous firing rate. The clustered bursts (brighter yellow symbols) are observed throughout the recording, and are interlaced with difference length of silent periods (usually 0.5 – 1 minute). Two adjacent bursts (blue shaded) are selected to demonstrate the raw trace in Figure 3.3 C. The current signals in cell-attached configuration are charging currents from membrane capacitance and thus have an inverted polarity to the V_m of the patched cell (negative signal is depolarization and vice versa). Figure 3.3 B displays a more relaxed burst pattern with ~4 Hz of mean firing rate (grey area at ~122 s in Figure 3.3 C) compared with a more rapid firing burst pattern at ~6 Hz in Figure 3.3 D (grey area at ~150 s in Figure 3.3 C). The baseline of the rapid firing burst (Figure 3.3 D) exhibited a rapid hyperpolarization during the bursting. The source of the hyperpolarization is unknown, but this event was found in IHC from both the control and the cKO animals. Except for the burst showed in Figure 3.3 D, none of the other spiking regions in this sample have similar hyperpolarization.

An example recording of a P6 IHC from a cKO animal is showed in Figure 3.4. This cell was extremely silent except for the two major bursts (blue shaded area in Figure 3.4 A). The raw recording of this region shows that these bursts were both initiated by the hyperpolarization period (Figure 3.4 D). Statistical quantities indicated the mean ISI in the example cKO IHC (2.4±13.7 s) is very similar to the observation in the example control IHC (2.8±11.5 s), but the median ISI in the cKO IHC (0.10 s) was only half that of the control IHC (0.23 s).

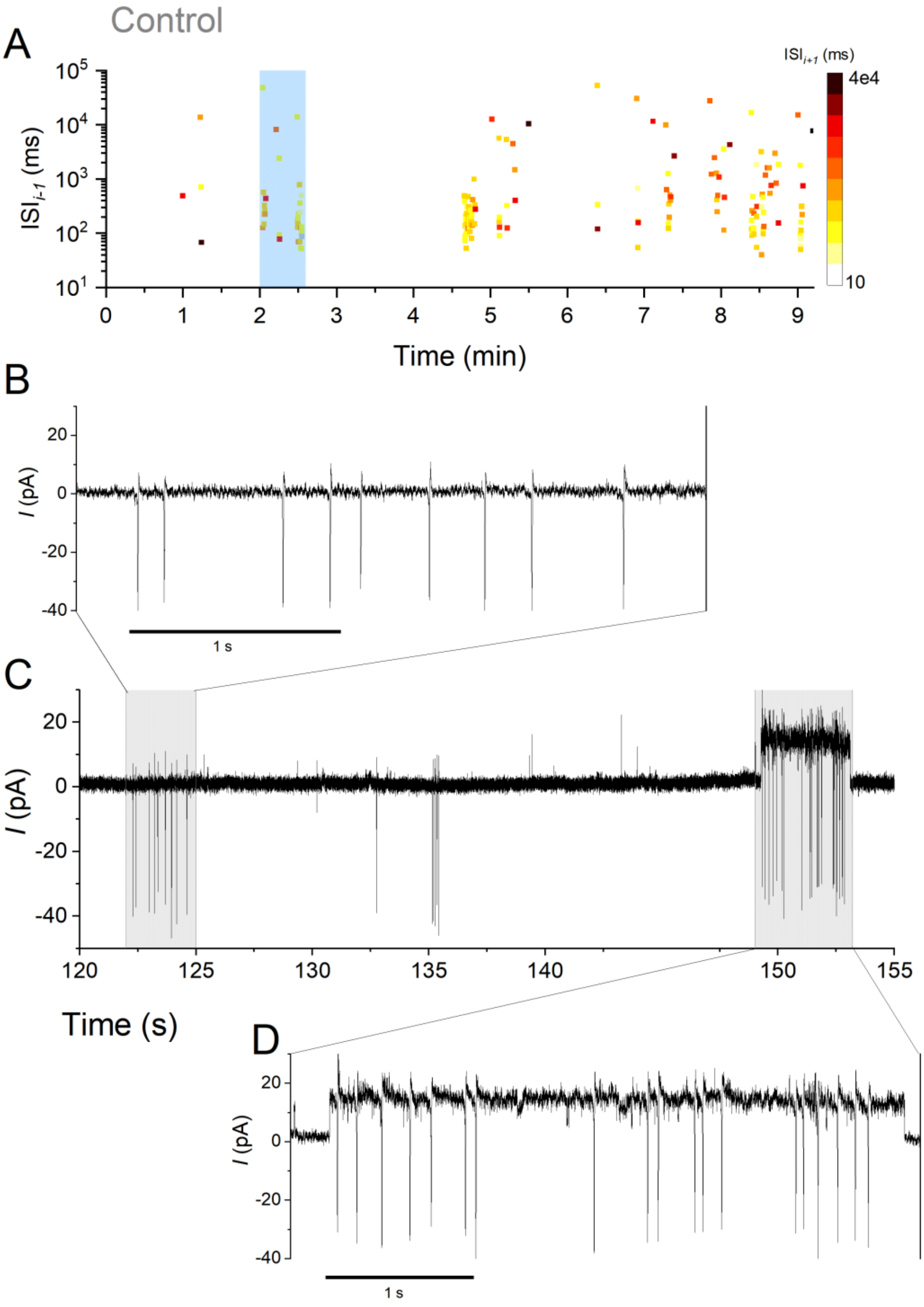

Figure 3.3 Example of SAP recording from a control IHC

Typical SAP characteristics extracted from the analysis workflow plotted in figures for analysis preview. A) ISI between the i^{th} and the $i\text{-}1^{th}$ spikes (ISI_{i-1}) plotted as a function of time, coloured from bright yellow to dark red indicates the ISI_{i+1}. The raw recording trace of the blue shaded area is shown in C), which contains two spike bursts in the areas highlighted in grey. B) The zoomed-in plot of the first burst (around 122 s) shows a mild burst with ~4 Hz of mean firing rate. D) The zoomed-in plot of the second burst (around 149 s) shows a more intense burst with ~6 Hz of mean firing rate and shorter ISIs.

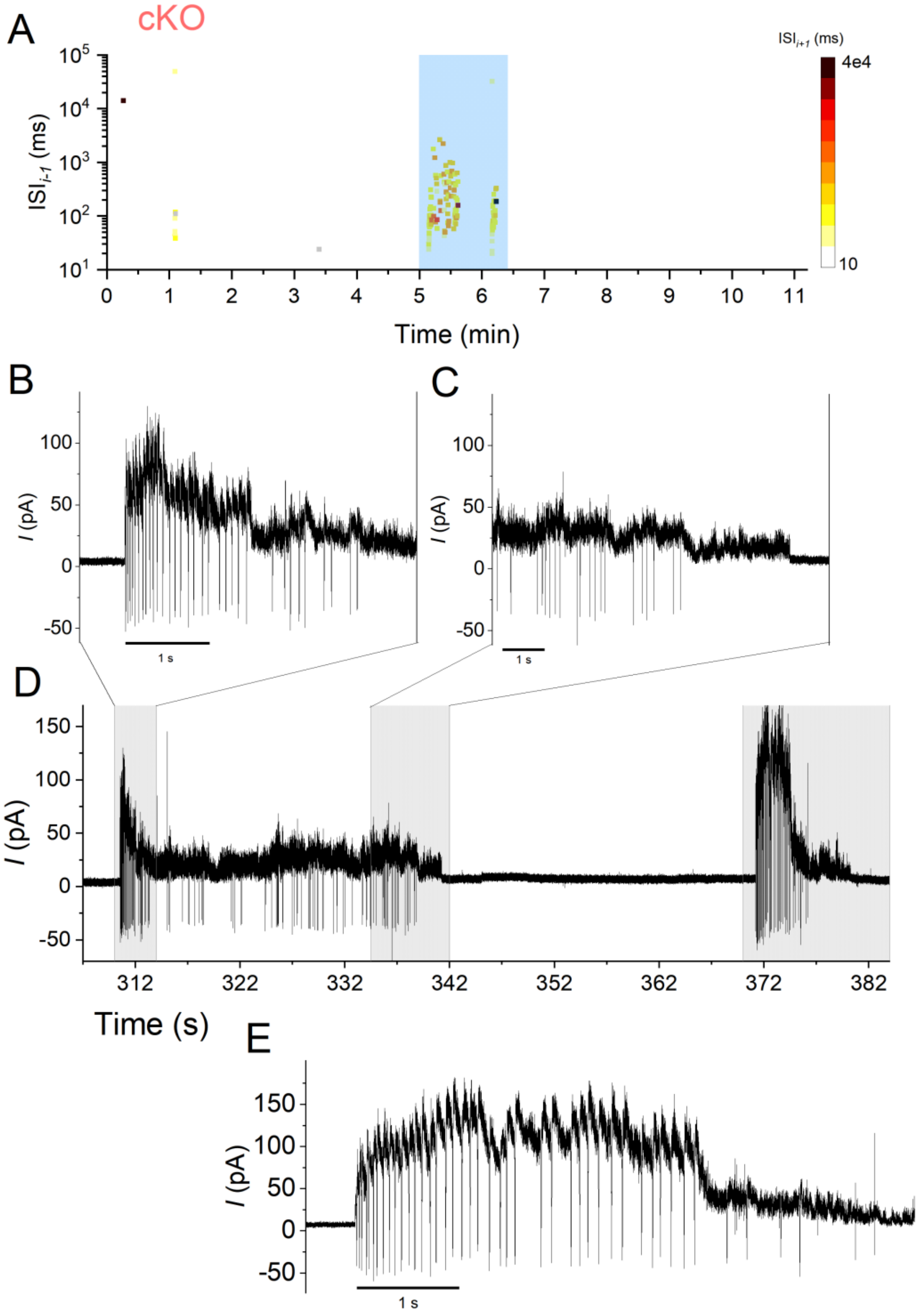

Figure 3.4 Example of SAP recording from a cKO IHC.
A) ISIs between the i^{th} and the $i\text{-}1^{th}$ spikes (ISI_{i-1}) plotted as a function of time, coloured from bright yellow to dark red indicates the ISI_{i+1}. The raw recording trace of the blue shaded area is shown in D), which contains two hyperpolarization-associated bursts in the areas highlighted in grey. B, C) The zoomed-in plot of the start and the end of the first burst (around 310 s). D) The zoomed-in plot of the second burst (around 370 s).

All of the analysed recordings were then plotted together in the formats of ISI or occurrence graph to generate an overall perspective of the burst firing pattern. The analysis of the ISI pairs from spike triplets (inset of Figure 3.5) did not reveal any pronounced difference between the control and cKO mice, both of which had similar distribution in sparse and burst firing region (Figure 3.5).

The occurrences of all sampled ISI were also very similar between the control and the cKO, with less spiking events observed in the IHCs from cKO animals in most of the ISIs (Figure 3.6 A). The distributions look almost identical after normalizing to the peak in each phenotype (Figure 3.6 B). Both phenotypes had the interval of the peak occurrence at 140-180 ms (Figure 3.6 B), which is consistent in most of the recordings.

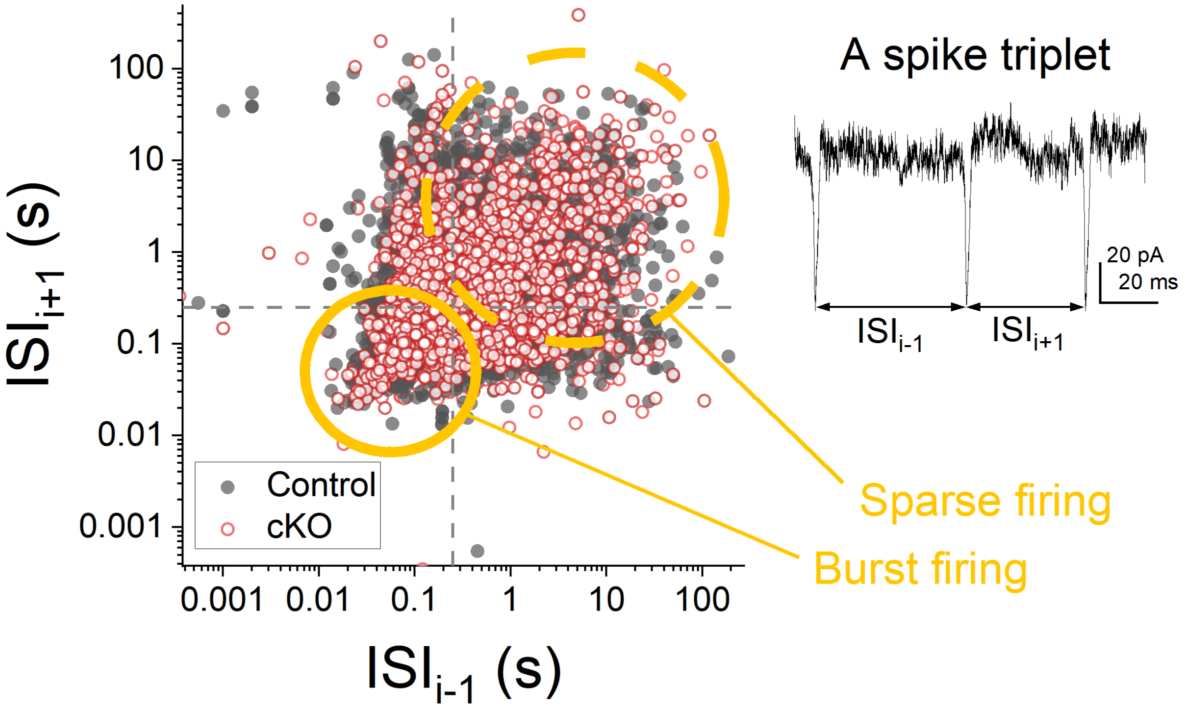

Figure 3.5 ISI graph did not show difference between phenotypes
The inset plot shows the definition of a spike triplet in graphic. The scatter plot is the ISI graph with all of the spike triplets plotted together. The IHCs from control animals (n=15, from 10 animals) are in solid grey symbol and the IHCs from cKO animals (n=13, from 8 animals) are in red open symbol. The dashed line marks the ISI with instantaneous firing rate of 4 Hz. The two circles highlight the area of burst (solid) and sparse (dashed) firing spike triplets.

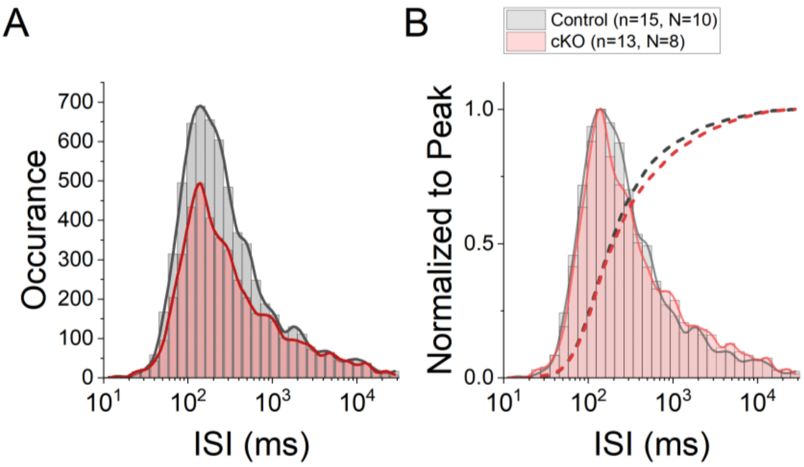

Figure 3.6 Distribution of ISIs did not differ between the control and the cKO animals. A) The occurrence of ISI_{i-1} from all of the data plotted in logarithmic histogram. The data from control animals is in grey and those from cKO animal is in red. B) the distribution normalized to the peak occurrence in individual phenotype. Dashed lines show the cumulative distribution. Colour scheme is the same as in A). For biological repeats in the legend, n indicates the number of cells and N indicates the number of animals.

All of the statistical quantities were not significantly different between the IHCs from the control and the cKO animals (Figure 3.7). Detailed statistical results are compiled in (Appendix 2). Despite the lack of statistical significance, I will still report some noteworthy trends here. The average of mean ISI was slightly longer in IHCs from control animals (1.8±1.3 s, n=15, from 10 animals) and had more variance compared to that measured in the IHCs from cKO animals (1.5±0.6 s, n=13, from 8 animals), but the median (~1.3 s) is almost identical between phenotypes (Figure 3.7 A). The median ISI, reciprocal to the burst firing, were almost identical on the average values and the median between the IHCs from control (0.2±0.1 s, n=15, from 10 animals) and the cKO (0.25±0.1 s, n=13, from 8 animals) animals (Figure 3.7 B). The shortest ISI observed also had identical distribution, from 30 ms to 50 ms, with similar mean (~ 30 ms) in both phenotypes (Figure 3.7 C). Most of the longest ISI stably located around 50 seconds in both phenotypes, but the SAPs measured from the IHCs from cKO animals seemed to have longer silent periods (*average*: 92±100 s, n=13, from 8 animals) compared with those from IHCs in control animals (*average*: 65±49 s, n=15, from 10 animals; Figure 3.7 D).

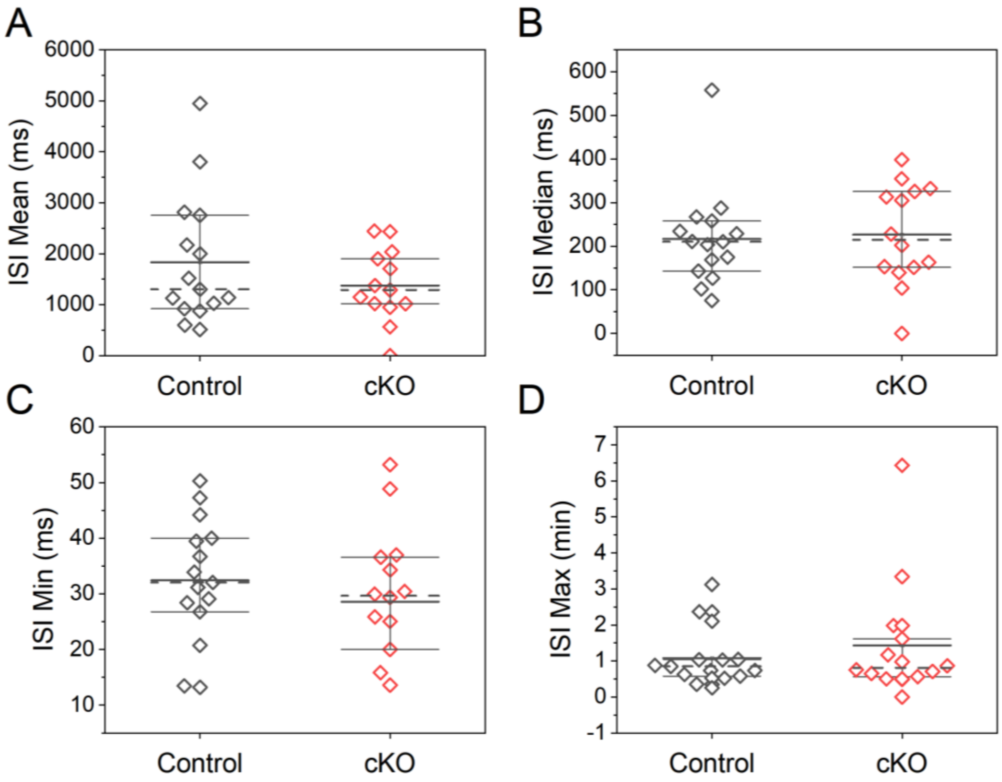

Figure 3.7 Statistical quantities on the ISI in individual IHCs did not report difference. The statistics on A) mean, B) median, C) minimum, and D) maximum ISI from individual IHC did not have any statistical difference. The data from control animals is coloured in grey and from cKO animals in red. The solid line in each plot indicates the population mean while the dashed line is the median. Since all of the data were not normally distributed, I-box marks the 1st and the 3rd quartile (25%-75%). None of the properties reported statistical differences. Detailed quantities and p-values are compiled in (Appendix 2).

The ISIs were further analysed for the lasting time of each burst (defined in 2.7.2) to investigate whether the KO of TMEM16A affected the IHC's capability to generate longer bursts. The collective burst firing from the cKO animals (*median*: 880.95 ms, n=15, from 10 animals) reported no statistical difference compared with the control animals (*median*: 854.85 ms, n=13, from 8 animals, p = 0.72, Mann-Whitney; Figure 3.8 A). The statistical quantities from individual recordings did not produce any significantly different either (Figure 3.8 B-F). The results of the test and the details of the quantities were compiled in Appendix 3.

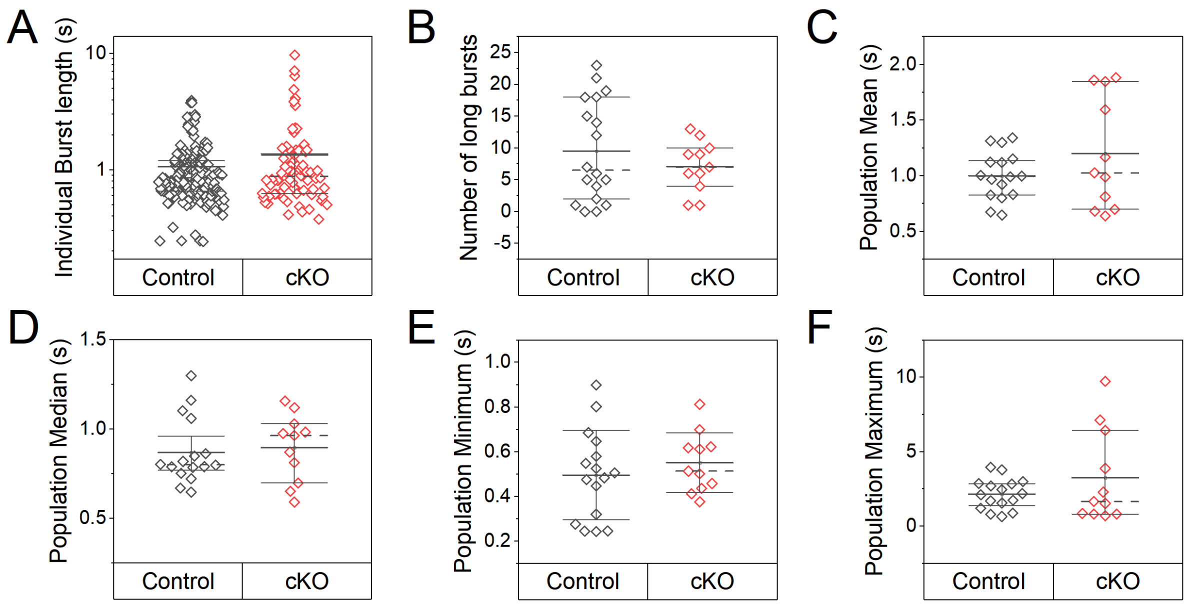

Figure 3.8 Similar burst lengths in both the control and the cKO animals

A) The calculated length of each burst was plotted together according to their phenotypes. The B) total number, C) mean, D) median, E) minimum, and F) maximum burst length from individual IHC did not differ between the control and the cKO animals. The data from control animals is coloured in grey and from cKO in red for all subplots. The solid line in each plot indicates the population mean while the dashed line is the median. The I-box marks the 1st and the 3rd quartile (25%-75%), except for the one in D) is SD since it is the only normally distributed data.

3.2.3 Synchronization of activity between nearby IHCs was reduced

The calcium activity in the apical organ of Corti from a P8 control mouse is showed in Figure 3.9 plotted as normalized dF/F0 against the recording time. Both the IHCs and GER non-sensory cells had robust activity throughout the recording (IHC: green, GER: black, Figure 3.9 A). An instance of synchronized activities between the GER and nearby IHCs (blue vertical line in Figure 3.9 A) is reconstructed in Figure 3.9 B. The fluorescence intensity in the two most left GER region was reaching maximum dF/F0 during a spontaneous calcium wave (Figure 3.9 A, B). Their activity synchronized calcium signals from firing SAPs in all of the nearby IHCs (#15 to #24) but not the further region (#5 to #11). The cross-correlation of the calcium activity between the IHCs during each calcium wave was calculated with the workflow described in 2.7.3, and were then averaged to produce a correlation matrix of the recorded sample (Figure 3.9 C). The matrix displays a strong correlation between nearby IHCs (along the orange diagonal line in Figure 3.9 C).

In comparison, the IHCs from a P6 cKO mice did not respond to the peak of a calcium wave in nearby GER (Figure 3.10 B). None of the region in the correlation matrix produced strong correlation, despite both the IHCs and the GER having robust activity comparable to the control animal (Figure 3.10 A).

The collection of Pearson’s *r* calculated during individual calcium wave revealed a strong decrease on the synchroneity between the nearby 3 IHCs in the cKO animals (*median*: 0.100, n=2778 from 15 animals) compared with the control animals (median: 0.197, n=846 from 5 animals; Figure 3.11 A). Separating the data with individual cell pairs indicated that this decrease on synchronization affected all 3 nearby cells (Figure 3.11 B). Further analysis showed the influenced region by TMEM16A cKO can be as far as 8 IHCs apart, and possibly wider (~60 µm, Figure 3.11 C). The significance was also prominent at population level as the median of each sample (p = 0.018, Mann-Whitney; Figure 3.12), with the median Pearson’s *r* in the cKO animals (0.096, n = 14 animals) being at a much lower value than in the control animals (0.189, n = 5 animals).

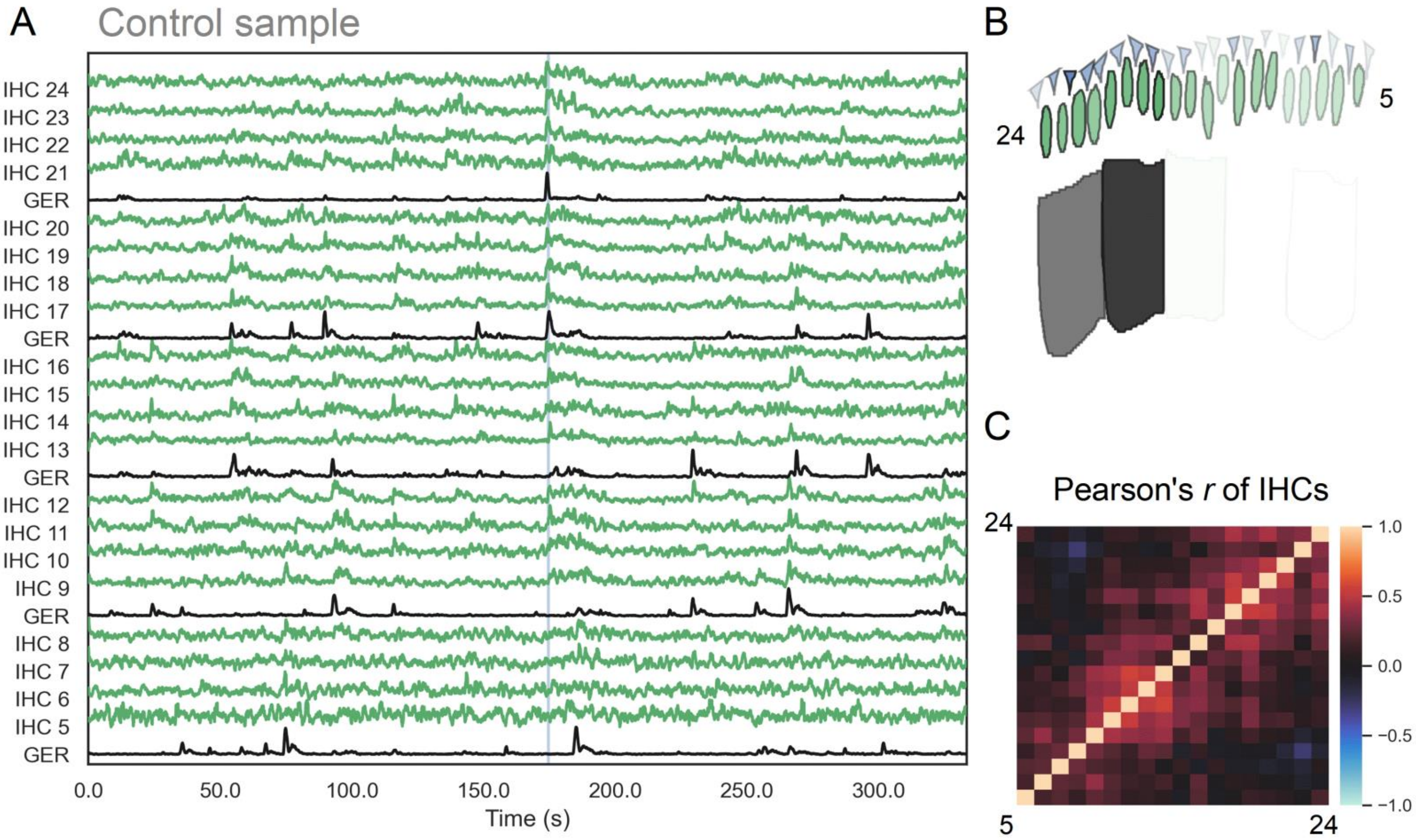

Figure 3.9 Example of the calcium activities from a control sample.
A) The dF/F0 traces are plotted in line graph to show a preview of the calcium activities in IHCs (green) and the nearby GER region (black). Each trace was individually normalized for easier viewing. B) Spatial representation of the activity at the blue vertical line in A). The opacity of each ROI indicates their normalized calcium level, 100% is opaque and 0% is transparent. C) A preview heat map of Pearson’s correlation between the calcium activities in each IHCs. Bright red indicates positive correlation and bright blue indicates negative.

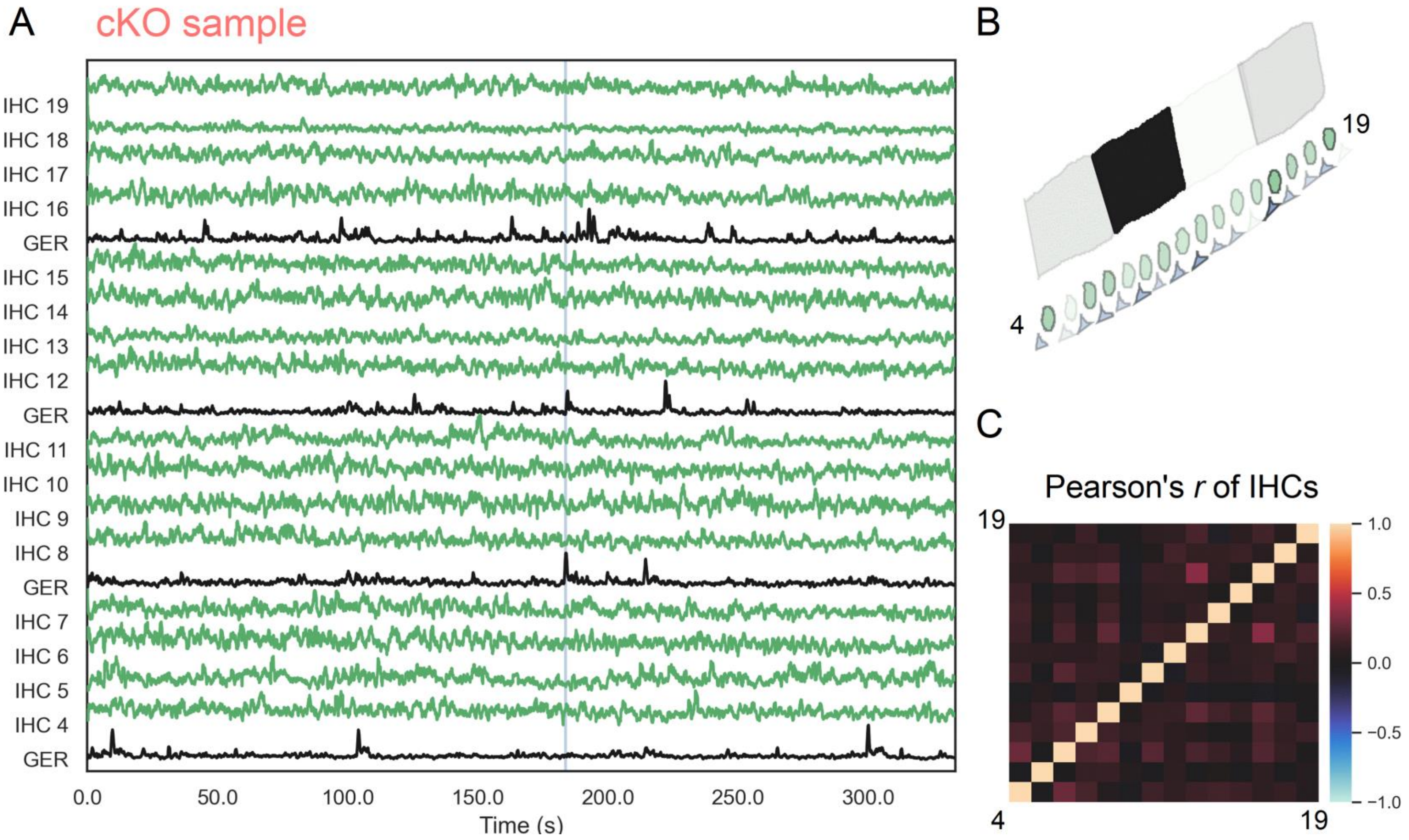

Figure 3.10 Example of the calcium activities from a cKO sample.

A) The dF/F0 traces are plotted in line graph to show a preview of the calcium activities in IHCs (green) and the nearby GER region (black). Each trace was individually normalized for easier viewing. B) Spatial representation of the activity at the blue vertical line in A). The opacity of each ROI indicates their normalized calcium level, 100% is opaque and 0% is transparent. C) A preview heat map of Pearson's correlation between the calcium activities in each IHCs.

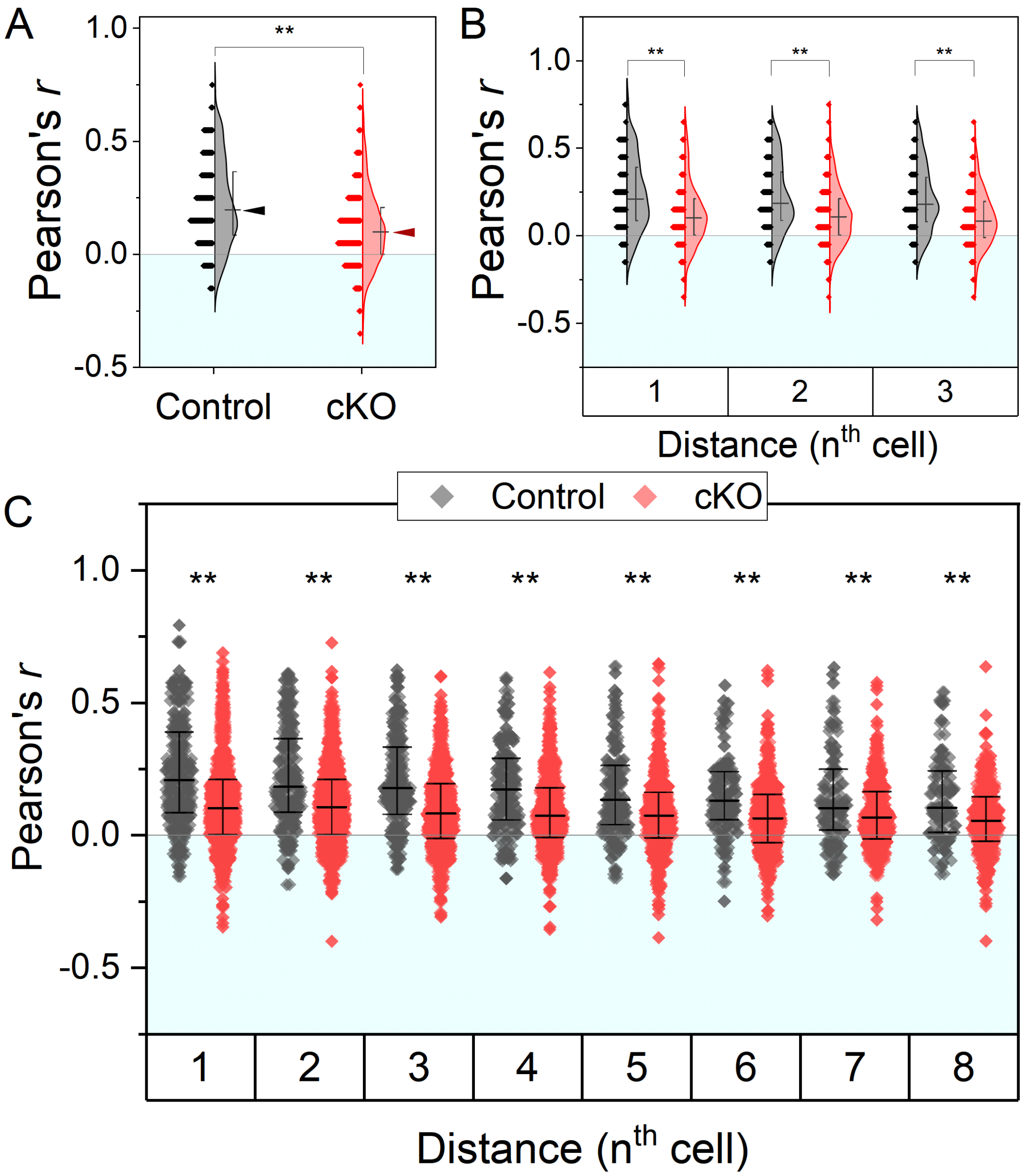

Figure 3.11 Activities in nearby IHC were less correlated in the cKO animals.
A) The distribution of correlation index between each IHC and three neighbouring IHC was significantly reduced in the cKO animals (**p < 0.005, Mann-Whitney) compared with the control. Grey (control) and red (cKO) arrowheads highlights the median of corresponding phenotype for an easier visual comparison. For all three panels, the I-box marks the 25% and the 75% percentiles and a short line marks the median. Horizontal line marks zero correlation, and the area below (negative correlation) was filled with light blue. B) Distribution breakdown of the correlation index with each nearby cells all showed significant difference. C) The influenced area in the cKO animals reached as far as the 8th cells away from the target IHC. Detailed statistical quantities are compiled in Appendix 4.

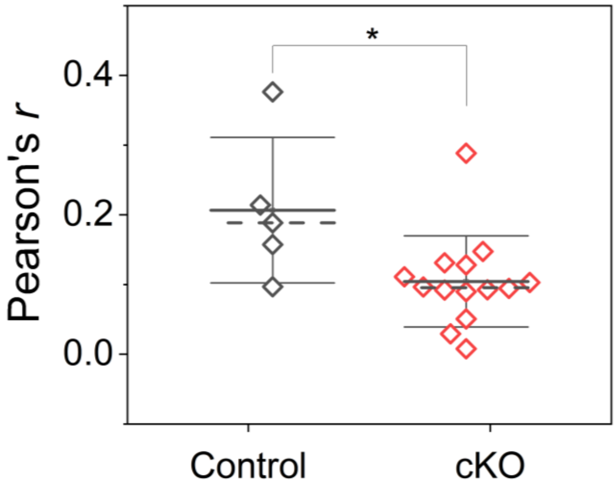

Figure 3.12 cKO animals had lower correlation coefficient between activities in IHCs. Population median of the Pearson's correlation from 3 nearby IHCs during calcium waves. The data from control animals is in grey and from cKO animals in red. The I-bar marks the mean and SD, while the dashed line marks the median. Detailed statistical quantities are compiled in Appendix 4.

3.2.4 Immature electrophysiological properties of IHC remained identical

Electrophysiological characteristics of IHC under current- and voltage-clamp configurations are shown in Figure 3.13. P5-P6 IHCs from both control and cKO animals displayed induced spiking activities with increasing firing frequency as the injecting current became larger (Figure 3.13 A, B). Although the size may vary between each recording, current responses in both phenotypes displayed the signature slow-activating outward K^+ currents upon stepping the voltage towards depolarised values (Figure 3.13 C, D). The recorded traces were analysed with the procedure introduced in 2.4.7. Detailed figures and statistical results for immature electrophysiology are compiled in Appendix 5.

Data collected from P5-P6 mice showed that the knockout of TMEM16A in the TMEM16A^{floxed}:Pax2-Cre model did not change the excitability of IHCs (Figure 3.14). The resting V_m (Figure 3.14 A) remained at similar range between the IHCs from control animals (−86.7±5.4 mV, n = 6) and the IHCs from cKO animals (−87.4±4.9 mV; n=9, $p = 0.9$, Student's t-test). Characteristics of induced spikes, namely the threshold and half-width, also remained unchanged (Figure 3.14 B, C).

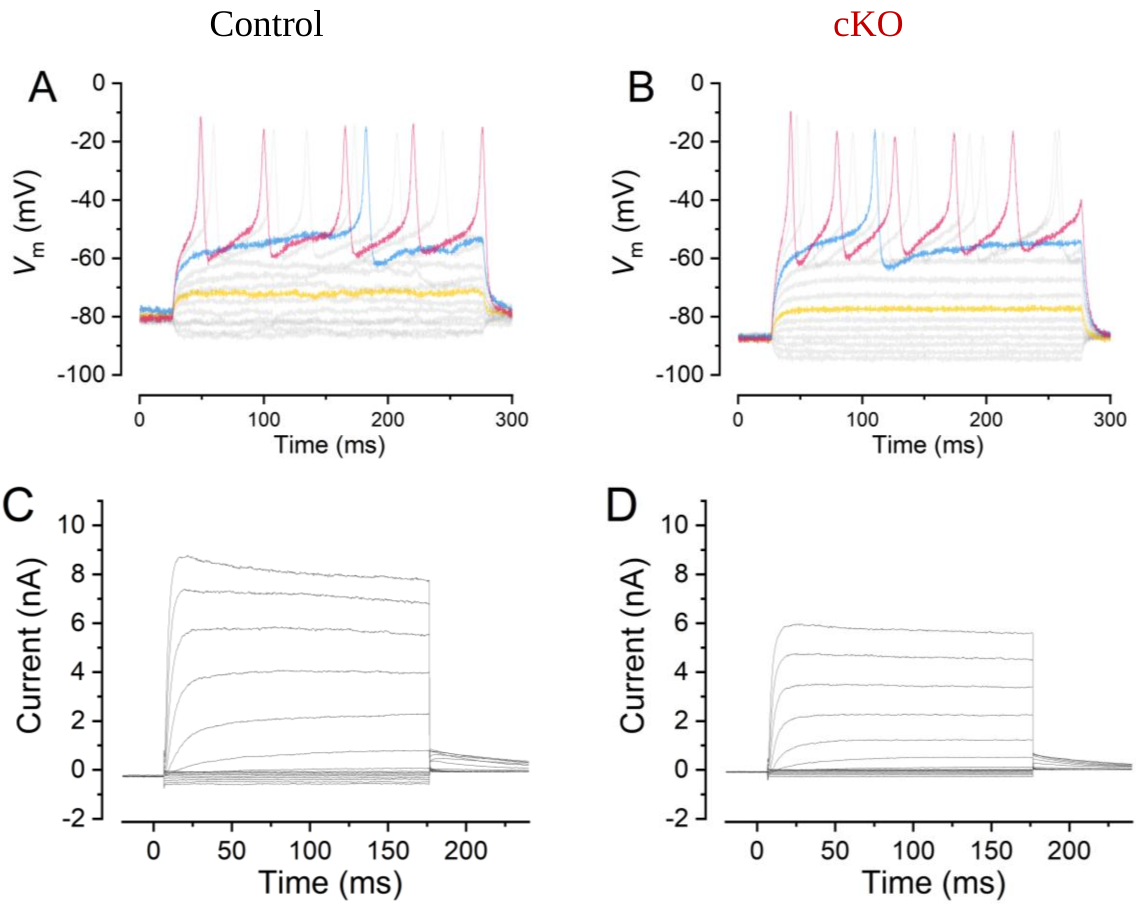

Figure 3.13 Example traces of electrophysiological responses in immature IHC.
Examples of electrophysiological characteristics from P6 IHCs in A, C) the IHC from a control animal and B, D) from a cKO animal. A) and B) are voltage responses upon different injected currents (grey). Coloured traces highlight the current steps at +30 pA (yellow), spiking threshold (blue) and +100 pA (magenta). C) and D) are current responses different voltage steps. The stimulation protocols were the same as introduced in 2.4.7 (Figure 2.3 and Figure 2.4).

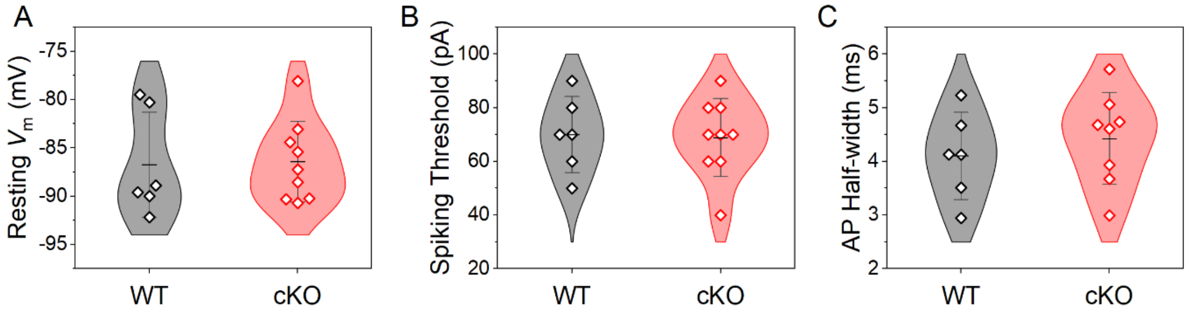

Figure 3.14 No significant changes on excitability of immature IHC.
The A) Membrane potential, B) spiking threshold, and C) half-width of the induced action potential were not different between IHCs from the control (grey) and cKO (red) littermates. Biological repeats: n = 6 from 6 mice for control and n = 9 from 9 cKO mice in all quantities except AP half-width, which has n = 8 from 8 cKO mice. Since all of the data were normally distributed, the I-box marks the SD of population.

The averaged current traces from all of the recordings (Figure 3.15 A) shows a high degree of consistency on the I-V responses between the IHCs from control and cKO animals. The I_{init} was nearly identical between the two phenotypes, while the I_{steady} had more variance when IHCs were held at more depolarized voltages (Figure 3.15 A). Statistics showed no significant difference on the mean of the I_{init} (−201.2±50.5 pA at −25 mV, n = 7; Figure 3.15 C) or I_{steady} (5.25±1.8 nA at 0 mV, n = 7; Figure 3.15 B) in IHCs from the cKO animals, compared with the measured current sizes in IHCs from control animals (I_{init}, −207.0±92.7 pA at –25 mv; I_{steady}, 5.4±0.4 nA; n = 9 for both currents). The distribution of the column scatter plots (Figure 3.15 B, C) revealed a much larger variance in I_{steady} in the IHC from cKO animals, but this trend does not exist in I_{init}. The detailed statistical results are compiled in Appendix 6.

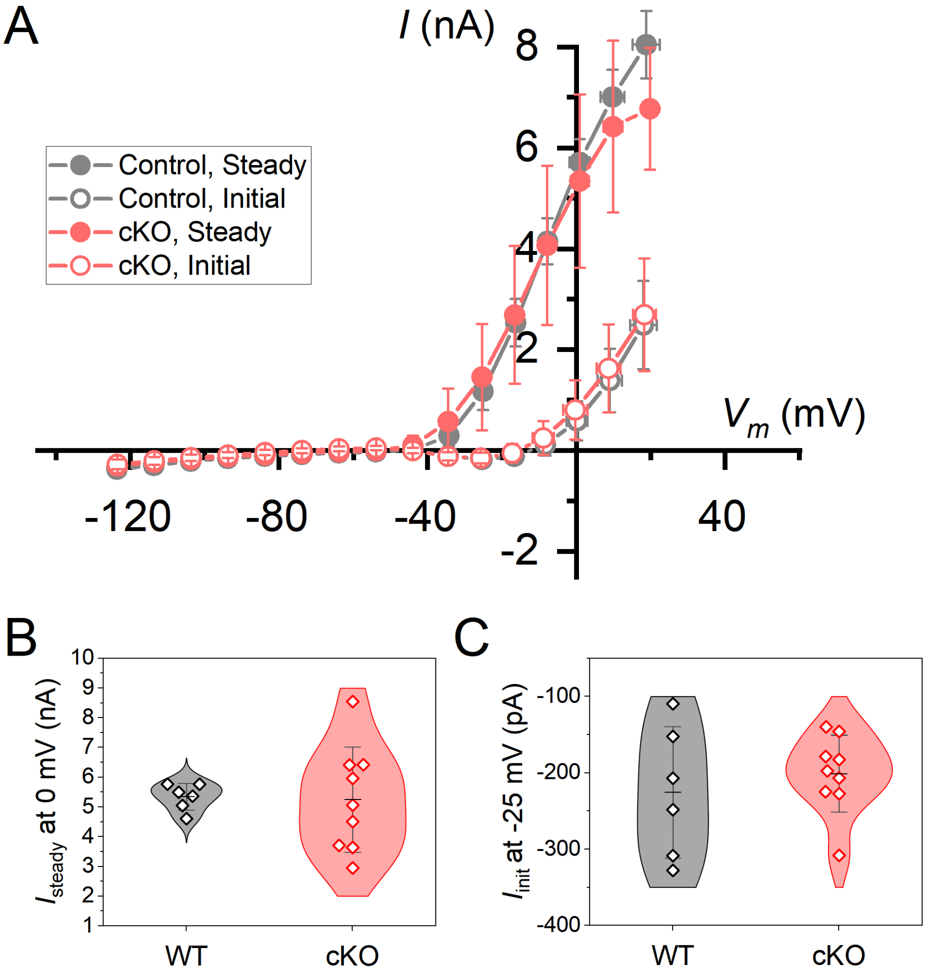

Figure 3.15 No significant changes on current responses of immature IHC.
A) The averaged initial (open symbol) and steady (filled symbol) I-V responses in the control (grey, 7 cells from 7 mice) and cKO (red, 9 cells from 9 mice) animals, with the error bars marking the SD. Neither B) the steady current nor C) the initial current had statistical difference between the control and cKO animals. Since all of the data were normally distributed, the I-box marks the mean and the SD of population.

3.2.5 Post-hearing electrophysiological properties of IHC reported abnormities

To investigate the influence of TMEM16A cKO on the development, post-hearing IHCs from P17 to P24 were tested with the same current- and voltage-clamp protocols as used in the immature stage. The IHC from control animals presented a typical fast-acting waveform upon current injection (Figure 3.16 A). Most of the IHCs in the cKO animals reported similar phenotype (Figure 3.16 B), but a few of them displayed much slower current dynamics (Figure 3.16 C) which resembles the dynamics in immature IHC membrane (Figure 3.13).

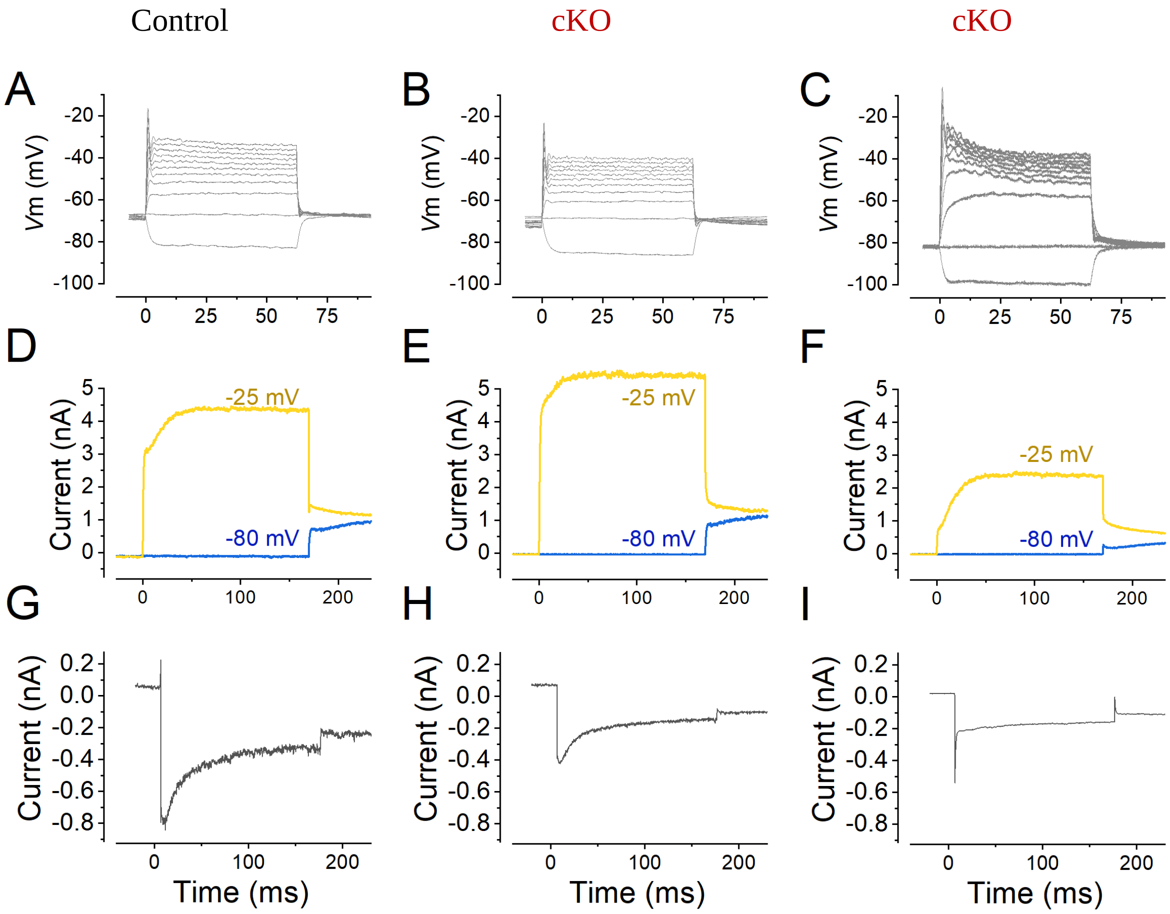

Figure 3.16 Immature phenotype detected in post-hearing IHCs
A-C) Voltage responses upon current stimulation from the IHCs from a control (left column) and cKO (centre and right column) animals. The cKO sample at the right panel presented atypical waveforms. D-E) Current responses with the basic voltage clamp protocol (described in 2.4.7). Only two voltage steps, -25 mV (yellow) and -80 mV (blue) were showed for a clearer comparison. The cKO sample at the right panel had a dramatically reduced $I_{K,f}$. G-I) $I_{K,n}$ was measured with a specialized voltage

clamp protocol (described in 2.4.7). The cKO sample at the right panel had very little inactivating current.

The rapid outward current $I_{\mathrm{K,f}}$ was observed in response of depolarization in IHCs from both phenotypes (Figure 3.16 D, E; yellow traces). However, in the IHC with abnormal I-V responses, the size of $I_{\mathrm{K,f}}$ was very small and the I_{steady} was nearly halved (Figure 3.16 F). Similar anomaly was found in $I_{\mathrm{K,n}}$, where the IHCs from the cKO animals presented either a smaller (Figure 3.16 H) or non-existing (Figure 3.16 I) current compared with the large size current in the control example (Figure 3.16 G).

The averaged I-V responses of I_{steady} at different voltage steps were very similar between the control and cKO animals (Figure 3.17 A). The averaged I_{init} was also similar between the control and cKO animals, but a much larger variance was observed in the IHCs from cKO animals (Figure 3.17 B). Further analysis revealed an age-dependent difference that only existed in the I_{init} of the cKO animals (Figure 3.17 C, D). The size of the averaged I_{init} towards positive voltages was much smaller in the cKO animals at P17-P19 compared with those measured in IHCs from the control animals, and those from the cKO animals at P23-P24 (Figure 3.17 D). Considering that the three IHCs without $I_{\mathrm{K,f}}$ (Figure 3.16 F) might bias the mean value due to their much smaller size (< 30% of population mean), the recordings of these cells were filtered out from the averaged I-V responses plotted in (Figure 3.17 E, F), but the trace of mean I_{init} in IHCs from cKO animals under P20 is still separated from the averaged I_{init} in control animals at the same age or in older cKO animals.

Statistical results (Figure 3.18 A) showed that the average size of I_{steady} was slightly smaller in the IHCs from cKO animals (12.7±2.9 nA, n = 13 from 8 animals) compared with the control animals (14.4±2.7 nA, n = 5 from 4 animals), but the trend was not statistically significant ($p = 0.0503$, Student's t-test). Similar trend (Figure 3.18 B) was observed on the I_{init}, where the cKO animals had a smaller averaged value with an almost doubled standard deviation (2.3±1.4 nA, n = 17 from 9 animals) compared with the control animals (2.9±0.8 nA, n = 6 from 5 animals). The range of $I_{\mathrm{K,n}}$ (Figure 3.18 C) was very similar between the cKO (−340.4±112.3 pA, n = 17 from 9 animals) and the control animals (−335.2±165.2 pA, n = 4 from 4 animals; $p = 0.955$, Student's t-test).

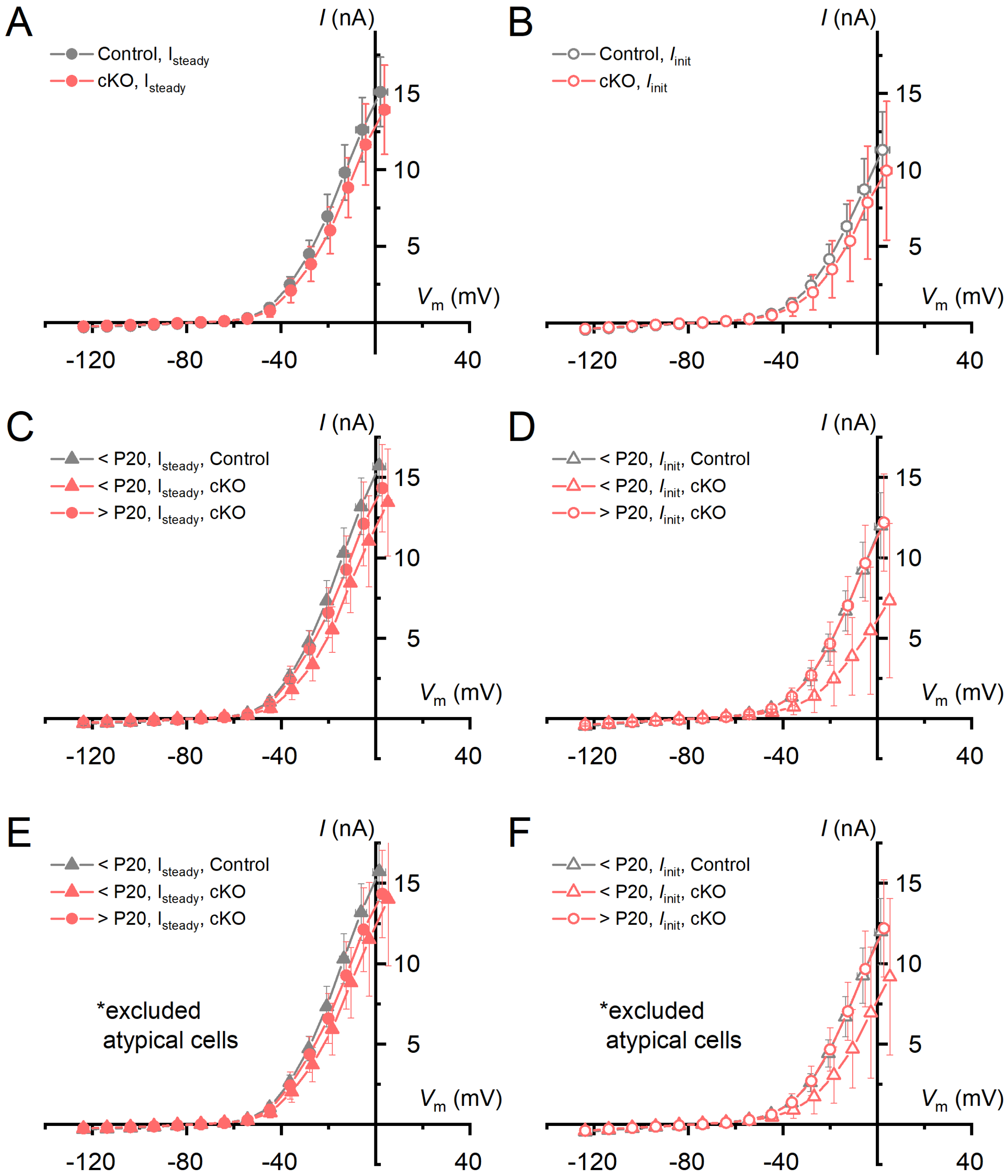

Figure 3.17 I_{init} in cKO animals had a larger, age-dependent variance

A) Averaged I-V responses of the whole cell steady state current from -124 mV to +10 mV. The IHCs from control (solid grey circle) and the cKO (solid red circle) animals had very similar results. B) I-V responses of the initial current (region of $I_{K,f}$) from -124 mV to +10 mV. There was no significant difference between the IHCs from control (open grey circle) and the cKO (open red circle) animals, but the I_{init} in the IHCs from cKO animals had a much larger variance towards positive voltages. C) I-V responses showed little difference among ages. The IHCs from cKO animals was labelled with red triangles (< P20) or red circles (> P20), and the IHCs from control animals under P20 was labelled with solid grey triangles. Only one recording older than P20 was from a control animal, so it was not showed here for better display. D) The IHCs from cKO animals under P20 (open red triangle) had a much smaller I_{init} compared to the IHCs from control animals at the same age (grey open triangle) or from the cKO animals older than P20 (red open circle). Both E) I_{steady} and F) I_{init} remained in similar trend when excluding the cells from the cKO animals with atypical electrophysiological responses as showed in Figure 3.16. For age analysis, IHCs < P20 were from P17 and P19 animals, and IHCs > P20 were from P23 and P24 animals.

Further analysis revealed an age-dependent difference in the cKO animals on the $I_{K,f}$ (Figure 3.18 E) but not the other two mature-type currents (Figure 3.18 D, F). At the age of P17-P19, the IHCs from the cKO animals had much smaller $I_{K,f}$ (1.5±1.2 nA, n = 9 from 4 animals) than the IHCs from the control animals at the same age (3.1±0.6 nA, n = 5 from 4 animals; $p = 0.016$, two-way ANOVA with Fisher's least significant difference procedure), and the IHCs from older cKO animals (3.2±1.1 nA, n = 8 from 5 animals; $p = 0.006$, two-way ANOVA with Fisher LSD). The I_{steady} seemed to have similar trend. The averaged I_{steady} at 0 mV was smaller at ages under P20 in the IHCs from the cKO animals (11.8±2.9 nA, n = 9 from 4 animals at P17 and P19), compared to the control animals at the same age (15.2±2.0 nA, n = 5 from 4 animals; $p = 0.07$, two-way ANOVA with Fisher's LSD test) and the older cKO animals (13.5±2.9 nA, n = 8 from 5 animals; $p = 0.31$, two-way ANOVA with Fisher's LSD test). However, this trend did not produce statistical significance.

The resting V_m was similar between the control (−73.7±5.6 mV, n = 6 from 5 animals) and the cKO animals (−78.8±5.0 mV, n = 17 from 9 animals). Interestingly, IHCs from the cKO animals under P20 presented a skewed cluster at more hyperpolarized voltage (*median*: −81.9 mV, n = 9 from 4 animals) and was statistically different from the median resting V_m in control IHCs at the same age (median: −75.3 mV, n = 5 from 4 animals; $p = 0.045$, Mann-Whitney). The IHCs from cKO animals older than P20 had normally distributed resting V_m at similar range (−77.7±5.7 mV, n = 8 from 5 animals) as the IHCs from control animals under P20 (−74.0±6.2 mV, n = 5 from 4 animals; $p = 0.3$, Student's t-test).

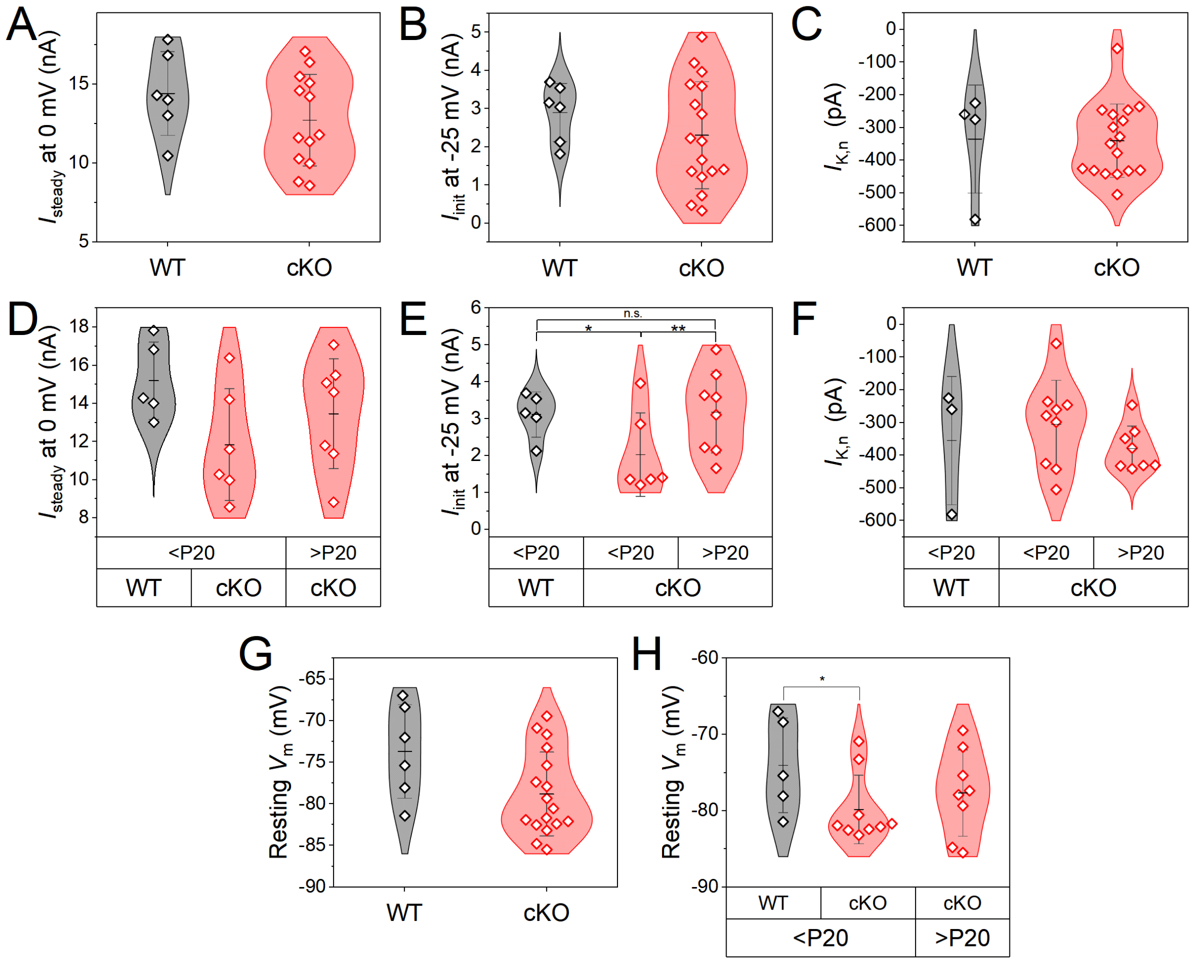

Figure 3.18 Statistics of electrophysiological properties in post-hearing IHCs
The distribution of A) I_{steady}, B) I_{init} and C) $I_{K,n}$ did not show any statistical difference between the IHCs from control (grey) and cKO (red) animals. D-F) Subgrouping the data with age revealed significantly smaller I_{init} in the cKO animals under P20 compared with other ages and the control animal (* $p < 0.05$, ** $p < 0.005$, n.s. no significance, two-way ANOVA with Fisher LSD). This trend was not observed in neither the I_{steady} or the $I_{K,n}$. G-H) The resting V_m did not differ between the genotypes or the ages. The IHCs from cKO animals under P20 had a slightly more hyperpolarized V_m but this trend did not report any statistical significance. The detailed statistical quantities were compiled in Appendix 6. Since all of the data were normally distributed, the I-box marks the SD of population.

3.3 Discussion

3.3.1 Varied KO rate in the TMEM16A^{floxed}:Pax2-Cre mice

In the study of Wang & Bergles (2015), both promoters (Pax2 and Sox2) hosting Cre expression should be active from embryonic stage (Burton *et al.*, 2004; Kempfle *et al.*, 2016). Although the spontaneous inward current from Cl⁻ efflux in the non-sensory cell was completely silenced in the TMEM16A^{floxed}:Sox2-Cre model, the spontaneous current in TMEM16A^{floxed}:Pax2-Cre model only had a reduced amplitude and remained comparable in terms of frequency (Figure 3.19; Wang & Bergles, 2015). However, the authors did not provide the level of efficiency of TMEM16A KO in their study. I found that half of the mice failed to KO the TMEM16A protein fully in IHCs while the rest of them had 100% of KO rate (Figure 3.1 A). The failed induction (0 %, Figure 3.1 C) was the only case observed, and it was likely to originated from human-error (mislabelling or mixing samples) made during tissue collection, genotyping, or immunolabelling.

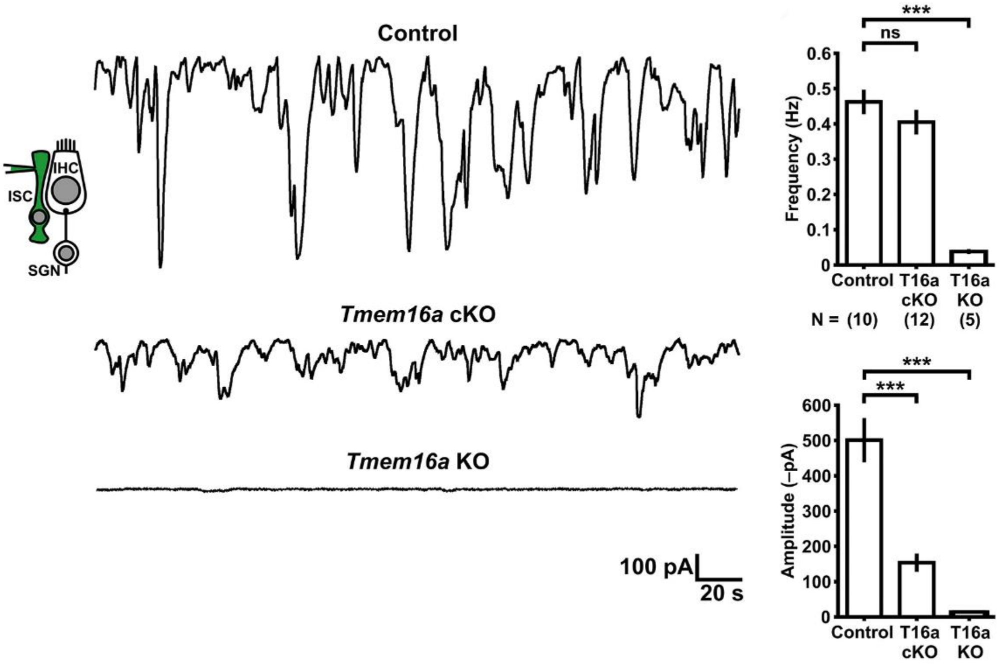

Figure 3.19 Pax2-Cre did not fully knockout TMEM16A in the literature
From top to bottom in the left panel, the traces show the spontaneous inward current in GER non-sensory cells in the control (top), TMEM16A^{floxed}:Pax2-Cre (middle, Tmem16a cKO), and TMEM16A^{floxed}:Sox2-Cre (bottom, Tmem16a KO). Statistics in the right panels shows a completely diminished spontaneous current in the TMEM16A^{floxed}:Sox2-Cre but not in the TMEM16A^{floxed}:Pax2-Cre which was only affected in the current amplitude. Images adapted from Wang & Bergles, (2015).

The Cre recombinase in the Pax2-Cre mouse strain is a constantly active type (Ohyama & Groves, 2004). Theoretically, it should produce a strong and consistent KO phenotype as the TMEM16A starts to be detectable only after P1. One possible explanation for the variance on the TMEM16A KO is that Pax2 promoter did not produce enough copy of Cre recombinase during the embryonic stage, as their expression became much more prominent at P1 (Burton *et al.*, 2004). This is also the period (P1-P3) that GER starts to express TMEM16A and spontaneous crenation (Tritsch & Bergles, 2010; Wang & Bergles, 2015). The amount of mRNA produced before the gene was knocked out could stochastically decide the phenotype of each cell. In fact, in samples under P5 I occasionally found faint traces or puncta of TMEM16A signal that similar to the partial KO in Figure 3.1 B, when boosting the gain or contrast of the images to an extreme setting. This gives hint that a certain amount of functioning TMEM16A mRNA was expressed before the gene was knocked out. This variance between individual animals on TMEM16A KO is likely to affect the statistical analysis in all of the results in the TMEM16A^{floxed}:Pax2-Cre model.

3.3.2 Role of TMEM16A-medated fluid secretion on IHC physiology.

The calcium wave in GER was proposed to exert bipolar influences on regulating IHC excitability. For the K^+ secretion hypothesis, accumulating $[K^+]_e$ from the TMEM16A-dependent K^+ efflux shifts the Nernst potential of K^+ (E_K) in IHC towards more positive voltages (Babola *et al.*, 2018; Wang & Bergles, 2015). The K^+ clearance hypothesis involves the release of water and the crenations, which expand the extracellular space and dilute the $[K^+]_e$ to promote outward I_K from the IHC (Babola *et al.*, 2020).

So far, there is no solid proof on the actual amount of K^+ secretion from SCs. The K^+ secretion was suggested to depolarize the dendritic boutons of SGNs and thus maintain their spontaneous firing and survival even without the synaptic transmission from the IHC (Babola *et al.*, 2018). However, the volume of a synaptic bouton is much smaller than an IHC. According to the Hodgkin-Huxley model (Hodgkin & Huxley, 1952), the derivative of depolarizing V_m from I_K could be represent in Equation 2, where du/dt is the change of membrane potential over time, C is the membrane capacitance and the $I_K(t)$ and $I(t)$ is the potassium current and the remaining currents at a given time point.

Equation 2 Membrane voltage change as a function of current

$$\frac{du}{dt} = \frac{1}{C} \times \left[- \sum I_K\ (t) + I(t)\right]$$

Setting the scene at the resting membrane potential, the I(t) should be a constant term. Assuming the inward I_K induced by the E_K change are identical, the level of depolarization is the reciprocal of the membrane capacitance which is positively correlate with the volume of the cell. As a result, synaptic boutons are more susceptible to the homeostatic changes on the E_K. Moreover, the excitability of SGNs were shifted to produce more intrinsic spikes in response of lacking input from the IHC (Babola *et al.*, 2018). Based on above reasons, the findings in the study by Babola *et al.* (2018) cannot really provide solid evidence to support the K^+ secretion hypothesis.

Other evidence claiming the K^+ secretion hypothesis were all acquired from experiments with 100 µM of ATP/UTP, which is nearly 3000-times higher than the measured ATP level (3-7 nM) in endolymph and perilymph (Muñoz, 2001; Gale *et al.*, 2004; Muñoz *et al.*, 1995). It is uncertain whether the depolarization in IHC described in the literature (Babola *et al.*, 2020; Wang & Bergles, 2015) could actually happen in a physiological setting. In comparison, the K^+ clearance seems to be a more convincing pathway. Alongside diluting K^+ with extra volume, TMEM16A-mediated Cl^- efflux could also promote the K^+ uptake through K^+-Cl^- cotransporters (KCCs) or Na^+-K^+-Cl^- cotransporters (NKCCs), which was considered to mediate the K^+ clearance near hair cells in mature cochlea (Boettger *et al.*, 2003; Zdebik *et al.*, 2009).

In the TMEM16A^{floxed}:Pax2-Cre model, I found that around 1/3 of the IHCs in cKO animals lost their capability to fire SAPs (Figure 3.2). This can be explained by either losing the depolarization generated by the K^+ secretion from the non-sensory cells, or losing the capability to repolarize from the spikes due to accumulated $[K^+]_e$ from lost K^+ clearance. In the former condition, non-spiking cells should produce a strong correlation with the thoroughness of cKO, but the data suggested otherwise (Figure 3.2 B). In addition, the characteristics of the spiking ISIs in the IHCs from the cKO animals did not differ from the control in every aspect (Figure 3.5 - Figure 3.7). Corresponding with this result, current injection in patch-clamp recording showed that the excitability of immature IHCs remained the same in the cKO animals (Figure 3.14).

All these results suggested K^+ secretion probably does not play a critical role in modulating SAPs in IHCs. In fact, a study based on the K^+ secretion hypothesis had established that the main source of $[K^+]_e$ accumulation is the outward I_K during the spontaneous firing of IHCs and SGNs (Babola *et al.*, 2020). As a result, the major function of the TMEM16A-mediated events on regulating the SAPs should be K^+ clearance around the IHCs.

Indeed, the study by Wang and Bergles (2015) reported a significantly depolarized resting V_m in TMEM16A*floxed*:Pax2-Cre and TMEM16A*floxed*:Sox2-Cre mice. This evidence strongly indicates the accumulating $[K^+]_e$ upon the KO of TMEM16A. In my experiments, the distribution of resting V_m from cKO animals also shift slightly towards a more positive range (Figure 3.14 A) but did not reach statistical significance as reported in the study by Wang and Bergles (2015). Two possible reasons might bias the statistic results. The first one is the incomplete KO in the TMEM16A*floxed*:Pax2-Cre model (3.2.1; discussed in 3.3.1). The remaining TMEM16A activity in the cKO animals might contribute to the varied distribution that covers the range of normal V_m (Figure 3.14 A). The second one is that being a secondary effect from the periodic GER calcium waves, an IHC under TMEM16A-mediated K^+ modulation could innately cycle between depolarization and resting V_m states. As a result, I might be sampling from the same data range with a higher probability of getting a IHC at resting V_m from control animals. This is a technical limitation of the model and further experiments are required for confirmation.

Another sign of accumulated/disrupted $[K^+]_e$ was that the cKO animals presented a much larger variance on the current responses at more depolarized holding voltages (Figure 3.15). The I_{steady} in the control animals had a very precise distribution (SD = 0.45 nA, n = 6) compared with the nearly 16 times larger variance in cKO animals (SD = 1.77 nA, n = 9). The median of I_{steady} in cKO animals (5.06 nA, n = 9) is at the same level as the 25% quartile of the control animals (5.05 nA, n = 6), indicating more IHCs produced lower outward I_K in the cKO animals. These phenotypes suggests a more positive E_K, possibly due to a higher $[K^+]_e$ produced by the KO of TMEM16A-mediated K^+ clearance.

3.3.3 Did SAP firing pattern really remain unchanged?

Based on the assumption that the IHCs from the cKO animals would have less repolarization power due to the accumulated $[K^+]_e$ from the deficient K^+ clearance, the firing rate of SAPs should be at least modified from the cells being depolarized. However, none of the analysis of ISI produced significant difference between the IHCs from control and cKO animals (Figure 3.5 to Figure 3.8). Did the characteristics of SAP really remain similar? In my opinion, there were indeed some subtle signs. For instance, some of the IHC went into a long silence after intense tonic firing (Figure 3.20 A). After the silent period, it recovered firing capabilities and maintained a normal bursting pattern.

This atypical long silence in the cKO animals resembles the phenotype observed in SK2-KO (Figure 3.21). IHCs with deficiency in the SK2 channels maintained a normal firing but were forced into a long refractory cycle (~ 2 minutes) due to the loss of a major repolarizing current I_{SK2} (Johnson *et al.*, 2007). The amplitude of the spikes was decreased before the SK2-KO IHC went into refractory (red trace in Figure 3.21). This characteristic was also observed in the recording sample given in Figure 3.20 B, where the peak of spikes was less than half of the larger spikes in later time points (Figure 3.20 C, D). This phenotype also explains the completely silent phenotype that was only observed in the IHCs from the cKO mouse (Figure 3.2). In the SK2-KO model, the $[\mathrm{K}^+]_\mathrm{e}$ homeostasis was normal and the depolarized V_m could be recovered by the remaining $I_{\mathrm{K,neo}}$. In comparison, the accumulated $[\mathrm{K}^+]_\mathrm{e}$ from TMEM16A-deficiency seemed to block the outward I_K indefinitely, and hence produce the completely silent phenotype over several minutes.

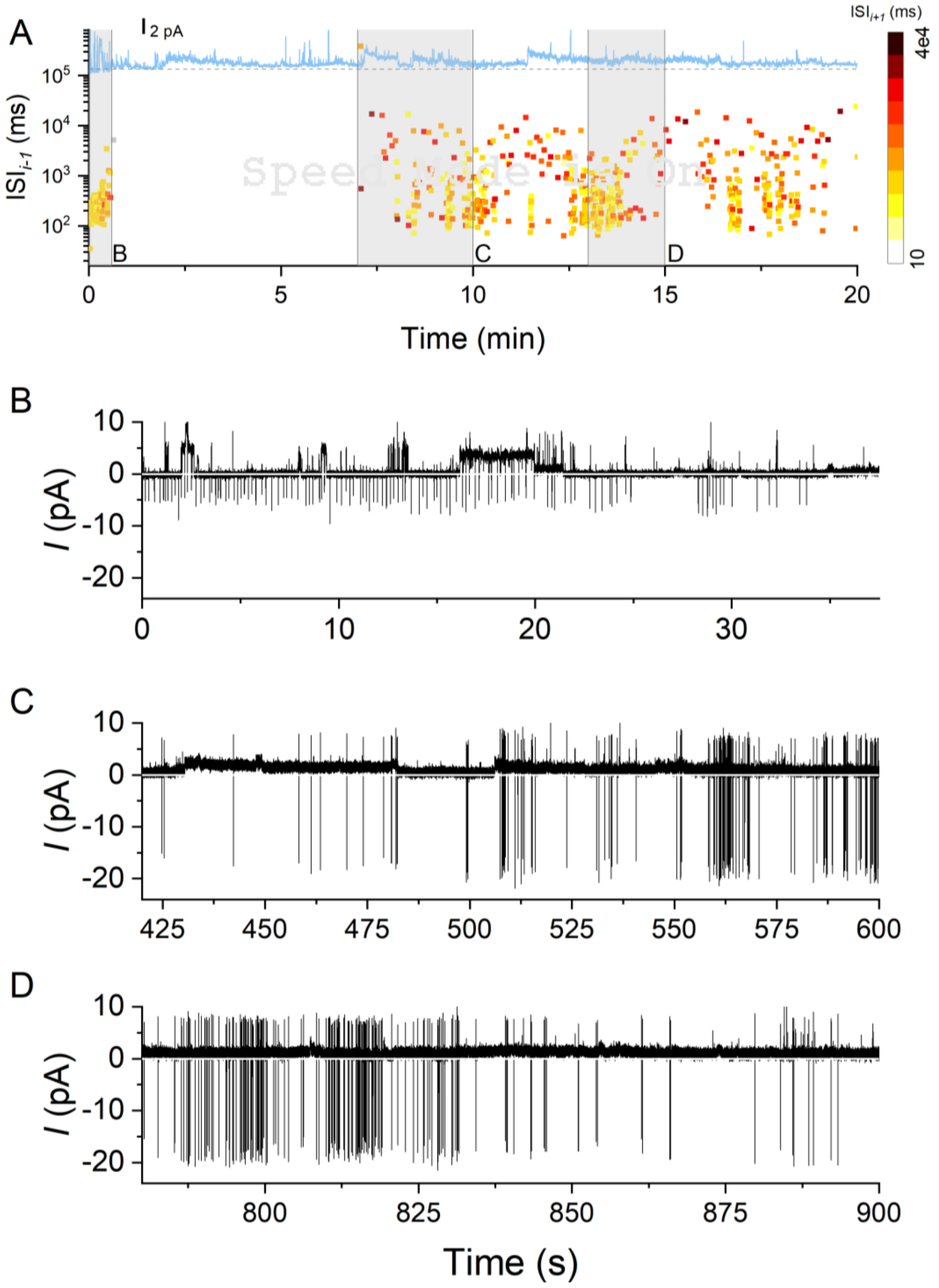

Figure 3.20 Longest silent period recorded from an IHC of cKO animal.
A) ISI between the i^{th} and the i-1^{th} spikes (ISI$_{i-1}$) plotted as a function of time, coloured from bright yellow to dark red indicates the ISI$_{i+1}$. The blue trace overlayed on top is the baseline change of the raw recording filtered with 5 Hz low pass Gaussian filter. Dashed line marks the 0 pA of the baseline, and the scale bar is 2 pA. B-D) The raw recordings from the grey shaded area with corresponding labels. The white line marks 0 pA.

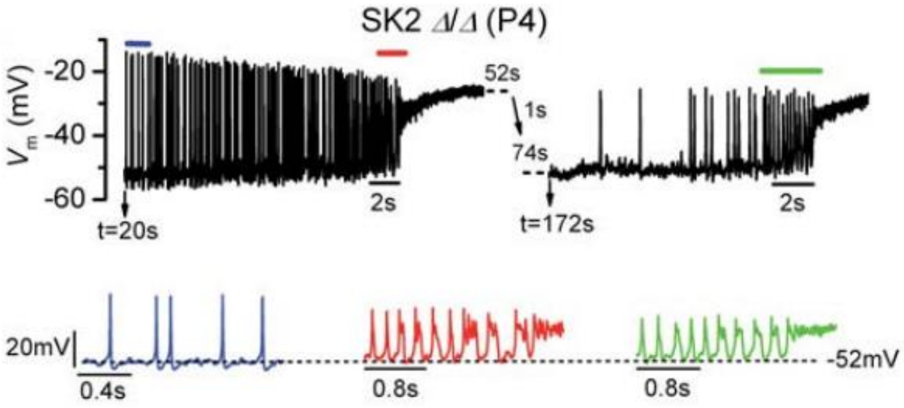

Figure 3.21 Atypical silence period with depolarized V_m in SK2-KO IHC.
The top panel show the spiking waveform from a SK2-deficient IHC under perforated patch-clamp recording. The two traces were recorded from the same cell with a break in between where no spikes were produced. The bottom panels are enlarged area or their corresponding colour in the top panel. The firing pattern of SAP was normal at the beginning of the recording (blue) and gradually lost the repolarizing phase at the end of continuous firing (red). This in the end depolarized the V_m and silenced the cell. After two minutes, the V_m recovered to the baseline level and the SAP activity continued again. However, the cell went into silent period cycle again after another rapid firing phase (green). Image adapted from Johnson *et al.*, (2007).

3.3.4 Synchronization of SAPs relies on TMEM16A-mediated events

One of the proposed influences of the GER calcium wave features the synchronize the SAPs between nearby IHCs (Tritsch *et al.*, 2007; Tritsch & Bergles, 2010). The proposed mechanism of action was that the K^+ secretion from non-sensory cells would depolarize the nearby IHC. Results from calcium imaging experiments agree with this hypothesis, with the correlation between nearby IHCs significantly reduced in the cKO group (Figure 3.11). This finding suggested that the synchronization of IHCs is indeed regulated by TMEM16A-mediated event.

Since K^+ secretion is unlikely to be the mechanism, the other hypothesis, the K^+ clearance, become the next candidate. However, lowering the $[K^+]_e$ would shift the Nernst equilibrium of potassium ions towards more negative voltages, and thus prefer to hyperpolarize the IHCs. How could a hyperpolarizing effect boost and synchronize the SAPs among IHCs? My hypothesis is, with the GER actively maintaining a lower $[K^+]_e$, it enhances the repolarizing power of I_{SK2} which is proven to be activated by ATP release (Johnson *et al.*, 2011). According to evidence from mice with overexpressed SK2 channels, the enhanced I_{SK2} quadrupled the mean frequency of the SAP by providing extra repolarization power (Johnson *et al.*, 2013).

This event probably involves mechanism similar to the post-hyperpolarization rebound firing which is common in the central nerve system (De Schutter & Steuber, 2009; Grenier *et al.*, 1998).

Similar dynamics were shown in the example recordings (Figure 3.3, Figure 3.4). During the cell-attached recording, different sizes of hyperpolarizing steps were spotted from animals of both phenotypes. In the example of control animal, the mild hyperpolarization boosted the firing rate of SAPs slightly, from 4 Hz to 6 Hz (Figure 3.3). In the example of cKO animal, it produced more dramatic effect which brought a nearly silent IHC into burst firing (Figure 3.4 D). Corresponding to the size of hyperpolarizing, the IHC produced a rapid burst train at 20 Hz during the first second of the hyperpolarization (Figure 3.4 B and E). The firing rate eased down to 4-5 Hz as the hyperpolarization gradually dropped down to a similar level as in the control sample (Figure 3.4 C). However, not all of the hyperpolarization events observed in the recordings produced the same effect. Some of them did not correlate with the burst firing in the recorded IHC (area C & D in Figure 3.20 A).

It is very tempting to link this hyperpolarization event with the K^+ clearance mechanism. However, the collected data yet allows me to identify the source of the hyperpolarization. Further testing with pharmaceutical experiments, TMEM16A antagonist for instance, would be required to confirm the source and effect of this hyperpolarization event.

3.3.5 TMEM16A cKO delayed but did not prevent the maturation of IHC

To investigate the influence from TMEM16A-mediated effects on the maturation of IHC, I recorded the whole cell current at around P20 and calculated the size of mature-type currents, $I_{K,f}$ and $I_{K,n}$, as indications of the maturation. Most of the IHC from both genotypes presented the fast-activating $I_{K,f}$ and the inactivating $I_{K,n}$ similar to the control (Figure 3.16 A, D, G), although the cells from cKO groups often had a smaller current size (Figure 3.16 B, E, H). However, there were several recordings presented immature-type currents without any fast current in the I_{init} region (Figure 3.16 C, F, I). These samples did not affect the averaged I-V response, as the I_{steady} and I_{init} were within similar range in both groups. Because the three recordings with immature-type currents were all from the same animal at P17, I decided to investigate further by separating the data at different ages. The cKO below P20 (P17 and P19) presented a significantly smaller I_{init} at more positive voltages than the littermate controls and older cKO groups at P24 (Figure 3.17 D, Figure 3.18 E). The difference is still identifiable in the I-V response plot excluding those recordings without the fast current (Figure 3.17 F), but the difference from the younger cKO group became non-significant (p = 0.126, Mann-Whitney).

Interestingly, with a smaller $I_{\text{K,f}}$ in the IHC from cKO animals under P20, I expected to see a smaller I_{steady} but it shows a similar range between ages or genotypes instead (Figure 3.18 D). A possible explanation is that IHC overexpress other K^+ channels to compensate the insufficient $I_{\text{K,f}}$ after hearing onset. The average size in the cKO group presented an increasing trend with age (Figure 3.18 D), but it has no statistical significance. However, the plot shows a possible grouping bias by the two outliers. Without any solid reason to reject the outliers the statistics including them was accepted.

The $I_{\text{K,n}}$ seemed to become larger in the cKO group with the increasing age (Figure 3.18 F), but it did not produce statistical significance (p = 0.17, Student's t-test) and the control group did not have enough N number to draw a conclusion.

There was an unexpected difference on the resting V_{m} between the control and the cKO group under P20 (Figure 3.18 H). Usually, a phenotype with less I_{K} would lead to more depolarized resting V_{m}, but in this case the readings from the cKO group under P20 were clustered at a more hyperpolarized potential (*median*: control, −75.4 mV; cKO, −81.9 mV). Cross-correlating between all available parameters (data not shown) revealed that the E_{rev} of I_{steady} came out as the only factor that has strong correlation with the resting membrane potential, which is expected as the resting V_{m} is determined by the interplay of the whole cell currents. However, the E_{rev} did not have any significant difference between the IHCs from control and cKO animals under P20 (p = 0.07, Mann-Whitney; data not showed). Another possible mechanism is that the IHCs in cKO group still had active I_{SK2} at P17-P19. This would explain the clustered resting V_{m} in younger cKO IHCs instead of a normal distribution as in the control IHCs at similar age or older cKO IHCs. (Figure 3.18 H).

The immature calcium efficacy and the atypical morphology of the synaptic ribbons were other frequently reported phenotypes from models with modified spontaneous calcium waves or SAP

(Corns *et al.*, 2018; Johnson *et al.*, 2017; Johnson *et al.*, 2007; Johnson *et al.*, 2013). Unfortunately, due to the impact of COVID, I did not have the time nor the resource to complete this section of experiment and have opted to leave it out of this thesis.

Chapter 4 TMEM16A^{floxed}:ROSA-tdTomato:Plp1-Cre^{ERT} model

4.1 Introduction

Except for the Pax2-Cre, proteolipid protein 1 (Plp1)-Cre^{ERT} mouse strain (see Table 3) was introduced to generate a more specific and confined cKO of TMEM16A. In the organ of Corti, Plp1 is only expressed in inner phalangeal cells and border cells which surround individual IHCs (Wan & Corfas, 2017). Compared with the global KO of TMEM16A in TMEM16A^{floxed}:Pax2-Cre, TMEM16A^{floxed}:Plp1-Cre^{ERT} model allows uninterrupted K$^+$ metabolism in the GER. With this scheme, we hope to find out whether all of the non-sensory cells participating in the calcium waves have influence on the SAP and the development in IHC, or if only the adjacent non-sensory cells are significant.

Cre-inducible ROSA-tdTomato gene was also introduced into the mouse strain. The fluorescent reporter enabled me to confidently identify phenotype of the target cell when performing patch-clamp recording. All of the recorded Cre-induction pattern in adjacent non-sensory cells of an IHC from cKO mouse can be categorised into four types and be assigned a 0 to 3 score (Figure 4.1). I will refer these Cre-induction pattern with their “KO score” in later sections.

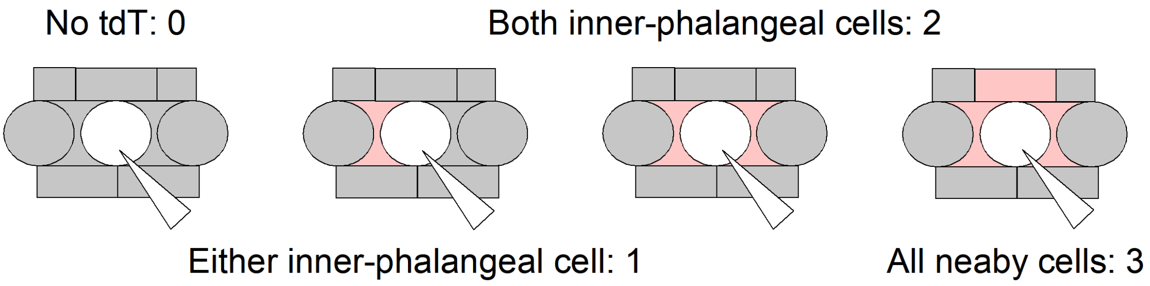

Figure 4.1 KO score assigned by tdTomato expression in non-sensory cells.
The Cre-induction rate in non-sensory cells (grey non-circle cells) around a target IHC (white circle cell) can be scored according to their tdTomato expression (in red). From the left, a control sample has none of the surrounding cells presenting tdTomato fluorescence, and receives 0 points for the KO score. If either inner-phalangeal cell had tdTomato, the sample score 1 point. If in both, 2 points. If all of the surrounding cells had tdTomato signal, the sample received the highest score of 3 points. Only the adjacent inner-phalangeal cells and the border cell are considered as TMEM16A was not detected in the pillar cells.

4.2 Results

4.2.1 High frequency SAPs were lost in the IHC of cKO animals

Spontaneous action potentials (SAPs) in the IHCs of TMEM16A^{floxed}:ROSA-tdTomato:Plp1-Cre$^{\mathrm{ERT}}$ mice were collected with cell-attached patch-clamp recording described in 2.4.6, and analysed with the workflow in 2.7.2 to extract relevant characteristics. Unlike in the TMEM16A^{floxed}:Pax2-Cre model, SAP were detected in all IHCs from both the control and the cKO animals in the TMEM16A^{floxed}:Plp1-Cre$^{\mathrm{ERT}}$ model.

An example recording from a P6 IHC of a control animal is showed in Figure 4.2 in the same format described in 3.2.2. Similar to the example, all of the IHCs from control animals produced robust bursting throughout the whole recording. Constant small hyperpolarizing events were found in the baseline of the recording with occasional shorter, larger ones overlapping with them (light blue trace, Figure 4.2 A). However, these hyperpolarizing events didn't seem to correlate with the bursting (Figure 4.2 B, C). Except one short burst of quadruple spikes shown in Figure 4.2 D, none of the other area presented hyperpolarization-associated bursting as in the TMEM16A^{floxed}:Pax2-Cre mice (Figure 3.3).

An example recording from a P6 IHC (KO score 3) of a TMEM16A cKO animal is showed in Figure 4.3. Unlike the robust burst firing in control animals, most of the IHC in the cKO animals had a typical phenotype similar to the cKO phenotype observed in TMEM16A^{floxed}:Pax2-Cre model (Figure 3.4), with SAPs bursting only when there were hyperpolarizing events (Figure 4.3 B-D). Non-bursting spikes were still found without hyperpolarization, but they were extremely scarce (around 8 and 10 minutes in Figure 4.3 A). The first and last three minutes of the recording did not have any spiking activity, and were trimmed off from the example traces for better viewing.

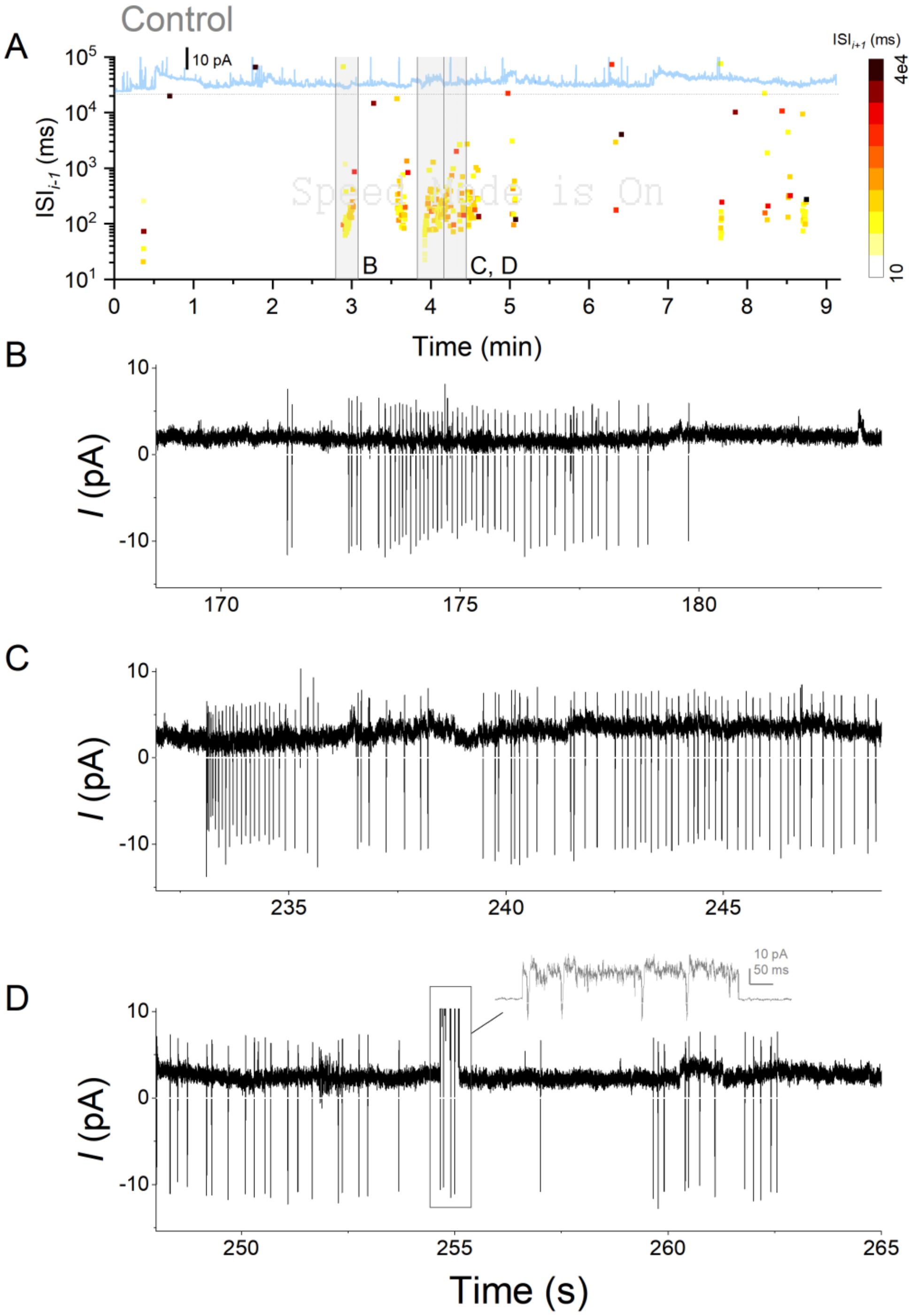

Figure 4.2 Example of SAP recording from a control IHC

A) ISI between the *i*th and the *i-1*th spikes (ISI$_{i-1}$) plotted as a function of time, coloured from bright yellow to dark red indicates the ISI$_{i+1}$. The blue trace overlayed on top is the baseline change of the raw recording filtered with 5 Hz low pass Gaussian filter. Dashed line marks the 0 pA of the baseline, and the scale bar is 10 pA. Raw recording of the grey shaded area is enlarged in B-D. B, C) Bursts without obvious hyperpolarizing. D) A short burst of spikes that seemed to be initiated by hyperpolarization event, as shown in the inset.

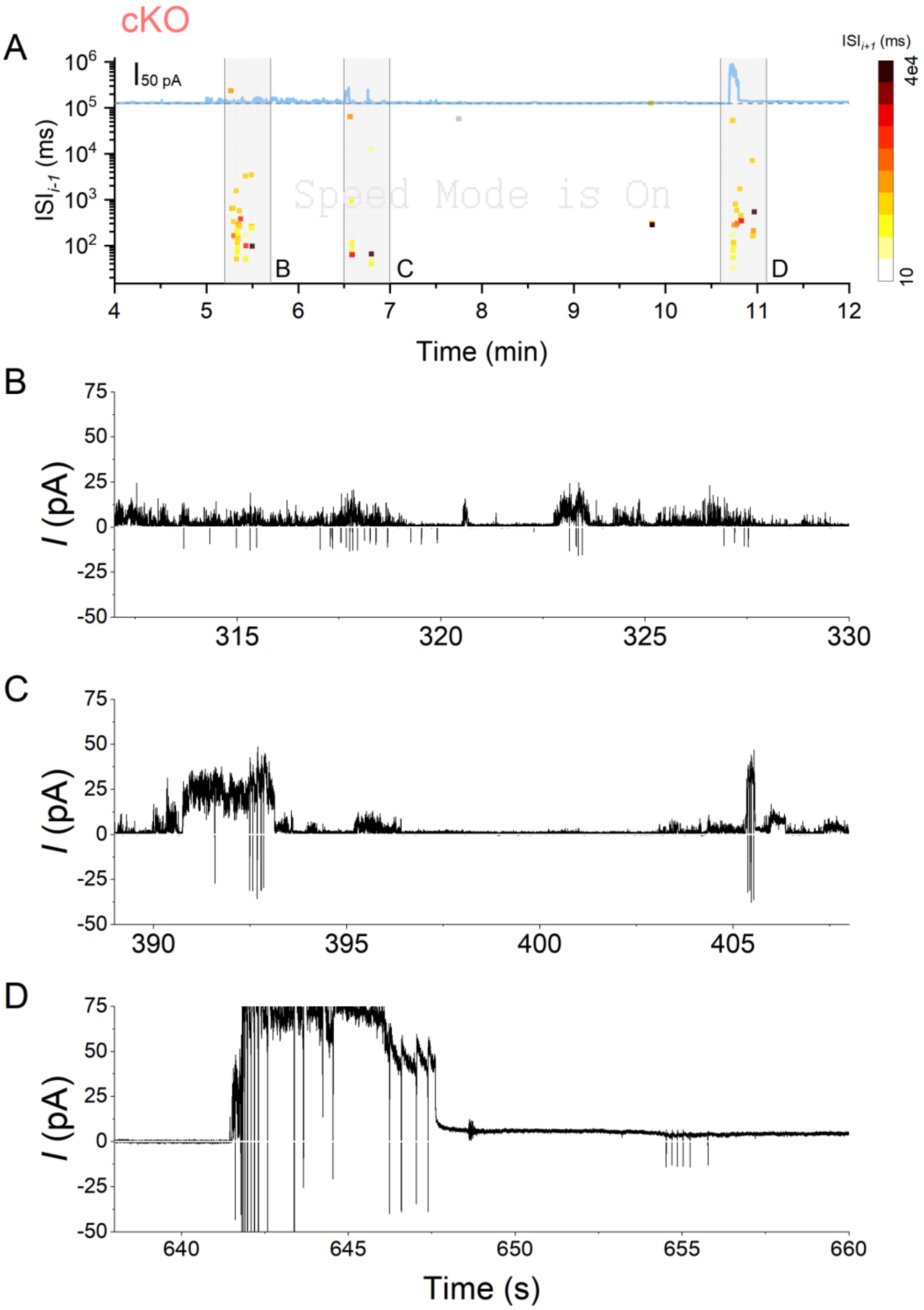

Figure 4.3 Example of SAP recording from a cKO IHC

A) ISI between the i^{th} and the $i\text{-}1^{th}$ spikes (ISI$_{i-1}$) plotted as a function of time, coloured from bright yellow to dark red indicates the ISI$_{i+1}$. The blue trace overlayed on top is the baseline change of the raw recording filtered with 5 Hz low pass Gaussian filter. Dashed line marks the 0 pA of the baseline, and the scale bar is 50 pA. Raw recording of the grey shaded area is enlarged in B-D). B-D) SAP bursts only occurs when there were large hyperpolarizing events.

The phenotype of decreased repolarising power was observed in one of the cKO samples (KO score 3, Figure 4.4). The IHC presented mild, shorter bursts in the first half of the recording (time < 6 minutes in Figure 4.4 A) and increased the firing rate after a larger (0.6±0.2 in 3-5 minutes vs 1.3±0.4 pA in 6-8 minutes) hyperpolarizing event appeared (Figure 4.4 B, C). The peak amplitude of the spikes started to decrease after robust repetitive bursting and eventually diminished (yellow framed region in Figure 4.4 B, C). Then, the baseline level transited from slight hyperpolarization into depolarization (positive to negative going, blue trace in Figure 4.4 B). The cell remained silent but alive under the depolarization for another minute until the recording was stopped at 10 minutes and passed the condition checked (described in 2.4.7).

The analysis of the ISI pairs from spike triplets (see inset of Figure 3.5) didn’t seem to vary between the control and the cKO animals (Figure 4.5 A). However, one of the recordings from cKO animals was from an IHC with only one of the two surrounding inner phalangeal cells presenting tdTomato fluorescence (KO score = 1, Figure 4.5 bottom inset). The distribution of ISI pairs from this IHC strikingly resembles the overall distribution in the control animals. Treating this sample as a control IHC revealed a major difference in the bursting pattern of IHCs from control animals (Figure 4.5 B), which had a dramatic decline in the bursts with frequency high than 10 Hz (ISI < 100 ms, marked with dotted line in Figure 4.5). Except for the high frequency bursts, the characteristics of overall bursting pattern did not seem to be affected (Figure 4.5 B).

The histogram of ISI occurrence shows similar distribution dynamics between phenotypes with the peak occurrence at 140-180 ms (Figure 4.6), with much less spikes observed the cKO animals. Even when including the sample with insufficient knockout, total number of spikes in cKO animals was only half (663 spikes, n = 6 from 6 animals) of which in the control (1137 spikes, n = 6 from 5 animals). These characteristics are similar to the observation in the TMEM16A^{floxed}:Pax2-Cre model (Figure 3.6 in chapter 3.2.2). Nevertheless, normalized distribution indicated that the cKO animals had slightly longer intervals between spikes (Figure 4.6 B). The cumulative probability also demonstrates a significant shift towards longer end on the ISI axis ($p = 0.001$, Kolmogorov-Smirnov Test, dashed line in Figure 4.6 B).

Note that the Figure 4.6 shows the distribution with the recording from IHC with insufficient cKO as a control sample, as this modification highlight the difference more and did not affect the significance even if treated the otherwise ($p = 0.035$, Kolmogorov-Smirnov Test). This particular IHC with insufficient cKO was treated as a control sample in the rest of the analysis.

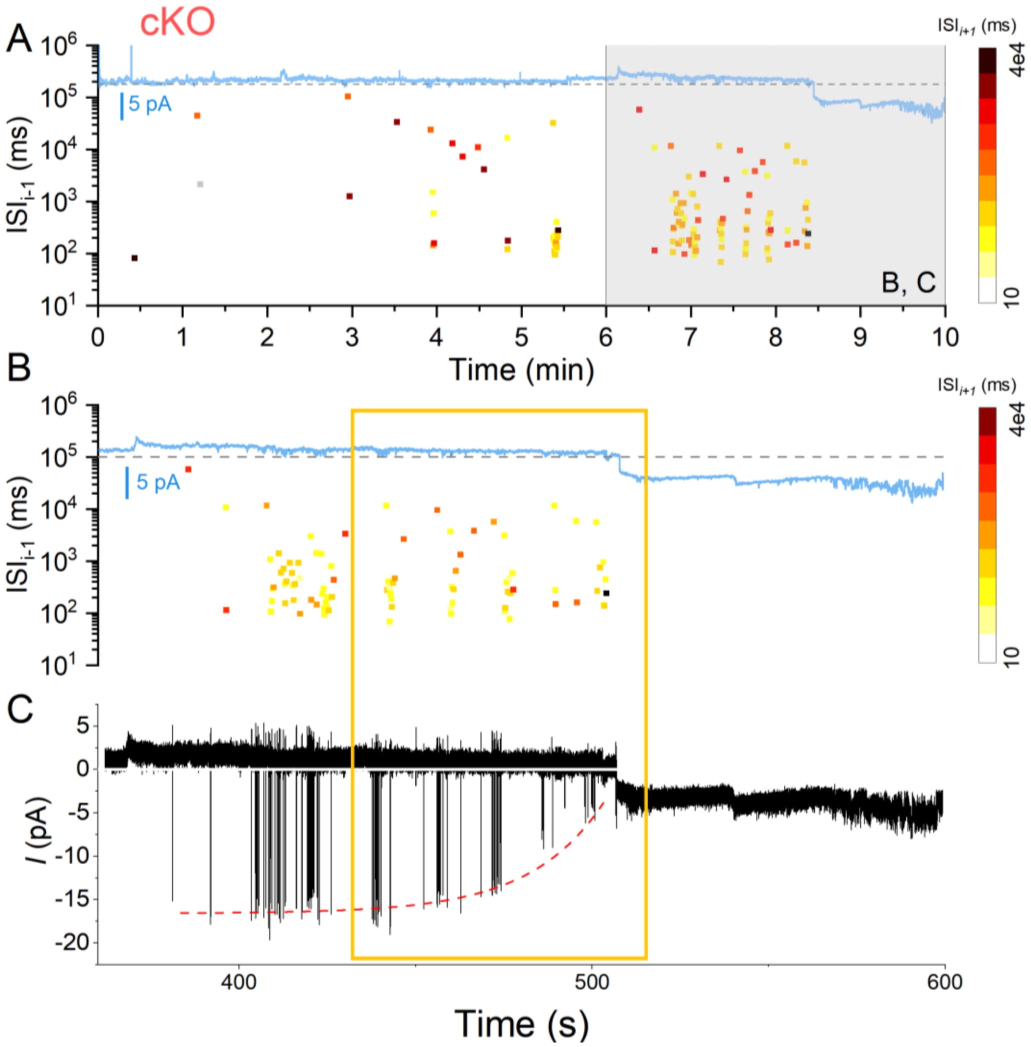

Figure 4.4 Example of saturating SAPs from a cKO IHC

A) ISI between the i^{th} and the $i\text{-}1^{th}$ spikes (ISI$_{i-1}$) plotted as a function of time, coloured from bright yellow to dark red indicates the ISI$_{i+1}$. The blue trace overlayed on top is the baseline change of the raw recording filtered with 5 Hz low pass Gaussian filter. Dashed line marks the 0 pA of the baseline, and the scale bar is 50 pA. B) displays a phenotype of depolarized baseline (blue trace) from 500 – 600 seconds after repetitive burst firing (yellow frame). The colour scheme is the same as in A) and the x-axis is shared with C). C) Raw recording shows a corresponding decrease in spike amplitude as the bursting continued. The white line marks 0 pA.

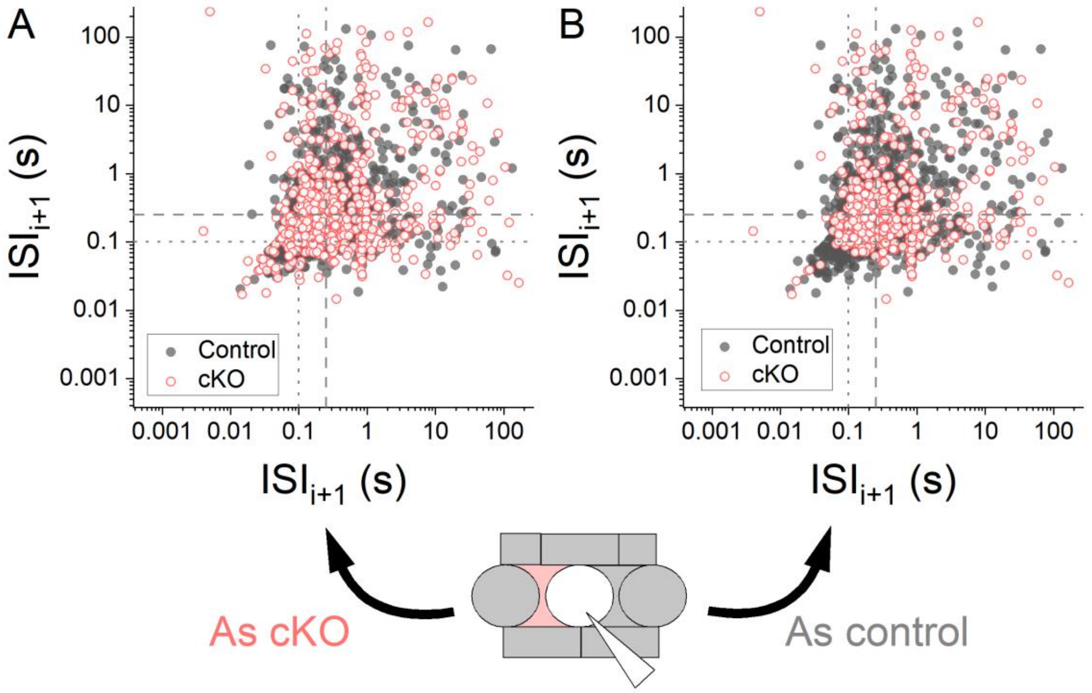

Figure 4.5 SAP burst pattern only changed when both inner-phalangeal cells lost TMEM16A.
A) If the only sample with partial cKO phenotype (KO score=1) was plotted as from a cKO animal, the ISI graph shows a very similar ISI graphs of burst characteristics between the control (grey solid symbol, n=6, from 5 animals) and cKO animals (red open symbol, n=6, from 6 animals). B) If the sample was treated as from a control animal, the ISI graph reveals a lack of high intensity bursts with ISI less than 100 ms (dotted lines).

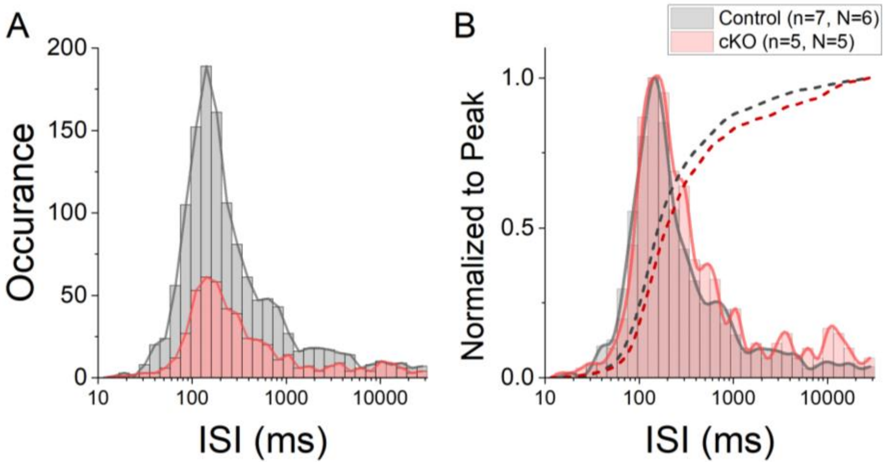

Figure 4.6 Distribution of ISIs slightly became longer difference between phenotypes.
A) The occurrence of ISI$_{i-1}$ from all of the data plotted in logarithmic histogram. The data from control animals is in grey and those from cKO animal is in red. B) the distribution normalized to the peak occurrence in individual phenotype. Dashed lines show the cumulative distribution. Colour scheme is the same as in A). For biological repeats in the legend, n indicates the number of cells and N indicates the number of animals.

Despite the obvious decrease on rapid firing, all of the statistical quantities were not significantly different between the IHCs from the control and the cKO animals (Figure 4.7). Although lacking statistical significance, the mean ISI (Figure 4.7 A) was nearly three times longer in the cKO animals (*median*: 3.7 s, n = 5 cells from 5 animals) than in the control (*median*: 1.7 s, n = 7 cells from 6 animals). The averaged maximum ISI (Figure 4.7 D) was nearly twice longer in the cKO animals (2.05±1.3 mins) than in the control (1.16±0.70 mins). The minimum and median ISI (Figure 4.7 B, C) also had mild increasing trend in cKO animals. Detailed statistics results are compiled in Appendix 7.

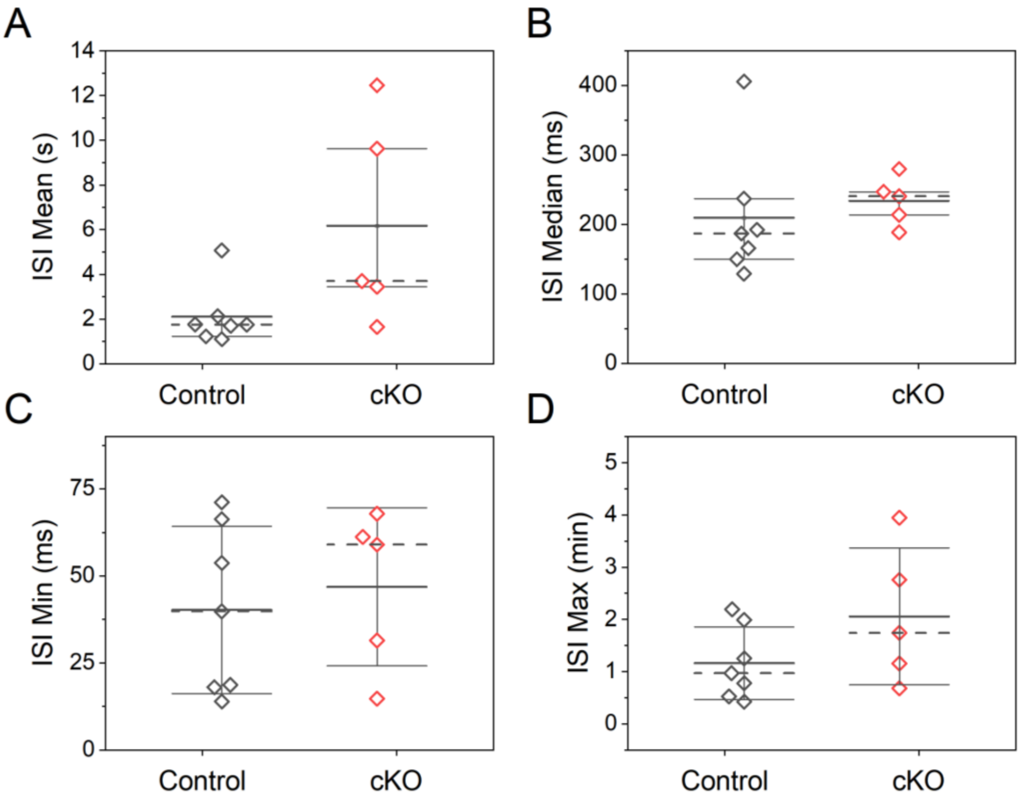

Figure 4.7 Statistical quantities on the ISI in individual IHCs did not report difference. The statistics on A) mean, B) median, C) minimum, and D) maximum ISI from individual IHC did not have any statistical difference. The data from control animals is coloured in grey and from cKO animals in red. The solid line in each plot indicates the population mean while the dashed line is the median. The I-box in A) and B) marks the 1st and the 3rd quartile (25%-75%), and in the C) and D) marks the SD. None of the properties reported statistical differences. Detailed quantities and p-values are compiled in Appendix 7.

Analysis on the length of continuous burst (defined in 2.4.6) did not show any difference between the control and the cKO animals either (control median: 0.93 s; cKO median: 1.24 s; p = 0.56, Mann-Whitney; Figure 4.8 A). However, the statistic on this aspect is probably not very representable, as the total number of bursts were 4 times more in the control animals (41 bursts, n = 7 from 6 animals) then in the cKO animals (11 bursts, n = 4 from 4 animals). One of the IHC from cKO animals did not present any continuous burst.

Nevertheless, there are some very noticeable trends among the statistical quantities. The average number of long bursts in each IHC (Figure 4.8 B) was halved in the IHCs of cKO animals (2.75±0.96 in 4 cells from 4 animals) than in the control (5.85±3.39 in 7 cells from 6 animals). However, this decrease did not have statistical significance. The mean burst length between the phenotypes were similar, but median and the minimum length of long bursts seemed to be slightly larger in the cKO animals, of whom the maximum burst length was extremely limited. The detailed statistical results on these quantities are compiled in Appendix 8.

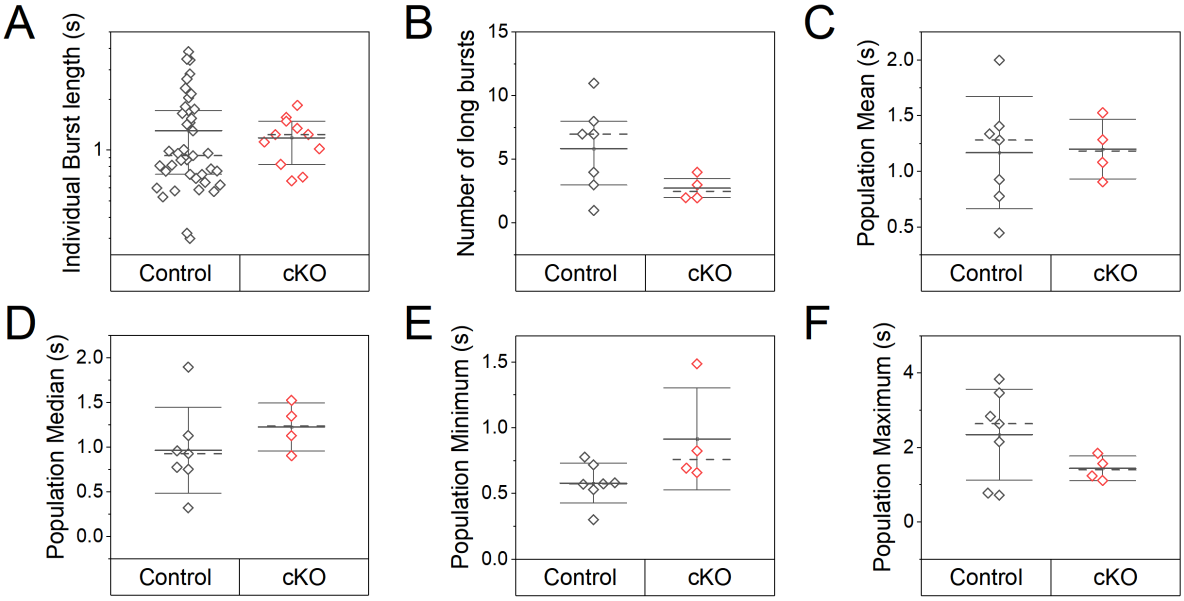

Figure 4.8 Similar burst lengths in both the control and the cKO animals
A) The calculated length of each burst was plotted together according to their phenotypes. The statistical quantities (B: number, C: mean, D: median, E: minimum, F: maximum) on the length of long bursts from individual recordings did not differ between the control and the cKO animals. The data from control animals is coloured in grey and from cKO in red for all subplots. The solid line in each plot indicates the population mean while the dashed line is the median. The I-box marks the SD except for the one in A) is the 1st and the 3rd quartile (25%-75%) since the data is not normally distributed.

4.2.2 Effect on the synchronization was limited.

The calcium activities in the apical organ of Corti from a P8 control mouse is showed in Figure 4.9, plotted as normalized dF/F0 against the recording time. Both the IHCs and GER non-sensory cells had robust activity throughout the recording (Figure 4.9 A, IHC: green, GER: black). An example of synchronized activities between the GER and nearby IHCs (blue vertical line in Figure 4.9 A) is reconstructed in Figure 4.9 B. The fluorescence intensity in the centre GER region was reaching maximum dF/F0 during a spontaneous calcium wave (Figure 4.9 A, B). From the reconstructed frame (Figure 4.9 B), the activity in GER synchronized calcium signals from SAPs in all of the nearby IHCs (#3 to #13) except two (#10 and #14), which still responded with slower and smaller calcium activities according to the dF/F0 traces (Figure 4.9 A). The cross-correlation of the calcium intensity between the IHCs during each calcium wave were calculated with the workflow described in 2.7.3, and were then averaged to produce a correlation matrix of the recorded sample (Figure 4.9 C). The matrix displays a strong correlation between the IHCs from #3 to #11 (Figure 4.9 C).

In comparison, although dF/F0 level in the IHCs from a P8 cKO mice did sparsely increased during calcium waves in nearby GER, they did not seem to be synchronized (Figure 4.10 A). The two separated IHC (arrowhead in Figure 4.10 B) did not responded to the GER calcium wave at all while nearby IHCs had slightly increased dF/F0 at the particular time frame (Figure 4.10 B). Confirming this result, none of the region in the correlation matrix produced strong correlation between IHCs (Figure 4.10 C).

The collection of Pearson's *r* calculated during individual calcium wave revealed a strong decrease on the synchroneity between the nearby 3 IHCs in the cKO animals (*median*: 0.08, n=228 from 1 animals) compared with the control animals (median: 0.18, n=912 from 5 animals; Figure 4.11 A). Separating the data with individual cell pairs indicated that this decrease on synchronization only happened in the most adjacent cells and not further IHCs (Figure 4.11 B, C). At population level, the median correlation coefficient between adjacent IHCs seemed to be much lower in the cKO animal (0.08, n = 4 recordings from 1 animals) than in the controls (0.25, n = 12 recordings from 5 animals; Figure 4.12). The statistical analysis will not be discussed as the recordings of the cKO samples were all from the same animal.

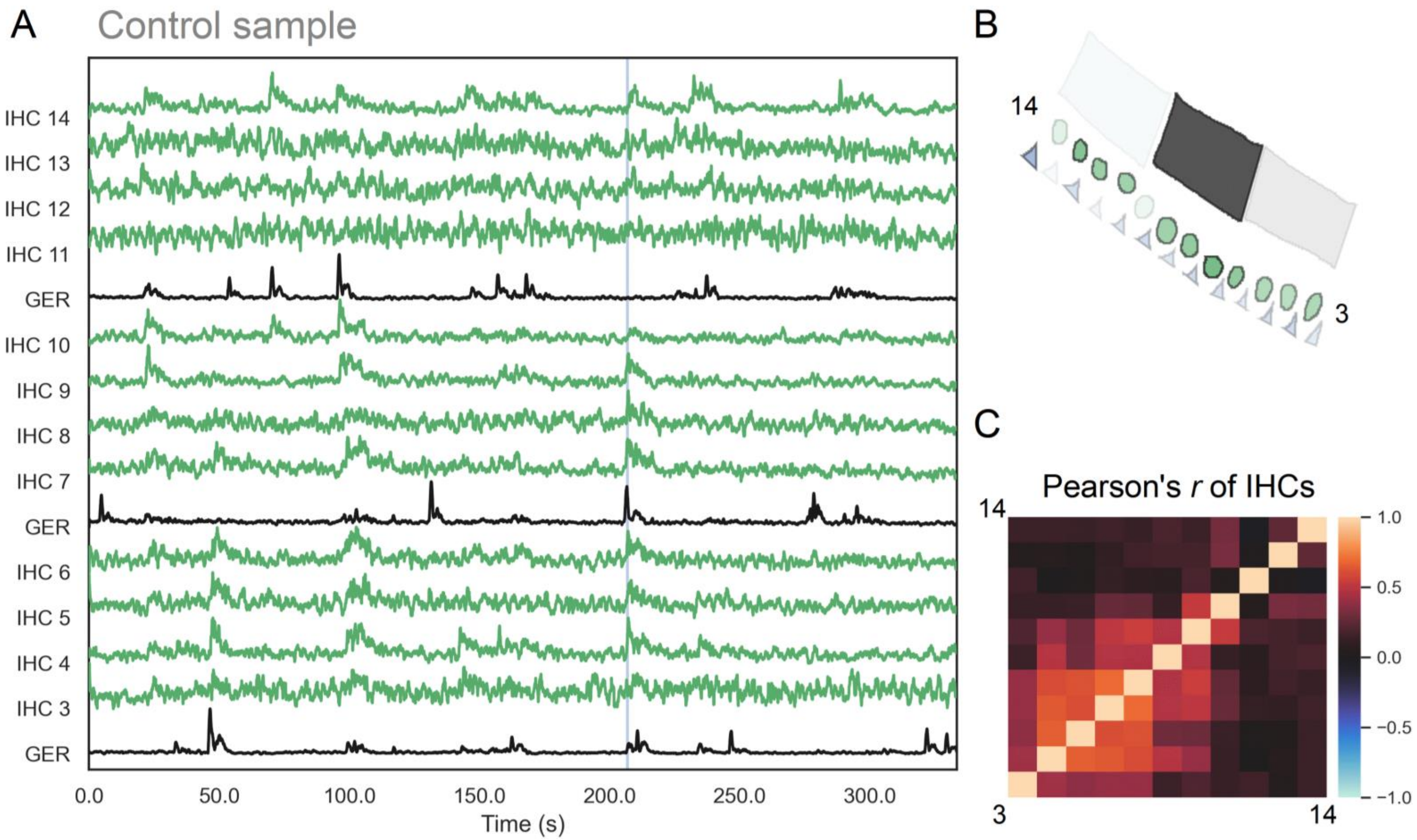

Figure 4.9 Example of the calcium activities from a P8 control sample.
A) The dF/F0 traces are plotted in line graph to show a preview of the calcium activities in IHCs (green) and the nearby GER region (black). Each trace was individually normalized for easier viewing. B) Spatial representation of the activity at the blue vertical line in A). The opacity of each ROI indicates their normalized calcium level, 100% is opaque and 0% is transparent. C) A preview heat map of Pearson's correlation between the calcium activities in each IHCs. Bright red indicates positive correlation and bright blue indicates negative.

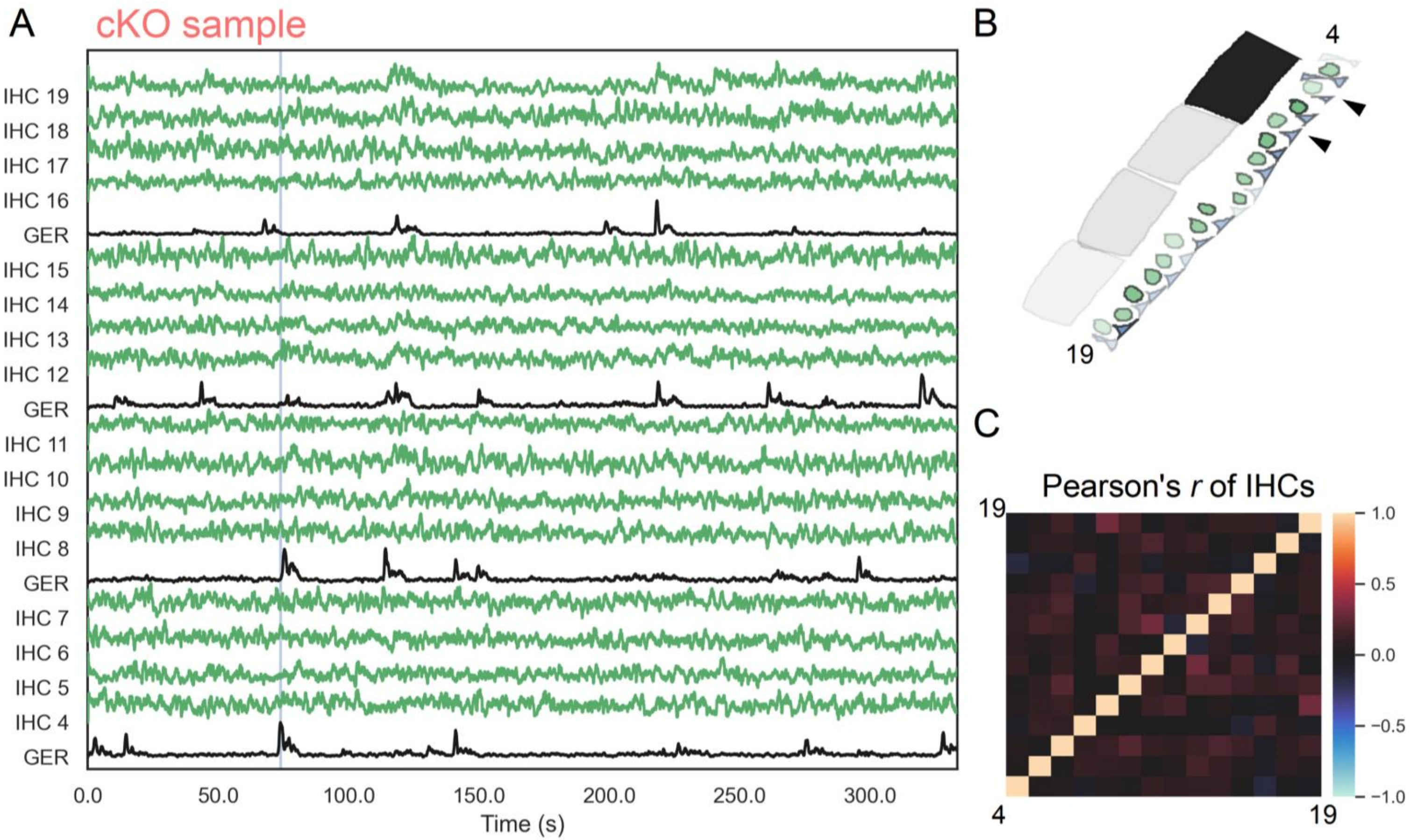

Figure 4.10 Example of the calcium activities from a P8 cKO sample.

A) The dF/F0 traces are plotted in line graph to show a preview of the calcium activities in IHCs (green) and the nearby GER region (black). Each trace was individually normalized for easier viewing. B) Spatial representation of the activity at the blue vertical line in A). The opacity of each ROI indicates their normalized calcium level, 100% is opaque and 0% is transparent. The arrowheads mark the two less synchronized cells (#5 and #7) within the calcium wave (opaque black GER region). C) A preview heat map of Pearson's correlation between the calcium activities in each IHCs. Bright red indicates positive correlation and bright blue indicates negative.

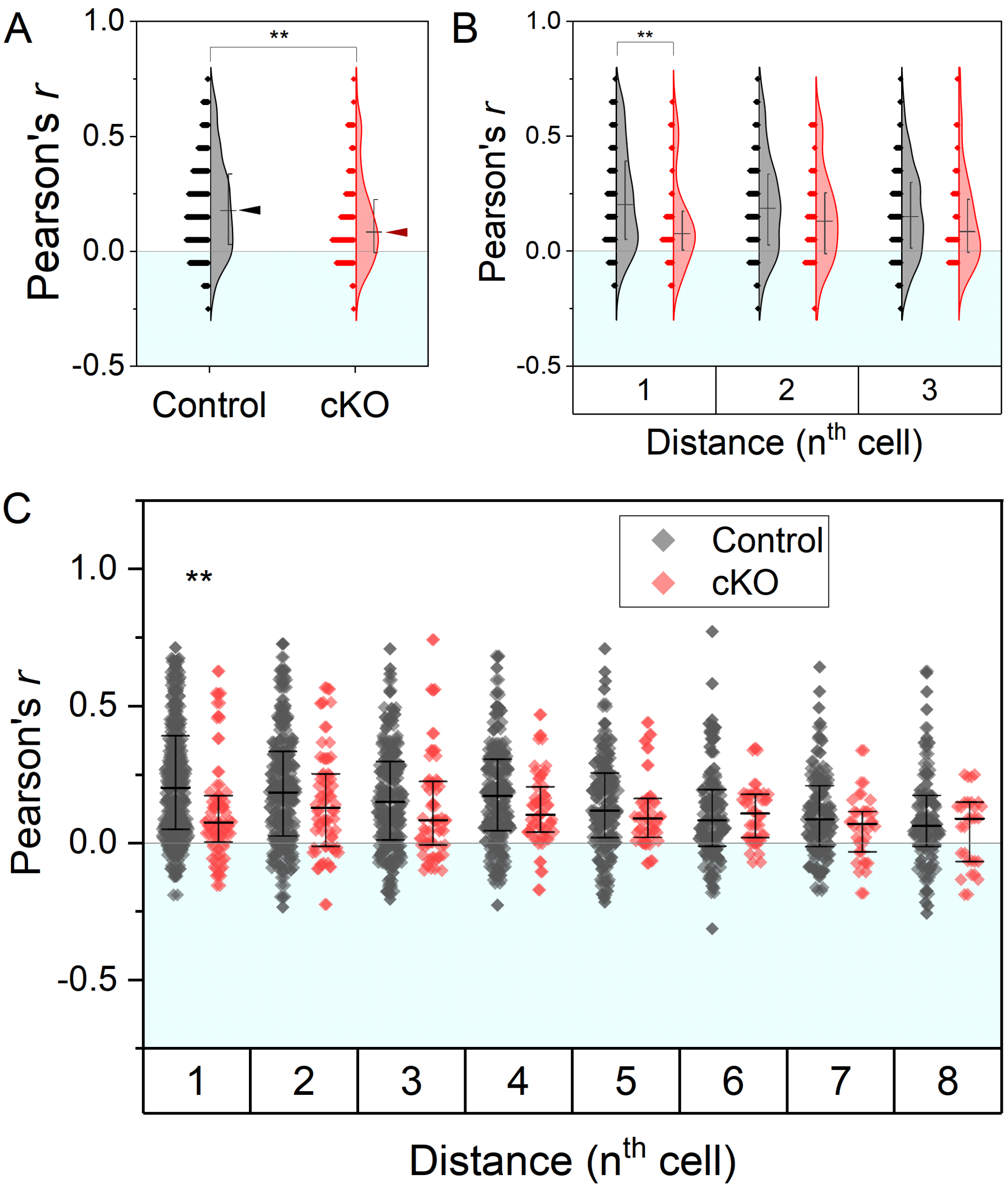

Figure 4.11 Only the activities in adjacent IHC were less correlated in the cKO animals. A) The distribution of correlation index between each IHC and three neighbouring IHC was significantly reduced in the cKO animals (**p < 0.005, Mann-Whitney) compared with the control. Grey (control) and red (cKO) arrowheads highlights the median of corresponding phenotype for an easier visual comparison. For all three panels, the I-box marks the 25% and the 75% percentiles and a short line marks the median. Horizontal line marks zero correlation, and the area below (negative correlation) was filled with light blue. B) Distribution breakdown of the correlation index only showed significant difference between adjacent IHCs. C) The influenced area in the cKO animals was limited to the cell right next to the target IHC. Detailed statistical quantities are compiled in Appendix 9.

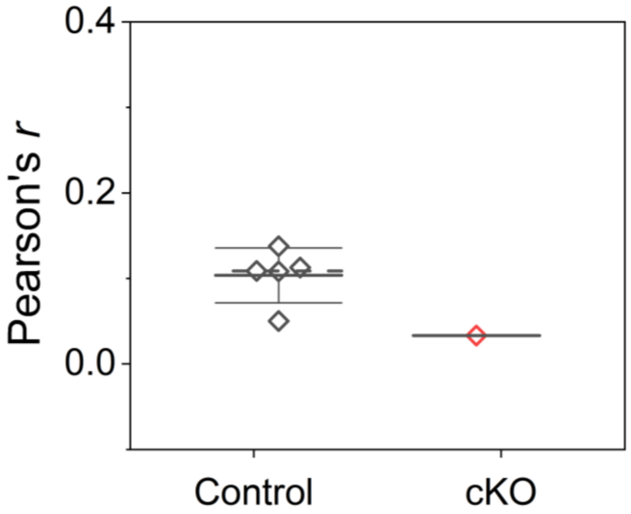

Figure 4.12 cKO animals showed a trend of lower correlation between IHCs.
Population median of the Pearson's correlation from adjacent IHCs during calcium waves. The data from control animals is in grey and from cKO animal in red. The I-bar marks the mean and SD, while the dashed line marks the median.

4.2.3 Immature electrophysiological properties of IHC remained identical

Electrophysiological characteristics of IHC under current- and voltage-clamp configurations are shown in Figure 4.13. P5 IHCs from both control and cKO animals displayed induced spiking activities with increasing firing frequency as the injecting current became larger (Figure 4.13 A, B). Due to an operational mistake on setting up the software, the period of current injection in the current-clamp protocol was shorter (62.5 ms) than described in the methods (250 ms). This might slightly raise detected threshold but should not affect the comparison between phenotypes. Although the size varied between each recording, current responses in both phenotypes displayed the signature slow-activating outward K^+ currents upon stepping the voltage towards depolarised values (Figure 4.13 C, D). The recorded traces were analysed with the procedure introduced in 2.4.7. Detailed figures and statistical results for immature electrophysiology are compiled in Appendix 10.

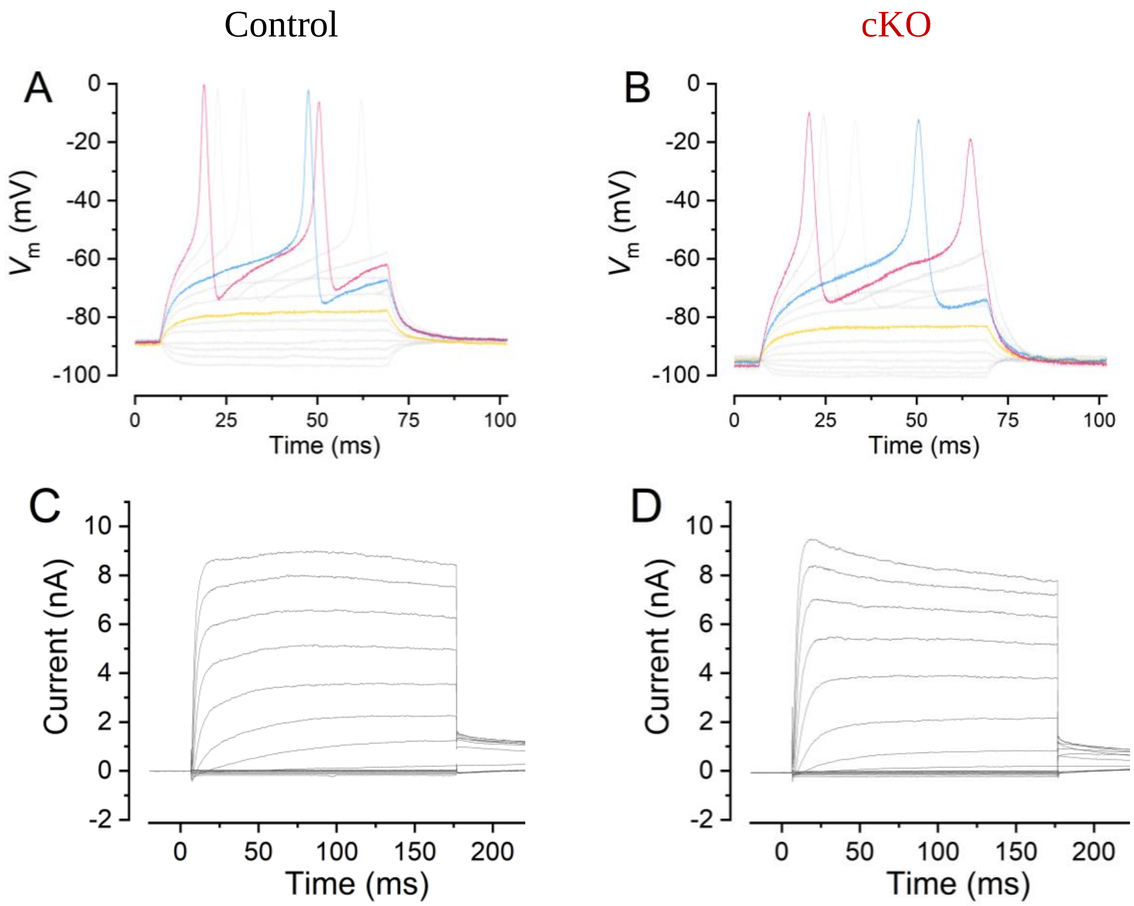

Figure 4.13 Example traces of electrophysiological responses in immature IHC. Examples of electrophysiological characteristics from P5 IHCs in A, C) the IHC from a control animal and B, D) from a cKO animal. A) and B) are voltage responses upon different injecting currents (grey). Coloured traces highlight the current steps at +30 pA (yellow), spiking threshold (blue) and +100 pA (magenta). C) and D) are current responses to different voltage steps. The stimulation protocols were similar to those introduced in 2.4.7 (Figure 2.3 and Figure 2.4), with a shorter current-injecting period in the current-clamp protocol (A and B).

Despite having no statistical significance ($p = 0.075$, Student t-test), the IHCs from the cKO animals had a +7 mV depolarization on resting V_m (−85.5±5.7 mV, n = 6 from 5 animals) compared with the IHCs from the control animals (−92.4±4.3 mV, n = 4 from 4 animals; Figure 4.14 A). This depolarization seemed to have a positive relationship with the KO score (Figure 4.14 B), but the linear fitting had no significant trend ($p = 0.11$, ANOVA).

Two of the IHC in the cKO group did not generate induced spikes during current injection up to +100 pA (Figure 4.14 C). After increased the amplitude of injected currents, the induced spike started to appear at +200 pA onward. Except those cells, the rest of the IHCs from cKO animals presented a mean spiking threshold (72.5±0.6 pA, n=4 from 4 animals) in similar range as in the control animals (75±12.9 pA, n=4 from 4 animals). The statistic indicated no difference between the phenotypes with (p = 0.6, Mann-Whitney) or without (p = 0.8, Student t-test) the two outliners. The rest of the spiking characteristics did not report any significancy neither. For both phenotypes, the mean half-width of induced action potentials locates in the same range (control: 4.00±0.65 ms; cKO: 4.11±0.55 ms), similar to which observed in the TMEM16A^{floxed}:Pax2-Cre mice (~4 ms).

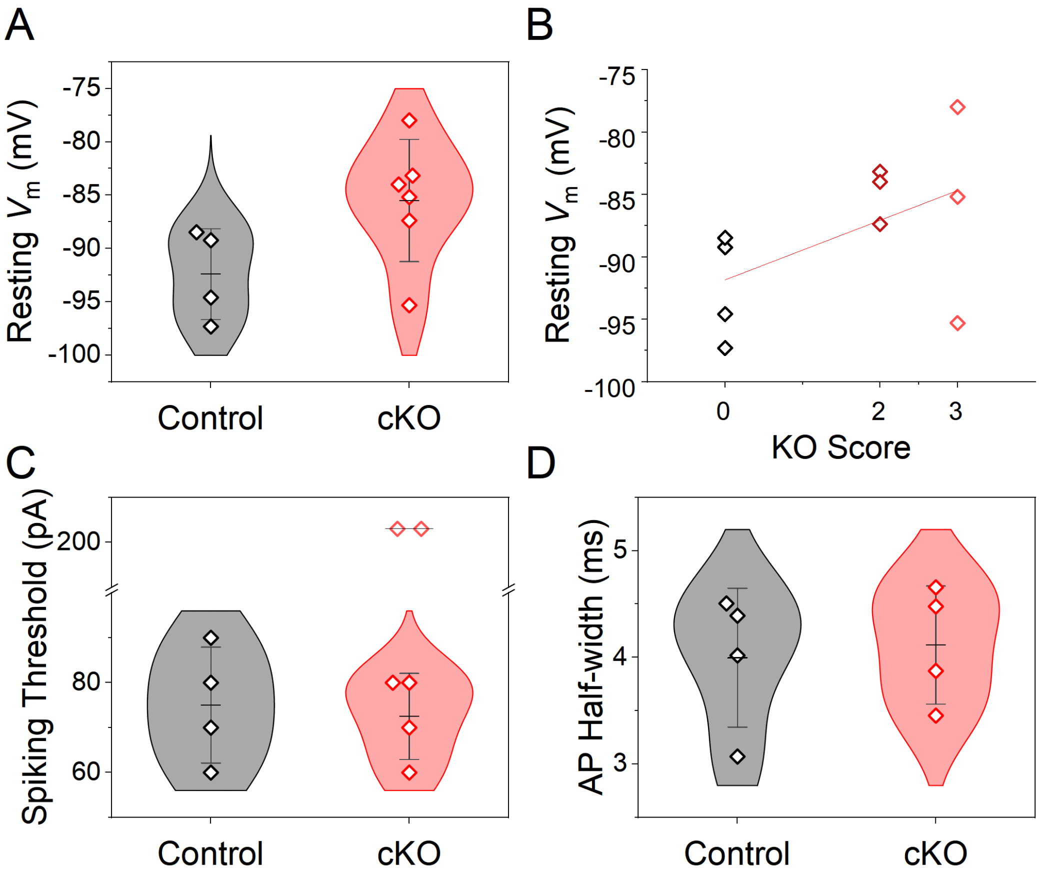

Figure 4.14 No significant changes on excitability of P5-P6 IHC.
The A) membrane potential, C) spiking threshold, and D) half-width of the induced action potential were not different between IHCs from the control (grey) and cKO (red) littermates. B) The resting membrane potential presented potential trend with the increasing KO score (number of the TMEM16A-KO non-sensory cells, introduced in chapter 4.1). Red straight is linear fitting of the data (no significance, p = 0.11, ANOVA). Biological repeats: n = 4 from 4 mice for control and n = 6 from 5 cKO mice for the resting V_m. For the spiking threshold and half-width, it is n = 4 from 4 cKO mice. Since all of the data were normally distributed, the I-box marks the SD of population.

The averaged current traces (Figure 4.15 A) shows a high degree of consistency on the I-V responses between the IHCs from control and cKO animals. The I_{init} was nearly identical between the two phenotypes, while the I_{steady} had more variance when IHCs were held at more depolarized voltages (Figure 4.15 A). Statistics showed no significant difference in the mean of the I_{init} (−194.2±118.0 pA at −25 mV, n = 6 from 5 animals; Figure 4.15 C) or I_{steady} (5.7±1.7 nA at 0 mV, n = 6 from 5 animals; Figure 4.15 B) in IHCs from the cKO animals, compared with the measured current sizes in IHCs from control animals (I_{init}: −216.3±114.5 pA at –25 mv; I_{steady}, 6.2±0.5 nA; n = 4 from 4 animals). The distribution of the column scatter plots (Figure 4.15 B, C) revealed a much larger variance in I_{steady} in the IHC from cKO animals, but this trend does not exist in I_{init}. This trend is very similar to which observed in the TMEM16A^{floxed}:Pax2-Cre mice (chapter 3.2.4). The detailed statistical results are compiled in Appendix 10.

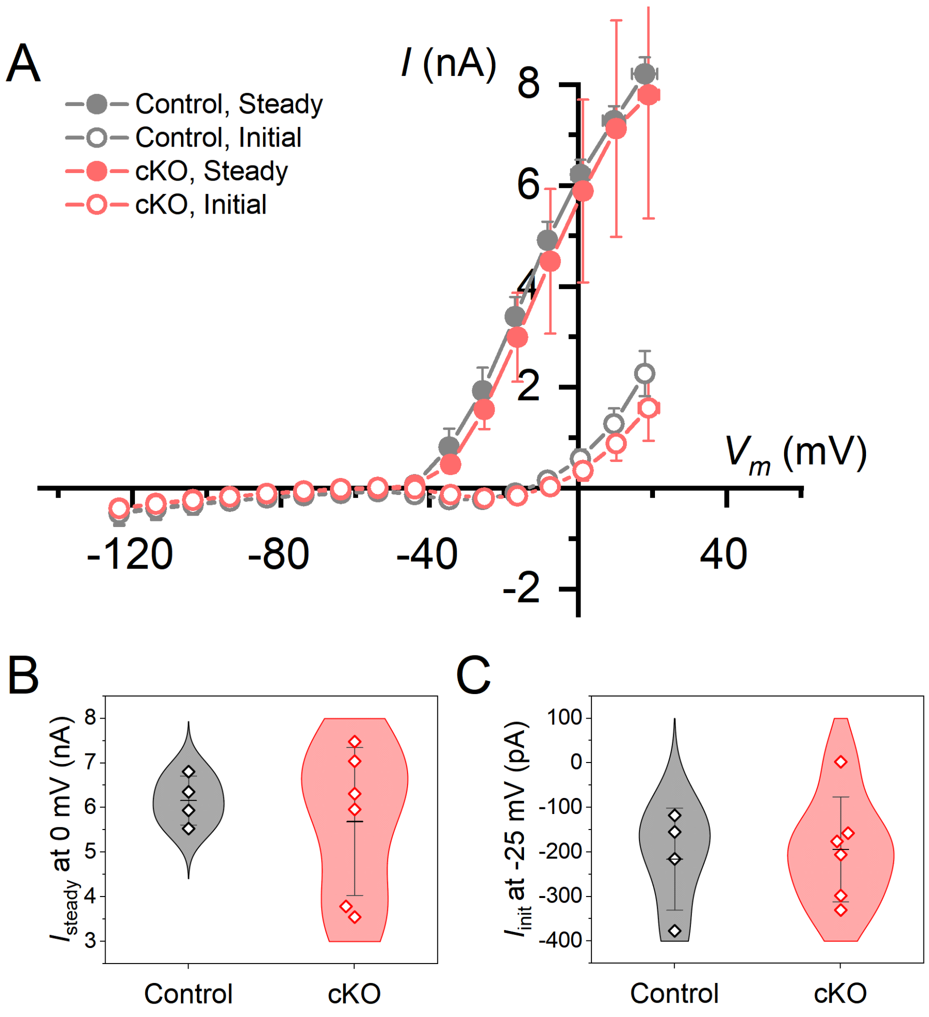

Figure 4.15 No significant changes on current responses of P5-P6 IHC.

A) The averaged initial (open symbol) and steady (filled symbol) I-V responses in the control (grey, 4 cells from 4 mice) and cKO (red, 6 cells from 5 mice) animals, with the error bars marking the SD. Neither B) the steady current nor C) the initial current had statistical difference between the control and cKO animals. Since all of the data were normally distributed, the I-box marks the SD of the population.

4.2.4 Post-hearing electrophysiological properties of IHC reported abnormities

Post-hearing IHCs from P19 to P24 were tested with the same current- and voltage- clamp protocols as used in the immature stage. The IHC from control animals presented a typical fast-acting waveform upon depolarization (Figure 4.16 A). Most of the IHCs from P23-24 cKO animals reported similar voltage response (Figure 4.16 B). However, two of the P24 IHCs displayed a much larger overshoot and oscillation after the depolarization (Figure 4.16 C) which resembles the slow-AP phenotype observed in the ATP-deficient connexin-KO mice (Johnson *et al.*, 2017).

The rapid outward current $I_{\mathrm{K,f}}$ was observed in response of depolarization in most of the P19-P24 IHCs from both phenotypes (Figure 4.16 D, E; yellow traces). However, the IHCs with atypical I-V response (Figure 4.16 C) presented none or very little $I_{\mathrm{K,f}}$, and the I_{steady} was less than halved (Figure 4.16 F). Unlike the TMEM16A^{floxed}:Pax2-Cre model, the $I_{\mathrm{K,n}}$ seemed to be fully developed in the examples from both phenotypes (Figure 4.16 G-I).

The averaged I-V responses of both the I_{steady} and the I_{init} were visibly lower in the IHCs from cKO animals, with a much larger variance observed (Figure 4.17 A, B). As shown in the individual current plotted against time (I-t trace, Figure 4.17 C), two out of five IHCs from the cKO animals did not present the fast initial current, and their size of the I_{steady} varied a lot compared with the control IHCs. Normalized to their tail current, the slow dynamics in the two samples were clearly revealed, while the other three presented similar ratio of $I_{\mathrm{K,f}}/I_{\mathrm{tail}}$ as the control samples (Figure 4.17 D).

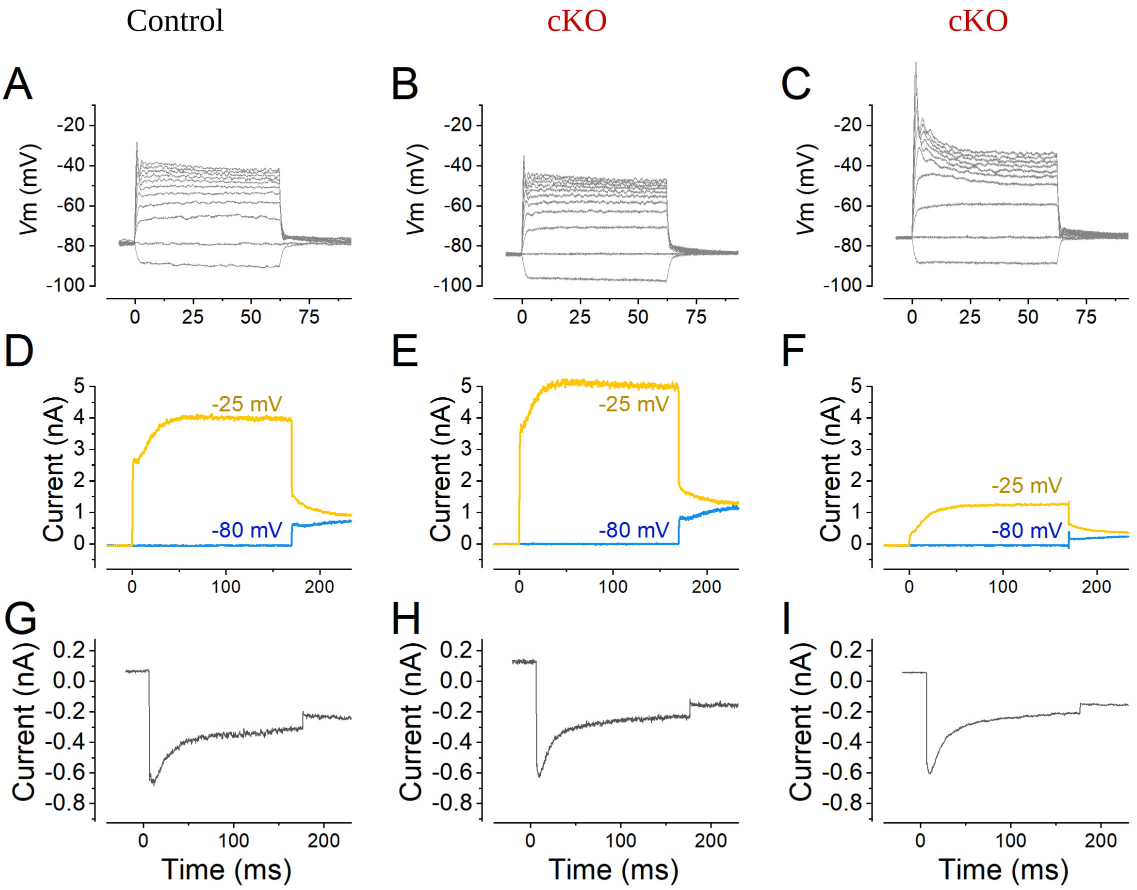

Figure 4.16 Immature phenotype detected in post-hearing IHCs

A-C) Voltage responses upon current stimulation from the IHCs from a control (left column) and cKO (centre and right column) animals. The cKO sample at the right panel presented atypical waveforms. D-E) Current responses with the basic voltage clamp protocol (described in 2.4.7). Only two voltage steps, -25 mV (yellow) and -80 mV (blue) were showed for a clearer comparison. The cKO sample at the right panel had a dramatically reduced $I_{K,f}$. G-I) $I_{K,n}$ measured with specialized voltage clamp protocol (described in 2.4.7).

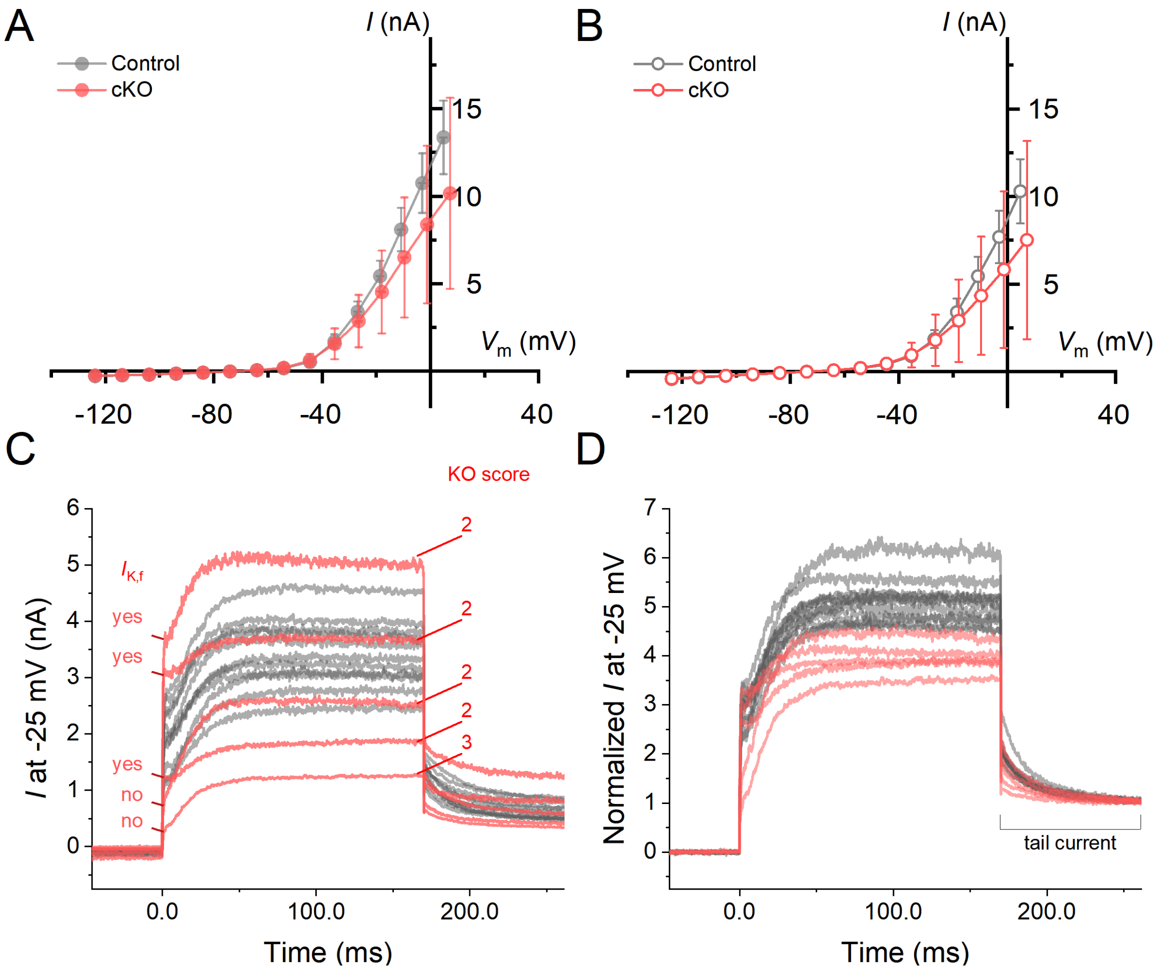

Figure 4.17 Some of the IHCs from cKO animals did not present mature-type current. A) Averaged I-V responses of the whole cell steady state current from -124 mV to +10 mV. The IHCs from control (solid grey circle) and the cKO (solid red circle) animals had very similar results. B) I-V responses of the initial current (region of $I_{K,f}$) from -124 mV to +10 mV. There was no significant difference between the IHCs from control (open grey circle) and the cKO (open red circle) animals, but the I_{init} in the IHCs from cKO animals had a much larger variance towards positive voltages. C) Individual whole-cell current upon -25 mV voltage step was plotted against recording time, with control samples in grey and cKO samples in red. D) The traces from C) normalized to the size of the tail current.

Despite the strong phenotype presented in individual recordings, statistical results did not find any significance between the control and the cKO animals in all of the mature-type currents and the resting V_m (Figure 4.18). The I_{steady} and I_{init} seemed to be more variant in the IHCs from the cKO animals compared with the controls (Figure 4.18 A, B), but the sample number was not ideal to test this observation. I prefer not to draw conclusion here and will leave the detailed figures in the Appendix 11.

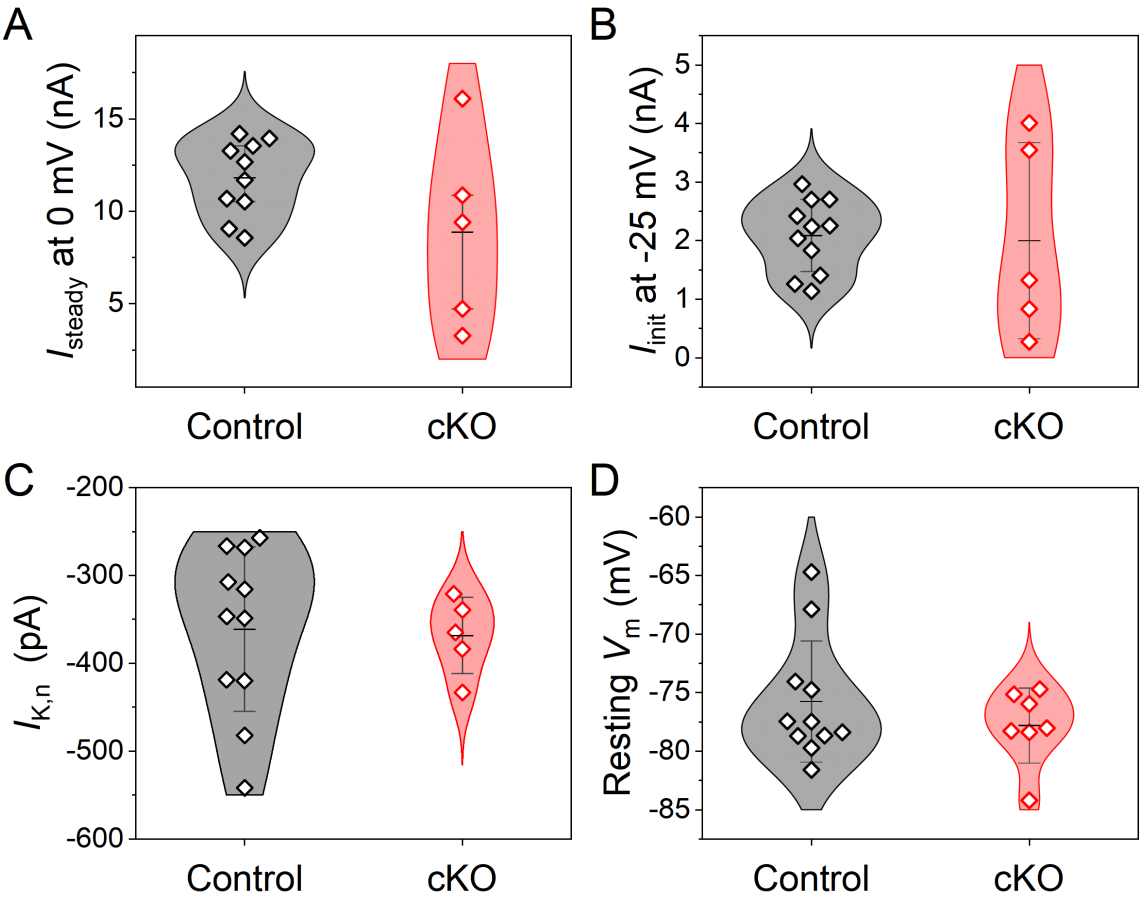

Figure 4.18 Statistics of electrophysiological properties in P19-P23 IHCs

The distribution of A) I_{steady}, B) I_{init}, C) $I_{K,n}$, and D) resting V_m did not show any statistical difference between the IHCs from control (grey) and cKO (red) animals. The control IHCs were from P19 and P23 animals, and the cKO IHCs were from P23-24 The I-box marks the 25% and 75% percentile in A) and the SD in the rest of the plots. The detailed statistical quantities were compiled in Appendix 11.

4.3 Discussion

4.3.1 Adjacent non-sensory cells are critical for the K^+ clearance near IHCs

One of the purposes for using the TMEM16A^{floxed}:Plp1-Cre^{ERT} model is to investigate whether all of the cells participate in GER calcium wave are important to the SAPs in the IHCs. The results suggests that the adjacent non-sensory cells, namely the inner-phalangeal cells and the border cell, are critical and enough for delivering the TMEM16A-mediated modulation on SAPs during GER calcium waves.

Plp1-Cre^{ERT}-driven TMEM16A cKO seemed to create a more distinctive and consistent atypical phenotype compared with the TMEM16A^{floxed}:Pax2-Cre. TMEM16A KO in both of the inner phalangeal cells, or all of the adjacent cells made the affected IHC lost their capability of firing high frequency bursts (> 10 Hz, Figure 4.5 B). In contrast, the IHC with TMEM16A KO in only 1 inner phalangeal cell produced a spiking pattern that was almost identical to the general observation from control animals (Figure 4.5). The cumulative distribution of the ISI from SAPs showed a significant shift towards longer intervals (Figure 4.6 B).

Three out of six IHCs from the cKO animals fired SAP only during the period with drifting baseline (Figure 4.3), which I interpreted as an event from hyperpolarising V_m. Interestingly, one of them produced saturated spiking followed by depolarization (Figure 4.4), similar to the phenotype in SK2-KO IHC (Figure 3.21). Both phenotypes were signs of accumulating $[K^+]_e$, as discussed in 3.3.2 and 3.3.3. These phenotypes imply a higher chance that the modulation from TMEM16A-mediated events to be the K^+ clearance. However, it can only be confirmed after the source of these baseline shift being identified.

Moreover, the benefit of knowing precise cKO in TMEM16A^{floxed}:Plp1-Cre^{ERT} model revealed that the repolarising power provided by K^+ clearance might be positively correlate with the number of functioning non-sensory cells (defined as KO score in chapter 4.1). The IHCs that spiked only in hyperpolarization all had a KO score of 3, while the rest of the IHCs with KO score 1 or 2 all produced SAPs with or without the hyperpolarization. Further analysis on those non-significant statistical quantities of ISI (Figure 4.7) revealed an increasing trend between the KO score and the mean, median, and maximum ISI (Figure 4.19 A, B, D). This trend was also found in the resting V_m of immature IHCs (Figure 4.14 B), where IHCs with KO score 3 were more depolarized than the one with KO score 2 and 0 (control). As lacking repetition number could easily be the reason of no statistical significance in this case, I feel these “trends” are worth mentioning and not to be neglected.

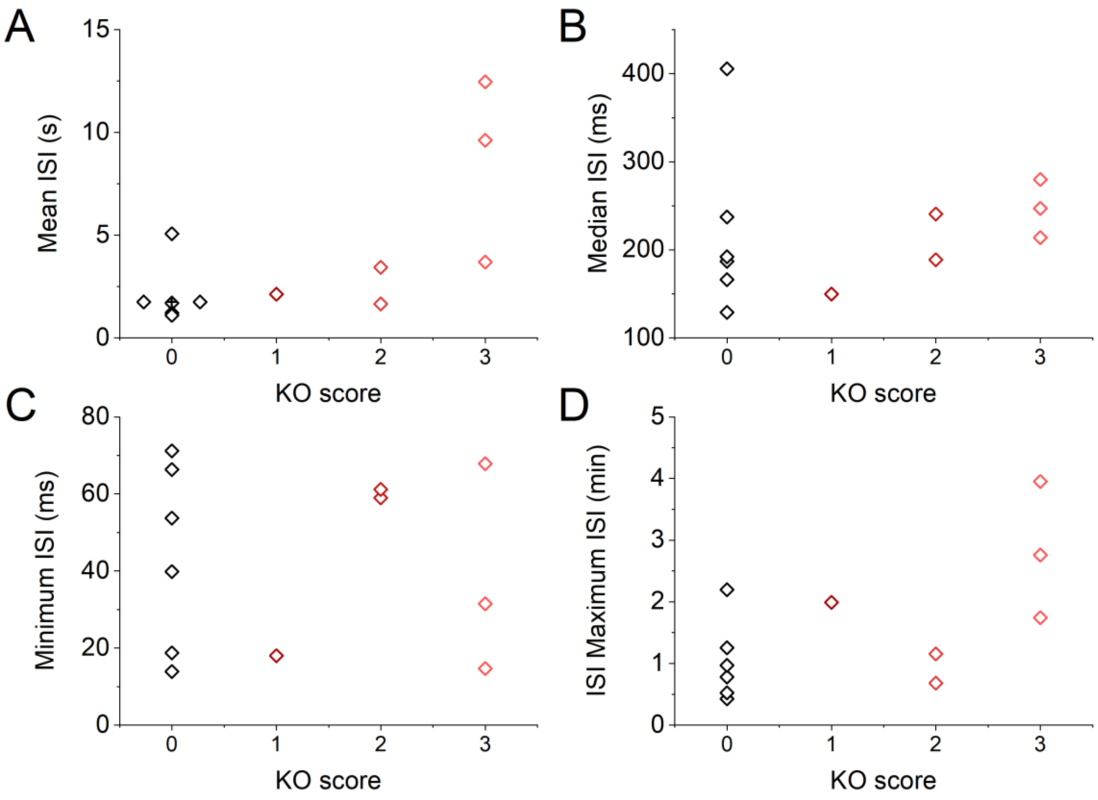

Figure 4.19 Potential trend on ISI quantities with KO score of the recording
The A) mean, B) median, C) minimum, and D) maximum ISI from the control (black) and the cKO (red) animals plotted against their KO score.

Considering the mechanism of the K^+ clearance hypothesis depends on the capability of the nonsensory cells to 1) efflux of water and Cl^- ions, 2) expand the extracellular space and dilute the $[K^+]_e$, 3) uptake the excessive K^+. It is reasonable for the phenotype of TMEM16A cKO animals to be correlated with the KO score. Nevertheless, these observations can also be interpreted in a different way. It is possibile that border cells are more important than the inner-phalangeal cells on mediating the K^+ clearance. In fact, a study suggested border cells might play a major role on initiating the GER calcium waves and uptaking the fluid near IHCs (Dayaratne *et al.*, 2015). Nevertheless, my data cannot confirm this hypothesis. Although the atypiical phenotypes (mostly silent) were only observed when TMEM16A were KO in the border cell, it could be the result of higher resting V_m due to the dose-dependency. More samples with only one functioning inner phalangeal cell are needed to draw a final conclusion on this topic.

4.3.2 Synchronization between IHCs in the TMEM16A^{floxed}:Plp1-Cre^{ERT} model

Due to a failed induction (reason unidentified), most of the samples in the calcium imaging were from control mice and the 4 cKO samples were all from the same mouse. Nevertheless, the correlation coefficient between adjacent IHCs during individual calcium waves still showed a dramatic reduction in the cKO mice (0.077, n = 84 waves from 1 animal) compared with the control mice (0.202, n = 328 waves from 5 animals; p = 4e-5, Mann-Whitney; Figure 4.11). Interestingly, the reduced correlation seemed to be limited within 1-cell apart unlike the wide-spread influence in the TMEM16A^{floxed}:Pax2-Cre mice. Except for the bias from insufficient sample number, two potential factors might cause this difference. The first one is that the average induction rate of the Plp1-Cre^{ERT} is around 51±28% with a tonotopical decrease toward the apex (n = 6 animals, sampled 4-10 kHz region). An innate variance on correlation is inevitable with this induction rate. Following that, the second reason is that the majority of GER non-sensory cells still maintained TMEM16A activity. The uptake-surge of extracellular K^+ during larger calcium waves might still be able to promote the diffusion of $[K^+]_e$ and thus synchronize the IHCs within coverage. An observation to support this assumption is that the IHCs with KO score 3 only fired SAP during hyperpolarizing baseline periods (Figure 4.3). Although, as discussed in 3.3.4, the origin of the hyperpolarization during the cell-attached recording has not been identified, the remaining TMEM16A activity in the GER is a logical source of generating such event.

4.3.3 Plp1-driven TMEM16A cKO seemed to impair the maturation of IHC

The electrophysiological properties of the immature IHCs in TMEM16A^{floxed}:Plp1-Cre^{ERT} model were similar to the observation in the TMEM16A^{floxed}:Pax2-Cre model, with mostly similar characteristics but a more depolarized resting V_m. Further details are discussed of this depolarization in 3.3.2.

As for the maturation of electrophysiological properties, TMEM16A^{floxed}: Plp1-Cre^{ERT} model produced a mixed result with both mature-type and immature-type currents observed in post-hearing IHCs from P19 to P24, similar to the results in the TMEM16A^{floxed}:Pax2-Cre model. I will leave the comparison between models to the general discussion and focus on the results from TMEM16A^{floxed}: Plp1-Cre$^{\mathrm{ERT}}$ mice first.

Three out of five P23 IHCs from the cKO mice acquired mature-type current $I_{\mathrm{K,f}}$. In the meantime, the rest two IHCs presented only the slow current at the beginning of depolarizing steps (Figure 4.17 B, C). Although the statistical result did not present significance on the mean size of the $I_{\mathrm{K,f}}$ between the control and the cKO animals (Figure 4.18), it is probably due to insufficient sample number. The lack of fast current is quite distinctly visible from the current trace as a function of recording time (Figure 4.17 C). Interestingly, all of the matured IHCs had TMEM16A KO in only inner-phalangeal cells but not the border cell (KO score 2). This might be interpreted as that the modulation of TMEM16A-mediated events from adjacent border cell is enough to drive the acquisition of $I_{\mathrm{K,f}}$. However, this interpretation was disproved by one of the two IHCs lacking $I_{\mathrm{K,f}}$ also being KO score 2. With insufficient sample number, I cannot draw conclusion on whether the chance of impaired $I_{\mathrm{K,f}}$ increases with the KO score.

One thing that can be deducted from the data is that the impaired $I_{\mathrm{K,f}}$ phenotype is unlikely to be the consequences of lacking high frequency (> 10 Hz) bursts (Figure 4.5), because most of the IHCs with KO score 2 or 3 presented similar firing pattern. These high frequency bursts might be more important for synaptic pruning, which happens around P4-P8 (reviewed in Coate *et al.*, 2019). Providing that the spike-time dependent model (Bi & Poo, 1998) applies to the ribbon synapses, higher firing rate would favours the consolidation of the synapse as it is more likely to induce a successful spike in the post-synaptic cell. Unfortunately, due to the impact of COVID, I did not have the time nor the resources to finish the investigation on the development of ribbon synapses.

In addition to the $I_{\mathrm{K,f}}$, the steady-state current seemed to be affected as well (Figure 4.17 A), with a smaller averaged size and a much larger variance. The overall statistics reported no significance on the I_{steady} between the control and the cKO animals (Figure 4.18 A), but the normalized traces showed that the cKO animals generally had a slightly smaller value of $I_{\mathrm{steady}}/I_{\mathrm{tail}}$ compared with the control animals (Figure 4.17 D). It requires more repeats to confirm whether this trend is part of the impaired phenotype or simple being an unfortunate sampling.

Chapter 5 General discussion

5.1 Silent P5-P6 IHC only found in TMEM16A^{floxed}:Pax2-Cre mice

Around one third (8 out of 23) of IHC from TMEM16A^{floxed}:Pax2-Cre mice did not produce any spiking activities. However, this silent phenotype was not observed in any of the IHCs (n = 5) from TMEM16A^{floxed}:Plp1-Cre$^{\mathrm{ERT}}$ mice. Despite the suboptimal sample number, I believe these are representative observations in each model.

In the TMEM16A^{floxed}:Plp1-Cre$^{\mathrm{ERT}}$ mice, most of the IHC with KO score 3 remained in silence throughout most of the recordings, and spiked only when there was a hyperpolarizing period. The source of these hyperpolarizing periods, though not confirmed, is probably the remaining K^+ clearance activity during the GER calcium waves. With a wider TMEM16A KO area in the GER, this event is likely to be very limited in the TMEM16A^{floxed}:Pax2-Cre mice and hence the completely silent phenotype.

5.2 Resting V_m seemed to be higher in both models

Surprisingly, I did not find obvious depolarization of resting V_{m} in the immature IHCs from TMEM16A^{floxed}:Pax2-Cre mice (Figure 3.14 A), as described in the literature (Wang & Bergles, 2015). The resting V_{m} were almost identical between the cKO and control (Figure 3.15 A). On the contrary, TMEM16A^{floxed}:Plp1-Cre$^{\mathrm{ERT}}$ mice produced quite distinct depolarizations in all but one of the IHCs with a KO score of 2 or 3 (Figure 4.14 A, B). The phenotype of the TMEM16A^{floxed}:Pax2-Cre animal were decided by genotyping and the immune labelling of TMEM16A in contralateral cochlea. As I only processed the cKO samples with a few controls for reference, I cannot confirm the real phenotype of those outliers with a more depolarized resting V_{m}.

Besides the difference between the models, there was a near 15 mV hyperpolarization on the resting V_{m} (*mean*: −86.5±5.7 mV, n=26 cells from both model) compared with previously reported value (−65 to −70 mV; Johnson *et al.*, 2011) at similar age with almost identical experimental setup. I could not think of any mechanism to account for the difference between published data, but the collected data should be reliable because the data range in

TMEM16A^{floxed}:Plp1-Cre$^{\mathrm{ERT}}$ mice (−97.3 to −78 mV, *Mdn* = −88.25) was similar to which in TMEM16A^{floxed}:Pax2-Cre (−95.8 to −78.1 mV, *Mdn* = −88.7), indicating that they are sampled from the same pool of phenotypes.

5.3 SAP characteristics were slightly different

The burst patten of ISI graph in TMEM16A^{floxed}:Pax2-Cre (Figure 3.5) produced a nearly identical mapping of the spiking dynamics between the control and the cKO animals. In contrast, the cKO animals in TMEM16A^{floxed}:ROSA-tdTomato:Plp1-Cre$^{\mathrm{ERT}}$ cKO model (excluding KO score 1) had a burst pattern completely lacks high frequency bursts (> 10Hz, Figure 4.5). Because it took both the border and an inner-phalangeal cells to produce a control-like burst pattern in the IHC with KO score 1, the most likely reason to explain this difference is that TMEM16A^{floxed}:Pax2-Cre failed to produce a clean KO of TMEM16A (discussed in 3.3.1). The incomplete KO also reflected on the different distribution of the mean ISI, which represents the amount of longer ISIs in the recording. The mean ISI in cKO IHCs from TMEM16A^{floxed}:Plp1-Cre$^{\mathrm{ERT}}$ animals presented a much longer mean ISI range (25-75% = 2.1 to 9.6 s; Figure 4.7 A), compared with the control animals and both phenotype in TMEM16A^{floxed}:Pax2-Cre animals (all with 25-75% around 1.2 to 2-3 s; Figure 3.7 A & Figure 4.7 A).

The incomplete TMEM16A KO in TMEM16A^{floxed}:Pax2-Cre mice also influenced IHC's capability of generating longer bursts. In the cKO animals from TMEM16A^{floxed}:ROSA-tdTomato:Plp1-Cre$^{\mathrm{ERT}}$ model, the number and length of longer bursts was highly supressed (Figure 4.8). In comparison, although the IHCs from TMEM16A^{floxed}:Pax2-Cre animal tended to have fewer long bursts, but length of continuous burst firing was longer in some occasion (Figure 3.8 A, C, F). My hypothesis on this difference is that the incomplete TMEM16A KO in TMEM16A^{floxed}:Pax2-Cre depolarized the IHCs but provided certain amount of K^+ clearance at the same time, and turned out to stimulate the IHCs to produce longer mid-range bursts upon calcium waves.

Compared with the TMEM16A^{floxed}:ROSA-tdTomato:Plp1-Cre$^{\mathrm{ERT}}$ cKO mode, these different observations on the SAP characteristics in the TMEM16A^{floxed}:Pax2-Cre animals are unlikely to be a result of mixed induction rate in the cKO samples. If that was the case, the distribution of data should present a similar range as in the control group, instead of a shift on the distribution. Based on this rationale, I believe the difference observed in these two models are both real, and not conflicting to each other.

5.4 Source of the positive currents in cell-attached recording

During cell-attached recording of SAP, different size of positive-going currents were often observed in IHCs from both the control and the cKO animals, as shown in the example traces (Figure 3.4, Figure 3.20, Figure 4.3, Figure 4.4). I interpreted these events as the hyperpolarizing current under the influence of K^+ clearance during the calcium waves (3.3.2 and 3.3.3). However, senior members in the lab reminded me that this event might also be caused by unstable seal resistance. If the seal resistance became larger, or the patch resistance became smaller, larger amplifier current will route through the cell, causing depolarization and change the spiking rate (Perkins, 2006).

When cell-attached recordings were set with a holding voltage at 0 mV and at not zero current, the injecting current from the amplifier (I_{amp}) could be a biasing factor to the firing rate. This limitation on experimental design needs to be highlighted in this study. Before resolving the source of the baseline shift, the interpretation of the baseline being an aftereffect of K^+ modulation should be treated as a hypothesis.

It would not be very feasible to exclude the area of baseline shift from statistics, as most of the data had small shifting baseline in over half of the recording period (Figure 4.2). Also, defining the filtering threshold of the shifts would be an arbitrary factor. A pharmaceutical study is a better way to test whether the shifts are a phenotype in the TMEM16A cKO animals. Comparing the recording before and after the TMEM16A blocker should provide good evidences on the involvement of TMEM16A-mediated K^+ modulation in firing rate modulation.

Al though I cannot provide a definite conclusion with the data on hand, there is a way to estimate whether these observations could be artefacts. I filtered the SAP recordings with 5 Hz low pass Gaussian filter to extract and examine the baseline shifts. The hypothesis is: the shifts should be homogeneously observed among the control and cKO animals if they were to be artefacts.

In all of the recorded 51 IHCs from both the control and cKO animals in both models, only 2 IHCs from TMEM16A$^{\text{floxed}}$:Pax2-Cre cKO mice did not present any positive baseline (hyperpolarising; Figure 5.1 A). These IHCs both did not present any spike, and had a slightly negative baseline current instead. Near half of the rest of the IHCs from cKO animals (8 out of 19 cells) had large positive-going baseline currents like shown in the example recordings Figure 3.4, Figure 4.3.

The others only presented very small (2-5 pA) positive baseline current with occasional larger peaks less than 20 pA (similar to Figure 3.3 D), which also is the phenotype in the majority of IHCs in the control animals (15 out of 16 cells). This difference on large positive-going currents is significant between the IHCs from the control and the cKO animals ($p = 0.022$, Fisher's Exact Test).

Similar trend was also found in the TMEM16A$^{\text{floxed}}$:Plp1-Cre model with 50% (3 out of 6) of the IHCs from cKO animals producing large positive currents. However, this trend had no statistical difference comparing with the control IHCs (1 out of 6; Figure 5.1 B), likely due to low sample numbers. Interestingly, all of them had KO score of 3 (all of the adjacent non-sensory cells had TMEM16A KO) and spiked only during the positive current periods.

Assuming the instability of the giga-seal is a stochastic event, the distribution of the large positive currents should be equally distributed among all of the samples. On the contrary, the rough observation on the baseline current revealed a significant difference of the observation of larger positive currents (> 50 pA) in the TMEM16A cKO genotype (p = 0.022; Fisher's Exact test; excluded the two samples without baseline stray). Based on this observation, the baseline shifts have a low probability to be artefacts, but they definitely require further investigation to identify the source and to prevent the observed firing rate being biased by I_{amp}.

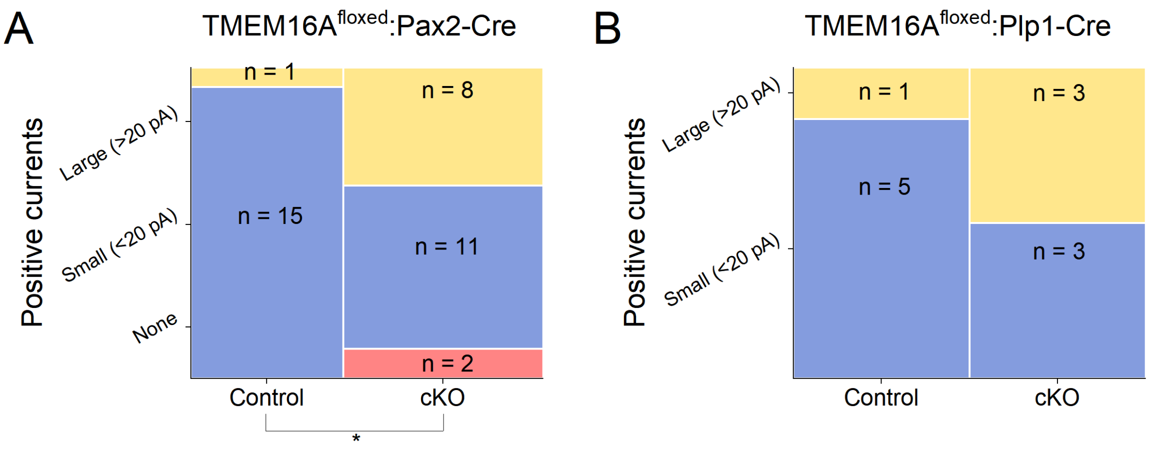

Figure 5.1 Positive currents during cell-attached recordings were larger in cKO animals. A rough categorization of positive-going baseline currents during SAP recordings from A) TMEM16A^{floxed}:Pax2-Cre mice and B) TMEM16A^{floxed}:Plp1-Cre mice. The size of the positive (hyperpolarizing) current were categorized as large (> 20 pA, yellow), small (< 20 pA) or none (no red) with the maximum size of the baseline currents.

5.5 How does TMEM16A affect the maturation of IHC?

In TMEM16A^{floxed}:Pax2-Cre model, the cKO IHCs seemed to remain immature at P17, with smaller $I_{K,f}$ and $I_{K,n}$ in some of the samples. However, these currents became fully matured after a week in IHCs at P24 (Figure 3.18). On the contrary, although three out of five IHCs presented normal $I_{K,f}$, the rest two IHCs from cKO TMEM16A^{floxed}:Plp1-Cre^{ERT} mice had very little $I_{K,f}$ even at P24 (Figure 4.17 C). Since there was no cKO samples from mice younger than P20, I cannot confirm whether this observation is a delayed development like which observed in the TMEM16A^{floxed}:Pax2-Cre mice (Figure 3.18 E). In addition, the size of I_{steady} seemed to be smaller in TMEM16A^{floxed}:Plp1-Cre^{ERT} mice (Figure 4.18 A) than in the TMEM16A^{floxed}:Pax2-Cre mice (Figure 3.18 A). These results indicate that TMEM16A KO might actually affect the development of IHCs after all, and that the deductions on the maturation drawn from the TMEM16A^{floxed}:Pax2-Cre model in my study and Maul *et al.* (2022) might have been biased by the incomplete TMEM16A cKO (discussed in 3.3.1).

Two possible models can be drawn to explain how TMEM16A cKO can affect the development of IHCs. The first mechanism is through modulating the SAP, as introduced in 1.3.4. I have discussed why high frequency bursts (>10 Hz) are probably not the target in 4.3.3. Nevertheless, mid-range bursts around 4 Hz remained active in three out of five IHCs from cKO TMEM16A^{floxed}:Plp1-Cre$^{\mathrm{ERT}}$ mice (Figure 4.5), while the rest two IHCs seemed to struggle on generating steady bursts and only fired sparse spike doublets even during the hyperpolarizing periods. This phenotype was also observed in one of the SAP recordings from TMEM16A^{floxed}:Pax2-Cre animal. If the sparse firing is representative to the SAP pattern in those IHCs, it could be the factor to cause the impaired $I_{\mathrm{K,f}}$ phenotypes. However, this cannot address why the TMEM16A^{floxed}:Pax2-Cre mice gain all their mature-type currents at P24 but not the TMEM16A^{floxed}:Plp1-Cre$^{\mathrm{ERT}}$ mice.

Another hypothesis is that the KO of TMEM16A affected the development through the depolarized resting V_{m}. Because the *in vivo* resting V_{m} was predicted to be around the threshold of I_{Ca} during the second postnatal week (Corns *et al.*, 2018; Corns, Johnson, *et al.*, 2014), the depolarization from TMEM16A cKO would constantly activate an extra fraction of I_{Ca} set the baseline calcium to a higher level. On the other hand, a raised resting V_{m} might also undermine the calcium influx from the P2XR during calcium waves. This model could explain the delayed maturation in the TMEM16A^{floxed}:Pax2-Cre mice. The remaining small TMEM16A activity form incomplete KO would eventually clear the high $[\mathrm{K}^+]_{\mathrm{e}}$ and bring the resting V_{m} back, it just takes longer. In this manner, required changes or checkpoints could still be made and the IHCs eventually became fully matured. Based on this model, the IHCs with KO score 3 in TMEM16A^{floxed}:Plp1-Cre$^{\mathrm{ERT}}$ model had no active non-sensory cells to clear repolarize the resting V_{m} and thus failed to gain mature-type currents at P24. However, this critical evidence is assumed from a single observation and thus definitely needs further repeats.

5.6 Conclusion and future perspectives

Both of the cKO models provided evidence towards K^+ clearance as the mechanism of TMEM16A-mediated event from GER calcium waves. Disrupt TMEM16A led to a depolarized resting V_{m} in IHCs and hindered the burst firing. However, the effect of the TMEM16A KO was biased too much by the Cre-induction rate of a particular sample and thus created a lot of variances. Using TMEM16A-inhibitor within the same recording as an internal negative control could be a good way to testify the data in future studies.

SAP might not be as important as considered in the development of IHC, because the silent or near-silent IHCs were found in the cKO animals of both models, but most of the IHCs acquired mature-type current sooner or later. ATP from the GER alone is likely to be enough to regulate the maturation of the IHCs. During calcium waves, the calcium influx in the IHC from the P2XR might be sufficient to activate the calcium-dependent gene expression.

Although not being investigated in my study, the boosting of SAPs from TMEM16A-mediated K^+ release is undoubtfully more important in promoting transmitter release to consolidates the ribbon synapses and on synchronizing the activity between IHCs to structure a sharp tonotopic innervation (Babola *et al.*, 2018; Clause *et al.*, 2014; Maul *et al.*, 2022). The investigation on the development of ribbon synapses and the de-efferent around the hearing onset is required to really delineate the role of the modulation from GER calcium waves.

Bibliography

Ahmad, S., Tang, W., Chang, Q., Qu, Y., Hibshman, J., Li, Y., Söhl, G., Willecke, K., Chen, P., & Lin, X. (2007). Restoration of connexin26 protein level in the cochlea completely rescues hearing in a mouse model of human connexin30-linked deafness. *Proceedings of the National Academy of Sciences of the United States of America*, *104*(4), 1337–1341. https://doi.org/10.1073/pnas.0606855104

Anselmi, F., Hernandez, V. H., Crispino, G., Seydel, A., Ortolano, S., Roper, S. D., Kessaris, N., Richardson, W., Rickheit, G., Filippov, M. A., Monyer, H., & Mammano, F. (2008). ATP release through connexin hemichannels and gap junction transfer of second messengers propagate Ca2+ signals across the inner ear. *Proceedings of the National Academy of Sciences of the United States of America*, *105*(48), 18770–18775. https://doi.org/10.1073/pnas.0800793105

Babola, T. A., Kersbergen, C. J., Wang, H. C., & Bergles, D. E. (2020). Purinergic signaling in cochlear supporting cells reduces hair cell excitability by increasing the extracellular space. *ELife*, *9*, e52160. https://doi.org/10.7554/eLife.52160

Babola, T. A., Li, S., Gribizis, A., Lee, B. J., Issa, J. B., Wang, H. C., Crair, M. C., & Bergles, D. E. (2018). Homeostatic Control of Spontaneous Activity in the Developing Auditory System. *Neuron*, *99*(3), 511-524.e5. https://doi.org/10.1016/j.neuron.2018.07.004

Békésy, G. V. (1960). *Experiments in Hearing*. McGraw-Hill.

Beltramello, M., Piazza, V., Bukauskas, F. F., Pozzan, T., & Mammano, F. (2005). Impaired permeability to Ins(1,4,5)P3 in a mutant connexin underlies recessive hereditary deafness. *Nature Cell Biology*, *7*(1), Article 1. https://doi.org/10.1038/ncb1205

Berglund, A. M., & Ryugo, D. K. (1987). Hair cell innervation by spiral ganglion neurons in the mouse. *Journal of Comparative Neurology*, *255*(4), 560–570. https://doi.org/10.1002/cne.902550408

Berridge, M. J., Lipp, P., & Bootman, M. D. (2000). The versatility and universality of calcium signalling. *Nature Reviews. Molecular Cell Biology*, *1*(1), 11–21. https://doi.org/10.1038/35036035

Beutner, D., & Moser, T. (2001). The Presynaptic Function of Mouse Cochlear Inner Hair Cells during Development of Hearing. *Journal of Neuroscience*, *21*(13), 4593–4599. https://doi.org/10.1523/JNEUROSCI.21-13-04593.2001

Bi, G., & Poo, M. (1998). Synaptic Modifications in Cultured Hippocampal Neurons: Dependence on Spike Timing, Synaptic Strength, and Postsynaptic Cell Type. *Journal of Neuroscience*, *18*(24), 10464–10472. https://doi.org/10.1523/JNEUROSCI.18-24-10464.1998

Bock, G., Gebhart, M., Scharinger, A., Jangsangthong, W., Busquet, P., Poggiani, C., Sartori, S., Mangoni, M. E., Sinnegger-Brauns, M. J., Herzig, S., Striessnig, J., & Koschak, A. (2011). Functional Properties of a Newly Identified C-terminal Splice Variant of Cav1.3 L-type Ca2+ Channels. *Journal of Biological Chemistry*, *286*(49), 42736–42748. https://doi.org/10.1074/jbc.M111.269951

Boettger, T., Rust, M. B., Maier, H., Seidenbecher, T., Schweizer, M., Keating, D. J., Faulhaber, J., Ehmke, H., Pfeffer, C., Scheel, O., Lemcke, B., Horst, J., Leuwer, R., Pape, H.-C., Völkl, H., Hübner, C. A., & Jentsch, T. J. (2003). Loss of K-Cl co-transporter KCC3 causes deafness, neurodegeneration and reduced seizure threshold. *The EMBO Journal*, *22*(20), 5422–5434. https://doi.org/10.1093/emboj/cdg519

Brandt, A., Striessnig, J., & Moser, T. (2003). CaV1.3 channels are essential for development and presynaptic activity of cochlear inner hair cells. *The Journal of Neuroscience: The Official Journal of the Society for Neuroscience*, *23*(34), 10832–10840.

Brockmann, L. C. A. (2009). *.mw-parser-output .tracked{float:right;clear:right;border:1px solid #999;border-radius:2px;background-color:#eee;font-size:85%;text-align:center;padding:0.5em;margin-left:1em;margin-bottom:1em;width:12em;color:black}.mw-parser-output .tracked p{margin:0}.mw-parser-output .tracked-url{font-weight:bold}.mw-parser-output .tracked .status,.mw-parser-output .tracked-status{font-weight:bold;text-transform:uppercase}.mw-parser-output .tracked .status.resolved,.mw-parser-output .tracked-resolved{color:green}.mw-parser-output .tracked .status.critical,.mw-parser-output .tracked-critical{color:red;font-size:1.5em}Tracked in PhabricatorTask T201207OpenEnglish: A diagram of the anatomy of the human ear*. Perception Space—The Final Frontier, A PLoS Biology Vol. 3, No. 4, e137 doi:10.1371/journal.pbio.0030137 (Fig. 1A/Large version), vectorised by Inductiveload. https://commons.wikimedia.org/wiki/File:Anatomy_of_the_Human_Ear.svg

Burda, H., & Branis, M. (1988). Postnatal development of the organ of Corti in the wild house mouse, laboratory mouse, and their hybrid. *Hearing Research*, *36*(1), 97–105. https://doi.org/10.1016/0378-5955(88)90140-2

Burnstock, G. (2007). Physiology and Pathophysiology of Purinergic Neurotransmission. *Physiological Reviews*, *87*(2), 659–797. https://doi.org/10.1152/physrev.00043.2006

Burton, Q., Cole, L. K., Mulheisen, M., Chang, W., & Wu, D. K. (2004). The role of Pax2 in mouse inner ear development. *Developmental Biology*, *272*(1), 161–175. https://doi.org/10.1016/j.ydbio.2004.04.024

Catalán, M. A., Kondo, Y., Peña-Munzenmayer, G., Jaramillo, Y., Liu, F., Choi, S., Crandall, E., Borok, Z., Flodby, P., Shull, G. E., & Melvin, J. E. (2015). A fluid secretion pathway unmasked by acinar-specific Tmem16A gene ablation in the adult mouse salivary gland. *Proceedings of the National Academy of Sciences of the United States of America*, *112*(7), 2263–2268. https://doi.org/10.1073/pnas.1415739112

Ceriani, F., & Mammano, F. (2012). Calcium signaling in the cochlea – Molecular mechanisms and physiopathological implications. *Cell Communication and Signaling : CCS*, *10*, 20. https://doi.org/10.1186/1478-811X-10-20

Ceriani, F., Pozzan, T., & Mammano, F. (2016). Critical role of ATP-induced ATP release for Ca2+ signaling in nonsensory cell networks of the developing cochlea. *Proceedings of the National Academy of Sciences of the United States of America*, *113*(46), E7194–E7201. https://doi.org/10.1073/pnas.1616061113

Cheatham, M. A., Huynh, K. H., Gao, J., Zuo, J., & Dallos, P. (2004). Cochlear function in Prestin knockout mice. *The Journal of Physiology*, *560*(Pt 3), 821–830. https://doi.org/10.1113/jphysiol.2004.069559

Clause, A., Kim, G., Sonntag, M., Weisz, C. J. C., Vetter, D. E., Rűbsamen, R., & Kandler, K. (2014). The Precise Temporal Pattern of Prehearing Spontaneous Activity Is Necessary for Tonotopic Map Refinement. *Neuron*, *82*(4), 822–835. https://doi.org/10.1016/j.neuron.2014.04.001

Clause, A., Lauer, A. M., & Kandler, K. (2017). Mice Lacking the Alpha9 Subunit of the Nicotinic Acetylcholine Receptor Exhibit Deficits in Frequency Difference Limens and Sound Localization. *Frontiers in Cellular Neuroscience*, *11*, 167. https://doi.org/10.3389/fncel.2017.00167

Coate, T. M., Scott, M. K., & Gurjar, M. C. (2019). Current Concepts in Cochlear Ribbon Synapse Formation. *Synapse (New York, N.Y.)*, *73*(5), e22087. https://doi.org/10.1002/syn.22087

Cohen-Salmon, M., Ott, T., Michel, V., Hardelin, J.-P., Perfettini, I., Eybalin, M., Wu, T., Marcus, D. C., Wangemann, P., Willecke, K., & Petit, C. (2002). Targeted Ablation of Connexin26 in the Inner Ear Epithelial Gap Junction Network Causes Hearing Impairment and Cell Death. *Current Biology*, *12*(13), 1106–1111. https://doi.org/10.1016/S0960-9822(02)00904-1

Corey, D. P., & Hudspeth, A. J. (1979). Ionic basis of the receptor potential in a vertebrate hair cell. *Nature*, *281*(5733), 675–677. https://doi.org/10.1038/281675a0

Corns, L. F., Bardhan, T., Houston, O., Olt, J., Holley, M. C., Masetto, S., Johnson, S. L., & Marcotti, W. (2014). Chapter 6—Functional Development of Hair Cells in the Mammalian Inner Ear. In R. Romand & I. Varela-Nieto (Eds.), *Development of Auditory and Vestibular Systems* (pp. 155–188). Academic Press. https://doi.org/10.1016/B978-0-12-408088-1.00006-3

Corns, L. F., Johnson, S. L., Kros, C. J., & Marcotti, W. (2014). Calcium entry into stereocilia drives adaptation of the mechanoelectrical transducer current of mammalian cochlear hair cells. *Proceedings of the National Academy of Sciences*, *111*(41), 14918–14923. https://doi.org/10.1073/pnas.1409920111

Corns, L. F., Johnson, S. L., Roberts, T., Ranatunga, K. M., Hendry, A., Ceriani, F., Safieddine, S., Steel, K. P., Forge, A., Petit, C., Furness, D. N., Kros, C. J., & Marcotti, W. (2018). Mechanotransduction is required for establishing and maintaining mature inner hair cells and regulating efferent innervation. *Nature Communications*, *9*(1), 4015. https://doi.org/10.1038/s41467-018-06307-w

Corti, A. (1851). *Recherches sur l’organe de l’ouïe des mammifères*. Akademische Verlagsgesellschaft.

Dallos, P., & Fay, R. R. (2012). *The Cochlea*. Springer Science & Business Media.

David J. B. Muñoz, I. S. K., Maysoon Rassam, Peter R. Thorne. (2001). Vesicular Storage of Adenosine Triphosphate in the Guinea-pig Cochlear Lateral Wall and Concentrations of ATP in the Endolymph during Sound Exposure and Hypoxia. *Acta Oto-Laryngologica*, *121*(1), 10–15. https://doi.org/10.1080/000164801300006209

Dayaratne, M. W. N., Vlajkovic, S. M., Lipski, J., & Thorne, P. R. (2015). Putative role of border cells in generating spontaneous morphological activity within Kölliker's organ. *Hearing Research*, *330*, 90–97. https://doi.org/10.1016/j.heares.2015.06.017

De Schutter, E., & Steuber, V. (2009). Patterns and pauses in Purkinje cell simple spike trains: Experiments, modeling and theory. *Neuroscience*, *162*(3), 816–826. https://doi.org/10.1016/j.neuroscience.2009.02.040

De Vuyst, E., Decrock, E., Cabooter, L., Dubyak, G. R., Naus, C. C., Evans, W. H., & Leybaert, L. (2006). Intracellular calcium changes trigger connexin 32 hemichannel opening. *The EMBO Journal*, *25*(1), 34–44. https://doi.org/10.1038/sj.emboj.7600908

Decrock, E., Krysko, D. V., Vinken, M., Kaczmarek, A., Crispino, G., Bol, M., Wang, N., De Bock, M., De Vuyst, E., Naus, C. C., Rogiers, V., Vandenabeele, P., Erneux, C., Mammano, F., Bultynck, G., & Leybaert, L. (2012). Transfer of IP3 through gap junctions is critical, but not sufficient, for the spread of apoptosis. *Cell Death and Differentiation*, *19*(6), 947–957. https://doi.org/10.1038/cdd.2011.176

Denk, W., Holt, J. R., Shepherd, G. M. G., & Corey, D. P. (1995). Calcium imaging of single stereocilia in hair cells: Localization of transduction channels at both ends of tip links. *Neuron*, *15*(6), 1311–1321. https://doi.org/10.1016/0896-6273(95)90010-1

Dierich, M., Altoè, A., Koppelmann, J., Evers, S., Renigunta, V., Schäfer, M. K., Naumann, R., Verhulst, S., Oliver, D., & Leitner, M. G. (2020). Optimized Tuning of Auditory Inner Hair Cells to Encode Complex Sound through Synergistic Activity of Six Independent K+ Current Entities. *Cell Reports*, *32*(1). https://doi.org/10.1016/j.celrep.2020.107869

Doerflinger, N. H., Macklin, W. B., & Popko, B. (2003). Inducible site-specific recombination in myelinating cells. *Genesis*, *35*(1), 63–72. https://doi.org/10.1002/gene.10154

Dulon, D., Luo, L., Zhang, C., & Ryan, A. F. (1998). Expression of small-conductance calcium-activated potassium channels (SK) in outer hair cells of the rat cochlea. *European Journal of Neuroscience*, *10*(3), 907–915. https://doi.org/10.1046/j.1460-9568.1998.00098.x

Eckrich, T., Blum, K., Milenkovic, I., & Engel, J. (2018). Fast Ca2+ Transients of Inner Hair Cells Arise Coupled and Uncoupled to Ca2+ Waves of Inner Supporting Cells in the Developing Mouse Cochlea. *Frontiers in Molecular Neuroscience*, *11*. https://doi.org/10.3389/fnmol.2018.00264

Eckrich, T., Varakina, K., Johnson, S. L., Franz, C., Singer, W., Kuhn, S., Knipper, M., Holley, M. C., & Marcotti, W. (2012). Development and Function of the Voltage-Gated Sodium Current in Immature Mammalian Cochlear Inner Hair Cells. *PLoS ONE*, *7*(9). https://doi.org/10.1371/journal.pone.0045732

Elgoyhen, A. B., Johnson, D. S., Boulter, J., Vetter, D. E., & Heinemann, S. (1994). α9: An acetylcholine receptor with novel pharmacological properties expressed in rat cochlear hair cells. *Cell*, *79*(4), 705–715. https://doi.org/10.1016/0092-8674(94)90555-X

Elgoyhen, A. B., Vetter, D. E., Katz, E., Rothlin, C. V., Heinemann, S. F., & Boulter, J. (2001). alpha10: A determinant of nicotinic cholinergic receptor function in mammalian vestibular and cochlear mechanosensory hair cells. *Proceedings of the National Academy of Sciences of the United States of America*, *98*(6), 3501–3506. https://doi.org/10.1073/pnas.051622798

Emadi, G., Richter, C.-P., & Dallos, P. (2004). Stiffness of the Gerbil Basilar Membrane: Radial and Longitudinal Variations. *Journal of Neurophysiology*, *91*(1), 474–488. https://doi.org/10.1152/jn.00446.2003

Eshete, F., & Fields, R. D. (2001). Spike Frequency Decoding and Autonomous Activation of Ca2+–Calmodulin-Dependent Protein Kinase II in Dorsal Root Ganglion Neurons. *Journal of Neuroscience*, *21*(17), 6694–6705. https://doi.org/10.1523/JNEUROSCI.21-17-06694.2001

Faria, D., Rock, J. R., Romao, A. M., Schweda, F., Bandulik, S., Witzgall, R., Schlatter, E., Heitzmann, D., Pavenstädt, H., Herrmann, E., Kunzelmann, K., & Schreiber, R. (2014). The calcium-activated chloride channel Anoctamin 1 contributes to the regulation of renal function. *Kidney International*, *85*(6), 1369–1381. https://doi.org/10.1038/ki.2013.535

Fettiplace, R. (2017). Hair Cell Transduction, Tuning, and Synaptic Transmission in the Mammalian Cochlea. *Comprehensive Physiology*, *7*(4), 1197–1227. https://doi.org/10.1002/cphy.c160049

Fettiplace, R., & Hackney, C. M. (2006). The sensory and motor roles of auditory hair cells. *Nature Reviews Neuroscience*, *7*(1), Article 1. https://doi.org/10.1038/nrn1828

Fettiplace, R., & Kim, K. X. (2014). The Physiology of Mechanoelectrical Transduction Channels in Hearing. *Physiological Reviews*, *94*(3), 951–986. https://doi.org/10.1152/physrev.00038.2013

Fex, J. (1967). Efferent inhibition in the cochlea related to hair-cell dc activity: Study of postsynaptic activity of the crossed olivocochlear fibres in the cat. *The Journal of the Acoustical Society of America*, *41*(3), 666–675. https://doi.org/10.1121/1.1910395

Flock, Å., & Duvall, A. J. (1965). THE ULTRASTRUCTURE OF THE KINOCILIUM OF THE SENSORY CELLS IN THE INNER EAR AND LATERAL LINE ORGANS. *The Journal of Cell Biology*, *25*(1), 1–8.

Froud, K. E., Wong, A. C. Y., Cederholm, J. M. E., Klugmann, M., Sandow, S. L., Julien, J.-P., Ryan, A. F., & Housley, G. D. (2015). Type II spiral ganglion afferent neurons drive medial olivocochlear reflex suppression of the cochlear amplifier. *Nature Communications*, *6*(1), Article 1. https://doi.org/10.1038/ncomms8115

Fuchs, P. A., & Murrow, B. W. (1992). Cholinergic inhibition of short (outer) hair cells of the chick's cochlea. *Journal of Neuroscience*, *12*(3), 800–809. https://doi.org/10.1523/JNEUROSCI.12-03-00800.1992

Furness, D. N., & Lawton, D. M. (2003). Comparative Distribution of Glutamate Transporters and Receptors in Relation to Afferent Innervation Density in the Mammalian Cochlea. *Journal of Neuroscience*, *23*(36), 11296–11304. https://doi.org/10.1523/JNEUROSCI.23-36-11296.2003

Furness, D. N., & Lehre, K. P. (1997). Immunocytochemical Localization of a High-affinity Glutamate-Aspartate Transporter, GLAST, in the Rat and Guinea-pig Cochlea. *European Journal of Neuroscience*, *9*(9), 1961–1969. https://doi.org/10.1111/j.1460-9568.1997.tb00763.x

Gabriele, M. L., Brunso-Bechtold, J. K., & Henkel, C. K. (2000). Plasticity in the development of afferent patterns in the inferior colliculus of the rat after unilateral cochlear ablation. *The Journal of Neuroscience: The Official Journal of the Society for Neuroscience*, *20*(18), 6939–6949.

Gale, J. E., Piazza, V., Ciubotaru, C. D., & Mammano, F. (2004). A Mechanism for Sensing Noise Damage in the Inner Ear. *Current Biology*, *14*(6), 526–529. https://doi.org/10.1016/j.cub.2004.03.002

Galli, L., & Maffei, L. (1988). Spontaneous Impulse Activity of Rat Retinal Ganglion Cells in Prenatal Life. *Science*, *242*(4875), 90–91. https://doi.org/10.1126/science.3175637

Géléoc, G. S. G., & Holt, J. R. (2003). Developmental acquisition of sensory transduction in hair cells of the mouse inner ear. *Nature Neuroscience*, *6*(10), 1019–1020. https://doi.org/10.1038/nn1120

Glowatzki, E., & Fuchs, P. A. (2002). Transmitter release at the hair cell ribbon synapse. *Nature Neuroscience*, *5*(2), 147–154. https://doi.org/10.1038/nn796

Glueckert, R., Johnson Chacko, L., Rask-Andersen, H., Liu, W., Handschuh, S., & Schrott-Fischer, A. (2018). Anatomical basis of drug delivery to the inner ear. *Hearing Research*, *368*, 10–27. https://doi.org/10.1016/j.heares.2018.06.017

Gold, T., null, null, Gray, J., & null, null. (1948). Hearing. II. The physical basis of the action of the cochlea. *Proceedings of the Royal Society B: Biological Sciences*, *135*(881), 492–498. https://doi.org/10.1098/rspb.1948.0025

Goldring, A. C., Beurg, M., & Fettiplace, R. (2019). The contribution of TMC1 to adaptation of mechanoelectrical transduction channels in cochlear outer hair cells. *The Journal of Physiology, 597*(24), 5949–5961. https://doi.org/10.1113/JP278799

Goodyear, R. J., & Richardson, G. P. (2003). A Novel Antigen Sensitive to Calcium Chelation That is Associated with the Tip Links and Kinocilial Links of Sensory Hair Bundles. *Journal of Neuroscience*, *23*(12), 4878–4887. https://doi.org/10.1523/JNEUROSCI.23-12-04878.2003

Goodyear, R., & Richardson, G. (1999). The Ankle-Link Antigen: An Epitope Sensitive to Calcium Chelation Associated with the Hair-Cell Surface and the Calycal Processes of Photoreceptors. *Journal of Neuroscience*, *19*(10), 3761–3772. https://doi.org/10.1523/JNEUROSCI.19-10-03761.1999

Graven, S. N., & Browne, J. V. (2008). Auditory Development in the Fetus and Infant. *Newborn and Infant Nursing Reviews*, *8*(4), 187–193. https://doi.org/10.1053/j.nainr.2008.10.010

Grenier, F., Timofeev, I., & Steriade, M. (1998). Leading role of thalamic over cortical neurons during postinhibitory rebound excitation. *Proceedings of the National Academy of Sciences*, *95*(23), 13929–13934. https://doi.org/10.1073/pnas.95.23.13929

Hakuba, N., Koga, K., Gyo, K., Usami, S., & Tanaka, K. (2000). Exacerbation of Noise-Induced Hearing Loss in Mice Lacking the Glutamate Transporter GLAST. *Journal of Neuroscience*, *20*(23), 8750–8753. https://doi.org/10.1523/JNEUROSCI.20-23-08750.2000

Hanson, P. I., Meyer, T., Stryer, L., & Schulman, H. (1994). Dual role of calmodulin in autophosphorylation of multifunctional cam kinase may underlie decoding of calcium signals. *Neuron*, *12*(5), 943–956. https://doi.org/10.1016/0896-6273(94)90306-9

Harrus, A.-G., Ceccato, J.-C., Sendin, G., Bourien, J., Puel, J.-L., & Nouvian, R. (2018). Spiking Pattern of the Mouse Developing Inner Hair Cells Is Mostly Invariant Along the Tonotopic Axis. *Frontiers in Cellular Neuroscience*, *12*. https://doi.org/10.3389/fncel.2018.00407

Hicks, G. A., & Marrion, N. V. (1998). Ca2+-dependent inactivation of large conductance Ca2+-activated K+ (BK) channels in rat hippocampal neurones produced by pore block from an associated particle. *The Journal of Physiology*, *508*(Pt 3), 721–734. https://doi.org/10.1111/j.1469-7793.1998.721bp.x

Hodgkin, A. L., & Huxley, A. F. (1952). A quantitative description of membrane current and its application to conduction and excitation in nerve. *The Journal of Physiology*, *117*(4), 500–544.

Housley, G. D., & Ashmore, J. F. (1992). Ionic currents of outer hair cells isolated from the guinea-pig cochlea. *The Journal of Physiology*, *448*(1), 73–98. https://doi.org/10.1113/jphysiol.1992.sp019030

Housley, G. D., Luo, L., & Ryan, A. F. (1998). Localization of mRNA encoding the P2X2 receptor subunit of the adenosine 5′-triphosphate-gated ion channel in the adult and developing rat inner ear by in situ hybridization. *Journal of Comparative Neurology*, *393*(4), 403–414. https://doi.org/10.1002/(SICI)1096-9861(19980420)393:4<403::AID-CNE1>3.0.CO;2-4

Huang, F., Zhang, H., Wu, M., Yang, H., Kudo, M., Peters, C. J., Woodruff, P. G., Solberg, O. D., Donne, M. L., Huang, X., Sheppard, D., Fahy, J. V., Wolters, P. J., Hogan, B. L. M., Finkbeiner, W. E., Li, M., Jan, Y.-N., Jan, L. Y., & Rock, J. R. (2012). Calcium-activated chloride channel TMEM16A modulates mucin secretion and airway smooth muscle contraction. *Proceedings of the National Academy of Sciences*, *109*(40), 16354–16359. https://doi.org/10.1073/pnas.1214596109

Huang, H., Yu, D., & Soong, T. W. (2013). C-Terminal Alternative Splicing of CaV1.3 Channels Distinctively Modulates Their Dihydropyridine Sensitivity. *Molecular Pharmacology*, *84*(4), 643–653.

Huang, L.-C., Thorne, P. R., Vlajkovic, S. M., & Housley, G. D. (2010). Differential expression of P2Y receptors in the rat cochlea during development. *Purinergic Signalling*, *6*(2), 231–248. https://doi.org/10.1007/s11302-010-9191-x

Hudspeth, A. J. (1982). Extracellular current flow and the site of transduction by vertebrate hair cells. *The Journal of Neuroscience: The Official Journal of the Society for Neuroscience*, *2*(1), 1–10.

Inagaki, A., & Lee, A. (2013). Developmental alterations in the biophysical properties of Cav1.3 Ca2+ channels in mouse inner hair cells. *Channels*, *7*(3), 171. https://doi.org/10.4161/chan.24104

Iyer, J. S., Batts, S. A., Chu, K. K., Sahin, M. I., Leung, H. M., Tearney, G. J., & Stankovic, K. M. (2016). Micro-optical coherence tomography of the mammalian cochlea. *Scientific Reports*, *6*(1), Article 1. https://doi.org/10.1038/srep33288

Järlebark, L. E., Housley, G. D., & Thorne, P. R. (2000). Immunohistochemical localization of adenosine 5`-triphosphate-gated ion channel P2X2 receptor subunits in adult and developing rat cochlea. *Journal of Comparative Neurology*, *421*(3), 289–301. https://doi.org/10.1002/(SICI)1096-9861(20000605)421:3<289::AID-CNE1>3.0.CO;2-0

Jeng, J., Ceriani, F., Hendry, A., Johnson, S. L., Yen, P., Simmons, D. D., Kros, C. J., & Marcotti, W. (2020). Hair cell maturation is differentially regulated along the tonotopic axis of the mammalian cochlea. *The Journal of Physiology*, *598*(1), 151–170. https://doi.org/10.1113/JP279012

Johnson, S. L. (2015). Membrane properties specialize mammalian inner hair cells for frequency or intensity encoding. *ELife*, *4*, e08177. https://doi.org/10.7554/eLife.08177

Johnson, S. L., Adelman, J. P., & Marcotti, W. (2007). Genetic deletion of SK2 channels in mouse inner hair cells prevents the developmental linearization in the Ca2+ dependence of exocytosis. *The Journal of Physiology*, *583*(Pt 2), 631–646. https://doi.org/10.1113/jphysiol.2007.136630

Johnson, S. L., Beurg, M., Marcotti, W., & Fettiplace, R. (2011). Prestin-Driven Cochlear Amplification Is Not Limited by the Outer Hair Cell Membrane Time Constant. *Neuron*, *70*(6), 1143–1154. https://doi.org/10.1016/j.neuron.2011.04.024

Johnson, S. L., Ceriani, F., Houston, O., Polishchuk, R., Polishchuk, E., Crispino, G., Zorzi, V., Mammano, F., & Marcotti, W. (2017). Connexin-Mediated Signaling in Nonsensory Cells Is Crucial for the Development of Sensory Inner Hair Cells in the

Mouse Cochlea. *Journal of Neuroscience*, *37*(2), 258–268. https://doi.org/10.1523/JNEUROSCI.2251-16.2016

Johnson, S. L., Eckrich, T., Kuhn, S., Zampini, V., Franz, C., Ranatunga, K. M., Roberts, T. P., Masetto, S., Knipper, M., Kros, C. J., & Marcotti, W. (2011). Position-dependent patterning of spontaneous action potentials in immature cochlear inner hair cells. *Nature Neuroscience*, *14*(6), 711–717. https://doi.org/10.1038/nn.2803

Johnson, S. L., Franz, C., Knipper, M., & Marcotti, W. (2009). Functional maturation of the exocytotic machinery at gerbil hair cell ribbon synapses. *The Journal of Physiology*, *587*(Pt 8), 1715–1726. https://doi.org/10.1113/jphysiol.2009.168542

Johnson, S. L., Kennedy, H. J., Holley, M. C., Fettiplace, R., & Marcotti, W. (2012). The resting transducer current drives spontaneous activity in pre-hearing mammalian cochlear inner hair cells. *The Journal of Neuroscience : The Official Journal of the Society for Neuroscience*, *32*(31), 10479–10483. https://doi.org/10.1523/JNEUROSCI.0803-12.2012

Johnson, S. L., Kuhn, S., Franz, C., Ingham, N., Furness, D. N., Knipper, M., Steel, K. P., Adelman, J. P., Holley, M. C., & Marcotti, W. (2013). Presynaptic maturation in auditory hair cells requires a critical period of sensory-independent spiking activity. *Proceedings of the National Academy of Sciences*, *110*(21), 8720–8725. https://doi.org/10.1073/pnas.1219578110

Johnson, S. L., & Marcotti, W. (2008). Biophysical properties of CaV1.3 calcium channels in gerbil inner hair cells. *The Journal of Physiology*, *586*(4), 1029–1042. https://doi.org/10.1113/jphysiol.2007.145219

Johnson, S. L., Marcotti, W., & Kros, C. J. (2005). Increase in efficiency and reduction in Ca2+ dependence of exocytosis during development of mouse inner hair cells. *The Journal of Physiology*, *563*(Pt 1), 177–191. https://doi.org/10.1113/jphysiol.2004.074740

Johnson, S. L., Olt, J., Cho, S., von Gersdorff, H., & Marcotti, W. (2017). The Coupling between Ca2+ Channels and the Exocytotic Ca2+ Sensor at Hair Cell Ribbon Synapses Varies Tonotopically along the Mature Cochlea. *The Journal of Neuroscience*, *37*(9), 2471–2484. https://doi.org/10.1523/JNEUROSCI.2867-16.2017

Johnson, S. L., Wedemeyer, C., Vetter, D. E., Adachi, R., Holley, M. C., Elgoyhen, A. B., & Marcotti, W. (2013). Cholinergic efferent synaptic transmission regulates the maturation of auditory hair cell ribbon synapses. *Open Biology*, *3*(11). https://doi.org/10.1098/rsob.130163

Jovanovic, S., & Milenkovic, I. (2020). Purinergic Modulation of Activity in the Developing Auditory Pathway. *Neuroscience Bulletin*, *36*(11), 1285–1298. https://doi.org/10.1007/s12264-020-00586-4

Kachar, B., Parakkal, M., Kurc, M., Zhao, Y., & Gillespie, P. G. (2000). High-resolution structure of hair-cell tip links. *Proceedings of the National Academy of Sciences*, *97*(24), 13336–13341. https://doi.org/10.1073/pnas.97.24.13336

Kazmierczak, P., Sakaguchi, H., Tokita, J., Wilson-Kubalek, E. M., Milligan, R. A., Müller, U., & Kachar, B. (2007). Cadherin 23 and protocadherin 15 interact to form tip-link filaments in sensory hair cells. *Nature*, *449*(7158), 87–91. https://doi.org/10.1038/nature06091

Keithley, E. M., & Feldman, M. L. (1982). Hair cell counts in an age-graded series of rat cochleas. *Hearing Research*, *8*(3), 249–262. https://doi.org/10.1016/0378-5955(82)90017-X

Kempfle, J. S., Turban, J. L., & Edge, A. S. B. (2016). Sox2 in the differentiation of cochlear progenitor cells. *Scientific Reports*, *6*, 23293. https://doi.org/10.1038/srep23293

Kennedy, H. J., Evans, M. G., Crawford, A. C., & Fettiplace, R. (2003). Fast adaptation of mechanoelectrical transducer channels in mammalian cochlear hair cells. *Nature Neuroscience*, *6*(8), Article 8. https://doi.org/10.1038/nn1089

Kharkovets, T., Dedek, K., Maier, H., Schweizer, M., Khimich, D., Nouvian, R., Vardanyan, V., Leuwer, R., Moser, T., & Jentsch, T. J. (2006). Mice with altered KCNQ4 K+ channels implicate sensory outer hair cells in human progressive deafness. *The EMBO Journal*, *25*(3), 642–652. https://doi.org/10.1038/sj.emboj.7600951

Kim, K. X., & Fettiplace, R. (2012). Developmental changes in the cochlear hair cell mechanotransducer channel and their regulation by transmembrane channel–like proteins. *Journal of General Physiology*, *141*(1), 141–148. https://doi.org/10.1085/jgp.201210913

Kluyver, T., Ragan-Kelley, B., P&#233, Rez, F., Granger, B., Bussonnier, M., Frederic, J., Kelley, K., Hamrick, J., Grout, J., Corlay, S., Ivanov, P., Avila, D., n, Abdalla, S., Willing, C., & Team, J. D. (2016). Jupyter Notebooks – a publishing format for reproducible computational workflows. *Positioning and Power in Academic Publishing: Players, Agents and Agendas*, 87–90. https://doi.org/10.3233/978-1-61499-649-1-87

Kollmar, R., Fak, J., Montgomery, L. G., & Hudspeth, A. J. (1997). Hair cell-specific splicing of mRNA for the α1D subunit of voltage-gated Ca2+ channels in the chicken's cochlea. *Proceedings of the National Academy of Sciences*, *94*(26), 14889–14893. https://doi.org/10.1073/pnas.94.26.14889

Kong, J.-H., Adelman, J. P., & Fuchs, P. A. (2008). Expression of the SK2 calcium-activated potassium channel is required for cholinergic function in mouse cochlear hair cells. *The Journal of Physiology*, *586*(22), 5471–5485. https://doi.org/10.1113/jphysiol.2008.160077

Kros, C. J. (1996). Physiology of Mammalian Cochlear Hair Cells. In P. Dallos, A. N. Popper, & R. R. Fay (Eds.), *The Cochlea* (pp. 318–385). Springer. https://doi.org/10.1007/978-1-4612-0757-3_6

Kros, C. J., & Crawford, A. C. (1990). Potassium currents in inner hair cells isolated from the guinea-pig cochlea. *The Journal of Physiology*, *421*(1), 263–291. https://doi.org/10.1113/jphysiol.1990.sp017944

Kros, C. J., Ruppersberg, J. P., & Rüsch, A. (1998). Expression of a potassium current in inner hair cells during development of hearing in mice. *Nature*, *394*(6690), 281–284. https://doi.org/10.1038/28401

Kubisch, C., Schroeder, B. C., Friedrich, T., Lütjohann, B., El-Amraoui, A., Marlin, S., Petit, C., & Jentsch, T. J. (1999). KCNQ4, a Novel Potassium Channel Expressed in Sensory Outer Hair Cells, Is Mutated in Dominant Deafness. *Cell*, *96*(3), 437–446. https://doi.org/10.1016/S0092-8674(00)80556-5

Leao, R. N., Sun, H., Svahn, K., Berntson, A., Youssoufian, M., Paolini, A. G., Fyffe, R. E. W., & Walmsley, B. (2006). Topographic organization in the auditory brainstem of juvenile mice is disrupted in congenital deafness. *The Journal of Physiology*, *571*(Pt 3), 563–578. https://doi.org/10.1113/jphysiol.2005.098780

Lee, B., Hong, G.-S., Lee, S. H., Kim, H., Kim, A., Hwang, E. M., Kim, J., Lee, M. G., Yang, J.-Y., Kweon, M.-N., Tse, C.-M., Mark, D., & Oh, U. (2019). Anoctamin 1/TMEM16A controls intestinal Cl− secretion induced by carbachol and cholera toxin. *Experimental & Molecular Medicine*, *51*(8), Article 8. https://doi.org/10.1038/s12276-019-0287-2

Lee, S. I., Conrad, T., Jones, S. M., Lagziel, A., Starost, M. F., Belyantseva, I. A., Friedman, T. B., & Morell, R. J. (2013). A null mutation of mouse Kcna10 causes significant vestibular and mild hearing dysfunction. *Hearing Research*, *300*, 1–9. https://doi.org/10.1016/j.heares.2013.02.009

Leybaert, L., Braet, K., Vandamme, W., Cabooter, L., Martin, P. E. M., & Evans, W. H. (2003). Connexin channels, connexin mimetic peptides and ATP release. *Cell Communication & Adhesion*, *10*(4–6), 251–257. https://doi.org/10.1080/cac.10.4-6.251.257

Li, L., Stefan, M. I., & Novère, N. L. (2012). Calcium Input Frequency, Duration and Amplitude Differentially Modulate the Relative Activation of Calcineurin and CaMKII. *PLOS ONE*, *7*(9), e43810. https://doi.org/10.1371/journal.pone.0043810

Liberman, M. C., Dodds, L. W., & Pierce, S. (1990). Afferent and efferent innervation of the cat cochlea: Quantitative analysis with light and electron microscopy. *The Journal of Comparative Neurology*, *301*(3), 443–460. https://doi.org/10.1002/cne.903010309

Liu, C., Glowatzki, E., & Fuchs, P. A. (2015). Unmyelinated type II afferent neurons report cochlear damage. *Proceedings of the National Academy of Sciences*, *112*(47), 14723–14727. https://doi.org/10.1073/pnas.1515228112

Liu, H., Pecka, J. L., Zhang, Q., Soukup, G. A., Beisel, K. W., & He, D. Z. Z. (2014). Characterization of Transcriptomes of Cochlear Inner and Outer Hair Cells. *The Journal of Neuroscience*, *34*(33), 11085–11095. https://doi.org/10.1523/JNEUROSCI.1690-14.2014

Liu, J., Cai, L., He, Y., & Yang, J. (2017). Apoptosis pattern and alterations of expression of apoptosis-related factors of supporting cells in Kölliker’s organ in vivo in early stage after birth in rats. *European Journal of Histochemistry*. https://doi.org/10.4081/ejh.2017.2706

Lumpkin, E. A., & Hudspeth, A. J. (1995). Detection of Ca2+ entry through mechanosensitive channels localizes the site of mechanoelectrical transduction in hair cells. *Proceedings of the National Academy of Sciences*, *92*(22), 10297–10301. https://doi.org/10.1073/pnas.92.22.10297

Madisen, L., Zwingman, T. A., Sunkin, S. M., Oh, S. W., Zariwala, H. A., Gu, H., Ng, L. L., Palmiter, R. D., Hawrylycz, M. J., Jones, A. R., Lein, E. S., & Zeng, H. (2010). A robust and high-throughput Cre reporting and characterization system for the whole mouse brain. *Nature Neuroscience*, *13*(1), 133–140. https://doi.org/10.1038/nn.2467

Maison, S. F., Parker, L. L., Young, L., Adelman, J. P., Zuo, J., & Liberman, M. C. (2007). Overexpression of SK2 Channels Enhances Efferent Suppression of Cochlear

Responses without Enhancing Noise Resistance. *Journal of Neurophysiology*, *97*(4), 2930–2936. https://doi.org/10.1152/jn.01183.2006

Mammano, F., & Ashmore, J. F. (1993). Reverse transduction measured in the isolated cochlea by laser Michelson interferometry. *Nature*, *365*(6449), Article 6449. https://doi.org/10.1038/365838a0

Manley, G. A. (2012). Evolutionary Paths to Mammalian Cochleae. *JARO: Journal of the Association for Research in Otolaryngology*, *13*(6), 733–743. https://doi.org/10.1007/s10162-012-0349-9

Marcotti, W. (2012). Functional assembly of mammalian cochlear hair cells. *Experimental Physiology*, *97*(4), 438–451. https://doi.org/10.1113/expphysiol.2011.059303

Marcotti, W., Erven, A., Johnson, S. L., Steel, K. P., & Kros, C. J. (2006). Tmc1 is necessary for normal functional maturation and survival of inner and outer hair cells in the mouse cochlea. *The Journal of Physiology*, *574*(Pt 3), 677–698. https://doi.org/10.1113/jphysiol.2005.095661

Marcotti, W., Johnson, S. L., Holley, M. C., & Kros, C. J. (2003). Developmental changes in the expression of potassium currents of embryonic, neonatal and mature mouse inner hair cells. *The Journal of Physiology*, *548*(2), 383–400. https://doi.org/10.1111/j.1469-7793.2003.00383.x

Marcotti, W., Johnson, S. L., & Kros, C. J. (2004a). Effects of intracellular stores and extracellular Ca(2+) on Ca(2+)-activated K(+) currents in mature mouse inner hair cells. *The Journal of Physiology*, *557*(Pt 2), 613–633. https://doi.org/10.1113/jphysiol.2003.060137

Marcotti, W., Johnson, S. L., & Kros, C. J. (2004b). A transiently expressed SK current sustains and modulates action potential activity in immature mouse inner hair cells. *The Journal of Physiology*, *560*(3), 691–708. https://doi.org/10.1113/jphysiol.2004.072868

Marcotti, W., Johnson, S. L., Rusch, A., & Kros, C. J. (2003). Sodium and calcium currents shape action potentials in immature mouse inner hair cells. *The Journal of Physiology*, *552*(Pt 3), 743–761. https://doi.org/10.1113/jphysiol.2003.043612

Marcotti, W., & Kros, C. J. (1999). Developmental expression of the potassium current IK,n contributes to maturation of mouse outer hair cells. *The Journal of Physiology*, *520 Pt 3*, 653–660.

Martini, M., Rossi, M. L., Rubbini, G., & Rispoli, G. (2000). Calcium currents in hair cells isolated from semicircular canals of the frog. *Biophysical Journal*, *78*(3), 1240–1254. https://doi.org/10.1016/S0006-3495(00)76681-1

Maul, A., Huebner, A. K., Strenzke, N., Moser, T., Rübsamen, R., Jovanovic, S., & Hübner, C. A. (2022). The Cl—Channel TMEM16A is involved in the generation of cochlear Ca2+ waves and promotes the refinement of auditory brainstem networks in mice. *ELife*, *11*, e72251. https://doi.org/10.7554/eLife.72251

Meister, M., Wong, R. O. L., Baylor, D. A., & Shatz, C. J. (1991). Synchronous Bursts of Action Potentials in Ganglion Cells of the Developing Mammalian Retina. *Science*, *252*(5008), 939–943. https://doi.org/10.1126/science.2035024

Michalski, N., Goutman, J. D., Auclair, S. M., Boutet de Monvel, J., Tertrais, M., Emptoz, A., Parrin, A., Nouaille, S., Guillon, M., Sachse, M., Ciric, D., Bahloul, A., Hardelin, J.-P., Sutton, R. B., Avan, P., Krishnakumar, S. S., Rothman, J. E., Dulon, D., Safieddine, S.,

& Petit, C. (2017). Otoferlin acts as a Ca2+ sensor for vesicle fusion and vesicle pool replenishment at auditory hair cell ribbon synapses. *ELife*, *6*, e31013. https://doi.org/10.7554/eLife.31013

Michanski, S., Smaluch, K., Steyer, A. M., Chakrabarti, R., Setz, C., Oestreicher, D., Fischer, C., Möbius, W., Moser, T., Vogl, C., & Wichmann, C. (2019). Mapping developmental maturation of inner hair cell ribbon synapses in the apical mouse cochlea. *Proceedings of the National Academy of Sciences of the United States of America*, *116*(13), 6415–6424. https://doi.org/10.1073/pnas.1812029116

Muñoz, D. J., Thorne, P. R., Housley, G. D., & Billett, T. E. (1995). Adenosine 5'-triphosphate (ATP) concentrations in the endolymph and perilymph of the guinea-pig cochlea. *Hearing Research*, *90*(1–2), 119–125. https://doi.org/10.1016/0378-5955(95)00153-5

Murthy, V., Maison, S. F., Taranda, J., Haque, N., Bond, C. T., Elgoyhen, A. B., Adelman, J. P., Liberman, M. C., & Vetter, D. E. (2009). SK2 channels are required for function and long-term survival of efferent synapses on mammalian outer hair cells. *Molecular and Cellular Neuroscience*, *40*(1), 39–49. https://doi.org/10.1016/j.mcn.2008.08.011

Nayagam, B. A., Muniak, M. A., & Ryugo, D. K. (2011). The spiral ganglion: Connecting the peripheral and central auditory systems. *Hearing Research*, *278*(1–2), 2–20. https://doi.org/10.1016/j.heares.2011.04.003

Nenov, A. P., Norris, C., & Bobbin, R. P. (1996). Acetylcholine response in guinea pig outer hair cells. II. Activation of a small conductance Ca2+-activated K+ channel. *Hearing Research*, *101*(1), 149–172. https://doi.org/10.1016/S0378-5955(96)00143-8

Ohyama, T., & Groves, A. K. (2004). Generation of Pax2-Cre mice by modification of a Pax2 bacterial artificial chromosome. *Genesis*, *38*(4), 195–199. https://doi.org/10.1002/gene.20017

Oliver, D., Klöcker, N., Schuck, J., Baukrowitz, T., Ruppersberg, J. P., & Fakler, B. (2000). Gating of Ca2+-Activated K+ Channels Controls Fast Inhibitory Synaptic Transmission at Auditory Outer Hair Cells. *Neuron*, *26*(3), 595–601. https://doi.org/10.1016/S0896-6273(00)81197-6

Oliver, D., Knipper, M., Derst, C., & Fakler, B. (2003). Resting Potential and Submembrane Calcium Concentration of Inner Hair Cells in the Isolated Mouse Cochlea Are Set by KCNQ-Type Potassium Channels. *Journal of Neuroscience*, *23*(6), 2141–2149. https://doi.org/10.1523/JNEUROSCI.23-06-02141.2003

Oliver, D., Plinkert, P., Zenner, H. P., & Ruppersberg, J. P. (1997). Sodium current expression during postnatal development of rat outer hair cells. *Pflugers Archiv: European Journal of Physiology*, *434*(6), 772–778. https://doi.org/10.1007/s004240050464

Pan, Y., & Monje, M. (2020). Activity Shapes Neural Circuit Form and Function: A Historical Perspective. *The Journal of Neuroscience*, *40*(5), 944–954. https://doi.org/10.1523/JNEUROSCI.0740-19.2019

Pangršič, T., Gabrielaitis, M., Michanski, S., Schwaller, B., Wolf, F., Strenzke, N., & Moser, T. (2015). EF-hand protein Ca2+ buffers regulate Ca2+ influx and exocytosis in sensory hair cells. *Proceedings of the National Academy of Sciences*, *112*(9), E1028–E1037. https://doi.org/10.1073/pnas.1416424112

Peeters, R. P., Ng, L., Ma, M., & Forrest, D. (2015). The timecourse of apoptotic cell death during postnatal remodeling of the mouse cochlea and its premature onset by triiodothyronine (T3). *Molecular and Cellular Endocrinology*, *407*, 1–8. https://doi.org/10.1016/j.mce.2015.02.025

Perkins, K. L. (2006). Cell-attached voltage-clamp and current-clamp recording and stimulation techniques in brain slices. *Journal of Neuroscience Methods*, *154*(1), 1–18. https://doi.org/10.1016/j.jneumeth.2006.02.010

Piazza, V., Ciubotaru, C. D., Gale, J. E., & Mammano, F. (2007). Purinergic signalling and intercellular Ca2+ wave propagation in the organ of Corti. *Cell Calcium*, *41*(1), 77–86. https://doi.org/10.1016/j.ceca.2006.05.005

Pickles, J. O., Comis, S. D., & Osborne, M. P. (1984). Cross-links between stereocilia in the guinea pig organ of Corti, and their possible relation to sensory transduction. *Hearing Research*, *15*(2), 103–112. https://doi.org/10.1016/0378-5955(84)90041-8

Platzer, J., Engel, J., Schrott-Fischer, A., Stephan, K., Bova, S., Chen, H., Zheng, H., & Striessnig, J. (2000). Congenital deafness and sinoatrial node dysfunction in mice lacking class D L-type Ca2+ channels. *Cell*, *102*(1), 89–97. https://doi.org/10.1016/s0092-8674(00)00013-1

Pujol, R., Lavigne-Rebillard, M., & Lenoir, M. (1998). Development of Sensory and Neural Structures in the Mammalian Cochlea. In E. W. Rubel, A. N. Popper, & R. R. Fay (Eds.), *Development of the Auditory System* (pp. 146–192). Springer. https://doi.org/10.1007/978-1-4612-2186-9_4

Redmond, L., & Ghosh, A. (2005). Regulation of dendritic development by calcium signaling. *Cell Calcium*, *37*(5), 411–416. https://doi.org/10.1016/j.ceca.2005.01.009

Ricci, A. J., & Fettiplace, R. (1998). Calcium permeation of the turtle hair cell mechanotransducer channel and its relation to the composition of endolymph. *The Journal of Physiology*, *506*(1), 159–173. https://doi.org/10.1111/j.1469-7793.1998.159bx.x

Ricci, A. J., Kachar, B., Gale, J., & Van Netten, S. M. (2006). Mechano-electrical Transduction: New Insights into Old Ideas. *The Journal of Membrane Biology*, *209*(2–3), 71–88. https://doi.org/10.1007/s00232-005-0834-8

Rickheit, G., Maier, H., Strenzke, N., Andreescu, C. E., De Zeeuw, C. I., Muenscher, A., Zdebik, A. A., & Jentsch, T. J. (2008). Endocochlear potential depends on Cl− channels: Mechanism underlying deafness in Bartter syndrome IV. *The EMBO Journal*, *27*(21), 2907–2917. https://doi.org/10.1038/emboj.2008.203

Roberts, W. M., Howard, J., & Hudspeth, A. J. (1988). Hair cells: Transduction, tuning, and transmission in the inner ear. *Annual Review of Cell Biology*, *4*, 63–92. https://doi.org/10.1146/annurev.cb.04.110188.000431

Roccio, M., & Edge, A. S. B. (2019). Inner ear organoids: New tools to understand neurosensory cell development, degeneration and regeneration. *Development*, *146*(17). https://doi.org/10.1242/dev.177188

Rodriguez, L., Simeonato, E., Scimemi, P., Anselmi, F., Calì, B., Crispino, G., Ciubotaru, C. D., Bortolozzi, M., Ramirez, F. G., Majumder, P., Arslan, E., Camilli, P. D., Pozzan, T., & Mammano, F. (2012). Reduced phosphatidylinositol 4,5-bisphosphate synthesis impairs inner ear Ca2+ signaling and high-frequency hearing acquisition. *Proceedings of the National Academy of Sciences*, *109*(35), 14013–14018. https://doi.org/10.1073/pnas.1211869109

Rodriguez-Contreras, A., & Yamoah, E. N. (2001). Direct measurement of single-channel Ca(2+) currents in bullfrog hair cells reveals two distinct channel subtypes. *The Journal of Physiology*, *534*(Pt 3), 669–689. https://doi.org/10.1111/j.1469-7793.2001.00669.x

Roux, I., Wersinger, E., McIntosh, J. M., Fuchs, P. A., & Glowatzki, E. (2011). Onset of Cholinergic Efferent Synaptic Function in Sensory Hair Cells of the Rat Cochlea. *Journal of Neuroscience*, *31*(42), 15092–15101. https://doi.org/10.1523/JNEUROSCI.2743-11.2011

Rutherford, M. A., von Gersdorff, H., & Goutman, J. D. (2021). Encoding sound in the cochlea: From receptor potential to afferent discharge. *The Journal of Physiology*, *599*(10), 2527–2557. https://doi.org/10.1113/JP279189

Sauer, G., Richter, C.-P., & Klinke, R. (1999). Sodium, potassium, chloride and calcium concentrations measured in pigeon perilymph and endolymph. *Hearing Research*, *129*(1), 1–6. https://doi.org/10.1016/S0378-5955(98)00230-5

Schreiber, R., Faria, D., Skryabin, B. V., Wanitchakool, P., Rock, J. R., & Kunzelmann, K. (2015). Anoctamins support calcium-dependent chloride secretion by facilitating calcium signaling in adult mouse intestine. *Pflügers Archiv - European Journal of Physiology*, *467*(6), 1203–1213. https://doi.org/10.1007/s00424-014-1559-2

Schwander, M., Kachar, B., & Müller, U. (2010). The cell biology of hearing. *Journal of Cell Biology*, *190*(1), 9–20. https://doi.org/10.1083/jcb.201001138

Sendin, G., Bourien, J., Rassendren, F., Puel, J.-L., & Nouvian, R. (2014). Spatiotemporal pattern of action potential firing in developing inner hair cells of the mouse cochlea. *Proceedings of the National Academy of Sciences of the United States of America*, *111*(5), 1999–2004. https://doi.org/10.1073/pnas.1319615111

Senften, M., Schwander, M., Kazmierczak, P., Lillo, C., Shin, J.-B., Hasson, T., Géléoc, G. S. G., Gillespie, P. G., Williams, D., Holt, J. R., & Müller, U. (2006). Physical and Functional Interaction between Protocadherin 15 and Myosin VIIa in Mechanosensory Hair Cells. *Journal of Neuroscience*, *26*(7), 2060–2071. https://doi.org/10.1523/JNEUROSCI.4251-05.2006

Sheridan, J. T., Worthington, E. N., Yu, K., Gabriel, S. E., Hartzell, H. C., & Tarran, R. (2011). Characterization of the Oligomeric Structure of the Ca2+-activated Cl− Channel Ano1/TMEM16A. *Journal of Biological Chemistry*, *286*(2), 1381–1388. https://doi.org/10.1074/jbc.M110.174847

Slepecky, N. B. (1996). Structure of the Mammalian Cochlea. In P. Dallos, A. N. Popper, & R. R. Fay (Eds.), *The Cochlea* (pp. 44–129). Springer. https://doi.org/10.1007/978-1-4612-0757-3_2

Spoendlin, H. (1972). Innervation Densities of the Cochlea. *Acta Oto-Laryngologica*, *73*(2–6), 235–248. https://doi.org/10.3109/00016487209138937

Teubner, B., Michel, V., Pesch, J., Lautermann, J., Cohen-Salmon, M., Söhl, G., Jahnke, K., Winterhager, E., Herberhold, C., Hardelin, J.-P., Petit, C., & Willecke, K. (2003). Connexin30 (Gjb6)-deficiency causes severe hearing impairment and lack of endocochlear potential. *Human Molecular Genetics*, *12*(1), 13–21. https://doi.org/10.1093/hmg/ddg001

Teudt, I. U., & Richter, C. P. (2014). Basilar Membrane and Tectorial Membrane Stiffness in the CBA/CaJ Mouse. *JARO: Journal of the Association for Research in Otolaryngology*, *15*(5), 675–694. https://doi.org/10.1007/s10162-014-0463-y

Toth, A. B., Shum, A. K., & Prakriya, M. (2016). Regulation of neurogenesis by calcium signaling. *Cell Calcium*, *59*(2–3), 124–134. https://doi.org/10.1016/j.ceca.2016.02.011

Tritsch, N. X., & Bergles, D. E. (2010). Developmental Regulation of Spontaneous Activity in the Mammalian Cochlea. *Journal of Neuroscience*, *30*(4), 1539–1550. https://doi.org/10.1523/JNEUROSCI.3875-09.2010

Tritsch, N. X., Yi, E., Gale, J. E., Glowatzki, E., & Bergles, D. E. (2007). The origin of spontaneous activity in the developing auditory system. *Nature*, *450*(7166), Article 7166. https://doi.org/10.1038/nature06233

V. Békésy, G. (1952). DC Resting Potentials Inside the Cochlear Partition. *The Journal of the Acoustical Society of America*, *24*(1), 72–76. https://doi.org/10.1121/1.1906851

Vicencio-Jimenez, S., Weinberg, M. M., Bucci-Mansilla, G., & Lauer, A. M. (2021). Olivocochlear Changes Associated With Aging Predominantly Affect the Medial Olivocochlear System. *Frontiers in Neuroscience*, *15*. https://www.frontiersin.org/article/10.3389/fnins.2021.704805

Vincent, P. F. Y., Bouleau, Y., Charpentier, G., Emptoz, A., Safieddine, S., Petit, C., & Dulon, D. (2017). Different CaV1.3 Channel Isoforms Control Distinct Components of the

Synaptic Vesicle Cycle in Auditory Inner Hair Cells. *The Journal of Neuroscience: The Official Journal of the Society for Neuroscience*, *37*(11), 2960–2975. https://doi.org/10.1523/JNEUROSCI.2374-16.2017

Waguespack, J., Salles, F. T., Kachar, B., & Ricci, A. J. (2007). Stepwise Morphological and Functional Maturation of Mechanotransduction in Rat Outer Hair Cells. *The Journal of Neuroscience*, *27*(50), 13890–13902. https://doi.org/10.1523/JNEUROSCI.2159-07.2007

Wan, G., & Corfas, G. (2017). Transient auditory nerve demyelination as a new mechanism for hidden hearing loss. *Nature Communications*, *8*, 14487. https://doi.org/10.1038/ncomms14487

Wang, H. C., & Bergles, D. E. (2015). Spontaneous activity in the developing auditory system. *Cell and Tissue Research*, *361*(1), 65–75. https://doi.org/10.1007/s00441-014-2007-5

Wangemann, P. (2006). Supporting sensory transduction: Cochlear fluid homeostasis and the endocochlear potential. *The Journal of Physiology*, *576*(1), 11–21. https://doi.org/10.1113/jphysiol.2006.112888

Watt, A. J., Cuntz, H., Mori, M., Nusser, Z., Sjöström, P. J., & Häusser, M. (2009). Traveling waves in developing cerebellar cortex mediated by asymmetrical Purkinje cell connectivity. *Nature Neuroscience*, *12*(4), 463–473. https://doi.org/10.1038/nn.2285

Weisz, C., Glowatzki, E., & Fuchs, P. (2009). The postsynaptic function of type II cochlear afferents. *Nature*, *461*(7267), 1126–1129. https://doi.org/10.1038/nature08487

Weisz, C. J. C., Lehar, M., Hiel, H., Glowatzki, E., & Fuchs, P. A. (2012). Synaptic Transfer from Outer Hair Cells to Type II Afferent Fibers in the Rat Cochlea. *The Journal of Neuroscience*, *32*(28), 9528–9536. https://doi.org/10.1523/JNEUROSCI.6194-11.2012

Wong, A. B., Rutherford, M. A., Gabrielaitis, M., Pangršič, T., Göttfert, F., Frank, T., Michanski, S., Hell, S., Wolf, F., Wichmann, C., & Moser, T. (2014). Developmental refinement of hair cell synapses tightens the coupling of Ca2+ influx to exocytosis. *The EMBO Journal*, *33*(3), 247–264. https://doi.org/10.1002/embj.201387110

Yi, E., Lee, J., & Lee, C. J. (2013). Developmental Role of Anoctamin-1/TMEM16A in Ca2+-Dependent Volume Change in Supporting Cells of the Mouse Cochlea. *Experimental Neurobiology*, *22*(4), 322–329. https://doi.org/10.5607/en.2013.22.4.322

Zdebik, A. A., Wangemann, P., & Jentsch, T. J. (2009). Potassium Ion Movement in the Inner Ear: Insights from Genetic Disease and Mouse Models. *Physiology (Bethesda, Md.)*, *24*, 307–316. https://doi.org/10.1152/physiol.00018.2009

Zhang, D.-S., Piazza, V., Perrin, B. J., Rzadzinska, A. K., Poczatek, J. C., Wang, M., Prosser, H. M., Ervasti, J. M., Corey, D. P., & Lechene, C. P. (2012). Multi-isotope imaging mass spectrometry (MIMS) reveals slow protein turnover in hair-cell stereocilia. *Nature*, *481*(7382), 520–524. https://doi.org/10.1038/nature10745

Zhang-Hooks, Y., Agarwal, A., Mishina, M., & Bergles, D. E. (2016). NMDA Receptors Enhance Spontaneous Activity and Promote Neuronal Survival in the Developing Cochlea. *Neuron*, *89*(2), 337–350. https://doi.org/10.1016/j.neuron.2015.12.016

Zidanic, M., & Brownell, W. E. (1990). Fine structure of the intracochlear potential field. I. The silent current. *Biophysical Journal*, *57*(6), 1253–1268.

Appendix

Appendix 1 Fisher's Exact Test on Spiking IHCs in TMEM16A$^{fl/fl}$::Pax2-Cre model

Age = 5	Prob	Significance
Left-sided test	1.000	
right-sided test	0.068	
two-sided test	0.106	
Age = 6	Prob	Significance
Left-sided test	1.000	
right-sided test	0.057	
two-sided test	0.096	
Age = Total	Prob	Significance
Left-sided test	1.000	
right-sided test	0.003	**
two-sided test	0.006	**

Appendix 2 Statistical quantities of ISIs in TMEM16A$^{fl/fl}$::Pax2-Cre model

	Mean		Minimum		Median		Maximum	
	Control	cKO	Control	cKO	Control	cKO	Control	cKO
Test	Mann-Whitney		Mann-Whitney		Mann-Whitney		Student t-test	
p-value	0.586		0.451		0.652		0.483	
Significance								
N total	13	11	13	11	13	11	13	11
Mean	411.12	312.14	398.69	300.73	411.12	311.86	423.54	323.82
SD	362.07	227.34	367.10	235.29	362.07	227.54	362.29	222.44
Minimum	46.00	2.00	46.00	2.00	46.00	2.00	46.00	2.00
Median	351.00	281.50	193.00	243.00	351.00	281.50	352.00	320.00
Maximum	1209.00	713.00	1209.00	713.00	1209.00	713.00	1209.00	713.00

Appendix 3 Statistical quantities of long bursts in TMEM16A$^{fl/fl}$::Pax2-Cre model

	Total burst lengths		N total		Mean		Minimum		Median		Maximum	
	Control	cKO	Control	cKO	Control	cKO	Control	cKO	Control	cKO	Control	cKO
Test	Mann-Whitney		Mann-Whitney		Mann-Whitney		Student t-test		Mann-Whitney		Mann-Whitney	
p-value	0.560		0.719		0.544		0.395		0.577		1.000	
Significance												
N total	171.00	78.00	18.00	11.00	16.00	11.00	16.00	11.00	16.00	11.00	16.00	11.00
Mean	1070.02	1372.92	9.50	7.09	1001.17	1200.31	495.17	550.76	869.88	896.38	2152.26	3256.99
Standard Deviation	672.46	1557.16	7.96	4.01	215.06	503.77	199.81	133.94	186.12	188.55	1011.06	3133.74
Minimum	242.15	375.85	0.00	1.00	647.30	638.91	242.15	375.85	647.30	590.98	647.30	698.75
Median	854.85	880.95	6.50	7.00	994.75	1026.69	494.18	513.05	800.24	964.45	2153.68	1650.25
Maximum	3959.80	9733.85	23.00	13.00	1341.45	1883.23	899.00	812.80	1300.38	1158.30	3959.80	9733.85

Appendix 4 Pearson's r from calcium imaging in TMEM16A$^{fl/fl}$::Pax2-Cre model

Control: 5 animals, cKO: 14 animals

Cell pairs	Pearson's r 1-3		Pearson's r 1-3 per recording		Pearson's r 1		Pearson's r 2		Pearson's r 3	
Grouping	Control	cKO	Control	cKO	Control	cKO	Control	cKO	Control	cKO
Test	Mann-Whitney		Mann-Whitney		Mann-Whitney		Mann-Whitney		Mann-Whitney	
p-value	1.07E-46		0.018233534		4.93E-19		8.44E-15		2.22E-16	
Significance	**		*		**		**		**	
N total (waves)	846	2778	5	14	306	1000	282	926	258	852
Mean	0.22	0.11	0.21	0.10	0.24	0.12	0.22	0.12	0.21	0.10
SD	0.19	0.17	0.10	0.07	0.20	0.18	0.19	0.16	0.18	0.15
Minimum	-0.18	-0.40	0.10	0.01	-0.15	-0.34	-0.18	-0.40	-0.13	-0.31
Median	0.20	0.10	0.19	0.10	0.21	0.10	0.19	0.11	0.18	0.08
Maximum	0.79	0.73	0.38	0.29	0.79	0.69	0.61	0.73	0.63	0.60

Cell pairs	Pearson's r 4		Pearson's r 5		Pearson's r 6		Pearson's r 7		Pearson's r 8	
Grouping	Control	cKO	Control	cKO	Control	cKO	Control	cKO	Control	cKO
Test	Mann-Whitney		Mann-Whitney		Mann-Whitney		Mann-Whitney		Mann-Whitney	
p-value	5.96E-12		3.59E-08		9.37E-10		2.14E-04		4.86E-06	
Significance	**		**		**		**		**	
N total (waves)	234	778	210	704	186	630	162	556	142	486
Mean	0.18	0.09	0.17	0.09	0.15	0.08	0.14	0.08	0.14	0.06
SD	0.17	0.15	0.18	0.15	0.16	0.14	0.18	0.14	0.16	0.14
Minimum	-0.16	-0.35	-0.16	-0.38	-0.25	-0.30	-0.15	-0.32	-0.14	-0.40
Median	0.17	0.08	0.13	0.08	0.13	0.07	0.10	0.07	0.11	0.06
Maximum	0.59	0.62	0.64	0.65	0.57	0.62	0.63	0.58	0.54	0.64

Appendix 5 Statistical quantities of electrophysiological properties in immature IHCs from TMEM16A$^{fl/fl}$::Pax2-Cre mice

	Resting V_m (mV)		Spiking Threshold (pA)		AP Half-width (ms)	
Grouping	**Control**	**cKO**	**Control**	**cKO**	**Control**	**cKO**
Test	**Student t-test**		**Student t-test**		**Student t-test**	
***p*-value**	0.908		0.886		0.489	
Significance						
N	6	9	6	9	6	8
Mean	-86.72	-86.43	70.00	68.89	4.10	4.43
SD	5.43	4.17	14.14	14.53	0.81	0.86
SEM	2.22	1.39	5.77	4.84	0.33	0.30
Median	-89.23	-87.23	70.00	70.00	4.13	4.64

	I_{steady} at 0 mV (pA)		I_{init} at -25 mV (pA)	
Grouping	**Control**	**cKO**	**Control**	**cKO**
Test	Student t-test		Student t-test	
***p*-value**	0.866		0.876	
Significance				
N	6	9	7	9
Mean	5343.62	5246.55	-207.00	-201.24
SD	449.90	1766.76	92.68	50.49
SEM	183.67	588.92	35.03	16.83
Median	5431.45	5064.68	-207.10	-197.44

Appendix 6 Statistical quantities of electrophysiological properties in post-hearing IHCs from TMEM16A$^{fl/fl}$::Pax2-Cre mice.

	Resting V_m (mV)		I_{steady} at 0 mV (pA)		I_{init} at -25 mV (pA)	
Grouping	Control	cKO	Control	cKO	Control	cKO
Test	Student t-test		Student t-test (Welch corrected)		Student t-test (Welch corrected)	
p-value	0.050		0.213		0.213	
Significance						
N	6	17	6	13	6	17
Mean	-73.70	-78.81	14407.78	12712.85	2899.71	2303.75
SD	5.62	5.04	2654.40	2905.41	761.56	1399.70
SEM	2.30	1.22	1083.65	805.82	310.90	339.48
Median	-73.70	-80.55	14152.71	11795.16	3101.71	2151.83

	$I_{K,n}$ at -144 mV (pA)	
Grouping	Control	cKO
Test	Student t-test (Welch corrected)	
p-value	0.955	
Significance		
N	4	17
Mean	-335.18	-340.38
SD	165.19	112.32
SEM	82.60	27.24
Median	-267.46	-348.74

	I_{init} at -25 mV (pA)		I_{init} at -25 mV (pA)		I_{init} at -25 mV (pA)	
Grouping	Control	cKO	Control	cKO	cKO	cKO
Age	< P20	< P20	< P20	> P20	< P20	> P20
Test	Student t-test (Welch corrected)		Student t-test (Welch corrected)		Student t-test	
p-value	0.006		0.891		0.009	
Significance	**				**	
N	5	9	5	8	9	8
Mean	3115.42	1522.46	3115.42	3182.71	1522.46	3182.71
SD	613.18	1177.12	613.18	1107.60	1177.12	1107.60
SEM	274.22	392.37	274.22	391.60	392.37	391.60
Median	3159.44	1360.05	3159.44	3350.28	1360.05	3350.28

Appendix 7 Statistical quantities of ISIs in TMEM16A$^{fl/fl}$::Plp1-Cre model

	Mean		Minimum		Median		Maximum	
	Control	cKO	Control	cKO	Control	cKO	Control	cKO
Test	Mann-Whitney		Student t-test		Mann-Whitney		Mann-Whitney	
p-value	0.106		0.641		0.149		0.256	
Significance								
N total	7	5	7	5	7	5	7	5
Mean	2104.49	6173.44	40.22	46.84	209.63	234.06	69704.70	123428.12
SD	1353.42	4621.50	24.04	22.72	93.06	34.55	41657.01	78686.54
Minimum	1102.29	1648.22	13.90	14.70	129.15	188.70	25459.40	40871.85
Median	1752.64	3699.18	39.80	59.00	186.98	240.73	58211.20	104456.15
Maximum	5070.85	12458.45	71.15	67.85	405.70	279.90	131647.65	236914.90

Appendix 8 Statistical quantities of long bursts in TMEM16A$^{fl/fl}$::Plp1-Cre model

	Total burst lengths		Number		Mean	
	Control	cKO	Control	cKO	Control	cKO
Test	Mann-Whitney		Student t-test		Student t-test	
p-value	0.560		0.055		0.893	
Significancy						
N total	41	11	7	4	7	4
Mean	1309.71	1186.58	5.86	2.75	1168.31	1200.34
Standard Deviation	894.12	372.29	3.39	0.96	503.00	267.40
Minimum	300.75	659.85	1.00	2.00	448.48	906.45
Median	929.65	1240.70	7.00	2.50	1282.30	1183.76
Maximum	3837.10	1846.15	11.00	4.00	1998.98	1527.38

	Minimum		Median		Maximum	
	Control	cKO	Control	cKO	Control	cKO
Test	Student t-test		Student t-test		Student t-test	
p-value	0.180		0.279		0.105	
Significancy						
N total	7	4	7	4	7	4
Mean	579.55	916.49	967.98	1228.74	2349.45	1443.54
Standard Deviation	152.27	387.19	481.91	269.11	1221.57	328.38
Minimum	300.75	659.85	323.25	906.45	721.45	1119.20
Median	574.65	759.37	929.65	1240.56	2642.00	1404.40
Maximum	777.35	1487.35	1899.25	1527.38	3837.10	1846.15

Appendix 9 Pearson's r from calcium imaging in TMEM16A$^{fl/fl}$::Plp1-Cre model

Control: 7 animals, cKO: 1 animal.

	Pearson's r		Pearson's r		Pearson's r		Pearson's r		Pearson's r	
Cell pairs	1-3		1-3 per recording		1		2		3	
Grouping	Control	cKO	Control	cKO	Control	cKO	Control	cKO	Control	cKO
Test	Mann-Whitney		Mann-Whitney		Mann-Whitney		Mann-Whitney		Mann-Whitney	
p-value	1.84536E-05		0.856		4.53327E-05		0.066		0.158	
Significancy	**				**					
N total	912	228	5	1	328	84	304	76	280	68
Min	-0.23	-0.22	0.12	0.08	-0.19	-0.15	-0.23	-0.22	-0.20	-0.10
Q1	0.03	-0.01	0.18	0.08	0.05	0.01	0.03	-0.01	0.01	-0.01
Median	0.18	0.08	0.25	0.08	0.20	0.08	0.19	0.13	0.15	0.08
Q3	0.34	0.23	0.28	0.08	0.39	0.17	0.33	0.25	0.30	0.23
Max	0.73	0.74	0.31	0.08	0.71	0.63	0.73	0.57	0.71	0.74

	Pearson's r		Pearson's r		Pearson's r		Pearson's r		Pearson's r	
Cell pairs	4		5		6		7		8	
Grouping	Control	cKO	Control	cKO	Control	cKO	Control	cKO	Control	cKO
Test	Mann-Whitney		Mann-Whitney		Mann-Whitney		Mann-Whitney		Mann-Whitney	
p-value	0.063		0.235		0.663		0.159		0.410	
Significancy										
N total	256	60	232	52	208	44	184	36	160	30
Min	-0.23	-0.17	-0.21	-0.07	-0.31	-0.07	-0.17	-0.18	-0.26	-0.19
Q1	0.04	0.04	0.02	0.02	-0.01	0.02	-0.01	-0.03	-0.01	-0.07
Median	0.17	0.10	0.12	0.09	0.08	0.11	0.09	0.07	0.06	0.09
Q3	0.31	0.21	0.26	0.16	0.20	0.18	0.21	0.12	0.17	0.15
Max	0.68	0.47	0.71	0.44	0.77	0.35	0.64	0.34	0.63	0.25

Appendix 10 Statistical quantities of immature electrophysiological properties in IHCs from TMEM16A$^{fl/fl}$::Plp1-Cre mice

	Resting *V*m (mV)		Spiking Threshold (pA)		AP Half-width (ms)	
Grouping	Control	cKO	Control	cKO	Control	cKO
Test	Student t-test		Student t-test		Student t-test	
p-value	0.075		0.766		0.790	
Significancy						
N	4	6	4	4	4	4
Mean	-92.39	-85.50	75.00	72.50	4.00	4.12
SD	4.26	5.73	12.91	9.57	0.65	0.55
Minimum	-97.30	-95.31	60.00	60.00	3.07	3.46
Median	-91.90	-84.58	75.00	75.00	4.21	4.18
Maximum	-88.47	-77.99	90.00	80.00	4.51	4.66

	I_{steady} at 0 mV (pA)		I_{init} at -25 mV (pA)	
Grouping	Control	cKO	Control	cKO
Test	Student t-test (Welch corrected)		Student t-test	
p-value	0.541		0.777	
Significancy				
N total	4	6	4	6
Mean	6158.17	5688.15	-216.31	-194.24
Standard Deviation	547.89	1655.15	114.46	118.07
Minimum	5530.96	3548.06	-377.04	-330.27
Median	6147.15	6135.71	-185.20	-191.06
Maximum	6807.41	7480.34	-117.81	2.40

Appendix 11 Statistical quantities of electrophysiological properties in post-hearing IHCs from TMEM16A$^{fl/fl}$::Plp1-Cre mice.

	Resting V_m (mV)		$I_{K,n}$ at -144 mV (pA)		I_{init} at -25 mV (pA)		I_{steady} at 0 mV (pA)	
Grouping	Control	cKO	Control	cKO	Control	cKO	Control	cKO
Test	Mann-Whitney		Student t-test (Welch corrected)		Student t-test (Welch corrected)		Student t-test (Welch corrected)	
p-value	0.860		0.275		0.912		0.836	
Significance								
N total	11	7	11	5	11	5	10	5
Mean	-75.77	-77.82	-361.24	-368.46	2085.84	1995.78	11812.76	8870.83
Standard Deviation	5.18	3.20	93.66	43.44	617.00	1676.30	2030.81	5123.47
Minimum	-81.60	-84.21	-541.92	-433.28	1134.49	269.99	8563.89	3271.07
Median	-77.49	-78.04	-346.70	-364.85	2237.61	1323.54	12176.25	9410.51
Maximum	-64.70	-74.72	-257.28	-321.12	2964.10	4008.06	14196.17	16091.12

Appendix 12 Copyright information of the materials used

Figure 1.2 Human cochlea "unrolled".	Copyright Clearance Center’s RightsLink® Order Number: 5440220141659
Figure 1.3 Histology of immature and mature-like organ of Corti	CC-BY-4.0 for Iyer *et al.* Copyright Clearance Center’s RightsLink® Order Number: 5440221011082
Figure 1.5 Organ of Corti in action	Copyright Clearance Center’s RightsLink® Order Number: 5440220141659
Figure 1.6 Innervation pattern in mature organ of Corti.	Copyright Clearance Center’s RightsLink® Order Number: 5440221184982
Figure 1.9 Development and structure of the hair bundles.	**Order License ID:** 1295958-1
Figure 1.10 Morphological maturation of hair bundles in rodent model.	CC-BY-4.0
Figure 1.11 Mechano-electro-transducer current in hair cells.	Copyright Clearance Center’s RightsLink® Order Number: 5440230563798
Figure 1.12 Calcium dependent modulation on mechano-electro-transducer current.	Author permission
Figure 1.13 A diagram of the timeline of ribbon synapse formation in mouse.	PNAS open access
Figure 1.14 Structure of a synaptic ribbon.	CC-BY-4.0
Figure 1.16 Maturation of Ca_V1.3 mediated calcium current and synaptic release.	Author permission
Figure 1.17 Delayed rectifier current in immature IHC.	Author permission
Figure 1.18 Physiology of sodium current from immature mouse IHC.	Author permission
Figure 1.19 Action potential waveforms with deleted or blocked SK2 current.	Author permission
Figure 1.20 Developmental change of outward current in inner hair cells.	Copyright Clearance Center’s RightsLink® Order Number: 5440231145919
Figure 1.21 Propagating calcium wave in supporting cell networks.	Copyright Clearance Center’s RightsLink® Order Number: 5441890157134

Figure 1.22 Current interplay in a single action potential.	Author permission
Figure 1.23 Tonotopic difference of spontaneous action potential in immature IHC.	Author permission
Figure 1.24 Generating the calcium wave in the GER.	Copyright Clearance Center's RightsLink® Order Number: 5440231251433
Figure 1.25 Crenation of GER supporting cells during calcium wave.	Copyright Clearance Center's RightsLink® Order Number: 5440231358289 5440231475428
Figure 1.26 Correlation of ATP response in the critical period of maturation in IHC.	Author permission CC-BY-4.0
Figure 1.27 Concentration-dependent effect of ATP on IHC membrane potential.	Author permission
Figure 1.28 Connexin deficiency impaired the maturation of IHC.	Author permission
Figure 3.19 Pax2-Cre did not fully knockout TMEM16A in the literature	Copyright Clearance Center's RightsLink® Order Number: 5440231475428
Figure 3.21 Atypical silence period with depolarized V_m in SK2-KO IHC.	Author permission